

ILLUMINATING MERGERS OF CARBON-OXYGEN WHITE-DWARFS
AND THEIR POSSIBLE LINK TO THERMONUCLEAR SUPERNOVAE

by

Chenchong Zhu

A thesis submitted in conformity with the requirements
for the degree of Doctor of Philosophy
Graduate Department of Astronomy & Astrophysics
University of Toronto

© Copyright 2016 by Chenchong Zhu

Abstract

Illuminating Mergers of Carbon-Oxygen White-Dwarfs
and Their Possible Link to Thermonuclear Supernovae

Chenchong Zhu
Doctor of Philosophy
Graduate Department of Astronomy & Astrophysics
University of Toronto
2016

The merger of two carbon-oxygen white dwarfs (CO WDs) can either create a more massive WD, lead to collapse into a neutron star, or explode spectacularly as a thermonuclear, or type Ia, supernova (SN Ia). It has traditionally been believed that SNe Ia result only from mergers at or above the Chandrasekhar mass (M_{Ch}), as these can subsequently become dense enough to trigger runaway fusion. Recently, however, it has been proposed that the merged product, or “remnant”, might instead ignite fusion from high temperatures reached during post-merger evolution. This opens the possibility of SNe Ia arising even from sub- M_{Ch} mergers.

To investigate the outcome of double CO WD mergers, I conducted a series of hydrodynamic simulations of the merging process. I first performed simulations spanning the range of possible mergers using the smoothed-particle hydrodynamics code GASOLINE, finding that remnant configurations are roughly homologous for mergers of WDs with the same difference in mass ΔM . In particular, “similar-mass” mergers with $\Delta M \lesssim 0.1 M_{\odot}$ generate remnants that are heated throughout their dense cores, making them candidates for subsequent explosion.

These results are challenged by my simulations of a $0.625 - 0.65 M_{\odot}$ merger using the moving-mesh code AREPO. Unlike in GASOLINE, the merger remnant in AREPO not only has a relatively cold core, but one that is crescent-shaped and launches a one-armed spiral wave into its surroundings. I also insert weak magnetic fields into the WDs in AREPO, and find exponential field growth during their merger, leading to a $> 10^{10}$ G field within the remnant. Further study is required to understand how these novel features alter post-merger evolution.

Lastly, I calculate the evolution of idealized CO WDs experiencing runaway nuclear burning in their centers, which ends either with an explosion or expansion into a carbon-burning star. I determine the minimum mass for an explosion to be $M_{\text{crit}} = 1.135 M_{\odot}$, which can be reached by the dense cores of some sub- M_{Ch} merger remnants. These remnants, however, are likely too underdense to explode.

“Quote...”

-Someone

Acknowledgements

some acknowledgements.

Contents

1	Introduction	1
1.1	Mergers of Two White Dwarfs	2
1.2	Merger Outcomes	4
1.3	The Mystery of Type Ia Supernovae	6
1.3.1	Traditional Formation Scenarios and Their Pitfalls	7
1.3.2	Brave New Channels	9
1.4	The Sub-Chandrasekhar CO WD Merger Channel	11
1.5	Massive Merger Remnants	12
1.6	Thesis Overview	14
1.7	Pre-Merger Evolution	15
1.7.1	Typical CO WD Masses	15
1.7.2	Merger Initial Conditions and Unstable Mass Transfer	16
2	A Parameter-Space Study of Carbon-Oxygen White Dwarf Mergers	19
2.1	Introduction	20
2.2	Code and Input Physics	21
2.2.1	The SPH Code	21
2.2.2	Initial Conditions	22
2.2.3	Merger Completion Time	24
2.3	Results	24
2.3.1	Representative Mergers	24
2.3.2	Merger Trends	28
2.3.3	A Qualitative Picture of the Merger	42
2.4	Variation of Merger Parameters and Robustness of Results	43
2.4.1	Changing the Composition	43
2.4.2	Varying the Initial Binary Separation	43
2.4.3	Synchronization	46
2.4.4	Running the Simulation Longer	48
2.4.5	Viscosity Prescription	50
2.4.6	Spurious Heating	50
2.4.7	Resolution	52
2.5	Comparison With Others	54
2.5.1	Comparison With Lorén-Aguilar et al. (2009)	54

2.5.2	Comparison with Others	56
2.5.3	The Importance of Accurate Initial Conditions	56
2.6	Post-Merger Evolution	60
2.6.1	Viscous Evolution and Possible Spin Down	60
2.6.2	Possible Explosions?	63
2.7	Conclusion	63
2.8	Postscript: Post-Merger Evolution Revisited	64
3	Mergers in Smoothed-Particle and Moving Mesh Hydrodynamics	69
3.1	Introduction	70
3.2	Codes and Initial Conditions	71
3.2.1	Traditional Smoothed-Particle Hydrodynamics	72
3.2.2	GASOLINE SPH Code	74
3.2.3	AREPO Moving Mesh Code	75
3.2.4	Initial Conditions and Completion Time	78
3.3	Improving Angular Momentum Conservation in Arepo	79
3.4	Results	83
3.5	Discussion	88
3.5.1	Resolution Test	88
3.5.2	Varying Viscosity in GASOLINE	91
3.5.3	Sources of Differences Between Simulations	92
3.6	Conclusions and Ramifications for Mergers	93
4	Magnetized Moving Mesh Merger of a Carbon-Oxygen White Dwarf Binary	96
4.1	Introduction	97
4.2	Methods	97
4.3	Results	98
4.4	Robustness Tests	102
4.4.1	Resolution Test	102
4.4.2	Changing the Seed Field Strength	103
4.5	Discussion	103
4.6	Postscript: Reconsidering Divergence Cleaning in AREPO	105
5	The Evolution of Simmering Sub-Chandrasekhar Mass WDs	108
5.1	Introduction	109
5.2	Modeling Sub- M_{Ch} WD Simmering	110
5.2.1	Analytical Description	110
5.2.2	Semi-Analytical Model	113
5.3	Results	115
5.3.1	Adiabatic Approximation	116
5.3.2	Superadiabatic Deviation Δ_{conv}	119
5.3.3	Rotation and Magnetic Fields	119
5.4	Discussion	121
5.4.1	Comparison to Observed $M_{\text{tot}}\text{-}M_{\text{Ni}}$ Relations	121

5.4.2	Implications for Mergers as SN Ia Progenitors	123
5.4.3	Accuracy of Magnetized Simmering Models	124
5.5	Conclusions	125
5.6	Appendix: Convective Suppression due to Rotation and Magnetic Fields	126
5.6.1	Simmering of Rotating White Dwarfs	128
5.6.2	Simmering of Magnetized White Dwarfs	130
5.6.3	Sensitivity to Mixing Length Theory Coefficients	133
6	Conclusion	136
6.1	Mergers and Early Post-Merger Evolution	136
6.2	Viscous Evolution and Ignition	138
6.3	Ignition, Simmering and Explosions	138
6.4	What are the Outcomes of CO WD Mergers?	141
6.5	Observational Avenues of Exploration	141
Bibliography		143

List of Tables

List of Figures

1.1	The expected compositions for white dwarfs undergoing a merger as a function of their masses, from Dan et al. (2012, their Fig. 1). M_1 is the mass of the accretor, or primary, WD (M_a in the text), and M_2 is the mass of the donor, or secondary (M_d). WDs with masses $M < 0.45 M_\odot$ are assumed to be He WDs, those with $0.45 < M < 0.6 M_\odot$ CO WDs with thick He envelopes, $0.6 < M < 1.05 M_\odot$ CO WDs, and $M > 1.05 M_\odot$ ONE WDs. See text, as well as Dan et al. (2012) Sec. 2, for discussion on these choices.	2
1.2	Regions of stable and unstable mass transfer for the WD merger parameter space from Marsh et al. (2004; their Fig. 1). M_1 is M_a and M_2 is M_d . The upper dashed line is a more accurate estimate for Eqn. 1.6, and the lower dashed one that for Eqn. 1.8. The solid “Direct/Disc” line represents the transition between direct impact and disk accretion. Dotted lines represent the boundary between stable and unstable mass transfer when the tidal synchronization timescale τ_s is 1000, 10 and 0.1 yr.	18
2.1	Structure of a $0.4 - 0.8 M_\odot$ merger remnant, representing the general outcome of a merger of white dwarfs with dissimilar mass. Upper left and middle – binned maps of density ρ and temperature T along slices in the xy and xz -planes. Lower left – binned maps and contours of density, temperature, and angular frequency Ω in the (ω, z) plane, averaged over cylindrical coordinate ϕ and over $\pm z$ (with 1 added to Ω to avoid problems with the logarithmic intensity scale). Middle – enclosed masses of donor and accretor material M_d and M_a (solid red and blue, resp.), and fraction of donor material f_d at a particular mass shell (dashed magenta). Middle, one but lowest – temperature-density profile with enclosed masses in $0.2 M_\odot$ increments indicated, both along the equatorial plane (solid curve, squares) and along the rotational axis (dot-dashed curve, circles). Middle, bottom – enclosed mass as a function of r , with the total mass indicated by the horizontal dashed red line. Right-hand column, top to bottom - density, temperature, entropy, angular (cyan) and Keplerian (blue) frequency, and degeneracy (blue), thermal (red) and rotational (cyan) specific energies as a function of enclosed mass M , both along the equatorial plane and along the rotational axis (solid and dot-dashed curves, respectively). In all graphs, the start of the disk (where the centrifugal acceleration equals half the gravitational one) and the equatorial radius (or mass enclosed within) of maximum temperature are marked by vertical green and blue dashed lines, respectively. [See the electronic edition of the Journal for Figs. 1.1–1.48.]	25
2.2	As Fig. Set 2.1, but for a $0.6 - 0.6 M_\odot$ merger remnant, representing the general outcome of a similar-mass merger.	26

- 2.3 Properties of mergers with $0.65 M_{\odot}$ (left) and $1.0 M_{\odot}$ (right) accretors, for donor masses of 0.4 (red), 0.5 (orange), 0.55 (lime), 0.575 (green), 0.6 (cyan), 0.625 (light blue), 0.64 (blue), 0.65 (dark blue), 0.7 (magenta), 0.8 (purple), 0.9 (brown), and $1.0 M_{\odot}$ (black). Shown are, from top to bottom, density ρ , fraction of donor material f_d , angular frequency Ω , temperature T , specific thermal energy E_{th} , and specific rotational energy E_{rot} , all as a function of fractional enclosed mass M/M_{tot} . All properties are determined along the equatorial plane, except for f_d which is defined spherically. The $1.0 - 1.0 M_{\odot}$ merger (dashed black line) is an outlier; see text. 29
- 2.4 Dependence of the properties of mergers on mass difference, with, from left to right, $\Delta M \equiv M_a - M_d = 0.0, 0.1, 0.2$, and $0.3 M_{\odot}$ mergers. Properties shown, coloring, and line styles are as in Fig. 2.3, except color represents accretor mass. 30
- 2.5 Relation between central density ρ_c and mass M for carbon-oxygen white dwarfs, showing both the results of relaxing white dwarf models in Gasoline (red points), and integrating hydrostatic equilibrium directly for spherically symmetric, non-rotating CO WDs with $T = 5 \times 10^6$ K (blue line). For the mass range considered, the central density depends roughly exponentially on mass. 31
- 2.6 Dependence of merger core properties on the ratio of the donor and accretor central densities, $\rho_{c,d}/\rho_{c,a}$. Shown are the ratio of central to maximum temperature T_c/T_{max} (squares), central to maximum angular velocity $\Omega_c/\Omega_{\text{max}}$ (triangles), and central core donor to accretor mass fraction $(f_d/f_a)_{\text{cc}}$ (circles), with colors representing different accretor masses, encoded as in Fig. 2.3. The vertical line marks $q_{\rho} \equiv \rho_{c,d}/\rho_{c,a} = 0.6$, where $\Omega_c/\Omega_{\text{max}}$ reaches unity, $(f_d/f_a)_{\text{cc}}$ becomes non-zero, and $T_c/T_{\text{max}} \simeq 0.5$. We suggest it separates “dissimilar” from “similar” mass mergers. 32
- 2.7 Structural properties of mergers. (a) Central scaleheights along the rotational axis (circles) and along the equatorial plane (squares) scaled to the scaleheight of the accretor, h_z/h_a and h_{ω}/h_a . (b) Central density of the merger remnant scaled to the central density of the accretor, $\rho_c/\rho_{c,a}$. Colors represent different accretor masses, encoded as in Fig. 2.3. Triangles represent the outlying $1.0 - 1.0 M_{\odot}$ merger. 34

2.8 Mixing, heating, and spin-up (left to right) for mergers. (a) Scaled mass of the remnant core-envelope (where scaling here and below is to the accretor mass). (b) Fraction of the accretor within the mass enclosing half the donor mass. (c) Scaled remnant mass enclosing half the donor mass. (d) Fraction of the accretor mass within the region enclosing 25–75% of the donor mass. (e) Maximum equatorial temperature T_{\max} (circles), with the approximation $T_{\max} = 0.20GM_a m_p / k_B R_a$ overdrawn. Maximum temperatures along the rotational axis are shown with crosses. (f) Scaled density at the location of T_{\max} (symbols as above). (g) Scaled mass enclosed within the radius of T_{\max} (symbols as above). (h) Scaled mass enclosing half of the remnant thermal energy. (i) Scaled mass of the region enclosing 25 – 75% of the remnant thermal energy. (j) Maximum angular velocity Ω_{\max} (circles) with best fit $\Omega_{\max} = 3.8\Omega_{\text{orb}}$ overdrawn. (k) Fraction of the angular momentum in the core-envelope. (l) Scaled mass enclosed within the radius of maximum angular velocity. (m) Scaled mass enclosing half of the total remnant rotational energy. (n) Scaled mass of the region enclosing 25 – 75% of the remnant rotational energy. Colors represent different accretor masses, encoded as in Fig. 2.3. Triangles represent equatorial plane values, and x-marks rotational axis values, of the 1.0 - $1.0 M_{\odot}$ merger.	36
2.9 Partition of energies in (a) the overall merger remnant, (b) the remnant core plus envelope, and (c) the remnant disk. In each panel, the fraction of total energy carried in degeneracy (triangles), thermal (squares), and rotational (circles) energy is shown. Colors represent different accretor masses, encoded as in Fig. 2.3. Triangles represent the 1.0 - $1.0 M_{\odot}$ merger.	39
2.10 As Fig. 2.3, but for 0.4 - $0.4 M_{\odot}$ (left) and 0.4 - $0.8 M_{\odot}$ (right) mergers with different compositions: pure ^4He (red), CO (orange), and pure ^{24}Mg (lime). Dash-dotted lines represent profiles along the rotational axis rather than the equatorial plane.	44
2.11 As Fig. 2.10, but for 0.6 - $0.6 M_{\odot}$ (left) and 0.6 - $0.8 M_{\odot}$ (right) mergers with varying initial orbital separation: 0.9 (red), 1.0 (green), and 1.1 (blue) times the value used for the parameter space study.	45
2.12 As Fig. 2.10, but for 0.6 - $0.6 M_{\odot}$ (left) and 0.6 - $0.8 M_{\odot}$ (right) mergers, comparing our default, irrotational case (blue) with that assuming synchronous rotation (red).	47
2.13 As Fig. 2.10, but for 0.6 - $0.6 M_{\odot}$ (left) and 0.6 - $0.8 M_{\odot}$ (right) mergers, comparing properties for our default simulation time of 6 initial orbital periods (blue) with those obtained after 8 orbital periods (red).	49
2.14 As Fig. 2.10, but comparing simulations of a 0.6 - $0.8 M_{\odot}$ merger with different viscosity prescriptions (left) and simulations of a 0.625 - $0.65 M_{\odot}$ merger with different numbers of particles (right). For the viscosity, we compare fixed low viscosity ($\alpha = 0.05, \beta = 0.1$; blue), standard variable viscosity (green), and fixed high viscosity ($\alpha = 1.0, \beta = 2.0$; red). For particle numbers, we show simulations at one quarter (red), half (orange), and double (blue) the default number of particles, as well as the default simulation (lime) and a rerun of the default simulation (green) to determine the effect of order-of-execution differences, round-off errors and other such numerical effects.	51

2.15 Specific thermal energy as a function of enclosed mass for a $0.4 - 0.8 M_{\odot}$ (blue) and a $0.7 - 0.8 M_{\odot}$ merger (red), shown both along the equatorial plane (solid curves) and along the rotational axis (dot-dashed). Also shown are the (spherical) profiles found for an isolated $0.8 M_{\odot}$ white dwarf (dashed) simulated using the same parameters, and for the same completion times (six initial orbital periods, equivalent to 489 s and 224 s). Spurious heating is estimated to be responsible for nearly all the thermal energy in the core of the $0.4 - 0.8 M_{\odot}$ remnant, and for about one third in the core of the $0.7 - 0.8 M_{\odot}$ remnant. It is not important in regions heated by interaction. (The “hook” in the outer layers of the white dwarf profile reflects the high initial temperature chosen; in a merger, this is erased by the interaction.) 53

2.16 Comparison of our results with those of LIG09, for a $0.6 - 0.6 M_{\odot}$ (left) and a $0.6 - 0.8 M_{\odot}$ (right) merger. Shown are surface density, remnant (solid) and Keplerian (dashed) angular frequency, and temperature, with profiles from LIG09 in blue, and our equivalent ones in red and orange. Here, the former are for our default completion time of 6 initial orbital periods and the latter for their completion times (514 s or 10.9 orbital periods for the $0.6 - 0.6 M_{\odot}$ merger, and 164 s or 3.4 orbits for the $0.6 - 0.8 M_{\odot}$ merger). . . 55

2.17 Left: merger remnant maximum temperature T_{\max} and corresponding density $\rho(T_{\max})$ for all merger remnants. Values along the equatorial plane are marked with circles, with lines connecting points with the same accretor mass, while values along the rotational axis (only plotted for similar-mass mergers) are marked with triangles (for all, colors indicate accretor mass, encoded as in Fig. 2.3). For similar-mass mergers, equatorial temperatures have been adjusted to account for mixing in convectively unstable cores. Right: maximum temperatures and corresponding densities following estimated post-merger evolution. The estimate assumes that the remnant spins down completely, that all rotational energy is used to drive matter to large distances, and that the remainder adjusts adiabatically (see text). Also shown are contours of constant neutrino cooling timescale $\tau^* \equiv C_p T / \epsilon_{\nu}$ and carbon fusion heating timescale $\tau_{\text{cc}} \equiv C_p T / \epsilon_{\text{CC}}$, both in years, as well as entropy S in erg K^{-1} . (Here, C_p is the heat capacity at constant pressure and ϵ the specific energy loss/gain rate.) The lines labeled $\tau_{\text{cc}} = \tau^*$ and $\tau_{\text{cc}} = \tau_{\text{dyn}}$ denote where the carbon fusion heating timescale balances the neutrino cooling and dynamical timescales, respectively. Finally, the $P = 2P(T=0)$ line is shown as an approximate upper bound of the region where degeneracy pressure dominates. All quantities were calculated using MESA (Paxton et al. 2011). 58

2.18 Estimate of post-merger viscous evolution for $0.4 - 0.8 M_{\odot}$ (top) and $0.6 - 0.6 M_{\odot}$ (bottom) mergers. In blue are shown the temperature-density structure of the merger remnant, on the equatorial plane before (dotted) and after (solid) correction for convection, as well as along the rotational axis (dot-dashed), with points marking the hottest locations (circles and squares) and steps of $0.2 M_{\odot}$ in spherical enclosed mass (triangles pointing up and down). In red, estimates of the structure following viscous evolution are shown, where it is assumed that the remnant spins down completely, that all rotational energy is used to drive matter to large distances, and that the remainder adjusts adiabatically (see text). For reference, also shown as dotted curves are the contours of constant entropy from Fig. 2.17 (green), as well as the lines where $\tau_{cc} = \tau^*$ (magenta), $\tau_{cc} = \tau_{dyn}$ (red), and $P = 2P(T=0)$ (black).

2.19 Ratio of post-viscous degenerate core mass $M_{c,pv}$ – estimated using the simple viscous evolution prescription in Sec. 2.6.1 – to the remnant total mass M_{tot} as a function of M_{tot} for the systems simulated in this chapter (“Estimate” points; colors have the same meaning as in Fig. 2.17) and the $0.625 - 0.65 M_{\odot}$ remnant from the AREPO MHD simulation (Ch. 4; red-blue star). Also plotted are estimates of $M_{c,pv}/M_{tot}$ from Schwab et al. (2012; using $M_c + M_{tp}$ in their Table 3) with magenta Xs and Ji et al. (2013) with a cyan X. The dotted line is a best fit to the Estimate points given by Eqn. 2.27. 66

2.20 Ratio of post-viscous degenerate core mass $M_{c,pv}$ to remnant core-envelope mass M_{ce} (Sec. 2.3.2.3) as a function of q_{ρ} for the systems simulated in this chapter (“Estimate” points), the $0.625 - 0.65 M_{\odot}$ remnant from the AREPO MHD simulation (red-blue star), the $0.6 - 0.6 M_{\odot}$ remnant of Ji et al. (2013; cyan X) and the $0.6 - 0.9 M_{\odot}$ remnant of Schwab et al. (2012; magenta X). The dotted line is a best fit to the Estimate points given by Eqn. 2.27.

3.1 Schematics for the SPH and AREPO hydrodynamic schemes. In SPH (left), the fluid is discretized into particles, each of which possesses a position \mathbf{r}_i , mass m_i , velocity \mathbf{u}_i and specific internal energy e_i . The density ρ_i of a given particle (red point) is determined by kernel sampling its neighbors (blue) within a smoothing length h_i (Eqn. 3.8); pressure P_i is then obtained using the density and internal energy. The particle is evolved by kernel sampling nearby pressures and densities, and applying the SPH equations of motion (Eqns. 3.11 and 3.12). In AREPO (right), the fluid is discretized using an unstructured mesh defined by Voronoi tessellation. Each Voronoi cell possesses a mesh-generating point \mathbf{r}_i and a set of conserved quantities equivalent to “primitive variables” $\mathbf{W}_i = (\rho_i, \mathbf{u}_i, P_i, \mathbf{B}_i)$, i.e. the values of density, velocity, pressure and magnetic field amplitude at the cell’s center of mass \mathbf{s}_i . Note that $\mathbf{r}_i \neq \mathbf{s}_i$, but their separation is typically a few percent of the cell’s radius, and has been exaggerated above. Fluxes between two cells L and R are calculated by propagating their primitive variables $\mathbf{W}_{L,R}$ to the centroid of their interface \mathbf{f} to obtain $\mathbf{W}_{L,R}^{\text{interface}}$ (Eqn. 3.19, or Eqn. 3.23 following Pakmor et al. 2016), and then solving the Riemann problem (in the frame of the interface). The mesh is evolved by moving the mesh generating points \mathbf{r}_i at roughly the fluid velocity \mathbf{u}_i , calculating fluxes between all cells, and then updating each cell’s conserved quantities. While evolving an SPH particle requires the use of dozens of its neighbors for kernel averaging, evolving an AREPO cell only requires those neighbors directly adjacent to it.

76

3.2 Evolution of total z-axis angular momentum $L_{z,\text{tot}}$ (top cluster of lines in each panel) and that within a cylinder of radius $\omega = 10^9$ cm, $L_{z,\omega < 9}$ (bottom cluster), for various simulations in 2013-2014, before AREPO was updated to better conserve angular momentum. All curves are shifted in time by $t_{\max(L_z)}$, the time in each simulation at which $L_{z,\omega < 9}$ achieved its maximum value, to synchronize the start of post-merger evolution. In the top panel, red and magenta lines represent the low and standard-resolution AREPO simulations, respectively, while the cyan and blue ones represents low and standard-resolution GASOLINE ones, respectively. Dotted lines represent angular momentum balance $L_{\text{bal}}(\omega < 10^9$ cm), which should be flat in the absence of spurious angular momentum losses. (Slightly different initial amounts of total angular momentum between AREPO and GASOLINE runs are due to inconsistencies in their initial conditions that have subsequently been eliminated.) In the bottom panel, the red line is again the low-resolution AREPO simulation, while the green line is an AREPO low-resolution run where the mesh is held static after $t = 200$ s. The dashed black line is a FLASH simulation that uses the AREPO low-resolution run at $t = 200$ s for initial conditions; its loss of total angular momentum is due to having outflow boundaries.

80

3.3 Evolution of total z-axis angular momentum $L_{z,\text{tot}}$ (top cluster of lines) and that within a cylinder of radius $\omega = 10^9$ cm, $L_{z,\omega < 9}$ (bottom cluster) for the AREPO-RKLSF simulations. All curves are shifted in time by t_c (rather than $t_{\max(L_z)}$ like in Fig. 3.2), the time when average separation between donor and accretor material reaches a tenth of its initial value. Colors indicate initial mass resolutions of 5×10^{28} g (red lines), 1×10^{28} g (green) 2×10^{27} g (cyan) and 1×10^{27} g (blue).

83

3.4 Series of equatorial (xy) plane density (left two columns) and temperature (right two columns) intensity plots for five snapshots in time (rows; the time for each snapshot is indicated at the top left of the density plots) during the GASOLINE and AREPO simulations. xz -plane plots are also included for the final snapshot.	84
3.5 Merger remnant profiles from the GASOLINE (red), AREPO (blue) and AREPO MHD (gray; Ch. 4) simulations 99 s after coalescence (around row four of Fig. 3.4). The profiles are, from top to bottom, density ρ , angular rotation speed Ω , temperature T , specific degeneracy energy e_{deg} , specific thermal energy e_{th} , and specific rotational energy e_{rot} , all as a function of the ratio of spherical enclosed to total mass M/M_{tot} . Solid lines represent profiles on the original binary's orbital plane, while dash-dotted lines represent profiles along the rotational axis.	86
3.6 Time evolution of z -axis angular momentum L_z for AREPO (solid lines) and GASOLINE (dashed) simulations. The purple line represents total L_z , while the others represent angular momentum within concentric cylinders aligned along the rotation axis and with radii $\omega = 5 \times 10^8$ (red), 7.5×10^8 (yellow), 1×10^9 (green), 1.5×10^9 (cyan), 3×10^9 (blue) and 6×10^9 cm (magenta).	88
3.7 Merger remnant profiles, as in Fig. 3.5, for GASOLINE (left column) and AREPO (right) simulations of various (initial, for AREPO) mass resolutions. The resolutions are 5×10^{28} g (equivalent to 5.1×10^4 particles or cells; red lines), 1×10^{28} g (2.6×10^5 ; green), 2×10^{27} g (1.3×10^6 ; cyan), and 1×10^{27} g (2.6×10^6 ; blue).	90
4.1 Series of temperature T (left column) and magnetic field strength $ B $ (right) logarithmic intensity profiles in the equatorial plane of the merger for four snapshots in time (rows; time indicated at the top left of each row).	99
4.2 Total magnetic energy E_B over time, with a best fit to the rapid exponential growth (dashed $E_B \propto e^{t/6.4\text{s}}$ line).	100
4.3 From leftmost to rightmost column, equatorial plane (top row) and polar (bottom) logarithmic intensity profiles of density ρ , temperature T , magnetic field strength $ B $ and ratio of magnetic to rotational energy density e_B/e_{rot} for the simulation at 400 s (~ 170 s after coalescence). The equatorial plane density plot includes a linear profile of the remnant core (with the same x and y scale as the logarithmic profile) to show its shape. Arrows in the magnetic field strength plots indicate field directions, with their lengths equal to the fraction of the field that lies along the xy plane (top frame) and xz plane (bottom).	101
4.4 Total magnetic energy E_B over time for the fiducial (solid blue; $m_{\text{cell}} \approx 1 \times 10^{-6} M_{\odot}$, equatorial surface field strength 10^3 G) simulation and the robustness tests. Dashed lines represent low (green; $m_{\text{cell}} \approx 5 \times 10^{-6} M_{\odot}$) and high resolution (red; $m_{\text{cell}} \approx 2 \times 10^{-7} M_{\odot}$) simulations. Dotted lines represent 1 G (magenta) and 10^{-3} G (cyan) low initial field simulations.	102
4.5 From top to bottom, equatorial plane intensity profiles for the magnetic field strength, relative divergence error (linear scale) and absolute relative divergence error (logarithmic) for the simulation at 200 s.	107

- 5.1 Evolution of the central temperature and density – “simmering tracks” – of simmering CO WDs with masses from $1.0 - 1.35 M_{\odot}$ (labeled in-line). Solid lines represent tracks of WDs with adiabatic temperature gradients, with dash-dotted track segments indicating regions that cannot be reached during simmering. Dotted lines represent tracks that include the superadiabatic deviation Δ_{conv} (Eqn. 5.26) required to transport the convective luminosity. Black circles along adiabatic simmering tracks indicate “WWK04 points” where Eqn. 5.19 is first satisfied signaling the end of simmering, and the black dotted WWK04 line represents a power-law fit to them. Red Xs are WWK04 points for Δ_{conv} -inclusive tracks. Also plotted are contours of constant neutrino cooling timescale τ_{ν} and carbon fusion heating timescale τ_{CC} , both in years, as well as specific entropy s in $\text{erg K}^{-1} \text{g}^{-1}$. The $\tau_{CC} = \tau_{\nu}$ and $\tau_{CC} = \tau_{\text{dyn}}$ lines denote where the fusion heating timescale becomes equal to the neutrino cooling timescale and dynamical timescale (Eqn. 5.16), respectively. Finally, the $P = 2P(T=0)$ approximates the upper bound of the region where degeneracy pressure dominates. Timescale contours were calculated using MESA (Paxton et al. 2011). 117
- 5.2 Relationships between total ejected mass M_{tot} and synthesized ^{56}Ni mass M_{Ni} for adiabatic and Δ_{conv} -inclusive WDs that experience a pure detonation immediately after the end of simmering, estimated using Sim et al. (2010). Also plotted are the M_{tot} and M_{Ni} yields of 31 observed SNe Ia from Childress et al. (2015), and the relationship derived by Scalzo et al. (2014b) from 337 observed SNe Ia. Childress et al. (2015)’s systematic error bars, indicating how much their values can be shifted in unison, are also included. The dashed magenta line is the relationship for the pure detonation of cold (uniform 10^5 K) WDs, with the simulation results of Sim et al. (2010) overdrawn. 122
- 5.3 Simmering tracks for (unmagnetized) solid-body rotating $1.15 M_{\odot}$ WDs. Track color represents $\Omega_i/\Omega_{\text{crit}}$, the ratio of the WD’s angular speed at the start of simmering to its numerically determined break-up value, and the thicker black track is the non-rotating Δ_{conv} -inclusive $1.15 M_{\odot}$ one from Fig. 5.1. WWK04 points are a black circle for the non-rotating track and orange squares for the rotating ones; the curves with $\Omega_i/\Omega_{\text{crit}} > 0.75$ never satisfy Eqn. 5.19. Dash-dotted track segments indicate solutions that cannot be reached during simmering. All other lines and symbols are as in Fig. 5.1. 129
- 5.4 Simmering tracks for (non-rotating) magnetized $1.15 M_{\odot}$ WDs. Track color represents the central magnetic field strength at the start of simmering, $B_{c,i}$, and the thicker black dotted track is the non-magnetized Δ_{conv} -inclusive $1.15 M_{\odot}$ one from Fig. 5.1. All other lines and symbols are as in Fig. 5.3, except that the orange circles represent WWK04 points for the magnetized (rather than rotating) tracks. 132
- 5.5 Comparison of a simmering track for a non-rotating, unmagnetized $1.15 M_{\odot}$ WDs calculated using Eqns. 5.37 and 5.38 (red line) with the “default” $1.15 M_{\odot}$ one that uses Eqns. 5.9 and 5.26 from Fig. 5.1 (black). Also plotted are tracks which use Eqn. 5.26 but multiply a prefactor of 2 (blue) or $1/2$ (cyan) to Eqn. 5.9. Circles along each track indicate their respective WWK04 points. All other lines and symbols are as in Fig. 5.3. . 134

- 6.1 Relationships between total ejected mass M_{tot} and synthesized ^{56}Ni mass M_{Ni} for the merger remnants of Sec. 2.6.1 if they were to (artificially) experience a pure detonation immediately after their estimated viscous spin-down. M_{Ni} is estimated by the mass of all remnant material with density $\rho > 10^7 \text{ g cm}^{-3}$, $M(\rho > 10^7)$. For the points, M_{tot} is estimated as the total mass of the remnant, but we also extend lines leftward from each point to indicate how much of M_{tot} is in the tenuous envelope. Colors indicate accretor mass, as in Fig. 2.3. Also plotted is the estimate for the AREPO MHD $0.625 - 0.65 M_{\odot}$ remnant (Ch. 4; red-blue star). All other features are as in Fig. 5.2. 140

Chapter 1

Introduction

Approximately two out of every three stars are born into a binary system. A substantial fraction of these stars will interact, some following the expansion of one or both constituent stars as they evolve off of the main sequence, and others after gravitational radiation, magnetic braking or three-body dynamics drastically shrink their orbital separation. These interactions primarily take the form of mass transfer between the stars, and if mass transfer becomes unstable, it ends with the violent coalescence of the two stars into one. These stellar mergers, like other forms of binary interaction, disrupt single star evolution and create merged products, or “merger remnants”, with unusual properties.

Mergers also liberate energy on the order of the gravitational binding energy of the binary and can eject copious amounts of mass, giving rise to a cornucopia of electromagnetic (and gravitational-wave) transients ranging from luminous red novae (from the merger of two (post-) main-sequence stars; eg. V838 Monocerotis and V1309 Scorpii ([Tylenda et al. 2011](#); [Nandez et al. 2014](#))) to short gamma-ray bursts (from two neutron stars or a neutron star and a black hole; eg. [Rosswog 2015](#)) and the gravitational wave outburst from coalescing stellar-mass black holes (as recently found by the Advanced Laser Interferometer Gravitational-Wave Observatory (LIGO); [Abbott et al. 2016](#)). Indeed, with current deep and short-cadence optical/near-infrared survey projects such as the Palomar Transient Factory ([Rau et al. 2009](#)) and Pan-STARRS ([Kaiser et al. 2010](#)) continuing to uncover more uncommon and even hitherto-unknown transients, and the ambitious Large Synoptic Survey Telescope ([LSST Science Collaboration et al. 2009](#)) under construction, a much more complete picture of merger-generated transients will form over the next decade.

In this thesis, I will be examining the merger and post-merger evolution of two carbon-oxygen white dwarfs to determine the sorts of merged products and transients they create. In particular, I investigate if they can produce thermonuclear, or type Ia, supernovae, even if their total mass is below the Chandrasekhar mass. I will first discuss the mergers of white dwarfs in general, and the diverse array of unusual stars and explosions they could potentially generate. I will then focus on the possible outcomes for mergers of sub-Chandrasekhar carbon-oxygen white dwarf binaries, and elaborate on why novel mechanisms for making type Ia supernovae are needed.

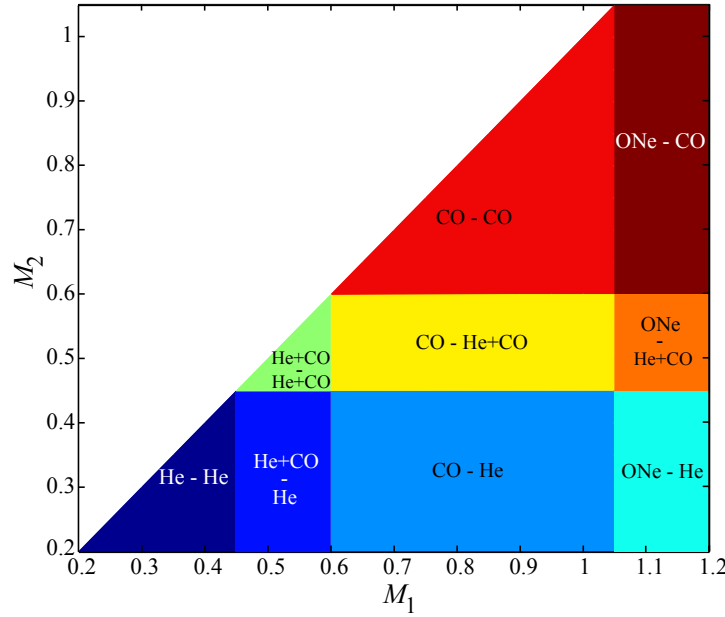


Figure 1.1: The expected compositions for white dwarfs undergoing a merger as a function of their masses, from [Dan et al. \(2012\)](#), their Fig. 1). M_1 is the mass of the accretor, or primary, WD (M_a in the text), and M_2 is the mass of the donor, or secondary (M_d). WDs with masses $M < 0.45 M_\odot$ are assumed to be He WDs, those with $0.45 < M < 0.6 M_\odot$ CO WDs with thick He envelopes, $0.6 < M < 1.05 M_\odot$ CO WDs, and $M > 1.05 M_\odot$ ONe WDs. See text, as well as [Dan et al. \(2012\)](#) Sec. 2, for discussion on these choices.

1.1 Mergers of Two White Dwarfs

Stars with masses $\lesssim 8 M_\odot$ generally end their lives as white dwarfs (WDs). On their own, WDs are inert: held up against gravity by electron degeneracy pressure and having ceased nuclear fusion, they will slowly radiate away their remaining thermal energy over billions of years. WDs in interacting binaries, on the other hand, can receive mass and energy from their stellar companion, leading to a whole host of energetic and potentially explosive phenomena.

Among double WD binaries, a fair number are in extremely close orbits, with periods ranging from hours to minutes. As these periods correspond to orbital separations well within the radii of red and asymptotic giant branch stars, the WD pairs are formed from systems that have experienced at least two episodes of mass transfer (eg. [Nelemans et al. 2001c](#); [Toonen et al. 2012](#); [2014](#)). These can sap the orbital angular momentum of the binary through mass loss, and so close double WDs tend to come from systems where (at least) the final mass transfer phase is a “common envelope event” where one star enters the envelope of the other and much of this envelope is ejected.¹

The mass and composition of each WD within the binary is dependent on the binary’s prior evolution. Broadly speaking, WDs with masses $M \lesssim 0.45 M_\odot$ are composed of helium (He); these come from stars that had their evolution interrupted by binary interaction while on the red giant branch (eg. [Marsh et al. 1995](#); [Nelemans et al. 2001a;c](#)), before their degenerate He core became massive

¹Binaries may also experience a “double common envelope event” – where both stars simultaneously envelop one another – and other unusual interactions. See eg. [Toonen et al. \(2012\)](#) and the Appendix of [Toonen et al. \(2014\)](#) for overviews of the formation channels of close double WD binaries.

enough to trigger a helium flash.² WDs with slightly higher masses have extensive He envelopes of $\sim 0.1 M_{\odot}$ surrounding cores composed of carbon and oxygen (CO; Iben & Tutukov 1985). Dan et al. (2012) approximate the mass range of these “hybrid WDs” to be $0.45 \lesssim M \lesssim 0.6 M_{\odot}$, and set the composition of the upper $0.1 M_{\odot}$ of these WDs to He in their simulations. From $0.6 \lesssim M \lesssim 1.1 M_{\odot}$ WDs are almost entirely composed of CO, with He atmospheres of $\sim 10^{-2} M_{\odot}$ (Iben & Tutukov 1985). WDs with masses $\gtrsim 1.1 M_{\odot}$ come from super-AGB stars (eg. Herwig 2005) that ignite carbon during their evolution (eg. García-Berro 2013), and thus are composed at least partly of oxygen and neon (ONe).

Fig. 1.1, from Dan et al. (2012), summarizes these relationships – in it, M_1 is the mass of the more massive primary WD, which accretes mass during the merger, and M_2 is the mass of the secondary, which donates mass (see Sec. 1.7.2 for why this is always the case). In this thesis, we refer to these as M_a and M_d , respectively. While sophisticated stellar evolution calculations are not always so clear-cut (eg. Iben & Tutukov 1985; Prada Moroni & Straniero 2009 for CO WDs with $M \lesssim 0.45 M_{\odot}$ and Hurley et al. 2000 for CO WDs with $M \gtrsim 1.2 M_{\odot}$), these relationships are used as rules of thumb for setting WD composition for a wide range of works (Lorén-Aguilar et al. 2009; Raskin et al. 2012; Dan et al. 2012; 2014, with slight variations between them). In this thesis, we look at binaries of pure CO WDs (without He atmospheres) with masses ranging from $0.4 - 1.0 M_{\odot}$.

Following their formation, WD binaries lose orbital angular momentum by emitting gravitational radiation (eg. Peters & Mathews 1963).³ This loss has a characteristic inspiral timescale of (Segretain et al. 1997)

$$\begin{aligned}\tau_{\text{grav}} = \frac{L_{\text{orb}}}{|\dot{L}_{\text{orb}}|} &= \frac{5c^5}{32G^3} \frac{a^4}{M_a M_d M_{\text{tot}}} \\ &= 5 \times 10^5 \left(\frac{a}{10^5 \text{km}} \right)^4 \frac{M_{\odot}}{M_a} \frac{M_{\odot}}{M_d} \frac{M_{\odot}}{M_{\text{tot}}} \text{yr.}\end{aligned}\quad (1.1)$$

where L_{orb} is the orbital angular momentum and a is the orbital separation. From this, we see that WD binaries with orbital periods on the order of hours or less ($a \lesssim 10^6 \text{ km} \sim 0.01 \text{ AU}$) will merge within a Hubble time.

As an aside, the gravitational waves emitted by inspiralling WD binaries are detectable from Earth. With periods on the order of minutes, they are too low-frequency to be detected by Advanced LIGO (LIGO Scientific Collaboration et al. 2015), but are expected to be the most numerous and dominant source of gravitational waves (Marsh 2011) detected by the proposed spaceborne detector eLISA (evolved Laser Interferometer Space Antenna; Amaro-Seoane et al. 2013), which probes the mHz - Hz frequency range. The instrument will likely resolve individual signals from thousands of binaries with orbital periods on the order ~ 10 minutes (and are thus close to merging; Amaro-Seoane et al. 2013; Marsh 2011; Dan et al. 2011), while numerous sources that are too far away or at longer orbital periods will comprise an unresolved background (Nelemans et al. 2001b; Amaro-Seoane et al. 2013). Measurement of either of these will probe the WD binary population of the Milky Way without the selection biases that often trouble electromagnetic binary searches (Marsh 2011). Note that gravitational radiation plays a negligible role in the actual merger, as the waves released during the merger have a

²He and CO WDs with $M \lesssim 0.5 M_{\odot}$ could in principle come from single stellar evolution, but these take longer than a Hubble time to evolve.

³They may also lose angular momentum through the influence of a third body (eg. Katz & Dong 2012); see Sec. 1.3.2.

total energy $\sim 10^{-10}$ of the binary's binding energy (eg. Lorén-Aguilar et al. 2009).

1.2 Merger Outcomes

Like any merger, those between WDs liberate or order their gravitational binding energy. This can lead to enough heating and/or compression to reignite the nuclear furnaces of normally inert WDs. As this may happen under either non-degenerate or degenerate circumstances, the end product of such mergers are diverse, ranging from stars with unusual properties undergoing stable nuclear burning to explosions. Additionally, hydrostatic WDs have a maximum mass beyond which they are unstable to collapse – the Chandrasekhar (1931) mass, or M_{Ch} , at $\sim 1.4 M_{\odot}$. This has long led to the notion that sufficiently massive WD mergers can result in the complete destruction of the merger product in a thermonuclear explosion that would resemble a type Ia supernova (SN Ia; Webbink 1984), or in its transformation into a neutron star (NS; Nomoto & Iben 1985; Saio & Nomoto 1985). We now know of a much greater range of possible merger outcomes for both systems with masses above and below M_{Ch} . Which outcome occurs depends on the compositions of the WDs involved, and are briefly summarized below (see also Dan et al. 2014, who produce a similar list):

- The merger of **two He WDs** is unlikely to lead to violent nuclear burning and an explosion (Dan et al. 2012; 2014; 2015). Instead, merger remnants with total masses $0.4 \lesssim M_{\text{tot}} \lesssim 0.8$ (Han et al. 2002; Iben & Tutukov 1985)⁴, which are the vast majority of double He WD remnants (Nelemans 2010), are expected to ignite He burning in a shell. Saio & Jeffery (2000) and Zhang & Jeffery (2012b) calculate that He shell burning increases the radius and luminosity of the remnant, turning it over $\sim 10^3 - 10^4$ yr into a yellow giant. Over the next $10^5 - 10^6$ yr, the burning shell migrates inward with a series of weakening shell flashes, while the radius slowly shrinks to $\sim 10^{-1} R_{\odot}$. Once the shell reaches the center of the remnant, the remnant settles onto the helium main sequence, and resembles a He-rich subdwarf B (sdB) or O (sdO) star (Saio & Jeffery 2000; Justham et al. 2011; Zhang & Jeffery 2012b; Heber 2016). Most subdwarf stars are in binaries – and likely arise from other formation channels – and there are multiple mechanisms theorized to produce single sdB stars (such as a merger between a low-mass star or brown dwarf and a red giant; Soker 1998), and so the contribution of mergers to the sdB population remains unclear (Nelemans 2010; Heber 2016).
- The outcome of a merger between **an He and a CO WD**, or a merger between an He and hybrid He-CO WD, depends on whether or not an He explosion is touched off during the merger. Roughly speaking, mergers with $M_{\text{tot}} \lesssim 0.8 M_{\odot}$ will lead to steady He burning in a shell, and are thought to be the progenitors to He-rich sdO stars (Justham et al. 2011). Mergers with $M_{\text{tot}} \gtrsim 0.8 M_{\odot}$ that do not experience an explosion will also ignite shell burning, but unlike their less massive counterparts they will retain their extended envelope over the lifetime of the He-burning shell (Iben & Tutukov 1985; Zhang & Jeffery 2012a). These mergers are believed to be the primary formation channel for Hydrogen-deficient Carbon (HdC) and R Coronae Borealis (R CrB) stars (eg. Webbink 1984; Iben & Tutukov 1984; Saio & Jeffery 2002; Clayton 2012; Zhang et al. 2014), which are H-deficient, He- and C-rich supergiants that, in the case of R CrB stars,

⁴This is lower than the He flash mass of $\sim 0.45 M_{\odot}$ because the merger remnant is partly non-degenerate (Iben & Tutukov 1985; Han et al. 2002).

feature abrupt variability by up to a factor of $\sim 10^3$ due to the formation of carbon dust above their photospheres.⁵ Following He shell exhaustion, they will contract in radius and heat their envelopes, resembling EHe stars (Saio & Jeffery 2002; Jeffery 2014).

Helium explosions become more likely for binaries with $M_{\text{tot}} \gtrsim M_{\text{Ch}}$ (Dan et al. 2012; 2014). In cases where an accreted He shell explodes, but the underlying CO WD remains, the result depends on a number of factors including the mass of the CO WD and amount of He it accretes, and spans a wide range of possible peak luminosities (Shen et al. 2010a; Waldman et al. 2011; Woosley & Kasen 2011). Detonations (or deflagrations; Woosley & Kasen 2011) of $\lesssim 0.1 M_{\odot}$ He shells lead to explosions that reach peak brightnesses $\sim 10 - 100$ fainter than SNe Ia over $\sim 2 - 10$ days (typical SNe Ia values are in Sec. 1.3), making them similar to the “.Ia SNe” theorized to occur in AM Canum Venaticorum binaries (Bildsten et al. 2007). They synthesize Ca, Cr and Ti, but relatively little of the radioactive ^{56}Ni typically seen in SNe Ia (Shen et al. 2010a; Woosley & Kasen 2011; Waldman et al. 2011). Denser He envelopes (which are either themselves more massive or lie over more massive CO cores), tend to synthesize more ^{56}Ni in detonations (Shen et al. 2010a; Waldman et al. 2011).

In the case where the the He shell detonates, and triggers the CO WD to do the same, a “double-detonation” SN Ia may be produced (Sec. 1.3.2).

- The merger of **two CO WDs** has long been suspected of producing an SN Ia under the right conditions (Sec. 1.3 and 1.4). If these conditions are not met, they will instead create a lone, massive, rotating and highly magnetized CO WD or, if steady carbon fusion is ignited, a carbon-burning star that eventually turns into an ONe WD (Sec. 1.5). If the ONe WD is above M_{Ch} , it may collapse into a neutron star (see below).
- Due to their mass, it is likely that the merger of **an ONe WD** with any companion will create a super- M_{Ch} remnant. Unlike their CO counterparts, an ONe WD that is compressed through accretion to $\gtrsim 3 \times 10^9 \text{ g cm}^{-3}$ initiates electron-capture reactions onto ^{20}Ne and ^{24}Mg , losing degeneracy support in the process (eg. Miyaji et al. 1980; Saio & Nomoto 1985; Schwab et al. 2015). This leads to further contraction, which likely ends⁶ in an accretion-induced collapse (AIC) into a neutron star soon after its central density reaches $\sim 10^{10} \text{ g cm}^{-3}$ (Schwab et al. 2015). Simulations (Dessart et al. 2006; 2007; Fryer et al. 2009) of the AIC find it expels only $\sim 10^{-2} M_{\odot}$ of ejecta and produces negligible amounts of radioactive ^{56}Ni , suggesting a very faint transient.

Dan et al. (2014) discusses the possibility that He - ONe and CO - ONe WD mergers will lead to enshrouded AIC that produce “hybrid supernovae”, where much of the outer envelope (of a different composition) explodes rather than collapsing. In particular, they suggest (based on the Shen et al. (2010a) and Waldman et al. (2011) simulations above) that the detonation of the thick He envelope of a significantly super- M_{Ch} He - ONe WD merger remnant could explain the SN 2005E-like class of low-luminosity SNe Ib that produce very little ^{56}Ni , have low ejecta masses and spectroscopically show strong lines of He and Ca (Perets et al. 2010).

⁵Subdwarf stars formed from double He WD mergers with $M_{\text{tot}} \gtrsim 0.8 M_{\odot}$ will also expand to become R CrB stars following core He exhaustion, but this formation channel accounts for only a few percent of all R CrBs (Zhang & Jeffery 2012a).

⁶Since the electron capture reactions are exothermic, they trigger a thermal runaway that eventually starts an O-deflagration at $\sim 10^{10} \text{ g cm}^{-3}$. Whether or not collapse or explosion occurs depends on exactly when the deflagration ignites; see eg. discussion in Schwab et al. (2015).

[Marquardt et al. \(2015\)](#) suggest that an ONe WD could be detonated through binary interactions in the same manner as CO WDs (Sec. 1.3.2). Due to their high densities, these would produce $\gtrsim 1 M_{\odot}$ of ^{56}Ni , but, because fusing to ^{56}Ni from O and Ne generates $\sim 30\%$ less energy than from C ([Marquardt et al. 2015](#)), they would also be weaker than CO WD detonations. Detonations during ONe mergers may explain supernovae such as SN 2009dc ([Taubenberger et al. 2011](#)) that have a peak brightness ~ 3 times higher, and decay from peak brightness ~ 3 times more slowly, than SNe Ia, and also have low expansion velocities.

Of these possibilities, ones that create SNe Ia are particularly intriguing, as they may hold the key to solving the long-standing problem of how these explosions arise.

1.3 The Mystery of Type Ia Supernovae

Type Ia supernovae, or SNe Ia, have been observed by astronomers for centuries. SN 1572, for example, was observed by Danish astronomer Tycho Brahe to be “far beyond the Moon”, and helped lead to the abandonment of the Aristotelian concept that the heavens were immutable (eg. [Clark & Stephenson 1977](#)).

Today, SNe Ia are classified (eg. [Filippenko 1997](#); [Li et al. 2011b](#)) by the lack of H and He, as well as the strong presence of ionized silicon (Si II), in their spectra. They comprise 24% of all supernovae in the local universe ([Li et al. 2011b](#)), but are spotted disproportionately often by surveys because they are among those that are the most optically luminous ([Howell 2011](#)). “Normal” SNe Ia ([Branch 1998](#); [Branch et al. 2006](#)) typically reach a maximum bolometric luminosity of $\sim 10^{43} \text{ erg s}^{-1}$ after 18 - 20 days, followed by an order-of-magnitude decline in brightness over a month, and finally a slower, exponential decline of a factor of ~ 2.5 every month due to the decreasing rate of heating by radioactive decay within the ejecta (eg. [Filippenko 1997](#); [Hillebrandt et al. 2013](#)). Their spectroscopic features show they are composed of a combination of intermediate-mass elements (eg. [Arnett 1996](#)) such as silicon and calcium, and peak-iron elements such as iron and nickel ([Filippenko 1997](#)). They seed both these elements and their kinetic energy into the interstellar medium, and so play an important role in star formation and galactic chemical evolution ([Maoz et al. 2014](#)).

Normal SNe Ia are remarkably homogeneous, and exhibit variations that can – to first order – be parameterized by a single variable ([Hillebrandt & Niemeyer 2000](#); [Howell 2011](#)). This is reflected most famously in the [Phillips \(1993\)](#) relation, where SNe Ia with greater peak brightnesses tend to evolve more slowly in time. Secondary correlations also exist, including the “color-luminosity” relation where SNe Ia that reach lower peak brightnesses have redder colors near them ([Riess et al. 1996](#)). Their parameterizability, as well as their intrinsic brightness, make SNe Ia outstanding cosmological distance indicators. They were most famously used in this context in the much-celebrated discovery of ([Riess et al. 1998](#)) and [Perlmutter et al. \(1999\)](#) that the expansion of the universe is accelerating under the influence of a “dark energy”, the exact nature of which remains mysterious.

Up to 30% ([Li et al. 2011b](#)) of explosions classified as SNe Ia are “peculiar” SNe Ia that are orders of magnitude fainter (eg. SN 2002cx ([Li et al. 2003](#); [Foley et al. 2013](#)), SN 1991bg ([Mazzali et al. 1997](#))) and occasionally substantially brighter (eg. SN 2009dc; [Yamanaka et al. 2009](#); [Taubenberger et al. 2011](#)) than normal ones. These do not adhere to normal SNe Ia correlations above, and are generally believed to have different progenitors or explosion mechanisms from normal SNe Ia. A number of

these progenitors have already been discussed discussed in Sec. 1.2, and several more are mentioned in Sec. 1.3.2.

Despite their ubiquity and utility, however, the exact nature (or natures) of the progenitors to normal SNe Ia remains mysterious. They were first proposed to be explosions of CO WDs by Hoyle & Fowler (1960) based on the composition of SNe Ia ejecta. This is now well-established by the similarity of the light curve, energetics and spectral evolution of a typical SN Ia to those calculated for an exploding CO WD. Also, early-time observations of the recent SN 2011fe have constrained the radius of the exploding object to be $\lesssim 0.1 R_\odot$ (Nugent et al. 2011; Bloom et al. 2012; Maoz et al. 2014), consistent with a CO WD, while late-time observations of SN 2014J have detected gamma-ray emission from the decay of ^{56}Ni (Churazov et al. 2014), produced by the burning of carbon and oxygen to nuclear statistical equilibrium. What is much less well-understood is how the CO WD is made to explode, leading to a vast body of literature exploring the various theoretical and observational lines of evidence. The references below are necessarily only a subsample of this literature; see Howell (2011), Hillebrandt et al. (2013), Maoz et al. (2014), and Tsebrenko & Soker (2015) for excellent reviews and further references.

1.3.1 Traditional Formation Scenarios and Their Pitfalls

Until recently, the most widely accepted progenitor scenarios have involved pushing a CO WD to carbon ignition by slowly adding mass to it (Hillebrandt & Niemeyer 2000). The added mass compresses and heats the WD’s interior, but the latter is at least partially balanced by cooling from neutrino emissions, which prevents carbon ignition due to high temperatures. As the CO WD approaches M_{Ch} and its central density approaches $\sim 2 \times 10^9 \text{ g cm}^{-3}$, the rate of heating from pycnonuclear carbon fusion – i.e. carbon fusion due to extreme density – starts to exceed that for neutrino cooling. Because ignition occurs under highly degenerate conditions, the WD does not respond to this heating by expanding, and so, unlike a non-degenerate star, experiences a nuclear runaway. This lasts $\sim 1000 \text{ yr}$, until the timescale for nuclear heating at the WD’s center becomes shorter than the star’s dynamical time. Dynamical burning then begins, and some kind of explosion is inevitable.

The various scenarios to get a CO WD to accrete slowly can be subdivided into two classes, or “channels”: the single-degenerate (SD) channel (Whelan & Iben 1973), where the WD steadily accretes from a non-degenerate companion (a main sequence star, a giant, or an sdOB star), and the double-degenerate (DD) channel (Iben & Tutukov 1984; Webbink 1984), where two CO WDs with a total mass $\gtrsim M_{\text{Ch}}$ merge, producing a merger remnant composed of a dense, degenerate “core” surrounded by a thick accretion disk. Both scenarios are beset by two issues, which we summarize below using arguments from van Kerkwijk et al. (2010, henceforth vK10; see also van Kerkwijk 2013).

The first issue is that in order to match the observed SN Ia rate of $\sim 0.0023 \pm 0.0006$ for every solar mass of stars formed (Maoz et al. 2011), $\sim 1\%$ of all WDs formed (of any composition and regardless of binarity) must produce SNe Ia. Compared to this relatively large number, there is an apparent paucity of CO WDs that can reach M_{Ch} from either channel. In hydrogen-accreting SD systems, efficient growth of the WD appears only achievable if the accretion rate is between $10^{-8} - 10^{-7} M_\odot \text{ yr}^{-1}$. Slower accretion results in nova outbursts that eject the accreted mass (Townsley & Bildsten 2004; though see Zorotovic et al. 2011), while faster accretion builds up an extended envelope that eventually engulfs the donor (Iben & Tutukov 1984). Systems that do accrete at the correct rate – and steadily burn hydrogen to helium – should radiate supersoft x-rays, but observations of galactic x-ray flux suggest a factor of 10 – 100 too few of these systems exist to explain the SNe Ia rate (Di Stefano 2010; Gilfanov & Bogdán

2010), and whether or not these systems can be “hidden” from view as rapidly-accreting enshrouded WDs is debatable (eg. Hachisu et al. 2010; Lepo & van Kerkwijk 2013; Johansson et al. 2014). Even if the accreted matter has been burned to helium, or the donor is He-rich, matter may still be ejected by subsequent helium flashes (Idan et al. 2013; Piersanti et al. 2014; though see Hillman et al. 2016).

Meanwhile, analytical estimates (van Kerkwijk et al. 2010), binary population syntheses (which simulate the evolution of a population of binaries from the zero-age main sequence onward; Mennekens et al. 2010; Ruiter et al. 2009; Toonen et al. 2012; Claeys et al. 2014) and empirical counting of candidate systems (Badenes & Maoz 2012) all estimate that the merger rate of CO - CO WD binaries with total mass greater than $\sim M_{\text{Ch}}$ falls short of the SN Ia rate by a factor of at least a few. Not all of these mergers will necessarily end as SNe Ia, either: if post-merger evolution leads to off-center carbon ignition in the merger remnant, carbon burning will transform the remnant into an ONe WD, and an $\gtrsim M_{\text{Ch}}$ ONe WD likely ends its life in an AIC, rather than exploding as an SN Ia (Nomoto & Iben 1985; Saio & Nomoto 1985; Yoon et al. 2007; Schwab et al. 2016).

The second issue is the difficulty for the thermonuclear explosion of an M_{Ch} mass CO WD to replicate the properties of normal SNe Ia. Normal SNe Ia synthesize $\sim 0.3 - 0.9 M_{\odot}$ of radioactive ^{56}Ni , peaking at $\sim 0.6 M_{\odot}$ (eg. Stritzinger et al. 2006; Piro et al. 2014), and feature ejecta that are compositionally stratified, with intermediate-mass elements sitting above the peak-iron ones (Howell 2011; Hillebrandt et al. 2013). If dynamical burning leads to an extended plateau of high overpressure, a detonation occurs: a supersonic shockwave drives through the WD and triggers nuclear fusion in its wake (eg. Seitenthahl et al. 2009). As most of the mass in an M_{Ch} WD is $\gtrsim 10^9 \text{ g cm}^{-3}$, nuclear burning would convert almost all of the WD to ^{56}Ni (Howell 2011; Hillebrandt et al. 2013). On the other hand, if the explosion propagates as a subsonic deflagration, where a steep temperature gradient – a flame front – moves outward via conduction, the WD is able to expand during the explosion. At lower densities, intermediate-mass elements are produced. The explosion, however, produces slower velocity ejecta than seen in SNe Ia, and mixes burned and unburned material such that the ejecta would not appear stratified. To resolve this, an *ad-hoc* deflagration-to-detonation transition (DDT) is often invoked (Khokhlov 1991), the timing of which can be tuned to vary the amount of ^{56}Ni generated (eg. Hillebrandt et al. 2013), though it remains unclear if this is a robust mechanism in realistic WD explosions (eg. Fisher & Jumper 2015). It is also not obvious how invoking the DDT can explain the dependence of observed SNe Ia on the properties of their host galaxies, for example why more luminous SNe Ia tend to be in star-forming galaxies (eg. Hamuy et al. 2000; Sullivan et al. 2010).

The SD channel has a number of additional complications (Maoz et al. 2014; Tsebrenko & Soker 2015) that have led it to decline in popularity compared to the DD one. For example, it requires a non-degenerate companion, which, under certain conditions, might be detectable, but attempts to spot the companion in pre-explosion archival data (Li et al. 2011a; Nielsen et al. 2013; 2014), during the supernova (as it responds to being hit by SN ejecta; Bloom et al. 2012; Olling et al. 2015), or after the explosion (eg. Kerzendorf et al. 2014a) have come up short. For SD scenarios involving hydrogen-rich donors, the explosion is also expected to strip and entrain donor material, but attempts to find such material either do not detect hydrogen, or, in one recent case, apparently too little hydrogen to be consistent with SD donor stars (Maguire et al. 2016).

1.3.2 Brave New Channels

The challenges posed by the evidence above has spurred research into alternative scenarios that lead to exploding CO WDs that are more physically viable and better fit observations. Notably, several of these channels relax the condition that the exploding WD must be at or above M_{Ch} , allowing for a wider range of exploding masses. The alternate scenarios include:

- The **double-detonation channel** (Livne 1990; Woosley & Weaver 1994), which involves a CO WD accreting a thin envelope from an He-rich source (a He star, merger with an He/hybrid WD, or even the He atmosphere of a CO WD). At some point – for slow accretion, when the base of the envelope becomes hot enough to ignite dynamical He burning (Woosley & Kasen 2011); for mergers, when a hotspot in the accretion stream or envelope reaches conditions for detonation (Guillochon et al. 2010; Raskin et al. 2012; Pakmor et al. 2013) – the He shell detonates. This then either drives compressional waves that converge at the core of the CO WD, or directly launches a detonation shock into the CO WD, both of which trigger the secondary detonation of the CO WD (though the former is more plausible; Moll & Woosley 2013).

Initially, double-detonations were believed to need massive He shells of $\gtrsim 0.1 M_{\odot}$, but these produce significant amounts of ^{56}Ni in the explosion, inconsistent with the stratified nature of SNe Ia ejecta (eg. Kromer et al. 2010; Woosley & Kasen 2011). While the robustness of the double-detonation remains a field of active research (eg. Woosley & Kasen 2011; Holcomb et al. 2013; Shen & Moore 2014; Shen & Bildsten 2014; Dan et al. 2015), more recent work suggests thin, $\lesssim 0.03 M_{\odot}$ He shells may detonate for both slow accretion and mergers onto $\gtrsim 0.8 M_{\odot}$ CO WDs (Woosley & Kasen 2011; Pakmor et al. 2013; Shen & Moore 2014), and that a CO detonation via converging shockwaves is likely as a result (Fink et al. 2010; Moll & Woosley 2013; Shen & Bildsten 2014). Pure detonations of bare sub- M_{Ch} CO WDs with masses between $\sim 1 - 1.15 M_{\odot}$ show light curves and spectra in good agreement with normal SNe Ia (Shigeyama et al. 1992; Sim et al. 2010), while the detonation of the much less massive He shell greatly reduces (but does not entirely eliminate) contamination from He shell nuclear ashes (Kromer et al. 2010; Hillebrandt et al. 2013).

If the double-detonation channel is indeed physically plausible, it opens up a range of WD masses beyond M_{Ch} that can explode, and more naturally explains the explosion. In particular, since peak luminosity of the explosion is dependent on the mass of the CO WD (since more ^{56}Ni is generated in the detonation of massive WDs), this could explain both the Phillips (1993) relation and the relationship between SN Ia luminosity and the age of its host stellar population (since lower-mass WDs take longer to form). The problem remains that to generate typical SN Ia ^{56}Ni yields of $\sim 0.6 M_{\odot}$, the CO WD needs to be $\sim 1.1 M_{\odot}$, far above the mass of typical field WDs (Piro et al. 2014). For both slowly accreting and merging systems, it might be possible to grow CO WDs by several $0.1 M_{\odot}$ through He accretion in a past phase of binary evolution (Ruiter et al. 2011; 2013; 2014), but the viability of these scenarios are sensitive to how mass transfer is treated (eg. the He retention efficiency). For slow accretion, current calculations also favor detonating CO WD masses closer to $\sim 0.8 M_{\odot}$ than $1.1 M_{\odot}$ (Ruiter et al. 2014), which would produce highly underluminous supernovae.

- The **violent merger channel** (Pakmor et al. 2010), a variant of the double-degenerate channel where, during the merging process, material being accreted from one WD to another is sufficiently

superheated and compressed to trigger a detonation, sidestepping the need for accretion following the merger. Only those binaries where the primary WD is $\gtrsim 0.9 M_{\odot}$ and the WD mass ratio is $\gtrsim 0.8 - 0.9$ (Pakmor et al. 2010; 2011b; Sato et al. 2016; Dan et al. 2012) suggests a higher minimum primary WD of $\gtrsim 1.0 M_{\odot}$ are violent enough to trigger a detonation. Mergers with primaries of $\gtrsim 1.0 M_{\odot}$ produce explosions consistent with normal or overluminous SNe Ia (Pakmor et al. 2012b; Moll et al. 2014). Lower-mass systems produce ones that only synthesize $\sim 0.1 M_{\odot}$ of ^{56}Ni , are much redder and have much slower velocities than typical SNe Ia, but could resemble the subluminous SN 1991bg-like subclass (Leibundgut et al. 1993; Pakmor et al. 2010). Whether a CO detonation can robustly be triggered during a merger requires further study, but regardless, the CO WD binaries needed are highly super- M_{Ch} , and may be too rare to explain the majority of SNe Ia (Badenes & Maoz 2012).

- The **direct collision channel**, in which two potentially sub- M_{Ch} CO WDs collide, rather than merge, either because they are in a dense stellar environment (such as a globular cluster; Benz et al. 1989; Lorén-Aguilar et al. 2010) or a hierarchical triple system (Katz & Dong 2012) under the influence of the Kozai-Lidov mechanism (Kozai 1962; Lidov 1962). Hydrodynamic simulations (Raskin et al. 2010; Kushnir et al. 2013; García-Senz et al. 2013) show that the impact of the the WDs leads to strong shocks that plow into both WDs and produce detonations. Explosion properties can be varied by changing the impact parameter or the masses of the stars, with the collision of two $\sim 0.65 M_{\odot}$ CO WDs able to produce $\sim 0.4 M_{\odot}$ of ^{56}Ni (García-Senz et al. 2013; Kushnir et al. 2013), somewhat consistent with normal SNe Ia. A minority of WDs reside in dense stellar environments, however, and only $\sim 10 - 20\%$ of stars are in triples, making it unlikely that this channel alone can reproduce a substantial fraction of SNe Ia (see Sec. 2.3 of Maoz et al. 2014 for details).
- The **core-degenerate channel** (Livio & Riess 2003; Kashi & Soker 2011; Tsebrenko & Soker 2015), which occurs when a progenitor system that would otherwise have produced a $> M_{\text{Ch}}$ close double WD binary does *not* survive its (second) common envelope phase (or survives in such a tight orbit that it merges within 10^5 years afterward). To account for most SNe Ia, the super- M_{Ch} remnant would have to live on for $10^8 - 10^{10}$ yr before exploding (since SNe Ia can occur in stellar environments that have long ceased star formation; eg. Pritchett et al. 2008; Maoz et al. 2010). Ilkov & Soker (2012) propose this extended lifespan is achievable by a gradual loss of solid-body rotational support through magnetic dipole radiation, but post-merger evolution likely occurs over much smaller timescales (Sec. 1.4). Nonetheless, mergers during or just after common-envelope events naturally explain peculiar SNe Ia that show interaction with substantial amounts of circumstellar material (eg. PTF 11kx; Dilday et al. 2012; Soker et al. 2013).

More unconventional channels have also been proposed where a CO WD detonates due to collisions with planets and planetoids (Di Stefano et al. 2015) or even due to compositional impurities near their core that help facilitate pycnonuclear fusion (Chiosi et al. 2015). Further work is required to show the physical viability of these channels, and whether they reproduce normal SNe Ia.

Regardless of whether or not any of these produce normal SNe Ia, studying them may be useful for explaining the diverse subclasses of SNe Ia. For instance, synthetic light curves and spectra of pure deflagrations of M_{Ch} CO WDs (Phillips et al. 2007; Kromer et al. 2013; Fink et al. 2014) reproduce the low peak brightness, slow ejecta velocity and hot photospheric emission of the SN IaX subclass (or

SN 2002cx-like subclass; [Li et al. 2003](#); [Foley et al. 2013](#)). Meanwhile, successful detonations of M_{Ch} CO WDs have been linked to the overluminous SN 1991T-like SNe Ia ([Fisher & Jumper 2015](#), but see [Seitenzahl et al. 2016](#)).

1.4 The Sub-Chandrasekhar CO WD Merger Channel

Another channel was recently proposed by [vK10](#), who hypothesize that the remnant from a double CO WD merger could subsequently become hot enough to ignite thermonuclear fusion (rather than dense enough to ignite pycnonuclear fusion). This opens the possibility for mergers with a total mass significantly below M_{Ch} to also explode.

[vK10](#) consider a fiducial merger of a $0.6 - 0.6 M_{\odot}$ CO WD binary, whose masses are chosen to be near the empirical peak of the WD mass distribution (Sec. 1.7.1). Hydrodynamic simulations ([Lorén-Aguilar et al. 2009](#)) find that the two WDs tidally destroy one another and coalesce into a remnant that is significantly heated throughout, but does not achieve temperatures sufficient to ignite fusion (as it is much less massive than the violent mergers considered in Sec. 1.3.2); moreover, the remnant central density, $\sim 2.5 \times 10^6 \text{ g cm}^{-3}$, is too low to produce ^{56}Ni in an explosion.

Following coalescence, however, the remnant, which is differentially rotating, enters a period of rapid angular momentum redistribution due to hydrodynamically or magnetically-mediated viscosity. Using the standard α -viscosity prescription ([Shakura & Sunyaev 1973](#)) – i.e. the kinematic viscosity $\nu = \alpha c_s H_P$, where c_s is the sound speed, H_P the pressure scale height and α a tunable parameter – the timescale for viscous evolution can be estimated as ([Shen et al. 2012](#))

$$\begin{aligned} t_{\text{visc}} &= \frac{R_{\text{disk}}^2}{\nu} \sim \frac{1}{\alpha} \left(\frac{R_{\text{disk}}}{H_P} \right)^2 \tau_{\text{dyn}} \\ &\sim 3 \times 10^4 \text{ s} \left(\frac{10^{-2}}{\alpha} \right) \left(\frac{R_{\text{disk}}/H_P}{10} \right)^2 \left(\frac{R_{\text{disk}}}{10^9 \text{ cm}} \right)^{3/2} \left(\frac{M_{\text{enc}}}{1 M_{\odot}} \right)^{-1/2}, \end{aligned} \quad (1.2)$$

where M_{enc} is the mass enclosed within the inner boundary of the disk, and we have used $\tau_{\text{dyn}} \approx H_P/c_s$ and inserted a fiducial viscosity and typical numbers for remnants. Thus the vast majority of the remnant’s angular momentum is transported away, and the remnant (including its disk) loses its rotational support against gravity over a period $\sim 10^4 \text{ s}$.⁷ This loss of rotational support combined with increasing weight from newly accreted disk material leads to compression and heating of the remnant core. Since $\sim 10^4 \text{ s}$ is far shorter than the thermal adjustment timescale of $\sim 10^4 \text{ yr}$ ([Shen et al. 2012](#)), compressional heating is adiabatic, and [vK10](#) estimates that for the $0.6 - 0.6 M_{\odot}$ remnant it leads both the central density and temperature to increase to $\gtrsim 1.5 \times 10^7 \text{ g cm}^{-3}$ and $\gtrsim 10^9 \text{ K}$, at which point the nuclear fusion timescale is smaller than even the compressional heating timescale, and a carbon nuclear runaway becomes inevitable. If the runaway leads to dynamical burning and an explosion occurs, the generally lower densities of merger remnants compared to M_{Ch} WDs means that burning leads to a larger pressure differential between the ashes and their surroundings, perhaps making a detonation favorable over a deflagration (e.g. [Mazurek et al. 1977](#); [Seitenzahl et al. 2009](#)).

⁷This is in contrast to earlier work (eg. [Nomoto & Iben 1985](#); [Yoon et al. 2007](#)) that assume any rotationally-supported material will slowly accrete onto the dense core of the remnant at a near-Eddington rate of $\dot{M} \sim 10^{-5} M_{\odot} \text{ yr}^{-1}$. Remnants are prone to magnetic instability ([Shen et al. 2012](#); [Ji et al. 2013](#)), and will almost certainly evolve over the much shorter timescale given by the α -viscosity estimate.

The sub- M_{Ch} merger scenario features a number of advantages over the traditional M_{Ch} double-degenerate channel. Like the double-detonation channel, this one substantially increases the number of binary systems that could potentially explode – perhaps by a factor of ~ 3 , which would be more consistent with the SN Ia rate (vK10, Badenes & Maoz 2012) – and naturally explains both the explosion mechanism and some of the trends seen in the observed SN Ia population, thus alleviating the issues discussed in Sec. 1.3.1. Unlike the double-detonation channel, however, a He detonation is not invoked to trigger the CO WD to explode, negating the complications of the He detonation ashes on the SN light curve, and the merger process provides a more natural means of producing the $\gtrsim 1 M_{\odot}$ of CO needed to synthesize the ^{56}Ni found in a typical SN Ia.

This scenario requires that carbon ignition occur under highly degenerate conditions close to the center of the merger remnant, which, in turn, requires the merger remnant be heated throughout its interior, which is the case for mergers of nearly equal-mass binaries. When very unequal masses merge, however, simulations show the less massive secondary WD is completely disrupted and forms a disk and envelope around the largely undisturbed primary (Lorén-Aguilar et al. 2009). Compression of this remnant will likely trigger off-center rather than central ignition, and could lead to stable carbon burning rather than an explosion (eg. Yoon et al. 2007; Shen et al. 2012).

1.5 Massive Merger Remnants

Below some mass, the remnant of a double CO WD merger will almost certainly not be destroyed in an explosion, and will live on as a single, massive, rapidly rotating and likely magnetized object. If off-center carbon burning is ignited, the WD will be transmuted into an ONe WD over $\sim 10^4$ yr (Nomoto & Iben 1985; Shen et al. 2012) but will not collapse into a neutron star, since its mass is below M_{Ch} .⁸ Discovering the products of these mergers, therefore, is an indirect means of investigating SN Ia progenitors (Dunlap & Clemens 2015).

A number of studies of the observed mass distribution of field WDs from sky surveys (eg. Liebert et al. 2005; Giambicane et al. 2012; Kleinman et al. 2013; Rebassa-Mansergas et al. 2015b;a) note a high-mass peak near $1 M_{\odot}$ that is substantially offset from the global peak of the distribution at $\sim 0.65 M_{\odot}$ (Sec. 1.7.1), which could be evidence for a population of merger remnants. This interpretation is controversial, as population synthesis studies (Rebassa-Mansergas et al. 2015b; Tremblay et al. 2016) give conflicting results for whether the peak can be explained by single star evolution. However, they are unlikely to specifically be double WD merger remnants: theoretical and observational estimates of the double WD merger rate (eg. Badenes & Maoz 2012; Toonen et al. 2012) indicate it is an order of magnitude too low (Tremblay et al. 2016) to contribute the majority of systems in the high-mass peak; a kinematic study of objects in the peak conclude they are kinematically young (Wegg & Phinney 2012); and the peak disappears when only examining brighter WDs, suggesting the population has not been reheated by the merging process (Rebassa-Mansergas et al. 2015a). The excess of massive WDs may alternatively be formed in common-envelope mergers akin to the core-degenerate scenario, which better fits the evidence above (Rebassa-Mansergas et al. 2015a; Briggs et al. 2015).

Studies targeting “high-field magnetic WDs” (HFMWDs; Kepler et al. 2013; García-Berro et al. 2016), which possess fields of $B \gtrsim 10^6$ G, suggest that population’s mass distribution has a mean of $\sim 0.8 M_{\odot}$, and overall does not resemble the non-magnetic WD ones. While this may suggest a double

⁸Schwab et al. (2015) find the critical mass needed to trigger an ONe WD to collapse is $1.38 M_{\odot}$, nearly at M_{Ch} .

WD merger origin for these WDs, it is also possible the fields are a vestige of single-star evolution (eg. Wickramasinghe & Ferrario 2005; Kissin & Thompson 2015) or mergers within common envelopes (García-Berro et al. 2012; Wickramasinghe et al. 2014; Briggs et al. 2015). HFMWDs have not been found in detached binaries with M and K dwarfs, despite such binarity being ubiquitous for non-magnetic WDs, which is strong evidence that HFMWDs are products of some kind of merger (Liebert et al. 2015; Ferrario et al. 2015). Population synthesis calculations (García-Berro et al. 2012; Briggs et al. 2015), however, find that common envelope mergers produce the overwhelming majority of HFMWDs, especially ones closer to $\sim 0.8 M_{\odot}$, with double CO WD mergers contributing only a minority of objects in the high-mass ($\gtrsim 1.1 M_{\odot}$) tail of the distribution.

Among the most massive HFMWDs is RE J 0317-853 (Barstow et al. 1995; Külebi et al. 2010), a $\gtrsim 1.3 M_{\odot}$ CO or ONe WD with a high effective temperature of $\gtrsim 3 \times 10^4$ K, a spin period of 700 s and a magnetic field strength of $B \sim 10^8$ G that is often cited as a double WD merger remnant. Another such object is PG 1658+441, with a mass of $\sim 1.3 M_{\odot}$, spin period of ~ 6 hr and field of $\sim 10^6$ G (Ferrario et al. 2015, and references therein). There are observational issues with attributing these objects to WD mergers. RE J 0317 is in a wide (non-interacting) binary with a $\sim 0.8 M_{\odot}$ companion, and Külebi et al. (2010) showed that the cooling age of both WDs is approximately the same. This, they claim, makes it unlikely for RE J 0317 to have formed either from single star evolution (since it should have become a WD before its companion) or a merger (since one of its two merger constituents must be $\lesssim 0.7 M_{\odot}$ and should have become a WD after the companion). It is also curious that RE J 0317, PG 1658 and most other $> 1 M_{\odot}$ HFMWDs (Ferrario et al. 2015) are DA WDs and have spectra with absorption lines of hydrogen, which is unlikely to survive mergers due to the high temperatures achieved in them. Indeed, these issues might indicate a common envelope merger origin for the WDs (which would naturally leave residual hydrogen and potentially yield an older cooling age than a double WD merger) consistent with the HFMWD population synthesis above.

Possibly better candidates for merger remnants are the hot DQs, a recently-discovered class of WDs that features effective temperatures of $\gtrsim 2 \times 10^4$ K and spectra with C and O absorption lines, suggesting that hot DQ atmospheres are dominated by CO (Dufour et al. 2007; 2008). The CO-rich atmospheres make mass-determination difficult, but preliminary estimates on a few hot DQs using either more advanced WD atmosphere models (Dufour et al. 2011) or combining radius (from parallax) with the WD mass-radius relation (Dunlap 2015) suggest they have masses around $1 M_{\odot}$. They also generally appear to have monoperiodic photometric variability, possibly due to rapid rotation on the order of minutes (Lawrie et al. 2013; Williams et al. 2016), and magnetic fields $\gtrsim 10^6$ G (Dufour et al. 2013). Dunlap & Clemens (2015) found that, if most known hot DQs are assumed to be near $\sim 1 M_{\odot}$, their population's kinematic age is much older than what would be inferred from their temperatures, suggesting they have been reheated since their birth. Dunlap (2015) uses a rough estimate of the hot DQ space density, along with their lifetime (given by the difference in cooling age between the hottest and coldest hot DQ), to determine that their formation rate is of order the observed (total) WD merger rate from Badenes & Maoz (2012). These class properties strongly suggest that hot DQs are a population of CO WD merger remnants, but an alternate hypothesis (Dufour et al. 2007; Althaus et al. 2009) claims they are the progeny of stars that experience a powerful late thermal pulse during the asymptotic giant branch phase. As many of their properties are still being fleshed out, their origins remain unclear for now.

1.6 Thesis Overview

If sub- M_{Ch} double CO WD mergers could either explode or leave behind isolated massive CO/ONe WDs, which fate might be preferred, and how does it depend on the masses of the two WDs? Can these mergers, as vK10 claims, serve as a novel SNe Ia progenitor channel that naturally coincides with SNe Ia rates and explosion properties? To answer these questions, we must scrutinize the vK10 sub- M_{Ch} merger scenario, and understand what is the range of properties of double CO WD merger remnants, how the subsequent viscous phase proceeds, and whether carbon ignition in a remnant can lead to an explosion. In this thesis, I shed light on some of these issues through semi-analytical calculations and hydrodynamic and magnetohydrodynamic simulations.

In Chapter 2, I perform simulations of merging CO WD binaries with the smoothed-particle hydrodynamics code GASOLINE in order to characterize the range of possible merger remnant configurations. In particular, I discern which mergers are “similar in mass”, and produce remnants that are substantially heated and rotationally supported throughout. As discussed in Sec. 1.4, these are potentially SN Ia progenitor candidates via the vK10 channel. I also make simple estimates of the compressional heating the remnants will experience during post-merger evolution to find which of them could eventually ignite carbon fusion.

The smoothed-particle hydrodynamics method is used by almost all simulations of WD mergers. In Chapter 3, I investigate whether the outcome of a merger simulation depends on the hydrodynamic scheme used by performing a merger of a $0.625 - 0.65 M_{\odot}$ CO WD binary using either GASOLINE or the moving-mesh magnetohydrodynamics code AREPO, and discover phenomena during the earliest phase of post-merger evolution that are unique to AREPO. I also detail work that led to a number of improvements in AREPO to prevent spurious loss of global angular momentum when simulating differentially rotating systems.

In Chapter 4, I use AREPO to simulate the evolution of initially weak magnetic fields within the $0.625 - 0.65 M_{\odot}$ merger. I find exponential field growth during the coalescence of the WDs that leads to a powerful, $> 10^{10}$ G magnetic field in the merger remnant that could affect its subsequent evolution.

Lastly, in Chapter 5, I consider the evolution of idealized and quasi-hydrostatic sub- M_{Ch} CO WDs experiencing a nuclear runaway in their centers. While, as stated in Sec. 1.3.1, such a runaway inevitably leads to some form of explosion for M_{Ch} WDs, in sub- M_{Ch} ones it may instead lead to the lifting of degeneracy and expansion into a carbon-burning star. I use analytical arguments and simple models to determine the minimum mass required for the runaway to produce an explosion, and discuss the consequences this has on merger remnants after their viscous evolution.

Chapters 2 and 4 have been published as Zhu et al. (2013) and Zhu et al. (2015), respectively, and Chapter 5 is being submitted for publication simultaneous to the submission of this thesis. For the most part, I have reproduced exactly the texts from each paper, only modifying the chapter introductions to minimize repetitious discussion of WD mergers and the vK10 channel. I have added postscripts to Chapters 2 and 4 that discuss their results in light of developments after their publication, and included an extensive appendix to Chapter 5 that details our calculation of convective suppression in magnetized, rotating WDs. Any additional changes are noted at the start of each chapter.

1.7 Pre-Merger Evolution

To preface the rest of the thesis, we briefly cover a few topics that are only mentioned in passing in subsequent chapters: what WD masses are typically involved in a CO WD binary merger, and the stability of mass transfer between WDs.

1.7.1 Typical CO WD Masses

While we can roughly estimate that CO WDs masses have a range from $\sim 0.4 - 1.0 M_{\odot}$ (Sec. 1.1), mergers between CO WDs of certain masses may statistically be more common. Here we discuss the difficulties in determining these typical masses.

[Tremblay et al. \(2016\)](#) find that the field distribution of single CO WDs is sharply peaked, with a mean mass of $\langle M_{\text{fld}} \rangle \approx 0.62 M_{\odot}$ and a dispersion of $\sim 0.1 M_{\odot}$; other studies report similar $\langle M_{\text{fld}} \rangle$ values ranging from $\sim 0.6 - 0.65 M_{\odot}$ ([Kleinman et al. 2013](#), and references therein). [vK10](#) argue that since mass transfer tends to shrink binary orbits, the progenitor systems of double WD binaries will tend to have constituents with similar masses, which minimizes the first phase of mass transfer. Consequently, the two WDs will also have similar masses, which, naively, suggests a typical merging binary system would consist of two $\langle M_{\text{fld}} \rangle$ WDs.

Detailed theoretical calculations using population synthesis do find close WD binaries with $\sim 0.65 M_{\odot}$ constituents, but generally predict a population that has a wider range of masses and mass ratios (eg. [Toonen et al. 2014](#) Fig. 8, 10). In [Toonen et al. \(2012\)](#), for example, the population is bimodal, with the peaks centered roughly around $0.5 - 0.6 M_{\odot}$ and $0.5 - 0.8 M_{\odot}$. The predicted populations, however, differ between population synthesis codes, and depend on how mass loss and WD formation for single stars, the initial mass distribution of binaries on the main sequence, mass transfer and transfer stability criteria, and common envelope evolution are implemented ([Toonen et al. 2014](#); [Claeys et al. 2014](#)). It is therefore unclear how robust they are.

Meanwhile, spectroscopic surveys for short-period WD binaries have yielded a few dozen that will merge within a Hubble time (eg. [Marsh 2011](#); [Gianninas et al. 2015](#)). Most of these have been discovered by the Extremely Low-Mass (ELM) WD survey (eg. [Brown et al. 2010](#); [Gianninas et al. 2015](#)); its systems show a wide range of mass ratios, but since the survey targets binaries where one WD has $M \lesssim 0.3 M_{\odot}$, it likely does not represent the overall distribution of binaries. Outside of ELM, few WD binaries of total mass $\gtrsim 1.0 M_{\odot}$ are known ([Napiwotzki et al. 2007](#); [Marsh 2011](#)), at least partly because WD surface area, and therefore luminosity, decreases with mass, making massive ones more difficult to find. [Badenes & Maoz \(2012\)](#) deduce WD merger rates through statistical analysis of the binary WD population from the Sloan Digital Sky Survey ([York et al. 2000](#)), but their analysis is not sensitive to mass ratio ([Maoz et al. 2012](#)). We note that the recently launched Gaia space mission ([Carrasco et al. 2014](#)) is expected to increase the number of known WDs by a factor of 10, discovering perhaps thousands of close WD binaries in the process, and – in concert with ground-based follow-up spectroscopy to determine masses and radial velocities – will bring better statistics for the merging WD binary mass distribution ([Gaensicke et al. 2015](#)).

In lieu of definitive answers above, we perform in Ch. 2 merger simulations for systems that span the range of possible CO WD masses and mass ratios, with additional mass resolution near $0.65 M_{\odot}$ (the $\langle M_{\text{fld}} \rangle$ reported by [Tremblay & Bergeron 2009](#)). Thereafter, we focus on a $0.625 - 0.65 M_{\odot}$ merger. This system is of interest not only because its constituents are near $\langle M_{\text{fld}} \rangle$ while its total mass is

substantially below M_{Ch} , but, from Sec. 1.4 (and Ch. 2), mergers of WDs with similar masses appear more likely to ignite fusion at their centers.⁹

1.7.2 Merger Initial Conditions and Unstable Mass Transfer

For all of the merger simulations we conduct in this thesis, we generate initial conditions by placing two unperturbed spherical WDs, whose rotation are unsynchronized with their orbital period, at an initial separation where the radius of the less massive WD is equal to its Roche lobe (the radius around a star within which any material is gravitational bound to the star). Note that the less massive WD is always the first to initiate mass transfer, since by the WD mass-radius relation (eg. Kippenhahn et al. 2012 Sec. 19.6),

$$R \propto M^{\frac{1-n}{3-n}} \approx M^{-1/3} \quad (1.3)$$

(approximating the low-mass cold WD equation of state with an $n = 3/2$ polytrope), it is larger and overflows its Roche lobe first. We therefore call the less massive WD the “donor” and the more massive the “accretor” throughout the thesis. The use of unsynchronized WDs is discussed in Sec. 2.2.2 and 2.4.3.

The use of spherical WDs, however, neglects the tidal bulges they develop close to the start of mass transfer. Hence, in our simulations, the WDs deform and radially pulsate in response to the new potential. The less massive WD overshoots the Roche lobe during each pulsation, resulting in an overestimate of the rate of early mass transfer. Dan et al. (2011) show that, for systems where the WD spin and orbital period are synchronized, “accurate initial conditions” that include tidal bulges extend the phase of mass transfer prior to the full tidal disruption of the donor by several tens of orbital periods. It is much more difficult to accurately create tidal bulges in unsynchronized systems, and we discuss the effects of our “approximate” initial conditions in Sec. 2.5.3.¹⁰

Because mass transfer rates are overestimated, however, our simulations cannot predict which binaries will experience runaway mass transfer and merge – indeed, every one of our simulations in Ch. 2 does so. Whether or not mass transfer between two stars is stable has long been studied analytically and semi-analytically, and it is known that it depends critically on the mass ratio $q_m = M_d / M_a$ between the donor star (M_d) and the accretor star (M_a ; from above, $M_a \geq M_d$ and $q_m \leq 1$), and whether or not spin and orbital angular momentum can be efficiently coupled to each other. We sketch a simple argument for stability below.

Let us first consider the case in which some dissipative process, such as tidal torquing between the donor and accretor or an accretion disk, is able to return any angular momentum from the WD spin back to the orbit, thus helping to stabilize mass transfer. This means that the orbital angular momentum $L_{\text{orb}} = (M_a M_d / M_{\text{tot}}) \sqrt{GM_{\text{tot}}a}$, where $M_{\text{tot}} = M_d + M_a$ and a is the orbital separation, is constant in time, i.e. $\dot{L}_{\text{orb}} = 0$. From this we may derive $\dot{L}_{\text{orb}} / L_{\text{orb}} = \dot{M}_d / M_d + \dot{M}_a / M_a - \dot{M}_{\text{tot}} / 2M_{\text{tot}} + \dot{a} / 2a$. We shall assume conservative mass transfer (this is backed by the simulations in Ch. 2 and 3, which show less than 1% of stellar material becomes unbound), meaning $\dot{M}_a = -\dot{M}_d$. Putting these together gives

⁹The masses are not made exactly equal, since this is improbable in nature.

¹⁰The effect of using accurate versus approximate initial conditions on the final inspiral phase and structure of the remnant will vary between mergers. For example, Dan et al. (2011, their Fig. 9) find the central density and temperature of a $0.6 - 0.9 M_{\odot}$ merger remnant changes by ~ 5 and $\sim 30\%$, respectively, but Pakmor et al. (2012a, their Figs. 5 and 6) show few changes to the density and temperature profiles during the coalescence of a $1.0 - 1.1 M_{\odot}$ binary.

us

$$\frac{\dot{L}_{\text{orb}}}{L_{\text{orb}}} = (1 - q_m) \frac{\dot{M}_d}{M_d} + \frac{\dot{a}}{2a} = 0. \quad (1.4)$$

We use Paczyński (1971)'s estimate for the Roche lobe of M_d , $R_L \approx 0.46a(M_d/M_{\text{tot}})^{1/3}$, valid for $q_m \lesssim 1$ (Eggleton 1983). Differentiating and using Eqn. 1.4, we obtain

$$\frac{\dot{R}_L}{R_L} = 2(q_m - \frac{5}{6}) \frac{\dot{M}_d}{M_d}. \quad (1.5)$$

For mass transfer to be stable, R_d must contract more quickly (or expand more slowly) than R_L , i.e. $\dot{R}_d/R_d < \dot{R}_L/R_L$. From Eqn. 1.3, $\dot{R}_d/R_d = -\dot{M}_d/3M_d$; combining this with Eqn. 1.5, we obtain the stability criterion $2(q_m - 5/6) < -1/3$, or:

$$q_m < \frac{2}{3}. \quad (1.6)$$

Most of the systems we simulate fall well outside of the stable regime, but a number (such as the $0.4 - 1.0 M_\odot$ merger in Ch. 2) do satisfy this, and naïvely should not merge.

In the case where spin and orbital angular momentum coupling is instead negligible – which is the case if the accretion stream does not form a disk but rather directly impacts the accretor (Nelemans et al. 2001a) – a similar analysis can be performed, using total angular momentum $L = L_{\text{orb}} + L_{\text{spin}} = (M_a M_d / M_{\text{tot}}) \sqrt{GM_{\text{tot}}a} + L_{\text{spin}}$, from which we may derive $\dot{L}/L_{\text{orb}} = \dot{M}_a/M_a + \dot{M}_d/M_d - \dot{M}_{\text{tot}}/2M_{\text{tot}} + \dot{a}/2a + \dot{L}_{\text{spin}}/L_{\text{orb}}$. Following Marsh et al. (2004) and Nelemans et al. (2001a), we assume only the spin of the accretor is relevant, and use Verbunt & Rappaport (1988)'s representation of the accretor spin-up from direct impact accretion, $\dot{L}_{\text{spin}} = -\dot{M}_d \sqrt{GM_a R_h}$ (\dot{M}_d is negative). R_h is the effective radius of the matter transferred onto the accretor, and the ratio $r_h = R_h/a$ is given by a fitting formula: $r_h \approx 0.0883 - 0.04858 \log(q_m) + 0.11489 \log^2(q_m) + 0.020475 \log^3(q_m)$, valid for all plausible WD binary mass ratios (Verbunt & Rappaport 1988). Dividing \dot{L}_{spin} by L_{orb} to obtain $\dot{L}_{\text{spin}}/L_{\text{orb}} = -\sqrt{(1 + q_m)r_h}(\dot{M}_d/M_d)$, and assuming conservative mass transfer ($\dot{L} = 0$), we obtain

$$\frac{\dot{a}}{a} = 2 \left(q_m - 1 + \sqrt{(1 + q_m)r_h} \right) \frac{\dot{M}_d}{M_d}. \quad (1.7)$$

Using the same argument that gave us Eqn. 1.6, this reduces to

$$q_m - \frac{2}{3} + \sqrt{(1 + q_m)r_h} < 0, \quad (1.8)$$

which, solved numerically, is

$$q_m \lesssim 0.219, \quad (1.9)$$

well-below any mass ratio for a CO WD binary (Sec. 1.7.1). Eqns. 1.6 or 1.9 represent the upper and lower-bounds of mass transfer stability, as seen in Fig. 1.2: a binary with $q_m > 2/3$ will experience unstable mass transfer even with perfect angular momentum coupling, while a binary with $q_m \lesssim 0.2$ will always be stable, even with no coupling. The critical q_m for an imperfect coupling will fall somewhere between these two.

The question then becomes which stability better represents mass transfer in WD binaries. In the

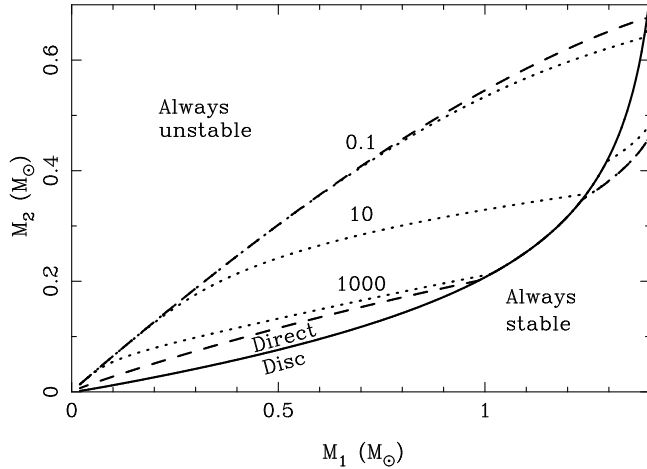


Figure 1.2: Regions of stable and unstable mass transfer for the WD merger parameter space from Marsh et al. (2004; their Fig. 1). M_1 is M_a and M_2 is M_d . The upper dashed line is a more accurate estimate for Eqn. 1.6, and the lower dashed one that for Eqn. 1.8. The solid “Direct/Disc” line represents the transition between direct impact and disk accretion. Dotted lines represent the boundary between stable and unstable mass transfer when the tidal synchronization timescale τ_s is 1000, 10 and 0.1 yr.

absence of other sources of spin-orbit coupling, this is determined solely by whether disk or direct impact accretion occurs. Following Lubow & Shu (1975), Nelemans et al. (2001a) determines when one transitions into the other by calculating the point where the minimum radius reached by the accretion stream becomes larger than the accretor; the corresponding critical surface in the merger mass parameter space is plotted in Fig. 1.2. For $0.4 \leq M_a \leq 1.0$, the line falls around $q_m = 0.15$, below even Eqn. 1.9.

Tides within the WDs can substitute for disks for spin-orbit coupling. While traditional estimates of the spin-orbit synchronization timescale in WD binaries ranges from $\tau_s \sim 10^{12}$ yr for radiative damping to $\tau_s \sim 10^{15}$ yr for molecular viscosity (Marsh et al. 2004), other sources of dissipation, such as turbulent viscosity (Mochkovitch & Livio 1989), may lead to much shorter τ_s . Recent work (Fuller & Lai 2012; Burkart et al. 2013; Fuller & Lai 2014) show resonant coupling between tidal forces and stellar pulsations favor a much shorter τ_s (though exactly how short remains unclear; Fuller & Lai 2014). Semi-analytical calculations (Marsh et al. 2004; Gokhale et al. 2007; Kremer et al. 2015), however, suggest that even for τ_s as small as 10 yr, all the systems we consider in this thesis should still experience unstable mass transfer and merge. All these systems also merge in simulations that more accurately model the binary at the onset of mass transfer (Dan et al. 2011; 2012), and so we proceed under the notion that all our binaries should merge. We note that there is evidence (Shen 2015; Brown et al. 2016) that even He - CO WD binaries with extremely low q_m do so as well.

Chapter 2

A Parameter-Space Study of Carbon-Oxygen White Dwarf Mergers

Chenchong Zhu, Philip Chang, Marten H. van Kerkwijk and James Wadsley
The Astrophysical Journal, Volume 767, Issue 2 - article id. 164, 32 pp., 2013
([Zhu et al. 2013](#))

As we discussed in Sec. 1.4 and 1.5, the merger of two carbon-oxygen white dwarfs can lead either to a spectacular transient, stable nuclear burning or a massive, rapidly rotating white dwarf. Previous simulations of mergers have shown that the outcome strongly depends on whether the white dwarfs are similar or dissimilar in mass ([Lorén-Aguilar et al. 2009](#)). In the similar-mass case, both white dwarfs merge fully and the remnant is hot throughout, while in the dissimilar case, the more massive, denser white dwarf remains cold and essentially intact, with the disrupted lower mass one wrapped around it in a hot envelope and disk.

In order to determine what constitutes “similar in mass” and more generally how the properties of the merger remnant depend on the input masses, we simulated unsynchronized carbon-oxygen white dwarf mergers for a large range of masses using smoothed-particle hydrodynamics. We find that the structure of the merger remnant varies smoothly as a function of the ratio of the central densities of the two white dwarfs. A density ratio of 0.6 approximately separates similar and dissimilar mass mergers. Confirming previous work, we find that the temperatures of most merger remnants are not high enough to immediately ignite carbon fusion. During subsequent viscous evolution, however, the interior will likely be compressed and heated as the disk accretes and the remnant spins down. We find from simple estimates that this evolution can lead to ignition for many remnants. For similar-mass mergers, this would likely occur under sufficiently degenerate conditions that a thermonuclear runaway would ensue.

Aside from redundant parts of the introduction, we also do not reproduce here the extensive Appendix to [Zhu et al. \(2013\)](#), which contains tables of binary input parameters and remnant properties for the simulations, and its online figure set, depicting merger remnant properties for all of our simulations.

2.1 Introduction

Until recent years, efforts to find SN Ia progenitors among merging CO WD binaries have focused on those with total mass $M > M_{\text{Ch}}$. The end result of such mergers is believed to be either stable off-center carbon ignition, which would turn the merger remnant into an oxygen-neon WD and possibly eventually result in accretion-induced collapse (Saio & Nomoto 1998), or slow accretion, which allows the remnant to stay cool and eventually ignite at high central density (Yoon et al. 2007). Less massive mergers were usually thought to result in more massive, rapidly rotating CO WDs (Segretain et al. 1997; Külebi et al. 2010), but more recently it has been realized these might eventually become hot enough to ignite (van Kerkwijk et al. 2010, vK10 hereafter; Shen et al. 2012; Schwab et al. 2012). Indeed, vK10 argue that type Ia supernovae result generally from mergers of CO WDs with similar masses, independent of whether or not their total mass exceeds M_{Ch} . For all these studies, the conclusions on whether and where ignition takes place depend critically on the structure of the merger remnant.

The merging process, and the merger remnant, have been studied quite extensively, mostly using smoothed-particle hydrodynamics (SPH; e.g. Monaghan 2005). These simulations have shown that the outcome strongly depends on whether the WDs are similar or dissimilar in mass. In the similar-mass case, both WDs disrupt fully and the remnant is hot throughout, while in the dissimilar case, the more massive, denser WD remains essentially intact and relatively cold, with the disrupted lower mass one wrapped around it in a hot envelope and disk. Less clear, however, is what constitutes “similar-mass,” and, more generally, how the merger remnant properties depend on the initial conditions.

In principle, for cold WDs of given composition, the remnant properties should depend mostly on the two WD masses, with a second-order effect due to rotation. In this paper, we try to determine these dependencies using simulations of WD mergers with the Gasoline SPH code, covering the entire range of possible donor and accretor masses, but limiting ourselves to non-rotating WDs. Our primary aim is to identify trends between mergers of different masses, both to guide analytical understanding and to help scale other, perhaps more precise simulations. Here, our hope is that while the results of individual simulations may suffer from uncertainties related to the precise techniques and assumptions used, the trends should be more robust. We also try to provide sufficient quantitative detail on the properties of merger remnants that it becomes possible to make analytical estimates or construct reasonable numerical approximations without having to run new simulations.

Our work is complementary to the recent surveys of remnant properties by Raskin et al. (2012) and Dan et al. (2012), in that they focus on different scientific questions (e.g., orbital stability; possible detonation). In contrast to our work, they assume that the WDs are co-rotating with the orbit. Whether this is a better assumption than no rotation depends on the strength of tidal dissipation, which unfortunately is not yet known (see Marsh et al. 2004; Fuller & Lai 2012).

This chapter is organised as follows. In Section 2.2, we describe the SPH code we used, as well as our initial conditions. In Section 2.3, we present our results and give trends for a number of pertinent remnant properties. In Section 2.4, we test the robustness of our results, and in Section 2.5 compare our results with those of LIG09 and others. Lastly, in Section 2.6, we speculate on the further evolution of our remnants, considering in particular whether, as suggested by vK10, some might lead to type Ia supernovae.

2.2 Code and Input Physics

We simulate the mergers by placing non-rotating white dwarfs in a circular orbit with an initial separation a_0 chosen such that rapid mass transfer begins immediately. We then follow the merger for six orbits, at which time the remnant has become approximately axisymmetric. As in prior work, the morphology of all merger remnants is similar, consisting of a dense, primarily degeneracy-supported center surrounded by a partly thermally-supported hot envelope (called a “corona” by LIG09) and a thick, sub-Keplerian disk. We will use the terms “core”, “envelope” and “disk” throughout this work. We also quite often refer to both the core and envelope simultaneously as the “core-envelope”.

We use simulation techniques and initial conditions that are standard in the field of WD merger simulations, both in order to compare with previous work, as well as to not introduce novel numerical effects into our simulations. We detail our code and initial conditions below so that they can easily be reproduced.

2.2.1 The SPH Code

With smoothed-particle hydrodynamics, one uses particles as a set of interpolation points to determine continuum values of the fluid and model its dynamics. SPH is a Lagrangian method, meaning movement is automatically tracked, and regions of high density contain more particles and therefore are automatically more resolved. Moreover, SPH inherently conserves angular momentum in three dimensions, which is difficult to reproduce in grid codes except under specific coordinate systems and symmetries. SPH therefore allows one to efficiently simulate complex phenomena with a large range of lengthscales. It has become the method of choice for merger simulations, and so we chose it as well.

For our simulations, we use Gasoline (Wadsley et al. 2004), a modular tree-based SPH code that was designed and has been used for a wide range of astrophysical scenarios, from galaxy interactions to planet formation. It aims for tight controls on force accuracy and integration errors. Gasoline implements the Hernquist & Katz (1989) kernel – we use 100 neighbors – and uses the asymmetric energy formulation (Wadsley et al., Eqn. 8) to evolve particle internal energy. In our simulations, total energy is on average conserved to 0.3%, and angular momentum to 0.006%.

By default, Gasoline uses the usual Monaghan and Gingold formulation for artificial viscosity (see Monaghan 2005), together with a Balsara switch (a standard feature of WD merger SPH simulations) to reduce viscosity in non-shocking, shearing flows. Guerrero et al. (2004) found that such a prescription did not reduce viscosity sufficiently, resulting in excess spin-up of the remnant core and associated shear heating. Yoon et al. (2007), in addition to a Balsara switch, used variable coefficients for the linear and quadratic viscosity terms in the SPH equations of motion and energy, setting these values to $\alpha = 0.05$ and $\beta = 0.1$, respectively, where shocks are absent, and around unity where they are present. A similar formulation was used in Dan et al. (2011; 2012). Since Gasoline includes it as well, we have used it for our study. Excess viscosity nevertheless remains a potential problem; we investigate its effects further in Sec. 2.4.5.

We modified Gasoline to include support for degenerate gas through the Helmholtz equation of state (EOS)¹ (Timmes & Swesty 2000). This code, also used in Raskin et al. (2012) and Dan et al. (2012)’s simulations, interpolates the Helmholtz free energy of the electron-positron plasma, along with analytical expressions for ions and photons, to determine pressure, energy and other properties

¹ Available at <http://cococubed.asu.edu/>.

from density and temperature. It is fast, spans a large range of density and temperature, and has, by construction, perfect thermodynamic consistency. To obtain quantities as a function of density and internal energy, we utilized a Newton-Raphson inverter. To keep the energy-temperature relation positive-definite, we did not disable Coulomb corrections in cases where total entropy became negative.

Gasoline keeps track of the internal energy of particles, using it to determine other thermodynamic properties for fluid evolution. A particle’s energy will naturally fluctuate due to noise, but for nearly zero-temperature particles this could result in their energy dipping below the Fermi energy. In such situations we keep the pressure at the Fermi pressure, while letting the energy freely evolve. A consequence of the floor is that a small amount of excess energy is injected into the system through mechanical work, which eventually manifests as additional thermal energy. The accumulated energy over a simulation is typically a small fraction of the internal energy, and therefore does not significantly affect the dynamics of the merger or most properties of the remnant. In cold, degeneracy-dominated material, however, a small change in internal energy corresponds to a large temperature change, at times comparable to the physically expected values, and thus the temperatures near the centers of some of our simulations have been affected. We characterize this spurious heating in Sec. 2.4.6 and show that it does not unduly affect our work’s conclusions. However, it makes it difficult to run much longer simulations.

We also place an energy floor at half the Fermi energy. This is to prevent particle energies from approaching zero (and consequently calling for tiny timesteps), which under rare circumstances occurs when particles perform a great deal of mechanical work. We find this happens primarily for particles that are flung out of the system by the merger and are cooling rapidly, and therefore are confident it has only a very minor effect on our simulations.

In our work, we ignore outer hydrogen and helium layers, composition gradients, and any nuclear reactions. This is mainly because previous work has found that nuclear processing was unimportant during the merger. For instance, LIG09 found fusion released $\sim 10^{41}$ erg for their $0.6 - 0.8 M_{\odot}$ merger, orders of magnitude smaller than the $\sim 10^{50}$ erg binding energy of the remnant. Only for mergers involving very massive, $\gtrsim 0.9 M_{\odot}$ WDs might this assumption break down, with the possibility of carbon detonations arising (Pakmor et al. 2010; 2011b; 2012b; but see Raskin et al. 2012; Dan et al. 2012). Similarly, Raskin et al. (2012), who included standard helium envelopes of $\sim 1 - 2\%$ of the WD mass in their simulations, found that only for accretors with masses above $\sim 1 M_{\odot}$ did it make a substantial difference: a helium detonation would inject $\sim 10^{49}$ erg into the merger remnant. While this led to additional heating, it was insufficient to trigger much carbon burning or unbind any portion of the remnant (helium detonations have also been found for lower-mass accretors with CO-He hybrid donors; Dan et al. 2012).

2.2.2 Initial Conditions

We created spherical white dwarfs using pre-relaxed cells of particles rescaled to follow the appropriate enclosed mass-radius relation determined using the Helmholtz equation of state. We assumed a composition of 50% carbon and 50% oxygen by mass, and a uniform temperature of 5×10^6 K. The stars were then relaxed in Gasoline for 81 s ($\sim 10 - 40$ dynamical times, depending on the white dwarf mass) with thermal energy and motion damped (to 5×10^6 K and 0 cm s^{-1} , respectively) during the first 41 s, and left free during the remaining 40 s. Particle energy noise prevented cooling of $\gtrsim 5 \times 10^6 \text{ g cm}^{-3}$ material to below 10^7 K. We checked that the density profile of each star after relaxation was consistent

with the solution from hydrostatic equilibrium, and found this was the case – central densities, for example, agreed to within 2%. The radii of the relaxed stars, as defined by the outermost particle of a relaxed WD, on the other hand were on average about 7% too small, reflecting our inability to model the tenuous WD outer layers².

We used a constant particle mass of 10^{28} g, so that a $0.4 M_{\odot}$ WD has 8×10^4 particles, and a $1.0 M_{\odot}$ WD has 2×10^5 . These numbers are similar to those used by LIG09 and Yoon et al. (2007), and exceed the $\sim 2 \times 10^4$ particles per star used by Dan et al. (2012). Raskin et al. (2012) performed a resolution test for a merger of two $0.81 M_{\odot}$ WDs, varying the number of particles per star from 10^5 to 2×10^6 . They found differences of $\sim 2\%$ in the mass of the core plus envelope, disk half-mass radius, and inner disk rotation frequency. The one qualitative difference they found was that at their highest particle resolution, the WDs failed to break symmetry and disrupt (note that they assumed co-rotating WDs, making such a stable contact configuration possible). We perform our own test in Sec. 2.4.7 and find similar results.

We relaxed $0.4, 0.5, 0.55, 0.6, 0.65, 0.7, 0.8, 0.9$ and $1.0 M_{\odot}$ white dwarfs, and combined them in all possible permutations to form our parameter space of binaries. These values were chosen to represent the range of possible CO WD masses, with greater resolution near the empirical peak at $\sim 0.65 M_{\odot}$ of the mass distribution of (single) CO WDs (Tremblay & Bergeron 2009). We also performed additional simulations with $0.575 - 0.65, 0.625 - 0.65$ and $0.64 - 0.65 M_{\odot}$ binaries to explore the outcomes of similar-mass mergers. We thus simulated 48 mergers in total.

We placed two relaxed, irrotational WDs in a circular orbit. We chose the initial separation a_0 such that the donor WD just fills its Roche lobe, taking the location of the donor’s outermost particle as its radius and using the Roche lobe approximation (for a synchronized binary) from Eggleton (1983).

This simple initial condition is similar to that of Pakmor et al. (2010), and implies that the binary system as a whole is not equilibrated. Therefore, as the simulation begins, the two WDs react to the tides, become stretched, and strong Roche lobe overflow ensues because the donor overshoots its Roche radius (in a widely separated binary, the donor would start to pulsate). As a result, the donor disrupts after just one to two orbits. For synchronized binaries, Dan et al. (2011) showed that the onset of mass transfer is much more gentle if the WDs are relaxed in the binary potential, disruption occurring only after several dozen orbital periods. They also showed that this results in systematic changes in the merger remnants. It is not clear whether the same will hold for unsynchronized binaries, since the accretion stream hits a surface that, in its frame, counterrotates, and therefore accretion is always much less gentle than for synchronized WDs. The difference is particularly dramatic for similar-mass binaries, where, in the synchronized case, the WDs can come into gentle contact, while in the unsynchronized case, any contact is violent. Unfortunately, it is difficult to test the effect of proper equilibration for unsynchronized binaries, since one has to relax to non-trivial initial conditions. A better approximation was attempted by LIG09 and Guerrero et al. (2004), who started their WDs further out and reduced the separation artificially until mass transfer began. In their simulations, disruption still followed very quickly. Given that, and wanting to avoid any partial synchronization, we kept our simpler setup, and tested it by running simulations with varying a_0 . We will discuss these tests in Sec. 2.4.2 and compare our results with those of others in Sec. 2.5.

²Our relaxed WDs also show evidence of sub-kernel radial banding of particles, which does not appear in any interpolated quantities. We do not believe this banding has an effect on our simulations except for a possible reduction in effective resolution, but will investigate remedies in future work.

2.2.3 Merger Completion Time

It is difficult to decide when a merger is “complete”, since for some cases remnant properties continue to evolve long after the two WDs coalesce, with (artificial) viscosity redistributing angular momentum and heating the remnant. As a visually inspired criterion, we decided initially to use the degree of non-axisymmetry, continuing simulations until they were less than 2.5% non-axisymmetric, as measured from the ratio of zeroth to largest non-zero Fourier coefficient of particles binned in azimuth. However, this had its own issues: in dissimilar-mass mergers – where most of the particles are in the accretor, already roughly axisymmetric following the merger – our convergence criterion was achieved while the outer disk was still obviously non-axisymmetric. In equal-mass mergers, which are inherently more axisymmetric, completion also was too soon, before the densest material had reached the center of the remnant.

For the majority of our systems, however, the time required to reach 2.5% non-axisymmetry was roughly constant in units of the initial orbital period, at 6.1 ± 1.2 . For about the same time, axisymmetry was also achieved (by subjective visual inspection) for both dissimilar-mass mergers (except, in extreme dissimilar-mass cases, the outermost regions of their disks) and for equal-mass mergers (where the densest material had reached the center). We therefore use 6 orbital periods of the initial binary as the completion time of our simulations. In Sec. 2.4.4, we discuss the effect of continuing our simulations for 2 further orbital periods.

2.3 Results

With our 48 simulated mergers in hand, we try to determine scaling relations of global quantities such as the remnant and disk mass, highest temperature, etc., and look for homologies in the remnant profiles. For our analysis, we use a cylindrical (ω, ϕ, z) coordinate system centered on the remnant core. Properties on the equatorial (ω, ϕ) plane – defined as the original orbital plane – are averaged over ϕ using particles within $\frac{1}{2}h_z$ of the equatorial plane, where h_z is the remnant’s rotational axis ($\omega = 0$) central scaleheight (see Sec. 2.3.2.2). Properties along the rotational (z) axis are averaged within a cylinder $\omega < \frac{1}{2}h_z$. We use $\frac{1}{10}h_z$ as the bin size along both the equatorial plane and rotational axis. We determine properties mostly as a function of enclosed mass $M(r)$, which we define spherically³. Thus, we show, e.g., equatorial plane temperature $T(\omega)$ as a function of $M(r = \omega)$, the mass enclosed within a sphere with radius $r = \omega$.

2.3.1 Representative Mergers

As found for previous simulations, qualitatively the most important factor controlling the merger outcome is whether the WD masses are “dissimilar” or “similar”. In the former case, where the donor is significantly less massive than the accretor, only the donor overflows its Roche lobe,⁴ is disrupted, and accretes onto the accretor. The accreted material is heated on impact, lifting degeneracy. Hence, the merger remnant consists of a partly non-degenerate hot envelope and small, thick sub-Keplerian disk, both surrounding a cold core containing the largely unaffected accretor.

³Arguably, enclosed mass is more properly defined within equipotential surfaces, but this makes comparison with other simulations harder. For dissimilar-mass mergers, the difference is slight.

⁴The lower mass WD is larger and thus always fills its (smaller) Roche lobe first.

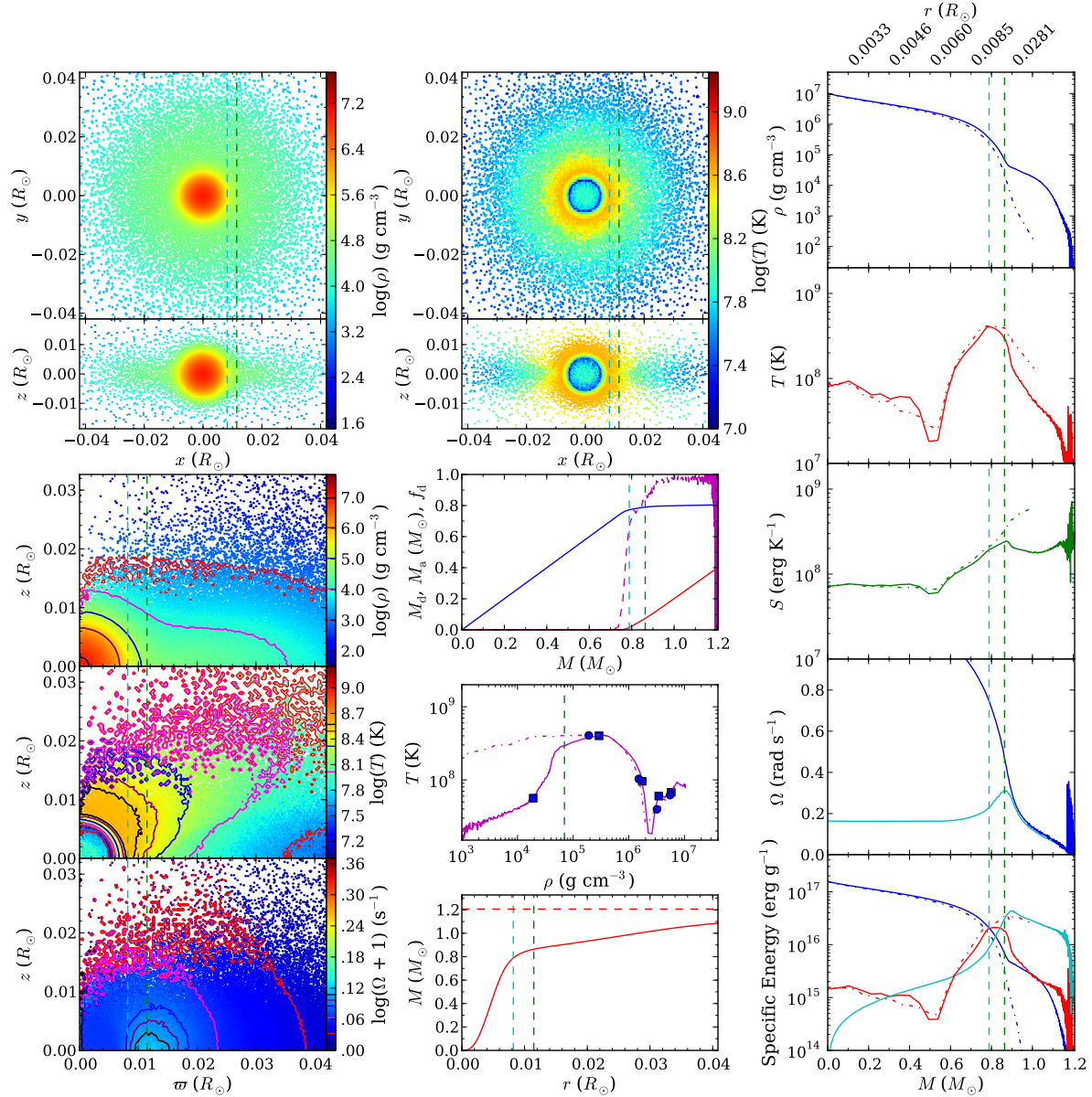


Figure 2.1: Structure of a $0.4 - 0.8 M_{\odot}$ merger remnant, representing the general outcome of a merger of white dwarfs with dissimilar mass. Upper left and middle – binned maps of density ρ and temperature T along slices in the xy and xz -planes. Lower left – binned maps and contours of density, temperature, and angular frequency Ω in the (ω, z) plane, averaged over cylindrical coordinate ϕ and over $\pm z$ (with 1 added to Ω to avoid problems with the logarithmic intensity scale). Middle – enclosed masses of donor and accretor material M_{d} and M_{a} (solid red and blue, resp.), and fraction of donor material f_{d} at a particular mass shell (dashed magenta). Middle, one but lowest – temperature-density profile with enclosed masses in $0.2 M_{\odot}$ increments indicated, both along the equatorial plane (solid curve, squares) and along the rotational axis (dot-dashed curve, circles). Middle, bottom – enclosed mass as a function of r , with the total mass indicated by the horizontal dashed red line. Right-hand column, top to bottom - density, temperature, entropy, angular (cyan) and Keplerian (blue) frequency, and degeneracy (blue), thermal (red) and rotational (cyan) specific energies as a function of enclosed mass M , both along the equatorial plane and along the rotational axis (solid and dot-dashed curves, respectively). In all graphs, the start of the disk (where the centrifugal acceleration equals half the gravitational one) and the equatorial radius (or mass enclosed within) of maximum temperature are marked by vertical green and blue dashed lines, respectively. [See the electronic edition of the Journal for Figs. 1.1–1.48.]

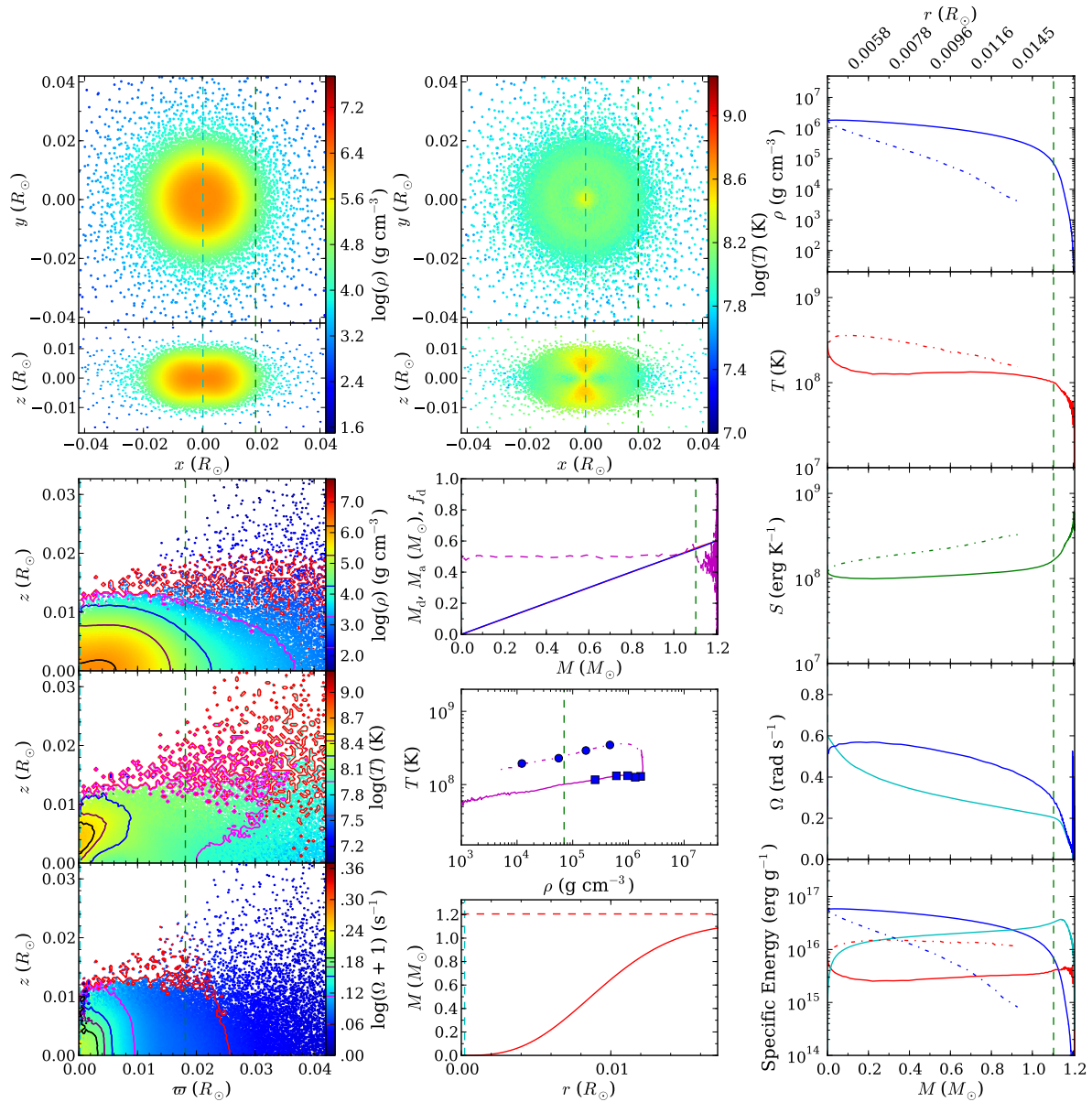


Figure 2.2: As Fig. Set 2.1, but for a $0.6 - 0.6 M_\odot$ merger remnant, representing the general outcome of a similar-mass merger.

In the latter case of a similar-mass merger, there is a large degree of mixing between the two stars. For exactly equal masses, both stars are disrupted simultaneously, and their accretion streams impact each other near the system's barycenter. Material from the centers of both stars initially forms a thick, cold, dense torus orbiting the barycenter; this torus slowly shrinks due to viscous drag, pushing the accretion stream material above and below the equatorial plane. When the stars have slightly different mass, the lower-mass one disrupts first, forming an accretion stream (or series of streams) that mixes with accretor material down to the center of the accretor (regardless of whether or not the other also disrupts).

We show the differences between similar and dissimilar-mass merger remnants using two representative examples in Figs. 2.1 and 2.2: a $0.4 - 0.8 M_{\odot}$ highly dissimilar and a $0.6 - 0.6 M_{\odot}$ equal-mass merger, respectively. One sees that the remnant morphologies are very different, consistent with previous work. The $0.4 - 0.8 M_{\odot}$ merger features a cold, nearly non-rotating and thus spherically symmetric remnant core, surrounded by a hot envelope with roughly equal degeneracy and thermal support, which itself is surrounded on the equatorial plane by a rotationally supported non-degenerate thick disk that holds most of the angular momentum. The accretor forms the core, largely undisturbed by the merger, while the envelope and disk are composed almost entirely out of donor material. The hottest points are on the interface between the core and the envelope.⁵ The $0.6 - 0.6 M_{\odot}$ remnant, on the other hand, has a massive, hot, partly rotationally supported and thus ellipsoidal core, and a very small but thick disk, both of which consist of material from both stars. No distinct envelope is formed. The hottest points are within the remnant core, just above and below the equatorial plane, arising from accretion stream material pushed out by the shrinking dense torus.

A good way to visualize how mergers transition between dissimilar and similar-mass is to look at changes in the remnant properties with varying donor mass. In Fig. 2.3, we show curves for accretors of 0.65 (left) and $1.0 M_{\odot}$ (right). One sees that remnants of highly dissimilar-mass mergers, with mass ratio $q_m \equiv M_d/M_a \lesssim 0.5$, have properties resembling the $0.4 - 0.8 M_{\odot}$ merger: their donor and accretor barely mixed, their temperature curves have off-center hot plateaus, and their angular velocity profiles feature an off-center bump. The equal-mass, $q_m = 1$ cases resemble the $0.6 - 0.6 M_{\odot}$ remnant: they have flat temperature profiles and centrally peaked angular velocity profiles. Intermediate cases have intermediate profiles, with the bumps in the temperature and angular velocity profiles widening with increasing q_m . The $0.4 - 0.8 M_{\odot}$ and $0.6 - 0.6 M_{\odot}$ remnants therefore lie at the extremes of what merger remnants look like.

The similarity between some of the curves for the 0.65 and $1.0 M_{\odot}$ accretors in Fig. 2.3 suggests a homology. The similarity is closest for mergers with the same mass difference ΔM , as can be seen in Fig. 2.4. For equal-mass mergers, all profiles are similar, simply scaled by a factor that depends on the total mass (except the $1.0 - 1.0 M_{\odot}$ merger; see below). As ΔM increases, the profiles are slightly less similar: with increasing total binary mass, the degree of mixing decreases, and the temperature and angular velocity maxima drift to slightly lower fractional enclosed mass. Nevertheless, the profiles still resemble one another far more closely than they resemble curves with other ΔM . The same holds for profiles along the rotational axis.

It may seem surprising that the controlling parameter between these approximate homologies is the mass difference ΔM rather than the mass ratio q_m . Empirically, however, the case is clear: e.g., the $0.4 - 0.5$ (second column, yellow) and $0.8 - 1.0 M_{\odot}$ (third column, black) mergers have the same

⁵The higher temperatures near the core are spurious; see Sec. 2.4.6

q_m , but different ΔM , and their structures clearly differ from one another. The same is true for the 0.4 - 0.6 (third column, cyan) and 0.6 - 0.9 (fourth column, brown) M_\odot mergers. As we discuss below, the similarity of mergers of similar ΔM likely reflects the close relation between the ratio of central densities and mass difference.

Before discussing the homologies and trends further, we should note the one dramatic exception. The 1.0 - 1.0 M_\odot simulation differs fundamentally from its fellow $\Delta M = 0$ mergers. During the evolution of this system, unlike for all other equal-mass mergers, one WD was fully disrupted before the other, and as a result material from one star (arbitrarily designated the “donor” before the start of simulation, hence the “inverted” mixing profile in Figs. 2.3 and 2.4) preferentially resides near the center of the remnant. This system also often appears as an outlier in Sec. 2.3.2 below. The 0.9 - 0.9 M_\odot merger also did not have equal mixing between the two stars, though the difference is much smaller. Raskin et al. (2012) noticed the same effect in their simulations, and concluded it reflected the fact that more massive WDs are much more concentrated and therefore harder to disrupt. This seems a likely explanation.

2.3.2 Merger Trends

A major goal of our work is to establish how various global properties of the merger remnant, such as remnant core and disk mass, maximum temperature, and maximum angular velocity, vary as a function of accretor and donor mass. By quantifying these trends, we hope to help develop a parametrized model of merger remnants. Before discussing trends, however, we stress that they are necessarily *approximate* - second order effects, numerical noise and our choice of stopping time all affect the remnant properties. Moreover, while integrated values like total thermal energy do not fluctuate from timestep to timestep, values at specific points in the remnant do (as noted the following sections). For instance, the mass enclosed within the radius of peak equatorial temperature becomes ill-defined for similar-mass mergers because these have rather flat temperature profiles (Fig. 2.3). To partly mitigate these fluctuations, the values presented below were determined by averaging frames from the simulation over an eight second span, centered on the time corresponding to six orbits of the initial binary.

As might be expected from the approximate homologies described above, we found that many properties scaled well with ΔM . Of course, a scaling with a dimensional mass difference makes little sense; we believe its success reflects the fact that over the range of $0.4 - 1.0 M_\odot$, the central density ρ_c depends approximately exponentially on mass, with $\rho_c \simeq 3.3 \times 10^7 \text{ g cm}^{-3} \exp[5.64(M/M_\odot - 1)]$ (see Fig. 2.5). Hence, a given mass difference ΔM corresponds to a given ratio of central densities, $\rho_{c,d}/\rho_{c,a}$. As argued in Sec. 2.3.2.3, $\rho_{c,d}/\rho_{c,a}$ has a straightforward interpretation: it characterizes the degree of mixing between the donor and accretor. We therefore discuss trends as a function of $q_\rho \equiv \rho_{c,d}/\rho_{c,a}$ from hereon. Where necessary, we refer to the mass ratio as q_m .

2.3.2.1 What Constitutes Similar-Mass?

As q_ρ increases from a small value toward unity, the merger remnant’s morphology shifts from resembling Fig. 2.1 (dissimilar-mass) to resembling Fig. 2.2 (equal-mass). From Fig. 2.3, ones sees that there is no particular q_ρ at which one transitions from “dissimilar” to “similar.” Nevertheless, we can determine a rough critical value of q_ρ that separates mergers in which the core is largely unaffected from those in which it is changed significantly, a separation that likely affects the outcome

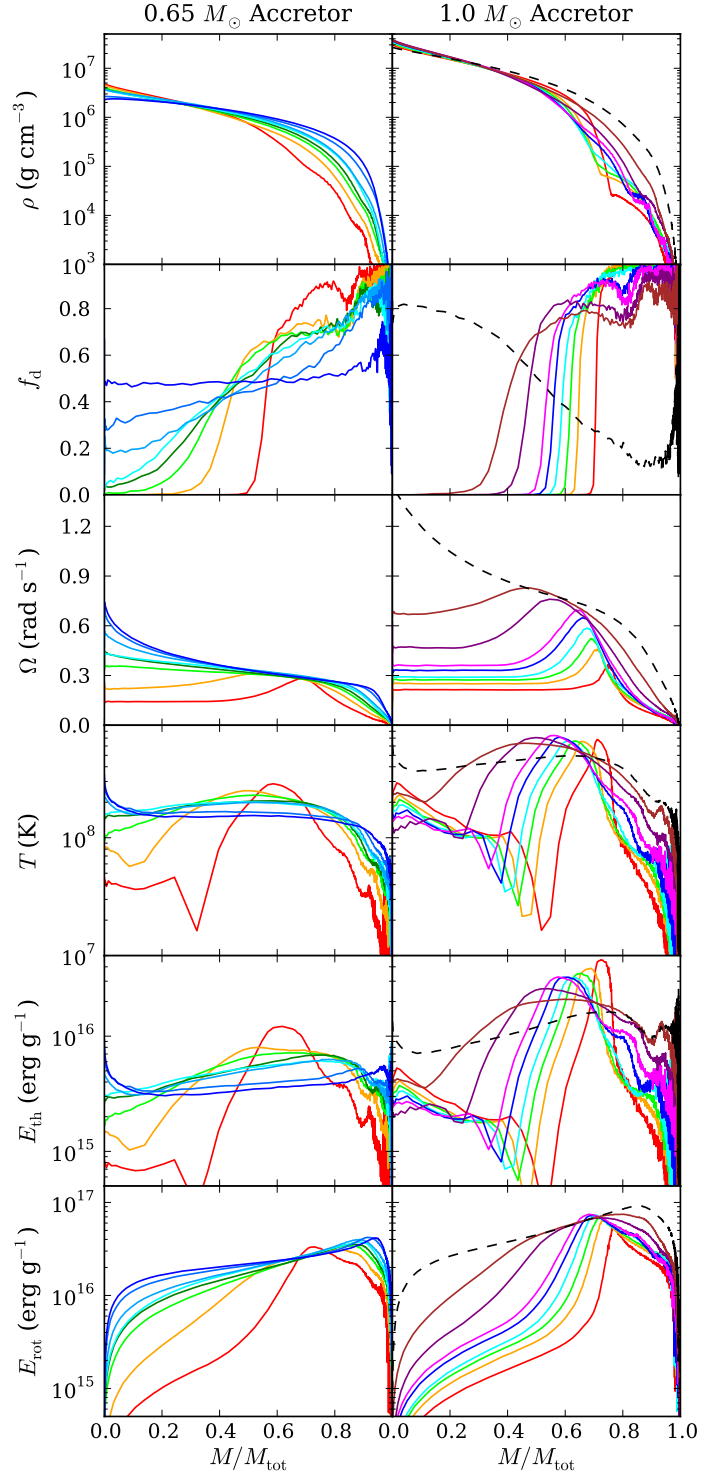


Figure 2.3: Properties of mergers with $0.65 M_{\odot}$ (left) and $1.0 M_{\odot}$ (right) accretors, for donor masses of 0.4 (red), 0.5 (orange), 0.55 (lime), 0.575 (green), 0.6 (cyan), 0.625 (light blue), 0.64 (blue), 0.65 (dark blue), 0.7 (magenta), 0.8 (purple), 0.9 (brown), and $1.0 M_{\odot}$ (black). Shown are, from top to bottom, density ρ , fraction of donor material f_d , angular frequency Ω , temperature T , specific thermal energy E_{th} , and specific rotational energy E_{rot} , all as a function of fractional enclosed mass M/M_{tot} . All properties are determined along the equatorial plane, except for f_d which is defined spherically. The $1.0 - 1.0 M_{\odot}$ merger (dashed black line) is an outlier; see text.

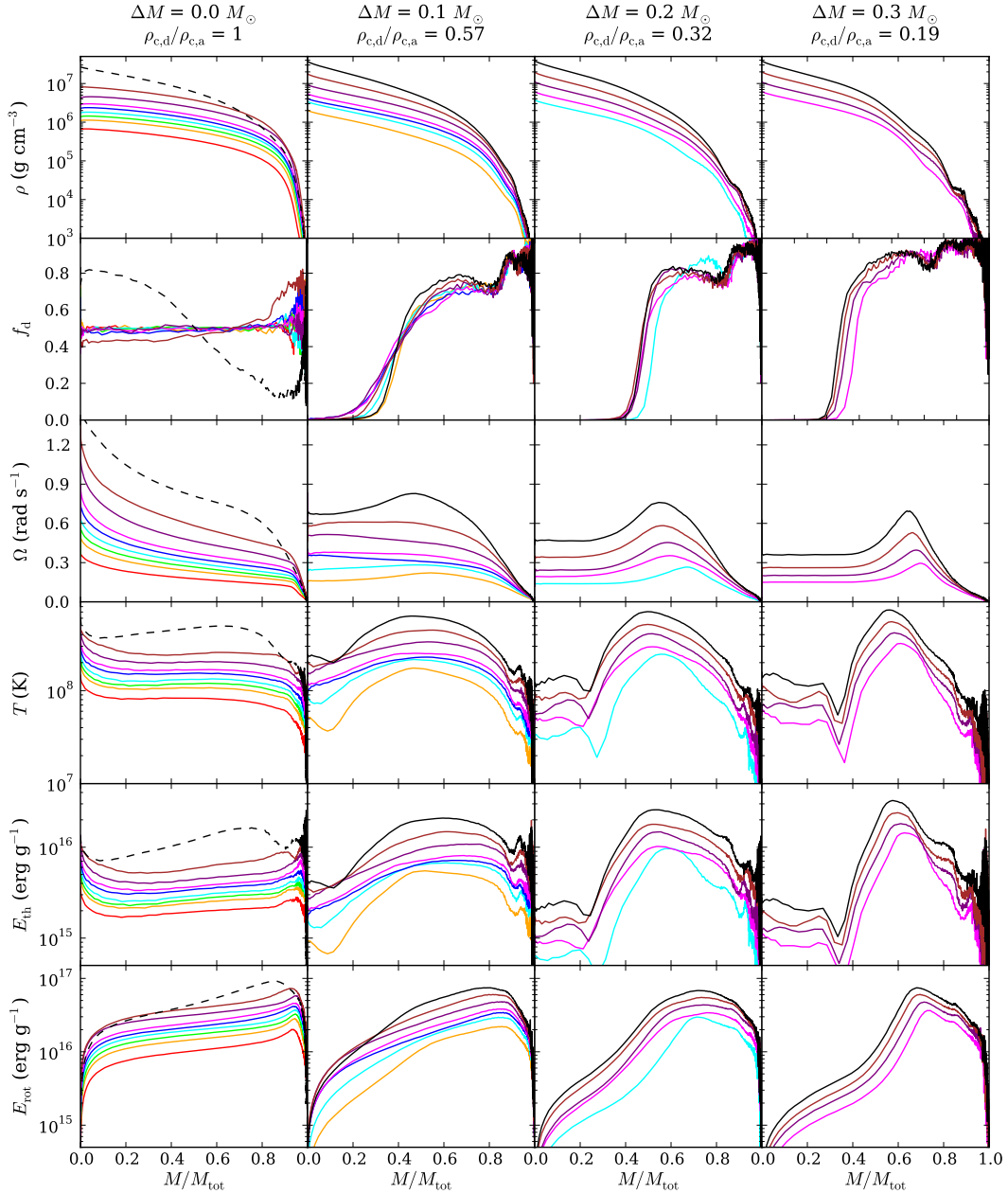


Figure 2.4: Dependence of the properties of mergers on mass difference, with, from left to right, $\Delta M \equiv M_a - M_d = 0.0, 0.1, 0.2$, and $0.3 M_\odot$ mergers. Properties shown, coloring, and line styles are as in Fig. 2.3, except color represents accretor mass.

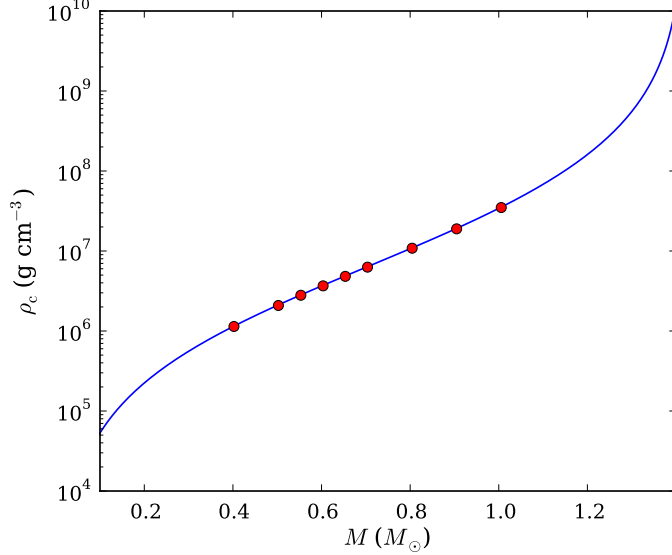


Figure 2.5: Relation between central density ρ_c and mass M for carbon-oxygen white dwarfs, showing both the results of relaxing white dwarf models in Gasoline (red points), and integrating hydrostatic equilibrium directly for spherically symmetric, non-rotating CO WDs with $T = 5 \times 10^6$ K (blue line). For the mass range considered, the central density depends roughly exponentially on mass.

of post-merger evolution.

To determine the critical value, we show in Fig. 2.6 the ratio of central to maximum temperature, T_c/T_{\max} , central to maximum angular velocity, Ω_c/Ω_{\max} , and the fraction of donor to accretor material within the central core, $(f_d/f_a)_{\text{cc}}$, where we define the central core as a sphere with radius h_z . All three properties are measures of the extent to which the core has been affected: mixed regions tend to be hotter and more spun up, and contain material from both stars.

From Fig. 2.6, one sees that Ω_c/Ω_{\max} approaches unity at $q_\rho \simeq 0.6$; at higher values, the angular velocity profile has a plateau or central peak rather than an off-center bump. Also at $q_\rho \simeq 0.6$, $(f_d/f_a)_{\text{cc}}$ starts to deviate from zero, i.e., donor material begins to penetrate the central core. The temperature points show the transition is not abrupt: T_c/T_{\max} starts to deviate from its downward trend (which reflects spurious heating in the most dissimilar-mass mergers; Sec. 2.4.6) around $q_\rho \simeq 0.3$ and continues to increase until $q_\rho = 1.0$; at $q_\rho \simeq 0.6$, $T_c/T_{\max} \simeq 0.5$. Overall, this suggests that while the dependence is gradual, the morphology changes most around $q_\rho \simeq 0.6$. This conclusion is confirmed by looking at the two-dimensional remnant temperature structures (Figs. 2.1 and 2.2). At $q_\rho \ll 0.6$, the remnant core has a large, spherically symmetric cold region, the nearly unperturbed accretor. This cold region shrinks with increasing q_ρ , and at $q_\rho \simeq 0.6$, spherical symmetry is broken. For still larger q_ρ , the cold region becomes a flat slice sandwiched between hotspots off the equatorial plane.

Given the above, we define “similar-mass” mergers as those with donor to accretor central density ratio $q_\rho > 0.6$, and “dissimilar-mass” mergers as those with $q_\rho < 0.6$. This critical density ratio corresponds to a mass difference $\Delta M \simeq 0.1 M_{\odot}$.

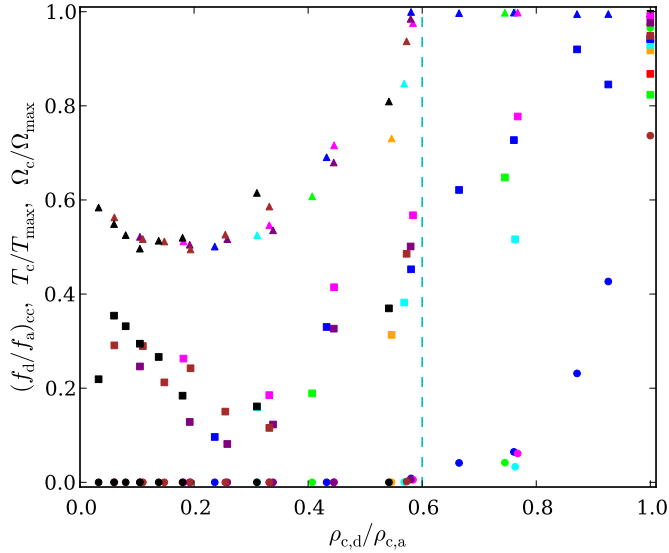


Figure 2.6: Dependence of merger core properties on the ratio of the donor and accretor central densities, $\rho_{c,d}/\rho_{c,a}$. Shown are the ratio of central to maximum temperature T_c/T_{\max} (squares), central to maximum angular velocity Ω_c/Ω_{\max} (triangles), and central core donor to accretor mass fraction $(f_d/f_a)_{cc}$ (circles), with colors representing different accretor masses, encoded as in Fig. 2.3. The vertical line marks $q_\rho \equiv \rho_{c,d}/\rho_{c,a} = 0.6$, where Ω_c/Ω_{\max} reaches unity, $(f_d/f_a)_{cc}$ becomes non-zero, and $T_c/T_{\max} \simeq 0.5$. We suggest it separates “dissimilar” from “similar” mass mergers.

2.3.2.2 Structural Trends

Here and in the following subsections of 2.3.2, we describe various trends of remnant properties in detail, hoping to help attempts to interpolate between different simulations and motivate analytical and semi-analytical depictions of the merger. Readers not requiring this level of detail may wish to skip to Sec. 2.3.3. We begin our discussion of trends with size and density parameters.

The rotational axis central scaleheight. We define the rotational axis central scaleheight h_z as the characteristic width σ of a Gaussian fit to the density distribution along the z axis at $\omega = 0$. h_z is a measure of the vertical extent of the remnant. We find that the ratio h_z/h_a , where h_a is the central scaleheight of the accretor, is reasonably well-approximated by,

$$\frac{h_z}{h_a} = 1.03 - 0.17 q_\rho^{1/2} \quad (\pm 0.02), \quad (2.1)$$

where the uncertainty listed in parentheses represents the root-mean-square (RMS) of the residuals around the approximation (see Fig. 2.7a). For highly dissimilar-mass mergers, h_z approximately equals the scaleheight of the accretor, while for similar-mass mergers, h_z is lower due to rotational support.

The vertical scaleheight increases with increasing ω : the scaleheight at the location of maximum temperature, $h(T_{\max})$, ranges from h_z to $1.21h_z$, and the scaleheight at maximum angular velocity $h(\Omega_{\max})$ ranges from h_z to $1.88h_z$. The prefactor for both heights increases with increasing accretor mass M_a and decreasing q_ρ .

The equatorial plane central scaleheight. Similar to h_z we define h_ω – the characteristic width of a Gaussian fit to the density distribution along the equatorial plane – as a measure of the equatorial extent of the remnant. The ratio h_ω/h_a can be parametrized by

$$\frac{h_\omega}{h_a} = 0.96 + 0.89q_\rho^2 \quad (\pm 0.08), \quad (2.2)$$

where we excluded the $1.0 - 1.0 M_\odot$ merger remnant for our fit (see Fig. 2.7a). The dependence on increasing q_ρ reflects the increased rotational support of the remnant core.

The central density of the remnant. The central density, ρ_c , is always within a factor two of the central density of the accretor, $\rho_{c,a}$. In Fig. 2.7b, one sees that for given accretor mass, $\rho_c/\rho_{c,a}$ increases with increasing q_ρ for highly dissimilar-mass mergers due to increasing compression of the remnant core, but begins to decrease because of increasing rotational support around $q_\rho \simeq 0.3$. We could not find a simple parametrization for these curves. Note that for some systems, as we continue running our simulations $\rho_c/\rho_{c,a}$ continues to increase. As discussed in Sec. 2.2.3, this is probably because artificial viscosity forces the merger remnant to undergo accelerated viscous evolution.

2.3.2.3 Mass Distributions

The merger mixes material between the donor and accretor. Here, we describe how this changes as a function of q_ρ , as well as how the material is distributed between the pressure-supported core and envelope and the rotationally supported disk.

The masses of the core-envelope and disk. We formally define the core-envelope as the part of the remnant inside the inner disk radius ω_{disk} , i.e., that is supported primarily by pressure (degeneracy for the core, thermal for the envelope) and not rotation. Since in every merger very little mass is ejected, a trend for either the core-envelope or the disk mass (M_{ce} and M_{disk} , resp.) suffices to determine both. The ratio of M_{ce} to the accretor mass M_a is well described by,

$$\frac{M_{ce}}{M_a} = 1 + 0.81q_\rho \quad (\pm 0.03), \quad (2.3)$$

if the $1.0 - 1.0 M_\odot$ merger is neglected, and the fit's y-intercept is forced to unity. See Fig. 2.8a.

(see the dashed green line in Figs. 2.1 and 2.2)

The mass enclosing 50% of the donor material. The further the donor penetrates, the smaller will be the mass enclosing half the donor's material, $M_{\text{enc}}(\frac{1}{2}M_d)$. For mergers with $q_\rho \lesssim 0.8$, $M_{\text{enc}}(\frac{1}{2}M_d)/M_a \simeq 1.30$, with an RMS residual of 0.03 (Fig. 2.8c). We present this trend mostly because we discuss similar thermodynamic and rotational enclosed masses, but it is somewhat difficult to interpret physically, since $M_{\text{enc}}(\frac{1}{2}M_d)$ increases with donor mass but decreases with mixing, which also depends on donor mass. The trend is easier to interpret using enclosed accretor mass rather than enclosed total mass, as done below.

The accretor mass enclosing 50% of the donor material. As a different measure of the depth to which the donor penetrates, we consider just the accretor material within the mass enclosing half the

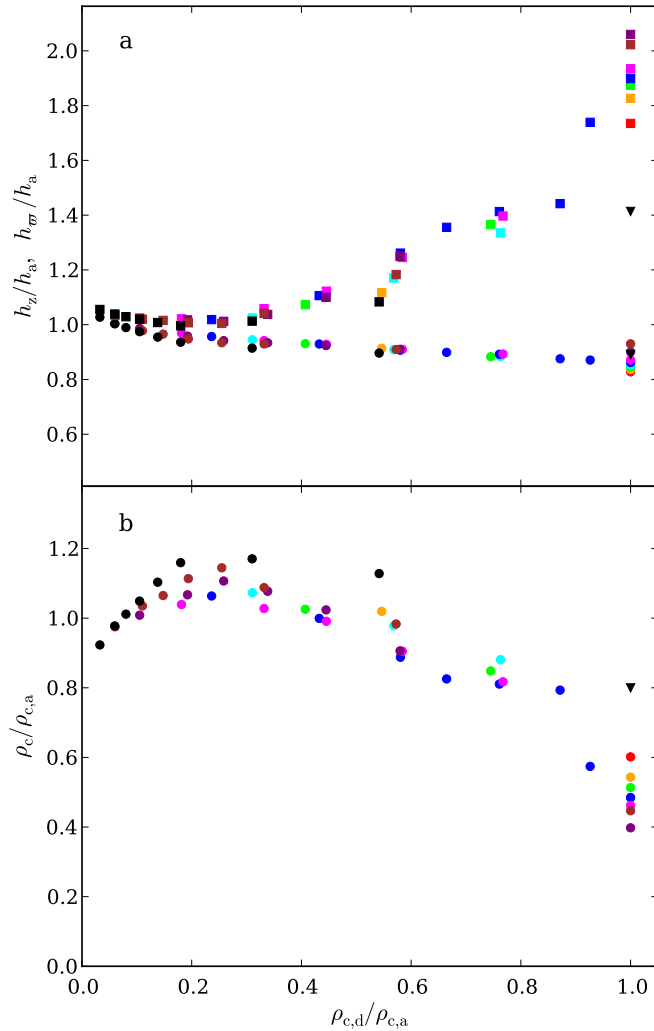


Figure 2.7: Structural properties of mergers. (a) Central scaleheights along the rotational axis (circles) and along the equatorial plane (squares) scaled to the scaleheight of the accretor, h_z/h_a and h_ω/h_a . (b) Central density of the merger remnant scaled to the central density of the accretor, $\rho_c/\rho_{c,a}$. Colors represent different accretor masses, encoded as in Fig. 2.3. Triangles represent the outlying $1.0 - 1.0 M_\odot$ merger.

donor, $M_{\text{enc}}(\frac{1}{2}M_d) - \frac{1}{2}M_d$. This should equal the accretor mass if the donor is deposited above the accretor, and half the accretor mass if the two stars are completely mixed. For $q_\rho \lesssim 0.8$, it can be approximated by (Fig. 2.8b),

$$\frac{M_{\text{enc}}(\frac{1}{2}M_d) - \frac{1}{2}M_d}{M_a} = 1 - 0.190q_\rho \quad (\pm 0.009), \quad (2.4)$$

where we forced the intercept to be unity. In this regime, roughly half of the donor remains outside of the accretor, though the trend discussed next indicates that the other half which does penetrate the accretor is spread across a much larger region at higher q_ρ . When $q_\rho \gtrsim 0.8$, the ratio drops sharply downward, indicative of the more thorough mixing expected for the similar-mass case. However, the existence and exact location of this drop may be a function of initial conditions (see Sect. 2.4.2).

The region over which the donor is spread. As a measure of the thickness of the region affected by the merger, we use the difference of the mass enclosing 75% of the donor material with that enclosing 25% of the donor material, i.e., $\Delta M_{\text{enc}}(M_d) = M_{\text{enc}}(\frac{3}{4}M_d) - M_{\text{enc}}(\frac{1}{4}M_d)$. Since 50% of the donor is within this range, $\Delta M_{\text{enc}}(M_d) - \frac{1}{2}M_d$ is a measure of the amount of accretor mixed with the donor. For $q_\rho \lesssim 0.8$, the ratio of the latter to the total accretor mass follows,

$$\frac{\Delta M_{\text{enc}}(M_d) - \frac{1}{2}M_d}{M_a} = 0.30q_\rho \quad (\pm 0.02), \quad (2.5)$$

while for $q_\rho \gtrsim 0.8$ the trend curls upward until it reaches 0.5, the value expected for completely mixed remnants. See Fig. 2.8d.

Combining the two above trends, we can formulate a qualitative picture of mixing. For $q_\rho \lesssim 0.8$, the donor can be thought of as being deposited onto the accretor and mixing with the accretor's outer layers, while for $q_\rho \gtrsim 0.8$, the accretor also disrupts substantially, leading to a regime where both stars mix more uniformly. The region over which the donor is spread, or thickness of the mixed layer, in both cases depends on q_ρ , which suggests that the relative densities of the donor and accretor govern mixing, i.e., the donor mixes significantly with all accretor material up to some fraction of the central density of the donor. Additional evidence of this will be seen in the thermodynamic trends below.

One might consider an alternate picture in which the donor dredges up a constant fraction of its own mass in accretor material. If this were the case, we would expect $(\Delta M_{\text{enc}}(M_d) - \frac{1}{2}M_d)/M_d$ to roughly be constant. Our results, however, show that for $q_\rho \lesssim 0.8$ this quantity is nearly a straight line that is close to zero for small q_ρ ($(\Delta M_{\text{enc}}(M_d) - \frac{1}{2}M_d)/M_d = 0.35q_\rho \pm 0.02$). This seems more consistent with mixing being determined by density.

2.3.2.4 Energy Balance

The energy balance of the remnants indicate their primary means of support. Since the remnants are virialized, we consider how the ratio of degeneracy, thermal, and rotational energy to the total internal energy of the remnants varies with q_ρ .

Energy balance of the entire remnant. The support against gravity changes from being due mostly to degeneracy pressure at low q_ρ to having a substantial rotational contribution at $q_\rho \simeq 1$. This is

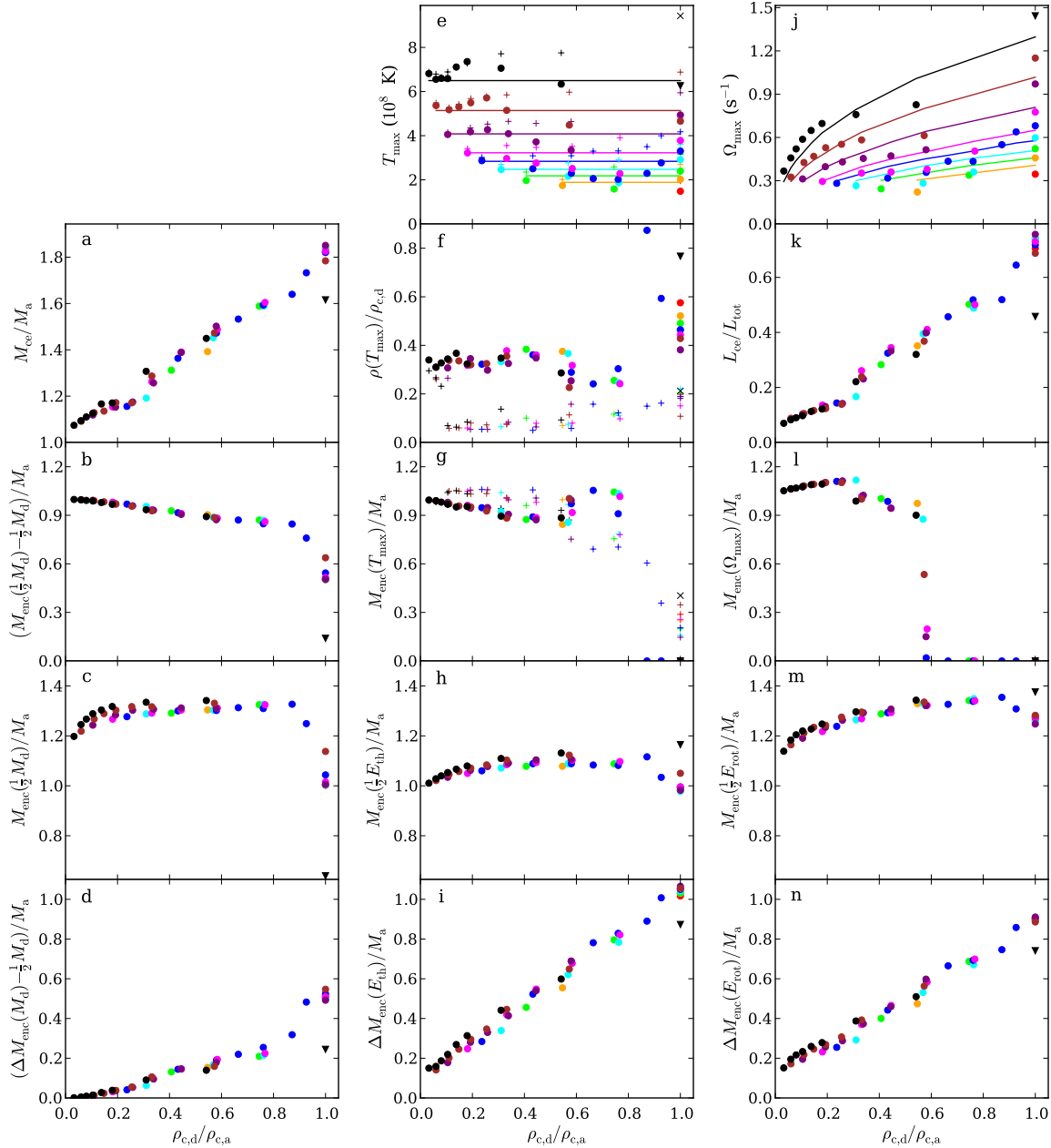


Figure 2.8: Mixing, heating, and spin-up (left to right) for mergers. (a) Scaled mass of the remnant core-envelope (where scaling here and below is to the accretor mass). (b) Fraction of the accretor within the mass enclosing half the donor mass. (c) Scaled remnant mass enclosing half the donor mass. (d) Fraction of the accretor mass within the region enclosing 25–75% of the donor mass. (e) Maximum equatorial temperature T_{max} (circles), with the approximation $T_{\text{max}} = 0.20GM_a m_p / k_B R_a$ overdrawn. Maximum temperatures along the rotational axis are shown with crosses. (f) Scaled density at the location of T_{max} (symbols as above). (g) Scaled mass enclosed within the radius of T_{max} (symbols as above). (h) Scaled mass enclosing half of the remnant thermal energy. (i) Scaled mass of the region enclosing 25–75% of the remnant thermal energy. (j) Maximum angular velocity Ω_{max} (circles) with best fit $\Omega_{\text{max}} = 3.8\Omega_{\text{orb}}$ overdrawn. (k) Fraction of the angular momentum in the core-envelope. (l) Scaled mass enclosed within the radius of maximum angular velocity. (m) Scaled mass enclosing half of the total remnant rotational energy. (n) Scaled mass of the region enclosing 25–75% of the remnant rotational energy. Colors represent different accretor masses, encoded as in Fig. 2.3. Triangles represent equatorial plane values, and x-marks rotational axis values, of the $1.0 - 1.0 M_{\odot}$ merger.

because for highly dissimilar-mass mergers most of the internal energy is locked up within the accretor, which is hardly heated or spun up. For similar-mass mergers, however, donor material mixes, to some degree, with the entire accretor, causing heating and spin-up throughout the entire remnant.

The total gravitational potential energy of the merger remnant can be described adequately by a constant fraction of GM_{tot}^2/R_a ,

$$\frac{-E_{\text{pot}}}{GM_{\text{tot}}^2/R_a} = 0.49 \quad (\pm 0.01). \quad (2.6)$$

From the virial theorem, the internal energy should be related to the potential energy by $3(\langle\gamma\rangle - 1)E_I = -E_{\text{pot}}$, where $\langle\gamma\rangle$ is an appropriately averaged equivalent to the adiabatic index. Since our remnants have cores where the electrons are becoming relativistic, one has $\langle\gamma\rangle$ somewhat smaller than $5/3$, especially for the more massive remnants. We find that the ratio $E_I/|E_{\text{pot}}|$ can be described by,

$$\frac{E_I}{|E_{\text{pot}}|} = 0.18 \frac{M_a}{M_\odot} + 0.42 \quad (\pm 0.01), \quad (2.7)$$

which is ~ 0.5 and ~ 0.6 for low and high M_a , respectively.

The fraction of the internal energy carried by degeneracy and rotation is fairly well described by,

$$\frac{E_{\text{rot}}}{E_I} = 0.31q_\rho^{1/2} \quad (\pm 0.01), \quad (2.8)$$

$$\frac{E_{\text{deg}}}{E_I} = 0.92 - 0.34q_\rho^{1/2} \quad (\pm 0.02). \quad (2.9)$$

With these, the fraction carried by thermal energy can also be calculated; as shown in Fig. 2.9a, the fraction in thermal energy first increases with increasing q_ρ , but turns over at $q_\rho \simeq 0.7$, decreasing afterwards. This reflects the competition between increased thermal energy from the two stars mixing, and increased rotational support from the spin-up of the core.

Overall, for highly dissimilar-mass mergers, the internal energy is partitioned into degeneracy, rotational and thermal energy with a ratio of approximately 8:1:1, reflecting that, as stated above, such mergers are almost entirely supported by degeneracy pressure. Similar-mass mergers, on the other hand, partition their internal energies with the ratio 6:3:1, i.e., rotational support is significant.

Energy balance of the core-envelope. Since the variations with q_ρ seen for the remnant as a whole are almost entirely due to variations in the core and envelope rather than in the disk, the trends we find for the core-envelope are very similar to those we found above for the entire remnant,

$$\frac{E_{\text{rot}}^{\text{ce}}}{E_I^{\text{ce}}} = 0.28q_\rho \quad (\pm 0.02), \quad (2.10)$$

$$\frac{E_{\text{deg}}^{\text{ce}}}{E_I^{\text{ce}}} = 0.94 - 0.32q_\rho \quad (\pm 0.02). \quad (2.11)$$

Note the dependency on q_ρ , rather than on $q_\rho^{1/2}$ as was found for the entire remnant. See Fig. 2.9b.

Energy balance of the disk. For the disk, we find very little dependence on q_ρ , consistent with the idea that most of the changes in the partitioning of energy have to do with increased mixing between the donor and accretor, which affects the core and envelope much more than the disk. Averaged over

all mergers, we find

$$\frac{E_{\text{rot}}^{\text{disk}}}{E_{\text{I}}^{\text{disk}}} = 0.74 \quad (\pm 0.03), \quad (2.12)$$

$$\frac{E_{\text{th}}^{\text{disk}}}{E_{\text{I}}^{\text{disk}}} = 0.19 \quad (\pm 0.02), \quad (2.13)$$

$$\frac{E_{\text{deg}}^{\text{disk}}}{E_{\text{I}}^{\text{disk}}} = 0.07 \quad (\pm 0.02). \quad (2.14)$$

Hence, the disk is composed of non-degenerate, primarily rotationally-supported material. See Fig. 2.9c. (Note that we do not try to define a ratio of internal to potential energy of the disk or core-envelope, since the potential energy of either is not straightforward to determine.)

2.3.2.5 Temperature and Thermal Energy

Since heating of the remnant is achieved through shocks and viscous dissipation, the most heavily mixed regions should also be the hottest. We focus on equatorial thermodynamic values, but consider the rotational axis as well for similar-mass mergers.

The maximum temperature. We find that the maximum temperature on the equatorial plane, T_{\max} , scales with the potential of the accretor (Fig. 2.8e),

$$\frac{kT_{\max}}{GM_{\text{a}}m_{\text{p}}/R_{\text{a}}} = 0.20 \quad (\pm 0.03). \quad (2.15)$$

This scaling is natural in the limit of highly dissimilar-mass merger – for each nucleon, of order $GM_{\text{a}}m_{\text{p}}/R_{\text{a}}$ is liberated and converted into thermal energy. The temperature and thermal energy profiles in Fig. 2.3 show that with increasing q_{ρ} , additional thermal energy is deposited into the remnant, but this energy is spread over a larger region, such that the maximum temperature remains roughly the same even as q_{ρ} approaches unity.

For a dissimilar-mass merger, the highest temperature along the rotational axis, T_{\max}^z , is found at the tenuous outer edge of the hot envelope. It is slightly higher than the maximum temperature found in the equatorial plane. With increasing q_{ρ} , however, the difference increases noticeably due to the two off-center hot spots found along the rotational axis in similar-mass mergers. Fitting T_{\max}^z , we find $kT_{\max}^z/(GM_{\text{a}}m_{\text{p}}/R_{\text{a}}) = 0.24 \pm 0.03$, though this does not capture the upturn for similar masses well.

All remnants with $q_{\rho} \gtrsim 0.8$ have convectively unstable cores along the equatorial plane. Artificially mixing these cores to make them isentropic decreases their maximum temperatures by 10 – 50% (not shown in Fig. 2.8, but see the left panel of Fig. 2.17). All remnants are stable against convection along the rotational axis.

The density at the point of maximum temperature. For dissimilar-mass mergers, the density at the hottest equatorial point, $\rho(T_{\max})$, depends mostly on the donor (see Fig. 2.8f). For $q_{\rho} \lesssim 0.5$, we find

$$\frac{\rho(T_{\max})}{\rho_{\text{c,d}}} = 0.34 \quad (\pm 0.02). \quad (2.16)$$

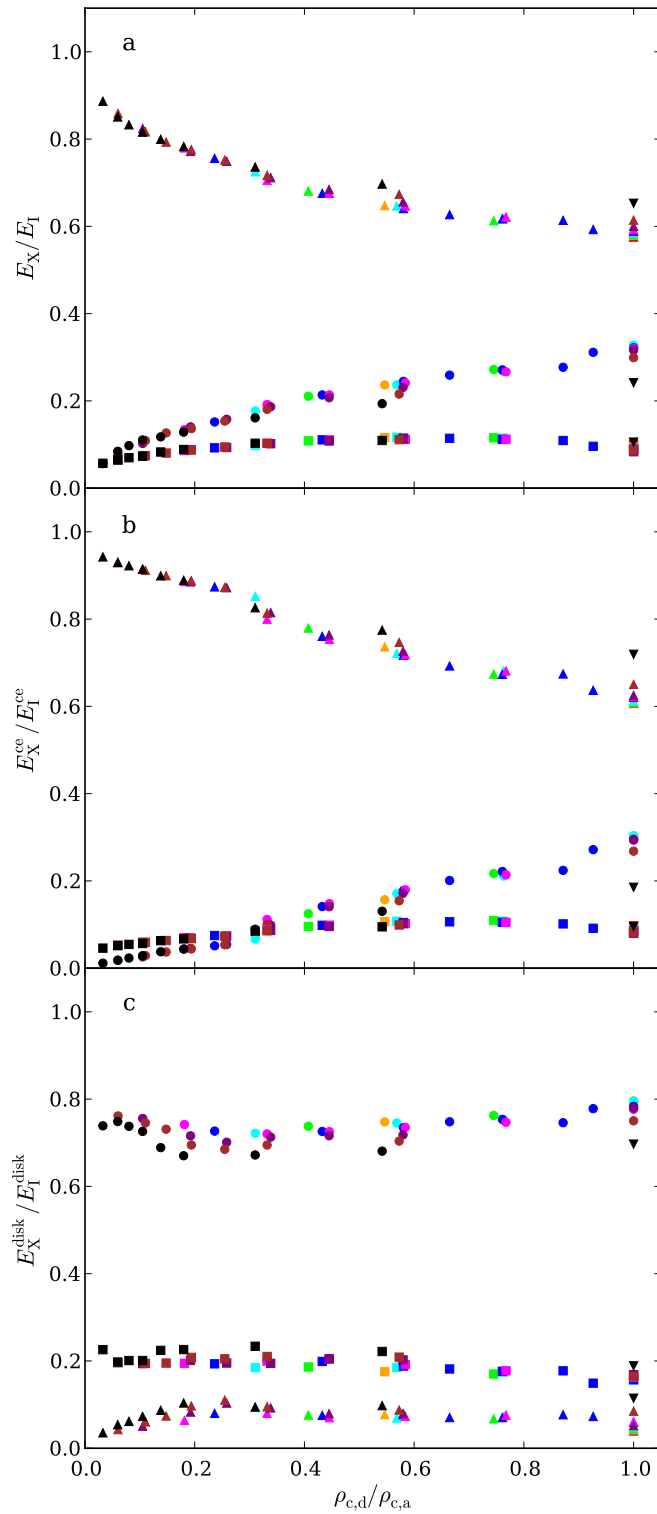


Figure 2.9: Partition of energies in (a) the overall merger remnant, (b) the remnant core plus envelope, and (c) the remnant disk. In each panel, the fraction of total energy carried in degeneracy (triangles), thermal (squares), and rotational (circles) energy is shown. Colors represent different accretor masses, encoded as in Fig. 2.3. Triangles represent the $1.0 - 1.0 M_\odot$ merger.

This proportionality again suggests that, at least for dissimilar-mass mergers, the donor mixes with the accretor up to a fraction of the central density of the donor, as alluded to earlier.

At $q_\rho \gtrsim 0.6$, the dependence becomes less obvious, with $\rho(T_{\max})$ varying from $\sim 25 - 90\%$ of $\rho_{c,d}$. Since for these density ratios, the donor material starts to penetrate the central core of the accretor – and the accretor starts to disrupt as well – the simple picture of the donor mixing up to a fraction of its own central density may be breaking down. Furthermore, part of the spread in density reflects that for high q_ρ the equatorial temperature profiles become nearly flat (see Fig. 2.3, left column), thus increasing the sensitivity to noise in the determination of the location (but not the value) of maximum temperature. This also affects our results for the enclosed mass, $M_{\text{enc}}(T_{\max})$, below.

Since for dissimilar-mass mergers, T_{\max}^z is located near the tenuous outermost regions of the hot envelope, where particle noise is high, the density at the point of maximum rotational axis temperature, $\rho(T_{\max}^z)$ (plus symbols in Fig. 2.8f), varies wildly between about $\rho(T_{\max})$ and one order of magnitude below $\rho(T_{\max})$. For similar-mass mergers, $\rho(T_{\max}^z)$ appears to be $\sim 20 - 50\%$ of $\rho(T_{\max})$.

The mass enclosed within the radius of maximum temperature. For dissimilar-mass mergers, the radius of maximum temperature occurs at an enclosed mass of $M_{\text{enc}}(T_{\max}) \simeq M_a$, while for mergers with $q_\rho \gtrsim 0.8$, maximum temperature occurs at the center and $M_{\text{enc}}(T_{\max}) \simeq 0$ (see Fig. 2.8g). For $q_\rho \lesssim 0.5$, we find

$$\frac{M_{\text{enc}}(T_{\max})}{M_a} = 1 - 0.28q_\rho \quad (\pm 0.01), \quad (2.17)$$

where the fit's y-intercept is forced to unity. Note that maximum temperature occurs near the bottom of the mixed zone, which is why $M_{\text{enc}}(T_{\max})$ is substantially smaller than $M_{\text{enc}}(\frac{1}{2}M_d)$. The reasons it starts to deviate from a tight trend at $q_\rho \simeq 0.6$ are the same as those for $\rho(T_{\max})$: the break-down of the simple mixing picture and the difficulty in determining the location of peak temperature for a broader plateau.

Since $M_{\text{enc}}(T_{\max}) < M_a$, it may be surprising that $\rho(T_{\max})$ is not higher than $\rho_{c,d}$. This is because the additional thermal and rotational support against gravity reduces the density gradient that would be required if degeneracy pressure were the only source of support.

For dissimilar-mass mergers, $M_{\text{enc}}(T_{\max}^z)$ is only slightly higher than $M_{\text{enc}}(T_{\max})$, since the remnant core is nearly spherically symmetric, apart from the fact that the hot envelope is slightly more extended in the vertical direction. For similar-mass mergers, the difference increases, reflecting the development of the off-center hot spots, until $M_{\text{enc}}(T_{\max}^z)/M_a \simeq 0.25$ for equal-mass mergers.

The mass enclosing half the remnant thermal energy. As a more robust measure of where thermal energy is deposited during the merger, we consider the mass enclosing half the remnant thermal energy, $M_{\text{enc}}(\frac{1}{2}E_{\text{th}})$ (see Fig. 2.8h). We find this is very close to the mass of the accretor,

$$\frac{M_{\text{enc}}(\frac{1}{2}E_{\text{th}})}{M_a} = 1.06 \quad (\pm 0.04), \quad (2.18)$$

if the $1.0 - 1.0 M_\odot$ merger is neglected. One sees turnovers at the extremes, for $q_\rho \lesssim 0.2$ and $q_\rho \gtrsim 0.8$. The former likely is because thermal energy is deposited into a narrow strip right on the surface of the accretor, while the latter is probably due to the disruption of the accretor.

While smaller than $M_{\text{enc}}(\frac{1}{2}M_d)$, $M_{\text{enc}}(\frac{1}{2}E_{\text{th}})$ is always larger than $M_{\text{enc}}(T_{\max})$. This reflects that

high density degenerate material has lower specific heat, so that for the same energy per unit mass the temperature is higher (see Fig. 2.3).

The width of the remnant thermal energy. The mass enclosed between the 25th and 75th percentiles of thermal energy, $\Delta M_{\text{enc}}(E_{\text{th}}) = M_{\text{enc}}(\frac{3}{4}E_{\text{th}}) - M_{\text{enc}}(\frac{1}{4}E_{\text{th}})$, is a measure of the extent of the remnant that has been heated (see Fig. 2.8i). Ignoring the 1.0 - 1.0 M_{\odot} merger, it can be fit by,

$$\frac{\Delta M_{\text{enc}}(E_{\text{th}})}{M_a} = 0.11 + 0.94q_{\rho} \quad (\pm 0.03). \quad (2.19)$$

Here, we did not force the y-intercept to go to zero, which is expected physically but gives a substantially poorer trend.

2.3.2.6 Angular Velocity and Rotational Energy

For a dissimilar-mass merger, the donor carries most of the angular momentum. As a result, the hot envelope contains more angular momentum and features higher angular velocities than the core, since the envelope is where most of the accreted donor material resides. Spin-up of the accretor is accomplished through shocks, PdV work and shearing forces. For a similar-mass merger, the two stars carry similar amounts of angular momentum and thoroughly mix. Conservation of angular momentum then implies that the entire remnant rotates rapidly.

The maximum angular velocity. On the equatorial plane, the highest angular velocity, Ω_{max} , scales linearly with the orbital angular velocity of the pre-merger binary, $\Omega_{\text{orb}} = 2\pi/P_{\text{orb}}$ (see Fig. 2.8j),

$$\frac{\Omega_{\text{max}}}{\Omega_{\text{orb}}} = 3.8 \quad (\pm 0.6). \quad (2.20)$$

The ratio of core-envelope to total angular momentum. For more similar-mass mergers, more angular momentum is deposited in the accretor and ends up in the core and envelope (see Fig. 2.8k). The ratio of core-envelope to total angular momentum, $L_{\text{ce}}/L_{\text{tot}}$, is approximately,

$$\frac{L_{\text{ce}}}{L_{\text{tot}}} = 0.70q_{\rho} \quad (\pm 0.03), \quad (2.21)$$

where we fit only for $q_{\rho} > 0.25$ and ignore the 1.0 - 1.0 M_{\odot} merger. For $q_{\rho} \lesssim 0.25$, the trend becomes shallower, resulting in a non-zero intercept. This suggests that even in cases where the donor has negligible mass some angular momentum is transferred to the accretor.

The mass enclosed inside the radius of maximum angular velocity. For dissimilar-mass mergers, both $M_{\text{enc}}(\Omega_{\text{max}})$ and $M_{\text{enc}}(T_{\text{max}})$ are about equal to M_a , with $M_{\text{enc}}(\Omega_{\text{max}})$ slightly larger than $M_{\text{enc}}(T_{\text{max}})$: for $q_{\rho} \lesssim 0.55$, $M_{\text{enc}}(\Omega_{\text{max}})/M_a = 1.05 \pm 0.06$. This is consistent with the idea that the hottest and most spun-up regions are those where the donor mixed most strongly with the accretor. For $q_{\rho} \simeq 0.6$, the off-center angular velocity peak is replaced by a plateau, and $M_{\text{enc}}(\Omega_{\text{max}})$ becomes ill-defined; for even larger q_{ρ} , the highest velocities occur in the center, and $M_{\text{enc}}(\Omega_{\text{max}}) \simeq 0$. See Fig. 2.8l.

The mass enclosing half the remnant rotational energy. Like for the thermal energy, for very dissimilar masses, the mass enclosing half the rotational energy, $M_{\text{enc}}(\frac{1}{2}E_{\text{rot}})$, is similar to the accretor mass (see Fig. 2.8m). For $q_\rho \lesssim 0.8$, we find

$$\frac{M_{\text{enc}}(\frac{1}{2}E_{\text{rot}})}{M_a} = 1.12 + 0.27q_\rho^{1/2} \quad (\pm 0.01) \quad (2.22)$$

Note that unlike $M_{\text{enc}}(\Omega_{\text{max}})$, $M_{\text{enc}}(\frac{1}{2}E_{\text{rot}})$ continues to increase with q_ρ (except for exactly equal-mass mergers), a consequence of particles with lower angular velocity but large lever arm that carry substantial rotational energy (see Fig. 2.3). Near $q_\rho \simeq 0.8$, the trend breaks as both stars are significantly disrupted. However, even exactly equal-mass mergers have more of their rotational energy stored in the outskirts (otherwise one would have $M_{\text{enc}}(\frac{1}{2}E_{\text{rot}})/M_a \simeq 1$).

The width of the remnant rotational energy. We measure the extent to which the remnant is affected by spin-up through the difference between the masses enclosing 25 and 75% of the rotational energy, $\Delta M_{\text{enc}}(E_{\text{rot}}) = M_{\text{enc}}(\frac{3}{4}E_{\text{rot}}) - M_{\text{enc}}(\frac{1}{4}E_{\text{rot}})$ (see Fig. 2.8n). Ignoring the $1.0 - 1.0 M_\odot$ merger, it is well-described by,

$$\frac{\Delta M_{\text{enc}}(E_{\text{rot}})}{M_a} = 0.12 + 0.77q_\rho \quad (\pm 0.03). \quad (2.23)$$

Like for the thermal energy, one sees that for more similar-mass mergers, rotational energy is spread more widely throughout the remnant.

2.3.3 A Qualitative Picture of the Merger

From our empirical results above, a qualitative picture of a merger emerges. A dissimilar-mass merger has the donor overflowing its Roche lobe and forming an accretion stream. This stream mixes with the accretor up to approximately the central density of the donor pre-merger, $\rho_{c,d}$. Those layers of the accretor that are denser than $\rho_{c,d}$ are hardly affected, and form the cold core of the merger remnant, while the mixed material will form a partly-thermally supported outer envelope, which somewhat compresses the core, as well as a rotationally supported disk.

At $q_\rho \gtrsim 0.6$, the above picture begins to break down, as portions of the donor start to penetrate to the center of the accretor. This results in substantial heating and spin-up of the central core: the merger becomes a similar-mass merger. As the masses become more similar, the distinction between donor and accretor is lost and both stars disrupt and form accretion streams. For all $q_\rho \gtrsim 0.6$, the remnants are similar: a large, ellipsoidal and partly rotationally supported hot core with two hotspots off the equatorial plane, surrounded by a small, hot disk.

For all mergers, the maximum temperature reached by dissipation of orbital energy is proportional to the accretor's gravitational potential energy. For increasing q_ρ , the maximum temperature remains similar, but the region over which the thermal energy is deposited widens. The density at maximum temperature is of the same order of magnitude as the central density of the donor, consistent with the mixing picture discussed above. The latter no longer holds for $q_\rho \gtrsim 0.6$, when the entire remnant is mixed and heated.

For a dissimilar-mass merger, the angular momentum remains in the outer regions, since most of it was originally carried by the donor. Angular momentum can be transferred between regions

through shocks, PdV work or shearing forces, all of which becomes increasingly important as the donor penetrates deeper. As a result, with increasing q_ρ , the remnant core is spun up further. Where both WDs disrupt, leading to colliding accretion streams, even the densest regions of the remnant have high rotational velocities.

2.4 Variation of Merger Parameters and Robustness of Results

In our parameter space study, we focused on the effects of varying the masses of the two WDs, fixing the initial separation a_0 , merger completion time criterion, and WD composition. To determine how robust our results are, we ran simulations varying these assumptions.

2.4.1 Changing the Composition

Ignoring fusion, WD mergers should be insensitive to changes in composition, since the dominant electron degeneracy pressure only depends on the mean molecular weight per electron, which is close to $\mu_e \simeq 2$ for all likely compositions. To confirm this, we ran simulations assuming pure helium and pure magnesium for an equal-mass case ($0.4 - 0.4 M_\odot$) and an dissimilar one ($0.4 - 0.8 M_\odot$). The results are shown in Figure 2.10. One sees that most quantities indeed have very similar profiles.

The set of profiles showing most variation are those of the temperature. These have similar shape, but different normalization. Since the thermal energy curves are very similar, it is clear that this reflects differences in heat capacity, which does depend on composition: for He composition, there are more (non-degenerate) ions than for our standard CO mixture, boosting the heat capacity (and thus lowering the temperature for given thermal energy), while for Mg composition, there are fewer, lowering the heat capacity (and increasing the temperature). As a result, the maximum equatorial plane temperatures for the $0.4 - 0.4 M_\odot$ simulations are 0.95, 1.48 and 1.68×10^8 K for He, CO, and Mg, respectively, while for the $0.4 - 0.8 M_\odot$ simulations, they are 2.92, 4.05, and 4.47×10^8 K.

The smaller differences seen for the other profiles reflect small differences in initial conditions. All WDs are constructed assuming $T = 5 \times 10^6$ K throughout, which implies more thermal energy for higher heat capacity. As a result, the relaxed He and Mg WDs are slightly larger and smaller, respectively, than the CO WD. These slight differences in radius translate into differences in initial separation, which in turn cause small differences in the angular velocity and rotational energy curves.

2.4.2 Varying the Initial Binary Separation

For our simulations, we chose an initial orbital separation a_0 for which a co-rotating donor would fill its Roche lobe. Since our (non-rotating) WDs are equilibrated in isolation, once the simulation starts they immediately begin to adjust to the tides and hence disrupt quickly. Ideally, one would allow them to adjust to the binary potential and start mass transfer properly. For non-synchronous rotation, however, this is not straightforward (see Sec. 2.5.2). Nevertheless, we try to get a sense of the influence of this by running simulations for two cases – $0.6 - 0.6 M_\odot$ and $0.6 - 0.8 M_\odot$ – with a_0 increased and decreased by 10% (see Fig. 2.11).

Our default simulations were considered complete at 6 orbits of the initial binary. For runs where a_0 was changed, we used 2.5% non-axisymmetry, and a requirement for the density to be highest at the

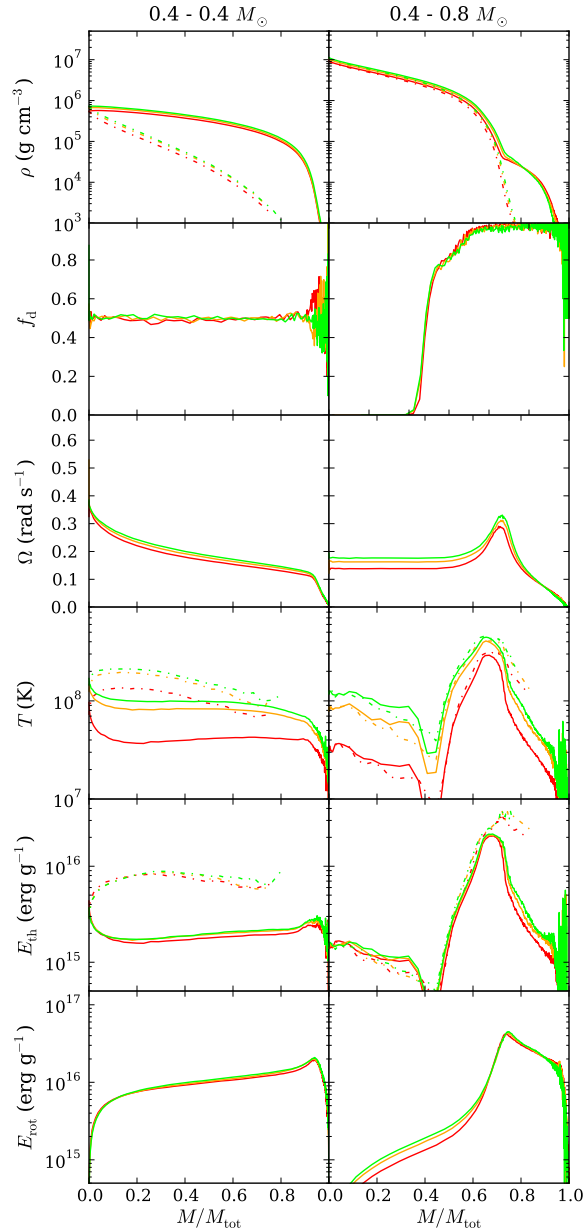


Figure 2.10: As Fig. 2.3, but for $0.4 - 0.4 M_{\odot}$ (left) and $0.4 - 0.8 M_{\odot}$ (right) mergers with different compositions: pure ${}^4\text{He}$ (red), CO (orange), and pure ${}^{24}\text{Mg}$ (lime). Dash-dotted lines represent profiles along the rotational axis rather than the equatorial plane.

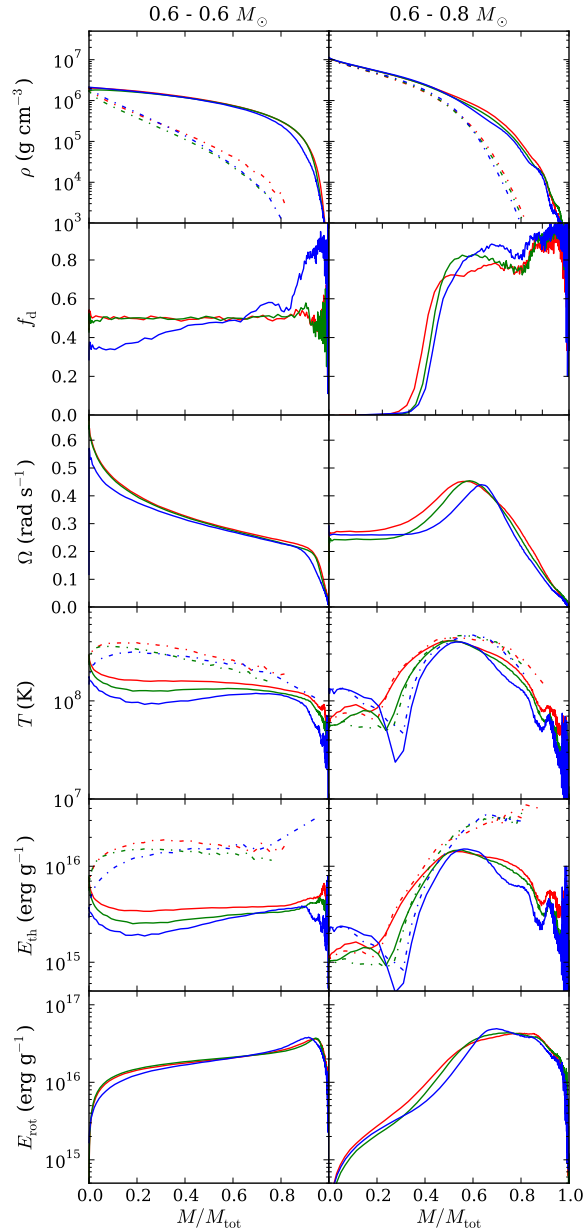


Figure 2.11: As Fig. 2.10, but for $0.6 - 0.6 M_{\odot}$ (left) and $0.6 - 0.8 M_{\odot}$ (right) mergers with varying initial orbital separation: 0.9 (red), 1.0 (green), and 1.1 (blue) times the value used for the parameter space study.

remnant's center, as the completion criteria⁶. Not surprisingly, runs with larger a_0 needed longer to achieve these criteria: with a 10% increase, the $0.6 - 0.8 M_{\odot}$ merger required 861 seconds, or ~ 15 orbits, to complete, while the one with a 10% decrease required 230 s, or ~ 5.5 orbits. Similarly, the $0.6 - 0.6 M_{\odot}$ merger with a 10% increase in a_0 required ~ 13 orbits (725 s) to complete, compared to the 7 orbits of a 10% decrease (283 s). In both cases, the increase simply reflects that it takes longer for the donor to be disrupted fully if a_0 is increased⁷. For instance, for the $0.6 - 0.8 M_{\odot}$ binary with increased separation, it took almost a dozen orbits before full disruption, while at the standard separation disruption occurred after just 1.5 orbits. This feature is of particular interest because for mergers of synchronously rotating WDs [Dan et al. \(2011; 2012\)](#) and [Raskin et al. \(2012\)](#) all note almost immediate disruption of the donor when approximate initial conditions are used, and much delayed disruption for more accurate initial conditions (up to ~ 30 orbits; see Sec. 2.5.2).

We find that the density profiles of the merger remnants are remarkably insensitive to varying a_0 (ρ_c changing by $\lesssim 2\%$ for the $0.6 - 0.8 M_{\odot}$ merger, and $\sim 20\%$ for the $0.6 - 0.6 M_{\odot}$ merger), and show substantial systematic changes only in the outer regions. The latter can be understood from the mixing and rotational profiles, where one sees that with increasing a_0 , donor material is mixed less deeply into the accretor, and rotational energy is shifted outward, causing the rotational frequency to peak at lower values and larger radii. This reflects the increase in angular momentum with increasing a_0 , which creates a more rotationally supported remnant (for both our systems, a 10% increase (decrease) in a_0 results in a 5% increase (decrease) in angular momentum). In the $0.6 - 0.8 M_{\odot}$ merger, the decreased mixing causes the accretor to be spun up less, thus lowering the rotational energy of the core, and narrowing the thermal energy plateau. These effects are also seen in the similar-mass case, where the center of the remnant receives less rotational support and becomes denser with increasing separation, and the mixing becomes less uniform.

Qualitatively, with increasing a_0 , the properties change in a way that is similar to the changes seen with decreasing q_{ρ} , i.e., similar to mergers with more dissimilar mass: reduced mixing, larger disks and less core rotational support, and shifts in the thermal and rotational energies toward larger radii. The converse is also true, decreasing a_0 has similar effects as increasing q_{ρ} , i.e., the mergers become similar to those with more equal masses. The changes are substantial at times: e.g. with a 10% increase in a_0 for the $0.6 - 0.6 M_{\odot}$ remnant, the maximum equatorial temperature is reduced by 40%, while the corresponding density increases by 25% (for the rotational axis hotspots, the values are a 13% and 30% reduction, respectively), and the mass of the disk increases by 65%. Similar, though far less extreme, changes are seen for the properties of the $0.6 - 0.8 M_{\odot}$ remnant. All this makes a_0 one of the parameters our mergers are most sensitive to.

2.4.3 Synchronization

In our simulations, the WDs have zero spin, i.e., we assume that tidal dissipation is too weak to synchronize their rotation. Whether or not this is correct is currently unknown, but to see what the effect could be, we ran simulations assuming synchronized rotation for $0.6 - 0.6 M_{\odot}$ and $0.6 - 0.8 M_{\odot}$ binaries (see Fig. 2.12). We used approximate initial conditions for these systems, identical to those of Sec. 2.2.2 except that the stars rotate at the orbital angular frequency.

⁶The 2.5% non-axisymmetry convergence time is 312 s (6.6 orbits) for our default $0.6 - 0.6 M_{\odot}$ run, and 250 s (5.2 orbits) for our default $0.6 - 0.8 M_{\odot}$ run.

⁷Of course, if placed far enough, the binary does not merge. For a $0.6 - 0.8 M_{\odot}$ binary, no mass transfer occurred within 500 s if a_0 was increased by 20%.

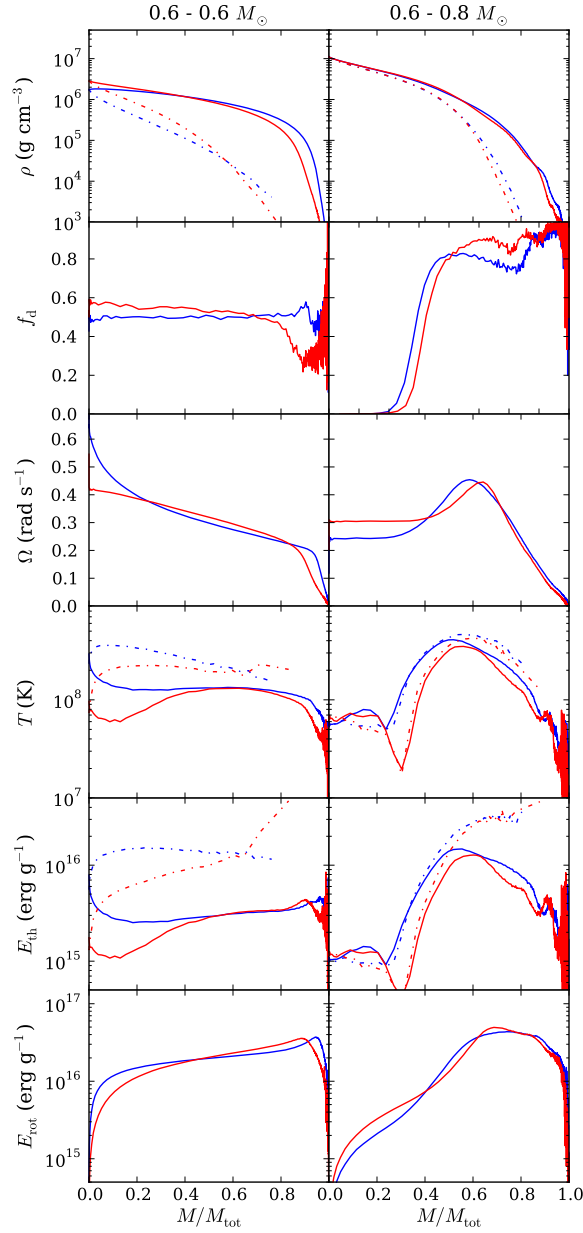


Figure 2.12: As Fig. 2.10, but for $0.6 - 0.6 M_{\odot}$ (left) and $0.6 - 0.8 M_{\odot}$ (right) mergers, comparing our default, irrotational case (blue) with that assuming synchronous rotation (red).

As in Sec. 2.4.2, our unsynchronized runs are from our parameter space study, and use 6 orbits as their completion criterion, while our synchronized runs use 2.5% non-axisymmetry, and a requirement for the density to be highest at the remnant’s center. Completion occurred at 407 s (~ 8.5 orbits) for the synchronized $0.6 - 0.6 M_{\odot}$ simulation, and 314 s (~ 6.5) orbits for the synchronized $0.6 - 0.8 M_{\odot}$.

The asynchronous and synchronous mergers differ mostly in the amount of heating and spin-up. This has two causes. First, for the synchronized binary, the total amount of angular momentum is about 10% larger, and high angular momentum material has more difficulty penetrating the accretor, as is evident in the $0.6 - 0.8 M_{\odot}$ mixing profile (because of the larger amount of angular momentum, the mergers also take about 1.5 orbits longer to achieve 2.5% non-axisymmetry). Second, in a synchronized binary, the donor and accretor have much less differential rotation with respect to each other, leading to much less spin-up and heating.

Both effects are largest for the equal-mass case. In particular, in a synchronized, equal-mass binary contact can occur without any friction, while in an unsynchronized one it involves shocks at the full orbital velocity. In consequence, for the synchronized case, rotational support is weaker in the center and stronger in the outskirts, causing the central density of our $0.6 - 0.6 M_{\odot}$ remnant to increase by $\sim 70\%$ and the disk mass to increase by a factor of 2. Furthermore, while for the non-synchronized case, the maximum temperature along the equatorial plane was found in the center, for the synchronized case it is found in the outskirts, and is more than a factor two lower (1.3×10^8 K instead of 2.9×10^8 K). The hotspots on the rotational axis also have much reduced temperature, 2.3×10^8 K instead of 3.6×10^8 K.

For the dissimilar-mass merger, the effects of synchronization are less dramatic: the accretor still spins up substantially, and rotational and thermal energy are deposited in roughly the same way. The main difference is that the synchronized case has slightly less mixing, causing a drop in total thermal energy and maximum temperature (from 4.1×10^8 K to 3.5×10^8 K on the equatorial plane, and from 4.6×10^8 K to 4.3×10^8 K on the rotational axis).

2.4.4 Running the Simulation Longer

We considered our mergers completed after 6 orbits, since in that time they on average had reached our convergence criterion of 2.5% non-axisymmetry (see Sec. 2.2.3). To test the robustness of our results, we also determined properties attained after 8 orbits. In Fig. 2.13, we compare the 6 and 8 orbit results for $0.6 - 0.6 M_{\odot}$ and $0.6 - 0.8 M_{\odot}$ binaries.

We find our mergers show little evolution between 6 and 8 orbits, with the largest changes seen for the angular velocity profiles. For the $0.6 - 0.8 M_{\odot}$ merger, the rigidly rotating core sped up and the off-center peak decreased in height and moved out, while for the $0.6 - 0.6 M_{\odot}$ merger, the center spun down and the rotational profile became flatter. In the dissimilar-mass merger, T_{\max} and $\rho(T_{\max})$ changed by $\lesssim 5\%$ and the density and temperature structures nearly overlap, while in the equal-mass merger T_{\max} and $\rho(T_{\max})$ changed by $\sim 20\%$ (2.9 to 2.3×10^8 K and 1.7 to 2.0×10^6 g cm $^{-3}$), reflecting an increase in central density and a shifting of the temperature profile, with temperature decreasing in the center but increasing elsewhere. The evolution of all properties is consistent with viscous evolution – expected to follow the merger proper – with the core driven into rigid rotation, and angular momentum transferred outward to the disk. In the dissimilar-mass merger, the net effect is spin-up of the core and spin-down of the envelope, while in the equal-mass case it is the reverse. Of course, in the process, rotational energy is turned into thermal energy, heating the remnants.

One curious aspect for equal-mass mergers is the evolution of the off-center hot spots (Fig. 2.2).

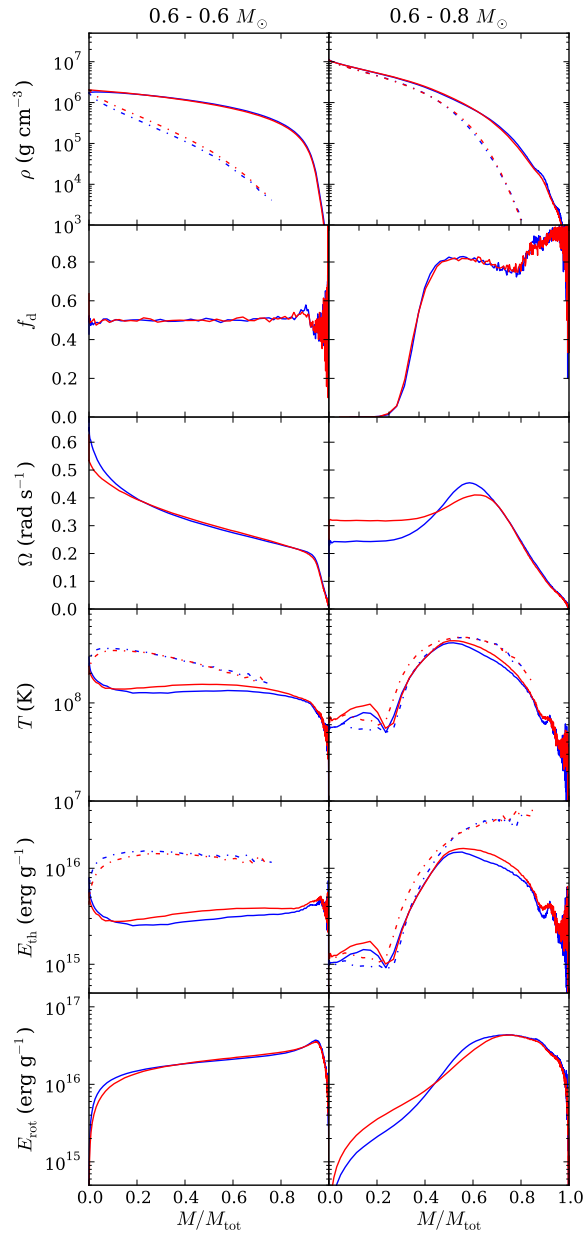


Figure 2.13: As Fig. 2.10, but for $0.6 - 0.6 M_{\odot}$ (left) and $0.6 - 0.8 M_{\odot}$ (right) mergers, comparing properties for our default simulation time of 6 initial orbital periods (blue) with those obtained after 8 orbital periods (red).

Over time, these broaden parallel to the equatorial plane, yet become narrower along the rotational axis. As a result, the hourglass shape is lost, and the center of the remnant stops being one of the hottest point in the system. After 8 orbits, the system resembles more closely what we find for typical similar-mass mergers, which have more pancake-shaped hot spots flanking a colder, denser region on the equatorial plane.

Comparing more broadly the 6 and 8-orbit results, we find changes at the $\sim 5\%$ level. The trends presented in Sec. 2.3.2 continue to hold to within $\sim 10\%$ except for h_ω (which becomes $h_\omega/h_a = 0.98 + 0.74q_\rho^2 (\pm 0.07)$), the fraction of disk energy in degeneracy energy ($E_{\text{deg,disk}}/E_{\text{L,disk}} = 0.07 (\pm 0.02)$), mass enclosed within the radius of maximum temperature ($M_{\text{enc}}(T_{\text{max}})/M_a = 1 - 0.21q_\rho (\pm 0.01)$), maximum rotational frequency ($\Omega_{\text{max}}/\Omega_{\text{orb}} = 3.4 (\pm 0.5)$) and the widths of the regions in which thermal and rotational energy are deposited ($\Delta M_{\text{enc}}(E_{\text{th}})/M_a = 0.13 + 0.87q_\rho (\pm 0.03)$; $\Delta M_{\text{enc}}(E_{\text{rot}})/M_a = 0.15 + 0.70q_\rho (\pm 0.02)$). Changes to these trends are consistent with the viscous evolution described above: the remnant is beginning to spin down, lose its rotational support, and energy is being redistributed.

2.4.5 Viscosity Prescription

The addition of artificial viscosity is required in SPH to accurately capture shocks, but no consensus exists on how best to implement it. We ran two additional simulations of a $0.6 - 0.8 M_\odot$ merger to check the robustness of our results with respect to changes in the viscosity, one with small and one with large artificial viscosity (fixed $(\alpha, \beta) = (0.05, 0.1)$ and $(1, 2)$, respectively). As before, these additional runs use 2.5% non-axisymmetry and a requirement for the density to be highest at the remnant's center as their completion criteria, and the low viscosity run completed at 198 s while the high completed at 242 s. Here, we expect that low values of α will lead to large particle noise and inaccurate shock capturing, while high values result in large viscous heating and rapid loss of differential rotation. Our results confirm this (Fig. 2.14): the simulation with low artificial viscosity leads to a remnant with stronger differential rotation, with the disk carrying 34% more rotational energy (and the remnant 33% less) than in the standard variable α simulation. Lower viscosity also leads to greater mixing of donor and accretor material, reflecting the stronger diffusion associated with the larger particle noise inherent to low viscosity.

Aside from the mixing and spin-up, the results for the three different viscosity prescriptions do not differ greatly. While one might have expected greater dissipation of rotational into thermal energy for higher viscosity, the maximum temperatures and rotation rates vary by $\lesssim 10\%$, and the thermal and rotational profiles are quite similar. The density profiles are virtually identical except near the outer parts, where the low viscosity simulation leaves matter with greater rotational support.

2.4.6 Spurious Heating

As discussed in Sec. 2.2.1 and throughout Sec. 2.3, noise combined with a pressure floor in the equation of state lead to small increases in internal energy. While this energy has a negligible effect on most remnant properties, in the most degenerate regions of the remnant it can cause significant temperature increases. Here, we discuss the extent to which spurious heating affects our results.

As a comparison for the spurious heating seen in some of the simulations, we relaxed a $0.8 M_\odot$ isolated white dwarf for 489 s longer than the standard 81 s we used for relaxing single stars. While the

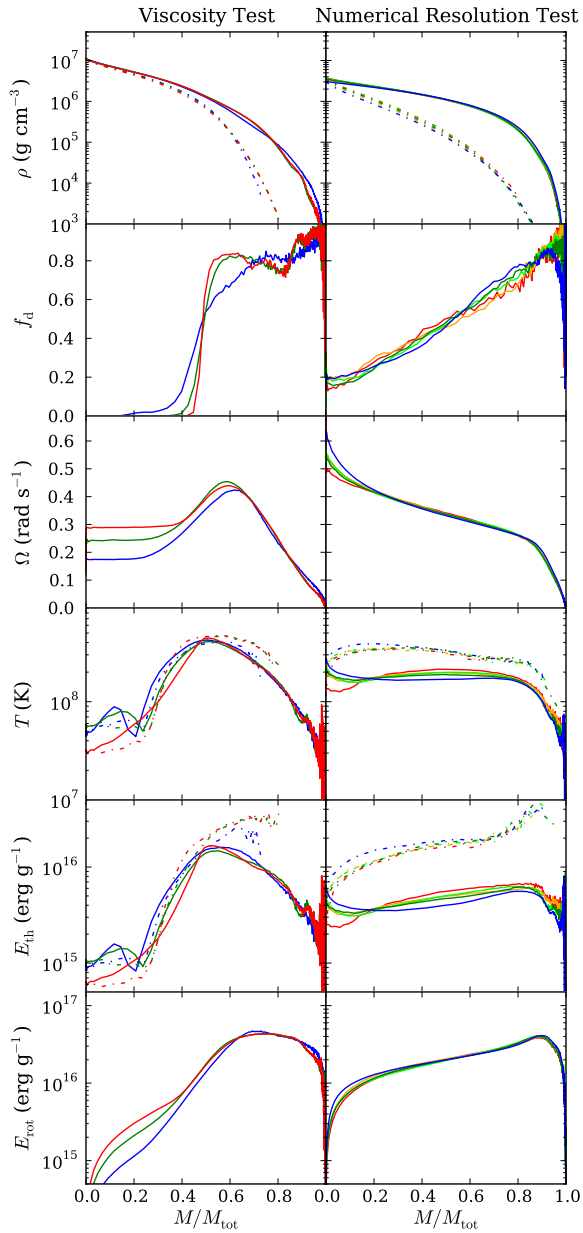


Figure 2.14: As Fig. 2.10, but comparing simulations of a $0.6 - 0.8 M_{\odot}$ merger with different viscosity prescriptions (left) and simulations of a $0.625 - 0.65 M_{\odot}$ merger with different numbers of particles (right). For the viscosity, we compare fixed low viscosity ($\alpha = 0.05, \beta = 0.1$; blue), standard variable viscosity (green), and fixed high viscosity ($\alpha = 1.0, \beta = 2.0$; red). For particle numbers, we show simulations at one quarter (red), half (orange), and double (blue) the default number of particles, as well as the default simulation (lime) and a rerun of the default simulation (green) to determine the effect of order-of-execution differences, round-off errors and other such numerical effects.

total energy of the WD (potential, degeneracy and thermal energy combined) increased by $\sim 1\%$ of the original total energy over the additional period of time, the change in thermal energy was enough to raise the central WD temperature from 1.2×10^7 K (increased from 5×10^6 K due to particle noise) to 1.2×10^8 K. In Fig. 2.15, we compare the thermal energy profile of this isolated $0.8 M_\odot$ WD with those of a $0.4 - 0.8 M_\odot$ and a $0.7 - 0.8 M_\odot$ merger, with the times for the isolated WD taken at 489 and 224 s (the mergers' respective completion times) longer than the standard 81 s. The total thermal energy generated in the WD at an additional 489 s is $\sim 10\%$ of the thermal energy generated in a $0.4 - 0.8 M_\odot$ merger.⁸ Indeed, given how well the specific thermal energy profiles match in the interior, it is clear that spurious heating dominates there.

Spurious heating is much less important for the $0.7 - 0.8 M_\odot$ merger, since its core has mixed to much greater extent and less time was needed for the merger to complete. The total thermal energy generated in the isolated WD at 224 s is only $\sim 3\%$ of the thermal energy generated during merger, and even at the very center spurious heating contributes $\sim 35\%$ (rather than nearly all) of the thermal energy. As a result, the central temperature of the merger, 1.4×10^8 K, is substantially higher than that of the isolated WD, 7.8×10^7 K. It is important to note this comparison overestimates spurious heating, since the isolated WD will have had many more particles that dip below the Fermi energy than the much hotter merger remnant core.

Overall, we conclude that spurious heating is present, but is recognized fairly easily and does not influence our conclusions. In particular, its effects on remnants should be small in both high-density regions with $T \gtrsim 3 \times 10^8$ K and in lower-density $\lesssim 10^6 \text{ g cm}^{-3}$ regions. Other simulations may suffer from spurious heating as well. In this respect, it is intriguing that our equatorial temperature curves for a $0.6 - 0.8 M_\odot$ merger are a good match those of LIG09, even in the center (Fig. 2.16; Sec. 2.5.1).

2.4.7 Resolution

To determine whether or not the numerical resolution matters for our results, we ran three additional simulations of a $0.625 - 0.65 M_\odot$ merger, with roughly a quarter, half, and double the number of particles (63,736, 127,525 and 510,047, respectively), corresponding to 0.63, 0.79 and 1.26 times the SPH smoothing length (resolution) we normally use. We also ran a second simulation with the same number of particles (255,035 particles). Here, we chose $0.625 - 0.65 M_\odot$ to see if numerical resolution has any effect on whether a merger is “similar-mass”. All simulations were considered complete at 6 orbits of the initial binary, though we also checked the 2.5% non-axisymmetry convergence times.

From Fig. 2.14, one sees that the two runs using the same number of particles – and identical initial conditions and the same version of Gasoline – still give slightly different results. This is due to the inherent non-linear nature of fluid dynamics, coupled with small, random perturbations, e.g., from differences in the order of force addition in parallel processing, round-off errors and slight inconsistencies in converting thermal energy to temperature. Overall, merger remnant properties change by $\sim 3.5\%$ between the two runs. The most prominent differences are seen in properties determined from low numbers of particles, such as T_c (varies by $\sim 10\%$), and those involving finding maxima of temperature plateaus, such as $\rho(T_{\max}^z)$ (40%) and $\rho(T_{\max}^{cv})$ (a factor of 3 – in one case convection shifts the temperature maximum off-center).

⁸A $\sim 10\%$ increase in thermal energy corresponds to $\sim 1\%$ increase in the overall energy of the $0.4 - 0.8 M_\odot$ remnant, somewhat larger than the typical $\sim 0.3\%$ level at which Gasoline conserves total energy in our simulations. We find that similar-mass simulations tend to lose total energy at the 0.05% level, while some of the low q_ρ mergers gain more than 1% in total energy due to spurious heating.

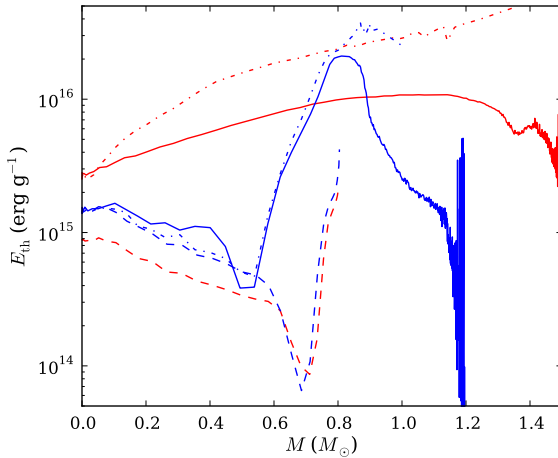


Figure 2.15: Specific thermal energy as a function of enclosed mass for a $0.4 - 0.8 M_{\odot}$ (blue) and a $0.7 - 0.8 M_{\odot}$ merger (red), shown both along the equatorial plane (solid curves) and along the rotational axis (dot-dashed). Also shown are the (spherical) profiles found for an isolated $0.8 M_{\odot}$ white dwarf (dashed) simulated using the same parameters, and for the same completion times (six initial orbital periods, equivalent to 489 s and 224 s). Spurious heating is estimated to be responsible for nearly all the thermal energy in the core of the $0.4 - 0.8 M_{\odot}$ remnant, and for about one third in the core of the $0.7 - 0.8 M_{\odot}$ remnant. It is not important in regions heated by interaction. (The “hook” in the outer layers of the white dwarf profile reflects the high initial temperature chosen; in a merger, this is erased by the interaction.)

The differences for different resolutions are larger. While to first order, the equatorial density and mixing profiles are very similar, there is a systematic $\sim 20\%$ drop in the equatorial density – $\sim 25\%$ in the rotational axis density – near the center of the remnant with increasing numerical resolution (top right panel of Fig. 2.14). The angular velocity and rotational energy profiles are again very similar, except in the central regions, where there is a $\sim 20\%$ increase in Ω_{\max} . For the temperature the effects are larger: with higher resolutions, most of the equatorial plane is colder, with a $\sim 20\%$ drop in the value of the temperature plateau near $M/M_{\text{tot}} = 0.5$. The temperatures along the rotational axis, however, increase with increasing resolution, by $\sim 10\%$ across the range of resolutions, as does the upturn in equatorial temperature near the center of the remnant, by $\sim 50\%$ ($\sim 30\%$ if we do not include the lowest resolution run). The latter effects are due to increasing prominence of the off-center hotspots at higher resolutions, which also tend to look more hourglass-shaped. Indeed, for our lowest resolution, the densest material in the two stars remains relatively cold throughout the entire merger, resembling the synchronized systems described in Sec. 2.4.3. Finally, we find that if we do not consider the lowest resolution run, the disk half-mass radius varies by 4%, angular velocity at the half-mass radius varies by 4%, and the core-envelope mass changes by 3%. This is similar to the results of the resolution tests of Raskin et al. (2012).

The 2.5% non-axisymmetry convergence times for the half and double-particle number runs are within 14 s of the 275 s non-axisymmetry convergence time of the default run, a small difference that implies a negligible amount of post-merger evolution. Only the quarter-particle number run deviated substantially, converging 57 s earlier. This may simply reflect the smaller number of particles in the disk, where the system is most asymmetric.

We stress that even though the order-of-magnitude change in particle number (factor of two change in resolution) generates 10 – 30% variations in some remnant properties, the overall shapes of the profiles in Fig. 2.14 are very similar. In particular, the merger remnant does not look more or less “similar-mass” (except, arguably, the temperature curve at the lowest resolution). Exact values of properties, therefore, will vary depending on resolution (and will vary on similar or larger levels if initial conditions like a_0 are changed), but the overall picture of the merger and trends should be more robust.

2.5 Comparison With Others

2.5.1 Comparison With Lorén-Aguilar et al. (2009)

[LIG09](#) simulated a number of WD mergers, and gave detailed temperature, surface density, and rotational frequency curves for three. In Fig. 2.16, we compare their results (from their Figs. 3 and 4) with ours for two of these, $0.6 - 0.6 M_{\odot}$ and $0.6 - 0.8 M_{\odot}$ (the third was a $0.4 - 0.8 M_{\odot}$ He - CO WD merger, whose temperature profile cannot be compared directly). We note that they used different initial conditions, starting their systems with an orbital separation too large for mass transfer to begin, and then slowly reducing the separation until it does. This point defines their $t = 0$ and the start of the merger simulation proper. Given this different setup, their merger completion times cannot be compared directly to ours. In their simulations, however, coalescence (the final consolidation of the two WDs into one) also occurs after just about one orbit, so the differences should not be too large. To give a sense of the effect of different completion criteria, we compare their results both with our standard results, taken after 6 orbits, and our results taken at their merger completion times.

For both mergers, the surface density curves are similar, although in their $0.6 - 0.6 M_{\odot}$ merger, the central peak is $\sim 30\%$ higher ($\sim 10\%$ if we use their completion time of 514 s). For the $0.6 - 0.8 M_{\odot}$ merger, the temperature profiles are also very similar, with maxima⁹ differing by only $\sim 10 - 15\%$, and having nearly identical shapes. Larger differences are seen for the $0.6 - 0.8 M_{\odot}$ rotational frequency profile, where the angular velocity peaks further out and at lower value ($\sim 0.3 \text{ s}^{-1}$ compared to our 0.45 s^{-1} – or 0.50 s^{-1} using their completion time of 164 s). Indeed, our entire remnant is more spun-up than theirs.

For the $0.6 - 0.6 M_{\odot}$ merger, [LIG09](#) have a plateau in their angular frequency profile, with $\Omega_{\max} \simeq 0.25 \text{ s}^{-1}$, while our profile is much more peaked and reaches a much higher frequency, of 0.60 s^{-1} . By their completion time, our rotation curve is not as sharply peaked, but still reaches 0.44 s^{-1} . The temperature profiles are also much less similar: our maximum temperature in the equatorial plane is a factor of 2 lower than theirs (factor of 3.3 at their completion time), and even our maximum temperature along the rotational axis is a factor 1.6 lower (factor 1.9 at their completion time).

Finally, we can compare how mass is distributed. In both our simulations and those of [LIG09](#), negligible mass is lost, so only the distribution between disk and core-envelope matters. For our $0.4 - 0.8 M_{\odot}$, $0.6 - 0.6 M_{\odot}$, and $0.6 - 0.8 M_{\odot}$ simulations, we infer disk masses of 0.31 , 0.10 , and $0.40 M_{\odot}$, respectively, which are reasonably close to the 0.28 , 0.10 , and $0.30 M_{\odot}$, respectively, listed by [LIG09](#) (their Table 1), especially considering that we likely use a different definition of what is “disk”.

⁹Maximum temperatures given in Table 1 of [LIG09](#) refer to hot spots in their simulations, and are about a factor of 2 higher than the hottest points on their temperature curves. As we have not done hot-spot finding, we cannot compare with those values.

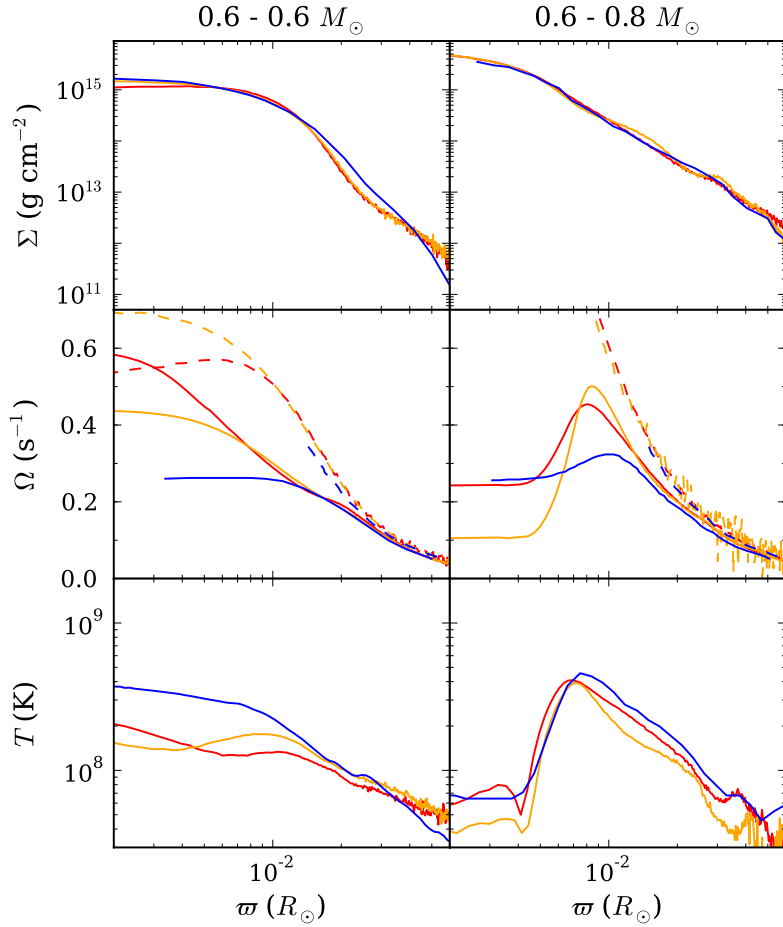


Figure 2.16: Comparison of our results with those of LIG09, for a $0.6 - 0.6 M_{\odot}$ (left) and a $0.6 - 0.8 M_{\odot}$ (right) merger. Shown are surface density, remnant (solid) and Keplerian (dashed) angular frequency, and temperature, with profiles from LIG09 in blue, and our equivalent ones in red and orange. Here, the former are for our default completion time of 6 initial orbital periods and the latter for their completion times (514 s or 10.9 orbital periods for the $0.6 - 0.6 M_{\odot}$ merger, and 164 s or 3.4 orbits for the $0.6 - 0.8 M_{\odot}$ merger).

Overall, the primary differences between our simulations appear to be the amount of spin-up and heating of the equal-mass merger. We believe it is unlikely that this reflects differences in initial conditions: we found much smaller changes in the angular velocity profile with increasing a_0 (see Fig. 2.11), and in the simulation of LIG09 the stars still seem to be quite close to spherically symmetric at the start and disrupt quickly (their Fig. 1), even though they were more properly relaxed. Instead, we believe the more likely explanation is that the viscosity prescription of LIG09, based on Riemann solvers, yields larger effective viscosity. This would explain both the reduction in angular velocity and increase in temperature (since viscous evolution converts rotational into thermal energy), as well as the fact that similar-mass mergers are affected more (they mix more, and LIG09 ran their equal-mass merger for a very long time). If we ran our simulations longer and thus included further viscous evolution, the similarity with their simulations would likely be closer.

2.5.2 Comparison with Others

Simulations of WD mergers have also been presented by [Yoon et al. \(2007\)](#), [Pakmor et al. \(2010; 2011b; 2012b\)](#), [Dan et al. \(2011; 2012\)](#), and [Raskin et al. \(2012\)](#). Unfortunately, comparison with those results is difficult, since, unlike [LIG09](#), all these authors are sparse with quantitative details about their results.

An exception is the $0.81 - 0.9 M_{\odot}$ merger simulated by [Dan et al. \(2012\)](#), shown in their Fig. 1. While that simulation is for synchronized WDs, it is still particularly useful to compare with, since [Dan et al.](#) show results for both approximate and accurate initial conditions. We find that their spherically enclosed mass profile is very similar to ours, with, e.g., $M = 0.9 M_{\odot}$ at 4.5×10^8 cm in both (though since spherically enclosed mass is a cumulative quantity, significant structural differences can remain hidden). Our spherically averaged density profile looks most similar to the profile they found using approximate initial conditions. Our central density, 1.9×10^7 g cm $^{-3}$, is within $\sim 10\%$ of theirs, and the density profile remains similar up to $r \simeq 5 \times 10^8$ cm ($\rho \simeq 10^6$ g cm $^{-3}$). Beyond, their profile becomes shallower while ours continues to decline; at $r = 10^9$ cm, they find $\rho \simeq 3 \times 10^5$ g cm $^{-3}$, while we find $\rho \simeq 10^5$ g cm $^{-3}$. This may be a consequence of the additional angular momentum associated with synchronized rotation. With accurate initial conditions, a difference with our results is that the density profile becomes flat beyond 10^9 cm.

Comparing temperature profiles, we roughly reproduce their spherically averaged one for approximate initial conditions, including the off-center peak – their T_{\max} is $\sim 20\%$ lower (to be expected since their binary is synchronized; see Sec. 2.4.3), but is also located at 4×10^8 cm (or $M_r \simeq 0.9 M_{\odot}$). However, our central temperature (2.2×10^8 K) is an order of magnitude higher than theirs (2×10^7 K) and at $r \gtrsim 10^9$ cm our temperatures are systematically hotter, perhaps a result of the much larger dissipation expected for non-rotating WDs. With accurate initial conditions they found an even narrower temperature peak than the one with approximate conditions, which thus deviates even more from our curve. This trend is similar to what we see when increasing a_0 (Sec. 2.4.2), so it seems likely we would reproduce their simulations more closely if we used the same initial conditions.

2.5.3 The Importance of Accurate Initial Conditions

Many of the recent simulations ([Dan et al. 2011; 2012](#); [Raskin et al. 2012](#)) assume co-rotating WDs. This assumption is numerically convenient, in that it is relatively straightforward to start the simulation in the physically correct state: since in the co-rotating frame there are no flow velocities, one can easily relax a simulated binary within an appropriate potential in the co-rotating frame, damping out any velocities resulting from an initial mismatch.

As a result, it has been possible to study the onset of mass transfer in detail. As first pointed out by [D’Souza et al. \(2006\)](#) from simulations using a grid code, the disruption of the donor is preceded by a rather long – dozens of orbits – phase of mass transfer. Further simulations by [Dan et al. \(2011; 2012\)](#) showed that in this initial phase a significant fraction, $\sim 10\%$ of the donor mass, is transferred. As a result, e.g., the disk is substantially colder and more extended. The remnant core seems more subtly affected, in that its appearance becomes “more dissimilar”, reflecting that coalescence is between two WDs whose masses have become more disparate than they were initially. As a consequence, e.g., even for similar-mass binaries, the hottest point of the merger is found to be well outside the center. Indeed, [Raskin et al. \(2012\)](#) find that even for equal-mass binaries, the final outcome for more massive mergers is one where the core of one of the WDs is virtually undisturbed.

At present, it is not clear how important accurate initial conditions would be for asynchronous mergers. Qualitatively, we expect the effects to be smaller than for synchronous mergers, for three reasons. First, from the analytic study of Lai et al. (1994), in which tidal and rotational distortion are approximated by ellipsoids, co-rotating binaries always reach contact or Roche lobe overflow before becoming dynamically unstable, while irrotational binaries become dynamically unstable first. While an exact treatment of the irrotational case found that, in fact, Roche contact preceded dynamical instability (Uryū & Eriguchi 1998), it suggests that WDs in irrotational binaries will disrupt much sooner. Second, the simulations of LIG09 use initial conditions that should be quite close to correct, yet their WDs disrupt quickly (see Sec. 2.5.1). Third, the two components are counterrotating in the rotating frame. Hence, any mass transferred will hit the accretor with a larger relative velocity than would be the case for co-rotating WDs. Indeed, in the limit of equal-mass WDs, very little would happen for co-rotating WDs when one reaches contact, while a strong shock would be expected for the irrotational case. In general, one expects part of the shocked material to enter a high-entropy halo around the accretor. For co-rotating WDs, Dan et al. (2011) found that this halo helps remove angular momentum from the orbit, leading to a shorter start-up phase. For the irrotational case, given the stronger expected shocks, the start-up phase would likely be reduced even further. On the other hand, we saw in Sec. 2.4.2 that remnant properties are sensitive to changes in angular momentum content through changes in a_0 . Simulating more realistically the onset of mass transfer through accurate initial conditions will likely change a_0 .

Ideally, one would still simulate the initial mass transfer phase accurately. Unfortunately, even though the equilibrium solution is known (Uryū & Eriguchi 1998), it is not straightforward to set up the initial binary properly, since it is difficult to relax to a state that includes substantial fluid motion, and to slowly evolve such a state to contact, while ensuring viscosity remains low enough that there is no artificial tidal dissipation. Such dissipation is seen in our tests with varying initial distance a_0 in Sec. 2.4.2 (and may affect the simulations of LIG09 as well). Prior to coalescence, strong dissipation of tidal bulges heats the outer envelope of the donor (both stars for similar-mass mergers), and spin-orbit coupling due to both tides and the direct-impact accretion stream result in both donor and accretor becoming 25 - 50% synchronized by coalescence.

Since it significantly affects the merger and merger outcome, whether or not tidal dissipation causes real CO WD binaries to synchronize before the merger remains a major source of uncertainty. For the radiative stellar envelopes appropriate for WDs, tidal dissipation is expected to be inefficient, with a timescale 10^{12} to 10^{15} yrs, suggesting that WDs do not synchronize (Marsh et al. 2004, and references therein). However, coupling of the tides to pulsations may dramatically increase dissipation (Fuller & Lai 2012). Fortunately, it may be possible to determine the rate of synchronization observationally. For instance, Piro (2011) suggested that tidal dissipation is responsible for the relatively high temperature of the primary WD in the 13-minute eclipsing binary SDSS J065133.33+284423.3, predicting that it would be about halfway to being synchronized. This could be tested by either measuring the rotational broadening of the narrow cores of the hydrogen lines, or looking for velocity deviations through the transit of the more massive secondary.

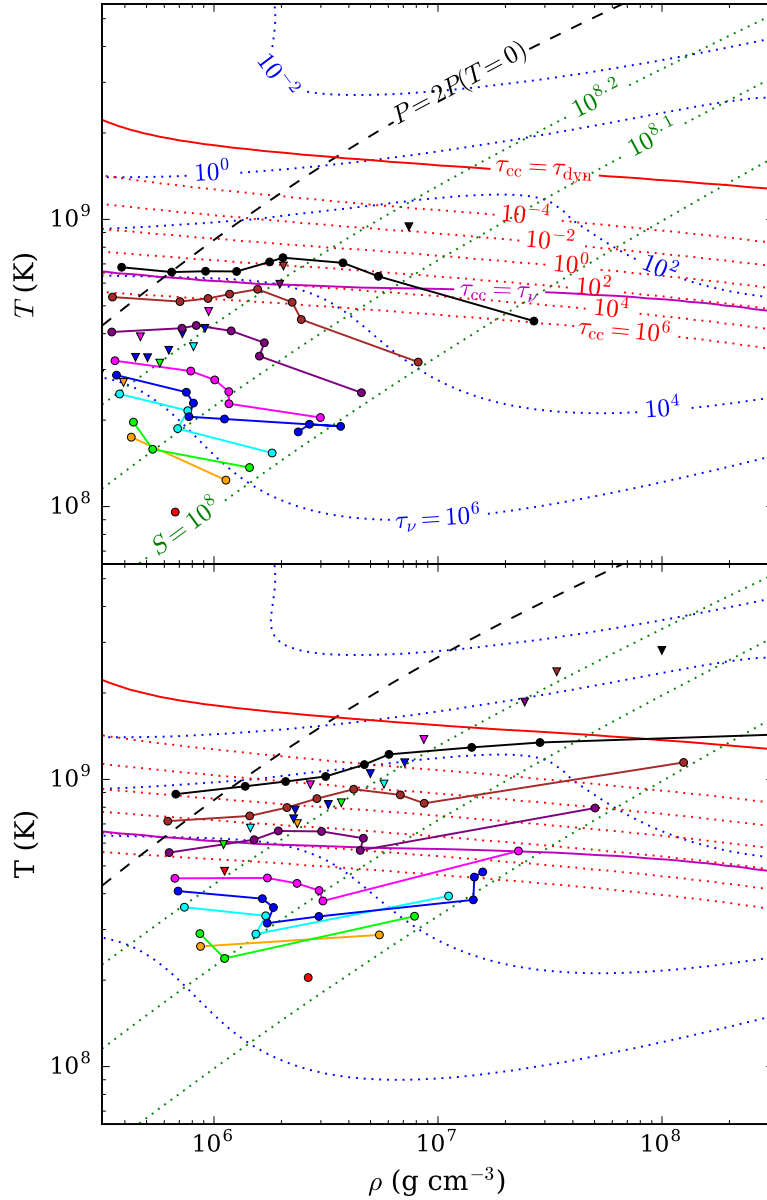


Figure 2.17: Left: merger remnant maximum temperature T_{\max} and corresponding density $\rho(T_{\max})$ for all merger remnants. Values along the equatorial plane are marked with circles, with lines connecting points with the same accretor mass, while values along the rotational axis (only plotted for similar-mass mergers) are marked with triangles (for all, colors indicate accretor mass, encoded as in Fig. 2.3). For similar-mass mergers, equatorial temperatures have been adjusted to account for mixing in convectively unstable cores. Right: maximum temperatures and corresponding densities following estimated post-merger evolution. The estimate assumes that the remnant spins down completely, that all rotational energy is used to drive matter to large distances, and that the remainder adjusts adiabatically (see text). Also shown are contours of constant neutrino cooling timescale $\tau_{\nu} \equiv C_P T / \epsilon_{\nu}$ and carbon fusion heating timescale $\tau_{\text{cc}} \equiv C_P T / \epsilon_{\text{CC}}$, both in years, as well as entropy S in erg K $^{-1}$. (Here, C_P is the heat capacity at constant pressure and ϵ the specific energy loss/gain rate.) The lines labeled $\tau_{\text{cc}} = \tau_{\nu}$ and $\tau_{\text{cc}} = \tau_{\text{dyn}}$ denote where the carbon fusion heating timescale balances the neutrino cooling and dynamical timescales, respectively. Finally, the $P = 2P(T=0)$ line is shown as an approximate upper bound of the region where degeneracy pressure dominates. All quantities were calculated using MESA (Paxton et al. 2011).

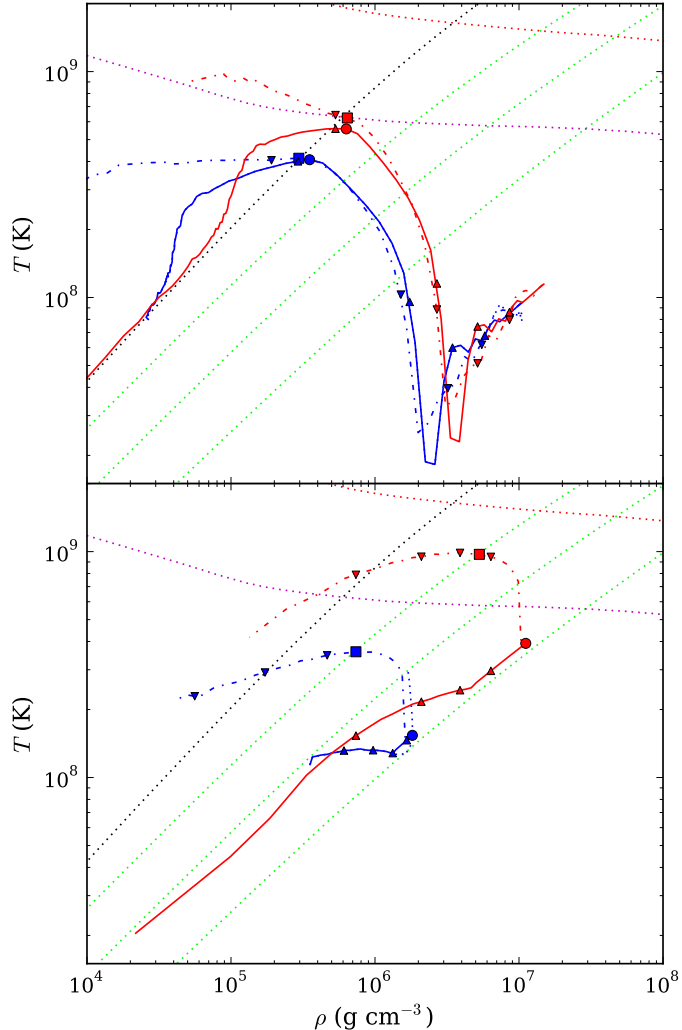


Figure 2.18: Estimate of post-merger viscous evolution for $0.4 - 0.8 M_{\odot}$ (top) and $0.6 - 0.6 M_{\odot}$ (bottom) mergers. In blue are shown the temperature-density structure of the merger remnant, on the equatorial plane before (dotted) and after (solid) correction for convection, as well as along the rotational axis (dot-dashed), with points marking the hottest locations (circles and squares) and steps of $0.2 M_{\odot}$ in spherical enclosed mass (triangles pointing up and down). In red, estimates of the structure following viscous evolution are shown, where it is assumed that the remnant spins down completely, that all rotational energy is used to drive matter to large distances, and that the remainder adjusts adiabatically (see text). For reference, also shown as dotted curves are the contours of constant entropy from Fig. 2.17 (green), as well as the lines where $\tau_{\text{cc}} = \tau^{\circ}$ (magenta), $\tau_{\text{cc}} = \tau_{\text{dyn}}$ (red), and $P = 2P(T=0)$ (black).

2.6 Post-Merger Evolution

We now turn to the question of how our merger remnants will evolve. To set the stage, we show in the left panel of Fig. 2.17 for all remnants the maximum temperature T_{\max} found along the equatorial plane¹⁰ as a function of the corresponding density $\rho(T_{\max})$. Here, for the similar-mass mergers for which we found convectively unstable cores (Sec. 2.3.2.5), we show the (lower) temperatures reached after artificially mixing them. For those mergers, the much higher temperatures reached along the rotational axis are shown as well (triangles). One sees the trends identified earlier: T_{\max} is mostly set by the accretor, while $\rho(T_{\max})$ depends more strongly on the donor. As a result, maximum temperature occurs in less degenerate conditions for dissimilar-mass mergers, crossing the degeneracy line for our most disparate cases. One also sees that for all but the most massive accretors, carbon fusion will not start: the neutrino cooling time is shorter than the fusion heating time. This is consistent with what was found in previous work (see Sec. 2.1).

2.6.1 Viscous Evolution and Possible Spin Down

Following the merger, processes that happen on timescales slower than the dynamical time can become important. These include viscous evolution, neutrino emission, radiative or convective thermal adjustment, and magnetic dipole radiation spin-down. Out of these, convection acts on the fastest timescale, and we already included its effect on the core in Fig. 2.17 left. Next fastest would almost certainly be viscous evolution. The merger remnant is unstable to both the magneto-rotational instability (Balbus & Hawley 1991) and Tayler-Spruit dynamo (Spruit 2002). Radiative adjustment is expected to be much slower, except at the surface, where radiative losses may also lead to convection in some systems (Shen et al. 2012; Schwab et al. 2012; Raskin et al. 2012). Using the standard Shakura & Sunyaev (1973) α -prescription for the viscosity $\nu = \alpha c_s H$, where c_s is the local soundspeed and H is the scale height of the system, the viscous evolution timescale for the remnant disk is

$$t_{\text{visc}} = \frac{R_{\text{disk}}^2}{\nu} = \frac{1}{\alpha} \left(\frac{R_{\text{disk}}}{H} \right)^2 t_{\text{dyn}} \sim \frac{10}{\alpha} t_{\text{dyn}}, \quad (2.24)$$

implying a timescale $t_{\text{visc}} \sim 10^3 - 10^5$ s for $\alpha \sim 10^{-3} - 10^{-1}$ and $t_{\text{dyn}} \sim 10$ s. This is orders of magnitude smaller than both the neutrino loss timescale ($\gtrsim 10^3$ yrs; see Fig. 2.17 left) and thermal adjustment timescale ($\gtrsim 10^4$ yrs; Shen et al. 2012).

It is possible that the strong differential rotation during a merger results in substantial amplification of magnetic fields. The one known probable WD merger remnant, RE J0317–853, has a surface magnetic field of 3.4×10^8 G (Barstow et al. 1995; Külebi et al. 2010). If mergers lead to strongly magnetized WDs, and these WDs additionally drive an ionized outflow, the magnetic coupling between the outflow and the WD could serve to transport angular momentum out of the system, spinning down the WD. The timescale for such a spin-down is roughly given by,

$$t_{\text{msd}} \sim \frac{L}{\dot{M} R_A^2 \Omega} \sim \frac{L}{(\dot{M} \Omega)^{3/5} (B^2 R^6)^{2/5}}, \quad (2.25)$$

¹⁰The central temperatures for the $0.625 - 0.65 M_{\odot}$ and $1.0 - 1.0 M_{\odot}$ mergers are $\sim 4\%$ and 10% lower than their respective maximum temperatures. In both cases, however, the center is much denser than the off-center hotspot, and since our estimated post-merger evolution more greatly affects central material, we show the central equatorial density and temperature for these two systems in Fig. 2.17 left, rather than the maximum.

where L is the angular momentum of the remnant, \dot{M} the mass loss rate, R_A the Alfvén radius, and Ω the angular spin frequency. For the second approximation, we used that $R_A \sim (B^2 R^6 / \dot{M} \Omega)^{1/5}$, with B the surface magnetic field and R the remnant radius. Scaling to $B = B_8 10^8$ G and $\dot{M} = \dot{M}_7 10^{-7} M_\odot \text{ yr}^{-1}$ (similar to what is observed for RE J0317–853 – see above – and [WR] cores of planetary nebulae [Hamann 1997]), and using the properties inferred for a $0.6 - 0.6 M_\odot$ remnant ($L \simeq L_{\text{tot}} \simeq 10^{50.5} \text{ g cm}^2 \text{ s}^{-1}$, $R \simeq R_{\text{disk}} \simeq 10^9 \text{ cm}$, $\Omega \simeq \Omega_{\text{max}} \simeq 10^{-0.3} \text{ s}^{-1}$, we find $t_{\text{msd}} \simeq 8 \times 10^3 B_8^{-4/5} \dot{M}_7^{-3/5} \text{ yr}$, which is of the same order as the neutrino cooling timescale of $\sim 10^4 \text{ yr}$ at the ignition line (for the whole range of remnants, $2 \times 10^3 \lesssim t_{\text{msd}} \lesssim 5 \times 10^4 \text{ yr}$).

Accretion from the disk, loss of rotational support, and possible cooling of the hot envelope could all compress and heat the remnant core. A detailed study of this is beyond the scope of this paper, but we can make first-order estimates of the effects on our merger remnants, and compare these with the more detailed analysis of Schwab et al. (2012) in one specific case.

For our estimates, we make four assumptions: (i) spin-down and accretion are much faster than thermal processes, and do not lead to local dissipation (i.e., particles entropies are constant in time); (ii) all angular momentum is carried away to large distances; and (iii) corresponding matter ends up with zero total energy (i.e., is at large distances and has negligible kinetic and internal energy). From energy conservation, the last assumption implies that the remaining object will have the same total energy as our merger remnant (but a lower mass), the first that it will have the same entropy structure, and the second that it has no rotational support. To determine the properties, we first determine the entropy profile of the merger remnant, by averaging entropy over isopotential surfaces. We then use this entropy profile and an estimated central density to construct a spherically symmetric (non-spinning) hydrostatic model, iterating on the central density until it has the correct total energy (inside of the zero-pressure surface). This automatically gives the mass contained in this object, which will be lower than our remnant mass, the remainder representing material that, due to dissipation of rotational energy, has expanded out to large distances and therefore provides negligible weight. To determine the evolution of hot spots, we order remnant particles by potential, and map them to their new positions in the final object, calculating new temperatures from the new densities, again assuming their entropy did not change (entropy is not constant over isopotential surfaces, so these temperatures are not strictly consistent with the hydrostatic model).

In Fig. 2.18, we show the results of our evolutionary estimate for our fiducial $0.4 - 0.8$ and $0.6 - 0.6 M_\odot$ systems. For the former case, the core-envelope, originally $0.90 M_\odot$, accretes $0.06 M_\odot$ from the disk, the remaining $0.25 M_\odot$ going to large distances. The central core is not significantly heated, while the lower-density hot envelope is, with the outer hot envelope along the rotational axis passing the ignition line. Since this material is almost non-degenerate, the resulting nuclear burning will likely be stable, or be extinguished by expansion. Thus, not unexpectedly, the hot envelopes of dissimilar-mass mergers are not good candidates for a nuclear runaway.

For the $0.6 - 0.6 M_\odot$ system, the center of the final, spun-down object is at much higher density and temperature than the remnant, while much of the outer regions have become less dense and cool. The latter happens because similar-mass mergers have strong rotational support, and if this is removed their binding energy increases significantly. To compensate for this, a large amount of mass has to expand to large distances, causing the core-envelope mass to decrease from $1.11 M_\odot$ to $0.91 M_\odot$. In the final object, the hottest point on the equatorial plane does not reach the ignition line, but the significantly hotter points above and below the equatorial plane do, at densities under which degeneracy pressure

still dominates. Hence, if the hot spots indeed compress with the rest of the remnant, a nuclear runaway could be triggered. (Of course, a nuclear runaway would start as soon as the heating timescale becomes shorter than the compression timescale, which may happen closer to the ignition line.)

In the right panel of Fig. 2.17, we show the results of applying our estimates to all our merger remnants. One sees that all compress and heat, and almost every remnant whose accretor mass is above $0.8 M_{\odot}$ will reach ignition somewhere on the equatorial plane, in many cases under degenerate conditions. We also chart the evolution of the off-center hot spots in similar-mass mergers (square points), and while they are at lower density, they remain degenerate and are all pushed substantially further above the ignition line than their counterparts on the equatorial plane. Almost all similar-mass mergers with an accretor mass above $0.5 M_{\odot}$ could therefore experience nuclear runaways due to their hot spots, though at least some of them will become non-degenerate before an explosion can occur.

The above suggests it is at least plausible that many of our mergers would eventually ignite in degenerate conditions, and that it thus is worthwhile to simulate their evolution in detail. Suitable simulations have recently been pioneered by [Shen et al. \(2012\)](#) and [Schwab et al. \(2012\)](#). [Shen et al.](#) started with a one-dimensional simulation, where they ported the remnant of a $0.6 - 0.9 M_{\odot}$ merger (from [Dan et al. 2011](#)), and evolved it assuming a $\gamma = 5/3$ polytropic equation of state and an $\alpha = 10^{-2}$ viscosity. They find the system spins down completely due to outward angular momentum transport, and the rotationally-supported thick disk is transformed into a tenuous, thermally-supported envelope that hardly affects the core. Over longer, thermal evolution timescales (simulated using MESA, [Paxton et al. 2011](#)), this tenuous hot envelope cools, compresses the core, and lights off-center convective carbon burning, eventually turning the remnant into an ONe WD (that may end its life in an accretion induced collapse).

[Schwab et al. \(2012\)](#) went a step further, porting the same $0.6 - 0.9 M_{\odot}$ simulation, as well as seven other systems, into two-dimensional ZEUS-MP2 simulations ([Hayes et al. 2006](#)), using the Helmholtz equation of state and an $\alpha = 3 \times 10^{-2}$ viscosity. They confirm the one-dimensional results, finding complete spin-down and transformation of the rotationally supported disk into a tenuous, spherically symmetric, hot envelope. They find a 50% increase in the temperature of the hottest point, and a factor of 3 increase in the corresponding density. They also find entropy to roughly be constant in the remnant, except in the outer regions and at the very center, where dissipation of rotational energy leads to heating.

It is encouraging that the results of the above detailed simulations are similar to what we find using our first-order estimates. For our $0.6 - 0.9 M_{\odot}$ remnant, our estimate give increases for the hottest equatorial point of a factor of 2.5 in density and 1.6 in temperature, reasonably close to what is found by [Schwab et al.¹¹](#). Thus, our simplifying assumptions appear to be appropriate at least for dissimilar-mass mergers, where most of the rotational dissipation will be in the disk and envelope, and the structure of the remainder is roughly spherically symmetric (both in density and temperature). It is not clear our estimates would be equally good for similar-mass mergers, where rotational dissipation should occur throughout the star, heating the entire remnant, and where there are substantial differences between the remnant's density and temperature structures. In particular, the rotational axis hotspots may dissipate, which would potentially make it more difficult for a similar-mass system to achieve a runaway. It will thus be particularly interesting to simulate the further evolution of those remnants in

¹¹For the hottest point along the rotational axis, we find a factor of 4.8 increase in density and 2.1 increase in temperature, suggesting our model does not depict as well the evolution of the outer hot envelope along the rotational axis.

more detail. Unfortunately, no such remnants were included by [Shen et al.](#) and [Schwab et al.](#).

2.6.2 Possible Explosions?

From our estimates, it seems that, as suggested by [vK10](#), many merger remnants will ignite carbon fusion. If a detonation is triggered, the resulting explosion may well resemble an SN Ia. Indeed, if the remnants spun down before ignition, their structures are sufficiently close to that of a cold WD that the calculations of [Sim et al. \(2010\)](#) should apply. From our estimates, for mergers that have a total mass between 1.2 and $1.4 M_{\odot}$ (which should be the most common ones), the final objects have masses between ~ 0.9 and $\sim 1.1 M_{\odot}$ which matches fairly nicely the range of ~ 1 to $\sim 1.2 M_{\odot}$ required to reproduce the observed range of SN Ia luminosities ([Sim et al. 2010](#)).

Of course, it is far from clear whether ignition leads to a detonation, since we do not currently understand how detonations are triggered ([Seitenzahl et al. 2009; Woosley et al. 2011](#), and references therein). Generally, it should help that ignition in our remnants is at much lower density (a few 10^7 g cm^{-3}) than is the case for near-Chandrasekhar models ($\sim 10^9 \text{ g cm}^{-3}$), because complete burning leads to much larger relative overpressures (e.g. [Mazurek et al. 1977; Seitenzahl et al. 2009](#)). Also, if a deflagration is started, plausible mechanisms to transition to a detonation all seem to require densities around 10^7 g cm^{-3} , where the conductive flame speeds are slower and the separation between the various burning fronts increases (e.g., [Woosley et al. 2009; 2011](#)).

An interesting aspect of our results is that for all cases ignition likely happens off-center: in shells for dissimilar-mass mergers and in hot spots along the rotational axis for similar-mass ones. Previous one-dimensional simulations suggested off-center ignition would lead to a slow deflagration flame that turns the CO WD into a ONe WD (e.g., [Saio & Nomoto 1985](#)). However, these calculations assumed a hot spot many pressure scale heights above the center. For ignition closer to the center, a deflagration plume is produced (e.g., [Aspden et al. 2011](#)), which may transition to a detonation ([Seitenzahl et al. 2011](#)) and unbind the star.

Given our findings, it seems likely that, if a detonation occurs, it will be triggered off-center. It would be interesting to simulate the resulting explosion, and see whether one could reproduce the observational evidence for asymmetries, which have been interpreted in terms of off-center ignition (though so far only in the context of near-Chandrasekhar models; [Maeda et al. 2010a;b](#)).

Finally, while we simulated only mergers of CO WDs, we can extrapolate our results to more massive ONe WDs. For these, the temperatures would be at least as high as for our $1 M_{\odot}$ accretors, and, after further viscous evolution, the mergers should become hot enough to ignite Ne burning. If this also leads to a detonation, the lower fusion energy released would likely lead to a less energetic explosion than expected for a CO WD merger, but it would produce far more ^{56}Ni and have a very large mass. Plausibly, it would resemble an SN Ia like SN 2009dc, which had unusually low ejecta velocities, produced $\sim 1.8 M_{\odot}$ of ^{56}Ni and had a total ejecta mass of $\sim 2.8 M_{\odot}$ ([Taubenberger et al. 2011](#)).

2.7 Conclusion

We have performed a large, detailed parameter-space study of CO WD mergers, extracting pertinent properties and profiles for each remnant, and studying how these vary across parameter space. For a

merger involving dissimilar-mass WDs, with low $q_\rho = \rho_{\text{c,d}} / \rho_{\text{c,a}}$, the outcome is a cold, slowly rotating, degeneracy-supported remnant core, which is essentially unaffected by the merger, surrounded by a hot, roughly spherical envelope and, further out, by a sub-Keplerian disk. For a similar-mass merger, with high q_ρ , an ellipsoidal core is produced along with a small disk, and the entire remnant is hot and partly supported by rotation. The transition between these two regimes is smooth, but occurs roughly at $q_\rho \simeq 0.6$, or equivalently a mass difference $\Delta M = M_{\text{a}} - M_{\text{d}} \simeq 0.1$. We found that for a fixed q_ρ , merger remnant curves are roughly homologous. We also presented trends for a number of merger remnant properties, providing linear scaling relations and best fits for most of them, hoping these can guide theoretical understanding and help analytical estimates.

We made first-order estimates of the post-merger viscous evolution and spindown, and found that it is plausible that a large fraction of the mergers simulated will eventually experience a nuclear runaway, as was suggested by [vK10](#), and thus possibly end as thermonuclear supernovae. Further, detailed, simulations of this evolution across the whole parameter space, using techniques similar to those of [Shen et al. \(2012\)](#) and [Schwab et al. \(2012\)](#), would be required to confirm this. If the evolution of these remnants results in a detonation, a detailed comparison of the resulting light curve with observations must be carried out.

Our work represents one of the most detailed parameter studies of WD mergers to date. It would benefit, however, from resolution of a number of topics. First, for greater precision, it will be necessary to use better initial conditions. For synchronized systems, it is already known this has nontrivial effect on the outcome ([Dan et al. 2011; 2012](#)), and our results suggest it is important also for non-synchronized systems. Unfortunately, for the non-synchronized case, it is not trivial to implement the initial conditions, but better approximations are possible. Second, it would be useful to try to compare with merger simulations done with a grid code, which should have become more straightforward now that good moving mesh codes have become available ([Springel 2010a](#); [Duffell & MacFadyen 2011](#)). More generally, whether or not WDs are synchronized before the merger remains unknown, yet clearly affects the resulting merger. Hopefully, this can be resolved empirically, by measuring the spin frequency for WDs in the very short-period binaries that have recently been discovered (e.g., [Brown et al. 2011](#)).

We thank Pablo Lorén-Aguilar, Enrique García-Berro, Stuart Sim, Enrico Ramirez-Ruiz, Marius Dan, James Guillochon, Evan Scannapieco, Cody Raskin and Ken Shen for insight into their simulations and useful discussion on the physics of mergers and post-merger evolution. We are grateful to Frank Timmes for creating the Helmholtz equation of state, and assisting us with its implementation in Gasoline, as well as to Bill Paxton and the MESA team for creating MESA and making it modular. This work made extensive use of NASA’s ADS and was supported by the Vanier and Discovery grants of Canada’s Natural Sciences and Engineering Research Council (NSERC).

2.8 Postscript: Post-Merger Evolution Revisited

Since the publication of Ch. 2 as [Z13](#), others have done work on the viscous evolution of merger remnants. [Raskin et al. \(2014\)](#) uses the machinery of [Schwab et al. \(2012\)](#) to generate post-viscous remnant profiles for massive (mostly dissimilar-mass) mergers with $> 0.9 M_\odot$ accretors, to determine their nucleosynthetic output if they then experienced a pure detonation. They do not discuss their viscous simulations in detail. Also published was [Ji et al. \(2013\)](#), a work of particular relevance to our

investigations not only because they simulate the post-merger evolution of an equal-mass $0.6 - 0.6 M_{\odot}$ remnant, but also because they eschew the use of an α -viscosity and instead directly evolve the magnetic field of the merger remnant. We have not performed our own post-merger evolution simulations¹², and use Schwab et al. (2012) and Ji et al. (2013)'s results extensively throughout this thesis. Since this thesis has no dedicated chapter on post-merger evolution, we expand and update the discussion in Sec. 2.6.1 below with Ji et al. (2013)'s results.

Ji et al. (2013) run 2.5D magnetohydrodynamic simulations with the Eulerian grid code FLASH (Fryxell et al. 2000), using the $0.6 - 0.6 M_{\odot}$ remnant of LIG09 as initial conditions. They utilize a axisymmetric cylindrical grid and the Helmholtz EOS. Since LIG09's remnants are unmagnetized, they artificially insert a purely poloidal magnetic field whose strength is $\sim 10^8$ G in the remnant disk, and $\lesssim 10^5$ G in the core (they determine their results are robust to changing initial field strength and spatial resolution by factors of 2). They advance their simulation to 2×10^4 s, comparable to the completion times in Schwab et al. (2012). They find that the magnetorotational instability (MRI) acts on the differentially rotating portions of the remnant to greatly amplify the field over several hundred seconds, until it reaches equilibrium with a peak field strength of $\sim 10^9$ G in the disk and $\gtrsim 10^{10}$ G in the core, as well as a total magnetic energy of $\sim 10^{48}$ erg, on par with the differential rotation energy of the system (see Ch. 4). This field produces Maxwell stresses that are roughly equivalent to an $\alpha \sim 10^{-2}$ viscosity, facilitating global outward angular momentum transport like in Schwab et al. (2012). It also generates a hot, magnetized corona by displacing disk material through magnetic buoyancy, and a biconal outflow along the remnant's rotational axis. These outflows eject $10^{-3} M_{\odot}$ of material at roughly twice the local escape speed (of ~ 1600 km s $^{-1}$).

Much like Schwab et al. (2012), Ji et al. (2013) find that the remnant loses most of its rotational support and evolves toward a spherically symmetric state with a dense, degeneracy-supported core and a more tenuous thermally-supported envelope. By the end of the simulation $\sim 0.08 M_{\odot}$ of material either resides in the magnetically dominated corona or has left the simulation domain, leaving $1.12 M_{\odot}$ remaining in the remnant, with $1.07 M_{\odot}$ of this residing within $r = 1.5 \times 10^9$ cm in the dense core (Suoqing Ji and Robert Fisher private communication, 2016). Accretion onto and loss of rotational support within the core leads to its center being compressionally heated by a factor of ~ 2.5 in density and ~ 2 in temperature. As their initial conditions are a factor of ~ 2 hotter than our $0.6 - 0.6 M_{\odot}$ remnant (Sec. 2.5.1), this additional compression ignites central nuclear fusion.

We can compare the results of Ji et al. (2013), along with Schwab et al. (2012), to our simple estimates of viscous evolution in Sec. 2.6.1. The most relevant quantities are the density and temperature at the center and at the hottest point of the post-viscous remnant, to determine whether carbon fusion ignites under highly degenerate conditions and the amount of material that remains a part of the dense, degeneracy-dominated remnant core. The latter is important for comparing against simmering WDs in Chapter 5. As stated in Sec. 2.6.1, we estimate the hottest point within our $0.6 - 0.9 M_{\odot}$ remnant increases by a factor of 2.5 in density and 1.6 in temperature, very similar to Schwab et al. (2012)'s results. The central density of their remnant is 1.75×10^7 g cm $^{-3}$ at the start of viscous evolution (Dan et al. 2011) and 2.8×10^7 g cm $^{-3}$ at the end – a factor of 1.6 increase, while we find a factor of 2.0. We tend to estimate much larger amounts of compressional heating for similar-mass systems, however, finding that the $0.6 - 0.6 M_{\odot}$ one increases its central density and temperature by a factor of 6.6 and 2.7,

¹²We experimented with FLASH-based 2.5D simulations that included an α -viscosity, but did not follow up with a detailed investigation.

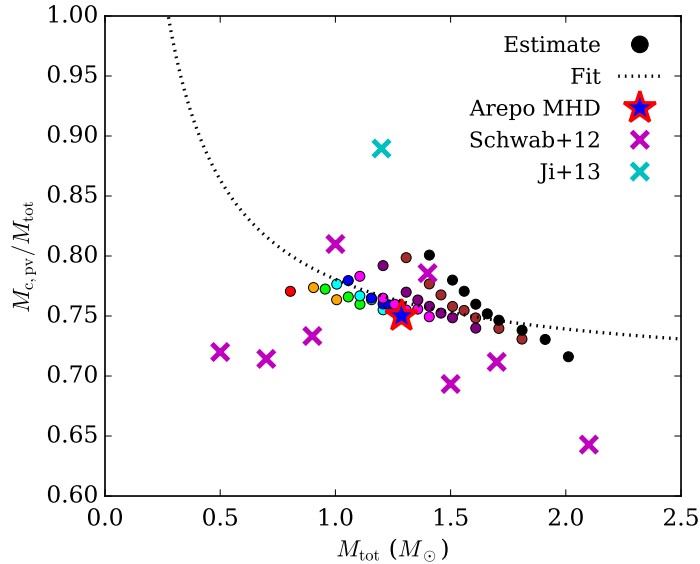


Figure 2.19: Ratio of post-viscous degenerate core mass $M_{\text{c,pv}}$ – estimated using the simple viscous evolution prescription in Sec. 2.6.1 – to the remnant total mass M_{tot} as a function of M_{tot} for the systems simulated in this chapter (“Estimate” points; colors have the same meaning as in Fig. 2.17) and the $0.625 - 0.65 M_{\odot}$ remnant from the AREPO MHD simulation (Ch. 4; red-blue star). Also plotted are estimates of $M_{\text{c,pv}}/M_{\text{tot}}$ from Schwab et al. (2012; using $M_{\text{c}} + M_{\text{tp}}$ in their Table 3) with magenta Xs and Ji et al. (2013) with a cyan X. The dotted line is a best fit to the Estimate points given by Eqn. 2.27.

respectively, substantially larger than those found by Ji et al. (2013). Similarly, Raskin et al. (2014) find the central density of their $1.0 - 1.0 M_{\odot}$ remnant increases from $7.1 \times 10^7 \text{ g cm}^{-3}$ to $2.4 \times 10^8 \text{ g cm}^{-3}$, a much smaller compression than the factor of ~ 13 we find. This is likely because our simple estimates assume all rotational energy is deposited as heat solely in the outermost regions of the remnant, while in reality remnants, particularly those of similar mass, are rotationally supported throughout and thus will likely also be heated throughout during viscous evolution, reducing the amount of core compression and associated compressional heating. We also note Ji et al. (2013)’s remnant also has not fully lost core rotational support at the end of their simulation¹³, still having $\Omega_c \approx 0.15 \text{ s}^{-1}$. We conclude our estimates are reasonable for dissimilar-mass systems, but overestimate by a factor of a few the degree of compression and heating in similar-mass ones.

In our simple estimate, the mass of the post-viscous core, $M_{\text{c,pv}}$, is given by the mass of the spherically symmetric hydrostatic model representing the spun-down remnant (Sec. 2.6.1). In Fig. 2.19, we plot the ratio of $M_{\text{c,pv}}$ to the total mass M_{tot} of the merging binary, as well as a linear fit to the $M_{\text{c,pv}}$ vs. M_{tot} relationship,

$$M_{\text{c,pv}} = 0.70M_{\text{tot}} + 0.08 M_{\odot}. \quad (2.26)$$

We also perform our estimate on the $0.625 - 0.65 M_{\odot}$ remnant from our AREPO (Springel 2010a) MHD simulation in Ch. 4, and find little difference from its GASOLINE counterpart. For Schwab et al. (2012), we estimate $M_{\text{c,pv}}$ as the combined mass of the core and isothermal region ($M_{\text{c}} + M_{\text{tp}}$) in their Table 3.

¹³We do not know if the same is true for Raskin et al. (2014)’s simulations. Ji et al. (2013) additionally note the central temperature at the end of evolution has not converged, increasing by $\sim 20\%$ with spatial resolution.

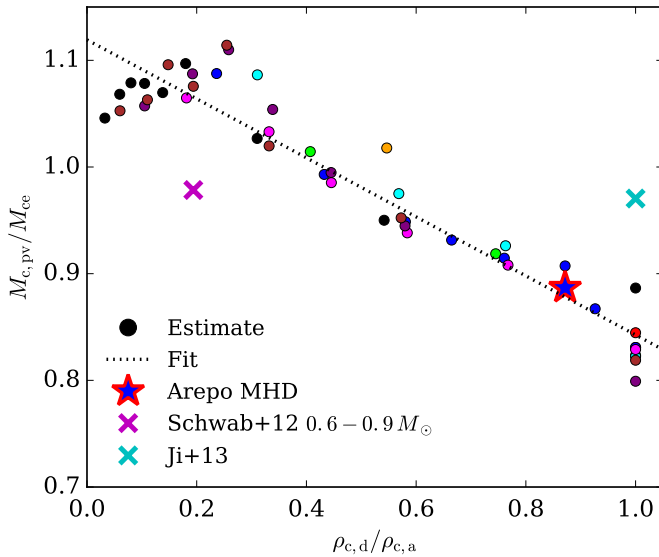


Figure 2.20: Ratio of post-viscous degenerate core mass $M_{c,pv}$ to remnant core-envelope mass M_{ce} (Sec. 2.3.2.3) as a function of q_ρ for the systems simulated in this chapter (“Estimate” points), the $0.625 - 0.65 M_\odot$ remnant from the AREPO MHD simulation (red-blue star), the $0.6 - 0.6 M_\odot$ remnant of Ji et al. (2013; cyan X) and the $0.6 - 0.9 M_\odot$ remnant of Schwab et al. (2012; magenta X). The dotted line is a best fit to the Estimate points given by Eqn. 2.27.

We find these follow the overall pattern of our estimates, but tend to be $\sim 0.07 M_\odot$ below it. For Ji et al. (2013), $M_{c,pv} \approx 1.07 M_\odot$ (see above), which is $\sim 0.15 M_\odot$ above our estimate. Our estimate therefore only roughly reproduces (with errors of $\sim 0.1 M_\odot$) the amount of mass remaining in the post-viscous core, partly because the assumption that material not in the core is marginally bound with $E = 0$ is overly simplistic, and partly because $M_{c,pv}$ is somewhat difficult to define in a system that may be supported by both degeneracy and thermal pressure.

In Fig. 2.20, we plot the ratio of $M_{c,pv}$ to the core-envelope mass M_{ce} of the merger remnant (Sec. 2.3.2.3) as a function of q_ρ , as well as a linear fit to the $M_{c,pv}/M_{ce}$ vs. q_ρ relationship,

$$\frac{M_{c,pv}}{M_{ce}} = -0.28q_\rho + 1.12 \quad (2.27)$$

We use the $0.6 - 0.6 M_\odot$ remnant core mass ($1.1 M_\odot$) from Lorén-Aguilar et al. 2009 for the M_{ce} of the Ji et al. (2013). The core masses of the remnants used in Schwab et al. (2012) are not reported, so for their $0.6 - 0.9 M_\odot$ remnant (the sole system which overlaps with our parameter space) we substitute with our own M_{ce} .

Figs. 2.19 and 2.20 show that, in all estimates of the viscous spin-down phase, a significant fraction of the total remnant mass is not accreted onto the core during viscous evolution. For similar-mass mergers, both Ji et al. (2013)’s simulation and our estimate suggest that the entire disk and a small amount of the core and envelope end up as a part of the hot envelope, leaving the core with slightly less mass than it had just after coalescence. This runs counter to vK10’s assumption that the most of the disk will rapidly accrete onto the remnant, and explains why the increases in density and temperature during viscous evolution reported in this section are all a factor of a few smaller than that given in

vK10.

For those systems that do not ignite nuclear fusion during the viscous phase, their next stage of evolution involves entropy being transported via neutrino cooling and radiative diffusion throughout and away from the remnant. Since the remnant hot envelope ($\rho \lesssim 10^4 \text{ g cm}^{-3}$, $T \sim 10^9 \text{ K}$) is radiation-dominated, it has a near-Eddington luminosity, and thermal evolution will occur over a timescale (Shen et al. 2012)

$$t_{\text{therm}} \sim E_{\text{th, envelope}} / L_{\text{edd}} \sim 10^4 \text{ yr.} \quad (2.28)$$

(For those systems that do ignite fusion, the nuclear runaway time is $\lesssim 10^2 \text{ yr}$, so this evolution will only occur to a very limited extent.) Shen et al. (2012) simulates this phase of thermal evolution using the MESA (Paxton et al. 2011; 2013; 2015) stellar evolution code, starting with an artificial radial profile that approximates their $0.6 - 0.9 M_\odot$ post-viscous remnant. Notably, they set the peak temperature at the base of the hot envelope (at $m \sim 0.9 M_\odot$) below the carbon ignition line. They find the entropy from the remnant interior diffuses outward over $\sim 10^4 \text{ yr}$, leading to the further compression and heating of the interior until carbon fusion ignites at the (non-degenerate) base of the envelope. Meanwhile, convection rapidly redistributes entropy to much of the envelope, expanding it until its photosphere reaches $10^{12} - 10^{13} \text{ cm}$, comparable to giant stars. They predict that their remnant will be converted into an ONe WD, much like in earlier calculations of near-Eddington accretion onto massive WDs (eg. Saio & Nomoto 1985).

More recently, Schwab et al. (2016) have used MESA to simulate the thermal evolution of their post-viscous $0.6 - 0.9 M_\odot$ remnant from Schwab et al. (2012), and a more massive $0.64 - 0.96 M_\odot$ one from Raskin et al. (2014). The peak temperatures of both remnants are already high enough to ignite carbon at the start; this generates a carbon-burning shell that propagates inward via conduction, reaching the center of the WD in $\sim 2 \times 10^4 \text{ yr}$. The result is a partly non-degenerate ONe proto-WD, which subsequently cools through neutrino losses and contracts. For remnants with masses $\gtrsim 1.35 M_\odot$, this leads to off-center *oxygen-neon* burning to silicon-group elements, and for super- M_{Ch} remnants, may even lead to fusion to iron followed by core-collapse into a neutron star. For substantially sub- M_{Ch} remnants that ignite non-explosive carbon burning, though, the likely end-result is a massive ONe WD. The radiation-dominated envelope alongside the remnant's carbon-oxygen composition suggest that the remnant drives strong winds, complicating the thermal evolution and potentially leading to considerable mass loss (Shen et al. 2012; Schwab et al. 2016).

Thermal evolution of post-viscous remnants that are hottest at their *center* have, to our knowledge, not yet been calculated. We expect it would be qualitatively similar to what Shen et al. (2012) and Schwab et al. (2016) found for their dissimilar-mass remnants: a further compression of the interior over $\sim 10^4 \text{ yr}$, with compressional heating partially offset by radiative and neutrino cooling. We thus expect that systems brought to the brink of ignition by viscous spin-down may subsequently ignite due to thermal contraction, though the number of such systems is likely small. Those whose central temperatures are significantly below $6 \times 10^8 \text{ K}$ will cool too much during their compression to ignite; since neutrino cooling is density-dependent, they may experience off-center ignition instead.

Chapter 3

Mergers in Smoothed-Particle and Moving Mesh Hydrodynamics

Chenchong Zhu, Rüdiger Pakmor, Marten H. van Kerkwijk, Philip Chang

The physics and final outcomes of the merger of two white dwarfs can currently only be directly studied through 3D hydrodynamic simulations, and to date merger simulations have largely relied on smoothed-particle hydrodynamics, a method known to produce numerical artefacts under certain conditions. In order to determine if the outcome of these simulations depends on the code being used, we followed the merger of a $0.625 - 0.65 M_{\odot}$ carbon-oxygen white dwarf binary in both the SPH code GASOLINE and the moving mesh code AREPO. We find that the two agree well with one another until the merger is complete. Afterward, the merger remnant becomes axisymmetric over the course of a few hundred seconds in GASOLINE, with most of its mass comprising a dense, oblate-spheroidal core. The remnant in AREPO, on the other hand, remains non-axisymmetric and features a crescent-shaped core flanked on one side by a hot, underdense “void”. This configuration has an offset gravitational potential, which launches an $m = 1$ spiral mode within the surrounding disk that transports disk angular momentum over a timescale of $\sim 10^3$ s, substantially faster than suggested by other post-merger evolution studies. These code-dependent differences could affect the early phase of post-merger viscous evolution. The final product of the merging process, however, likely remains a spherically symmetric dense core surrounded by a hot, non-degenerate envelope, regardless of which code is used.

3.1 Introduction

Simulations of white dwarf (WD) mergers are a window into the detailed dynamics of the merging process and – since mergers cannot directly be seen using current observational capabilities – a link between observations of strange stars and explosive transients and theories about their formation. Since the pioneering work of Benz et al. (1990), these simulations have overwhelmingly used a single numerical hydrodynamics implementation, smoothed-particle hydrodynamics (SPH). Within SPH, regions of high density are automatically more resolved and advection is simulated without errors; its equations of motion also inherently conserve energy, linear and angular momentum. These features make it attractive for modeling the complex fluid flows present in mergers. Building on Benz et al. and other early works such as Segretain et al. (1997) and Guerrero et al. (2004), more recent efforts have focused on more precise binary initial conditions (Dan et al. 2011), exploration of remnant properties across parameter space (Ch. 2; Lorén-Aguilar et al. 2009; Raskin et al. 2012; Dan et al. 2014) and exploring the possible instigation and consequences of a nuclear explosion caused by the merger (eg. Pakmor et al. 2010; Dan et al. 2012; Pakmor et al. 2013; Moll et al. 2014; Raskin et al. 2014).

The traditional SPH formulation, however, is not without its problems (eg. Springel 2010a; Hopkins 2015): to be able to capture shocks, it uses an artificial viscosity, which can produce spurious heating and angular momentum transport in shear flows; it is known to suppress hydrodynamic instabilities; and it captures shocks and steep gradients relatively poorly compared to other schemes at the same resolution. Shocks, large-scale shear flows and the formation of instabilities are all expected for WD mergers, and comparisons between SPH and Eulerian grid codes for other astrophysical phenomena (eg. de Val-Borro et al. 2006; Trac et al. 2007; Mitchell et al. 2009) have often shown qualitative and resolution-independent differences. Reproducing simulations across different types of codes is essential both for the development of numerical hydrodynamic schemes and for ensuring the physical validity of their results, and so we are motivated to simulate mergers with other hydrodynamic schemes.

A recent alternative to SPH, as well as Eulerian grid codes, is AREPO (Springel 2010a), one of a growing class of codes (eg. Duffell & MacFadyen 2011; Gaburov et al. 2012; Vandenbroucke & De Rijcke 2016) that render fluid evolution on a dynamically moving, unstructured mesh. AREPO retains the accurate treatment of shocks and instabilities as well as low velocity noise and negligible artificial viscosity in smooth flows that Eulerian grid codes feature, while gaining the automatic refinement and Galilean invariance inherent to SPH. These features, coupled with a tree-based self-gravity solver, make it particularly attractive for astrophysical simulations (eg. Vogelsberger et al. 2012; Pakmor & Springel 2013; Hayward et al. 2014; Marinacci et al. 2014; Ohlmann et al. 2016), and, with the notable exception of formal angular momentum conservation, ideal for simulating WD mergers. Pakmor et al. (2013) has already used AREPO to investigate initial mass transfer, and the possibility that transfer sets off a helium detonation, in a $0.9 - 1.1 M_{\odot}$ CO WD merger.

In this work, we compare the merger of a $0.625 - 0.65 M_{\odot}$ carbon-oxygen (CO) WD binary simulated in AREPO with one simulated in the SPH code GASOLINE (Wadsley et al. 2004). We generate identical initial conditions for both simulations, and disable chemical and nuclear evolution to focus solely on the hydrodynamic differences, aiming to learn whether critical hydrodynamic phenomena might have been missing or misrepresented in past SPH-based merger simulations. Our results show that the two simulations closely resemble one another until the two WDs coalesce, after which the GASOLINE merger remnant becomes axisymmetric over several hundred seconds, while the AREPO one remains

asymmetric for much longer, potentially altering post-merger evolution.

In Section 3.2, we review the hydrodynamic schemes of SPH and AREPO, and discuss the parameters and initial conditions used in each simulation. In Section 3.3, we summarize efforts to improve angular momentum conservation within AREPO. In Section 3.4, we present results for each code and compare their outcomes. Lastly, in Sections 3.5 and 3.6, we discuss which code represents the more physical result, and implications for mergers.

3.2 Codes and Initial Conditions

All hydrodynamic and magnetohydrodynamic codes seek to properly evolve the continuum dynamics of a fluid on a discrete set of points in space and time. Most astrophysical fluid codes (including the two we use) explore the simpler regimes of ideal hydro- or magnetohydrodynamics, where molecular viscosity and electrical resistance are negligible, as such is generally the case in astrophysical settings outside of planetary interiors. The coupled partial differential equations of ideal magnetohydrodynamics, in their conservative form and with Gaussian units (eg. Goedbloed & Poedts 2004; Pakmor & Springel 2013; Spruit 2013, Feiden & Chaboyer 2012 Sec. 3), is

$$\begin{aligned} \partial_t \rho + \partial_j(\rho u^j) &= 0 \\ \partial_t(\rho u^i) + \partial_j(\rho u^i u^j + \delta^{ij} P_{\text{tot}} - \frac{1}{4\pi} B^i B^j) &= -\rho \partial^i \Phi \\ \partial_t(\rho e) + \partial^j \left(u_j (\rho e + P_{\text{tot}}) - \frac{B_j}{4\pi} (u^l B_l) \right) &= -u_j \rho \partial^j \Phi \\ \partial_t B^i + \partial_j(u^j B^i - u^i B^j) &= 0, \end{aligned} \quad (3.1)$$

where ρ , u^i , B^i , and Φ are the density, velocity, magnetic field and gravitational potential, respectively, $P_{\text{tot}} = P + \frac{1}{8\pi} B_j B^j$ is the total pressure, $e = \frac{1}{2} u_i u^i + e_{\text{int}} + \frac{1}{8\pi\rho} B_j B^j$ is the specific total energy, and the usual Einstein summation convention holds. This can be written in compact form:

$$\frac{\partial \mathbf{U}}{\partial t} + \nabla \cdot \mathbf{F}(\mathbf{U}) = \mathbf{G} \quad (3.2)$$

where

$$\mathbf{U} = \begin{pmatrix} \rho \\ \rho \mathbf{u} \\ \rho e \\ \mathbf{B} \end{pmatrix}, \quad (3.3)$$

$$\mathbf{F}(\mathbf{U}) = \begin{pmatrix} \rho \mathbf{u} \\ \rho \mathbf{u} \mathbf{u}^T + P_{\text{tot}} - \frac{1}{4\pi} \mathbf{B} \mathbf{B}^T \\ \mathbf{u}(e + P_{\text{tot}}) - \frac{\mathbf{B}}{4\pi} (\mathbf{u} \cdot \mathbf{B}) \\ \mathbf{B} \mathbf{u}^T - \mathbf{u} \mathbf{B}^T \end{pmatrix}, \quad (3.4)$$

$$\mathbf{G} = \begin{pmatrix} 0 \\ \rho\mathbf{g} \\ \rho\mathbf{u} \cdot \mathbf{g} \\ 0 \end{pmatrix}, \quad (3.5)$$

and $\mathbf{g} = -\nabla\Phi$ is the gravitational acceleration. Eqn. 3.2 shows that the time-derivative of the fluid's values is given by the sum of a flux term (since, by the Green-Gauss theorem, the integral of $\nabla \cdot \mathbf{F}(\mathbf{U})$ within a volume is equivalent to a flux across its boundary) and a (self-)gravitational source term \mathbf{G} . These are generally calculated separately, and then combined.

To better understand the code comparison in this chapter, and to preface the discussion of improving AREPO's angular momentum conservation in Sec. 3.3, we present an extremely short and semi-qualitative discussion of how these equations are implemented within SPH and AREPO. The historical development of both methods is long and involved, and, as improving hydrodynamic simulations is not the focus of this thesis, we will refer the reader to a number review articles referenced throughout this section for further details.

3.2.1 Traditional Smoothed-Particle Hydrodynamics

SPH, first introduced in [Lucy \(1977\)](#) and [Gingold & Monaghan \(1977\)](#), is a mature simulation method used in a host of astrophysical contexts ranging from star formation to cosmology. Our overview summarizes the first few sections of ([Springel 2010b](#)); we also refer readers to [Monaghan \(2005\)](#) and [Rosswog \(2009\)](#) for further details.

SPH represents a fluid with a set of particles. The fluid's continuum properties at some point \mathbf{r} in the simulation are sampled by using these particles as interpolation points. Representing any given continuum property (the most important of which is density, since it factors into the equations of motion) as $F(\mathbf{r})$, we can use a “kernel” $W(\mathbf{r}, h)$ to generate its approximate, locally-averaged value

$$F_s(\mathbf{r}) = \int F(\mathbf{r}') W(\mathbf{r} - \mathbf{r}', h) d\mathbf{r}'. \quad (3.6)$$

In the (computationally impossible) case of infinite resolution, we can choose $W(\mathbf{r}, h)$ to be a Dirac delta, and $F_s(\mathbf{r}) = F(\mathbf{r})$, but in practice we choose $W(\mathbf{r}, h)$ to extend over some characteristic “smoothing length” h . If $W(\mathbf{r}, h)$ were a Gaussian, $h = \sigma$, the standard deviation. The most popular form of $W(\mathbf{r}, h)$ is a cubic spline that goes to zero when $\mathbf{r} > 2h$, and h is generally set to ensure a user-defined number of neighboring particles N fall within the kernel. For a set of particles with associated mass m_i and known values of $F_i = F(\mathbf{r}_i)$, we can discretize the integral as

$$F_s(\mathbf{r}) = \sum_j \frac{m_j}{\rho_j} F_j W(\mathbf{r} - \mathbf{r}_j, h). \quad (3.7)$$

where ρ_i can be estimated using

$$\rho_i = \sum_j m_j W(\mathbf{r}_i - \mathbf{r}_j, h) \quad (3.8)$$

Derivatives of the field can also be determined using the gradient of the kernel $\nabla_i W_{ij}$.

Meanwhile, the Euler equations (Eqn. 3.2 without the gravitational and magnetic terms) can be shown to follow the Lagrangian:

$$L = \int \rho \left(\frac{\mathbf{u}^2}{2} - e \right) dV \quad (3.9)$$

which can be discretized for a set of particles as

$$L_{\text{SPH}} = \sum_i \frac{1}{2} m_i u_i^2 - m_i e_i. \quad (3.10)$$

This suggests a time-evolution scheme for the fluid. Each particle representing the fluid is given a (time-independent) mass m_i , position \mathbf{r}_i , velocity \mathbf{u}_i and specific internal energy e_i ; the fluid can then be simulated by time-evolving the latter three terms for all particles. The equations governing \mathbf{u}_i and e_i are derived by applying the Euler-Lagrange equation ($\frac{d}{dt} \frac{\partial L}{\partial \dot{\mathbf{r}}_i} - \frac{\partial L}{\partial \mathbf{r}_i} = 0$) to L_{SPH} . They traditionally take the form:¹

$$\frac{d\mathbf{u}_i}{dt} = - \sum_j m_j \left(\frac{P_i}{\rho_i^2} + \frac{P_j}{\rho_j^2} \right) \nabla_i W_{ij} \quad (3.11)$$

$$\frac{de_i}{dt} = \frac{P_i}{\rho_i^2} \sum_j m_j (\mathbf{u}_i - \mathbf{u}_j) \cdot \nabla_i W_{ij} \quad (3.12)$$

where pressure P_i is determined from ρ_i and e_i using a user-prescribed equation of state. The left panel of Fig. 3.1 summarizes this scheme. Note that since Eqn. 3.9 has no time-dependence and is translationally and rotationally invariant, SPH naturally conserves total energy, momentum and angular momentum. Self-gravity can be added as an additional force to Eqn. 3.11 (see Springel 2010b, Sec. 2.4, and Wadsley et al. 2004, Sec. 2.1) using methods originally developed for N -body simulations. Magnetic fields can also be included (eg. Price 2012; Lewis et al. 2016), but the resulting “SPHMHD” formulation is not used in this thesis.

As given, the SPH equations of motion conserve entropy, but entropy must increase in the presence of shocks. The most popular solution is to add an artificial viscosity term

$$- \sum_j m_j \Pi_{ij} \nabla_i W_{ij} \quad (3.13)$$

to Eqn. 3.11, where, defining $\mathbf{r}_{ij} = \mathbf{r}_i - \mathbf{r}_j$ and $\mathbf{u}_{ij} = \mathbf{u}_i - \mathbf{u}_j$,

$$\Pi_{ij} = \begin{cases} \frac{-\alpha \frac{1}{2} (c_i + c_j) \mu_{ij} + \beta \mu_{ij}^2}{\frac{1}{2} (\rho_i + \rho_j)} & \text{for } \mathbf{u}_{ij} \cdot \mathbf{r}_{ij} < 0 \\ 0 & \text{otherwise,} \end{cases} \quad (3.14)$$

where $\mu_{ij} = \bar{h} \mathbf{u}_{ij} \cdot \mathbf{r}_{ij} / (|\mathbf{r}_{ij}|^2 + 0.04 \bar{h}^2)$, $\bar{h} = \frac{1}{2}(h_i + h_j)$, c_i is the sound speed and α and β are tunable parameters ($\beta = 2\alpha$ is used in GASOLINE). In addition to facilitating shock capture, Π_{ij} also prevents spurious particle interpenetration between interacting flows (Hernquist & Katz 1989). It, however, can also introduce spurious viscous forces, and so must be damped in the absence of shocks. In shear flows, this can be done with a “Balsara switch”, which multiplies Π_{ij} with a prefactor, proportional to

¹We state Wadsley et al. (2004)’s formulation of Eqns. 3.11 and 3.12, as Springel (2010b) assumes a different method of controlling the smoothing length h_i .

the ratio between the divergence and curl of velocity, that goes to zero in the presence of a pure shear flow. It is also possible to make the α and β coefficients in Π_{ij} time-variable (eg. Morris & Monaghan 1997; Dolag et al. 2005) with

$$\frac{d\alpha_i}{dt} = -\frac{\alpha_i - \alpha_{\min}}{\tau_i} + S_i \quad (3.15)$$

where $\tau_i = h_i/(c_i l)$, l is a tunable parameter of order unity, S_i is a source term that becomes large in the presence of shocks, and $\alpha_{\min} > 0$ is a minimum α value to negate noise and spurious particle interpenetration in smooth flows. Eqn. 3.15 exponentially damps α_i to its minimum value over timescale τ_i in the absence of shocks, and increases it via the source term when shocks are present. Both these methods are used in GASOLINE.

As explained in the introduction, SPH’s Lagrangian nature allows it to automatically resolve regions of high density, simulate advection without errors, and conserve energy, linear and angular momentum to high accuracy. These features make it much easier to model mergers in SPH than in Eulerian grid schemes, which discretize the simulation volume on a static grid, and time-evolve the system by tracking fluid fluxes between grid cells. These traditionally have issues with simulating advection and adaptively increasing the spatial resolution ahead of moving fluids, such as orbiting binary stars, except under specific coordinate systems and symmetries. Thus, they have rarely been used to simulate WD mergers (see Katz et al. (2016) for recent developments).

The limitations of SPH (and Eulerian codes) have also been well-covered in literature (see, eg., the introductions to Springel 2010a; Hopkins 2015; Katz et al. 2016). Chief among them is the artificial viscosity discussed above, which can produce spurious heating and angular momentum transport in shear flows even in codes that utilize the Balsara switch and time-variable viscosity (Cullen & Dehnen 2010). Classical formulations of SPH have also been known to suppress hydrodynamic instabilities (eg. Agertz et al. 2007) due to poor treatment of contact discontinuities manifesting as a “surface tension” (eg. Read et al. 2010; Heß & Springel 2010). While this has subsequently been resolved (eg. Hopkins 2013; Hu et al. 2014; Keller et al. 2014) by introducing artificial mixing terms (Price 2008) and smoothing the pressure as well as the density across discontinuities (eg. by replacing the $P_i/\rho_i^2 + P_j/\rho_j^2$ term in Eqn. 3.11 with $(P_i + P_j)/(\rho_i\rho_j)$; Keller et al. 2014) the vast majority of merger simulations in the literature come from before these alterations became widely used. SPH resolves shocks and steep gradients relatively poorly compared to Eulerian schemes due to kernel smoothing of the density, and can corrupt smooth flows with particle velocity noise (Springel 2010b). Lastly, SPH particles naturally tend toward a locally isotropic and regular configuration (Price 2012), and in physical systems where they are irregularly distributed, such as in shear flows and after shocks, Eqn. 3.11 produces spurious forces to restore regularity (eg. Read et al. 2010; Dehnen & Aly 2012). In some situations, this resolution-independent “ E_0 error” produces enough noise to drown out large-scale structures (Hopkins 2015). All of these issues motivate both the further development of SPH and competing hydrodynamic schemes, and simulating mergers in a diversity of codes.

3.2.2 GASOLINE SPH Code

GASOLINE is a modular, tree-based SPH code that we previously used to explore the parameter space of CO WD mergers in Ch. 2. Code settings and initial conditions used in this work are nearly identical to those used in Ch. 2. We utilize GASOLINE’s default Hernquist & Katz (1989) kernel with 100 neighbors,

and use the asymmetric energy formulation (Wadsley et al. Eqn. 8) to evolve particle internal energy. Artificial viscosity is dynamically controlled using a combination of the Balsara switch and time-variable coefficients for the α and β viscosity terms ($\alpha = 0.05$, $\beta = 0.1$ when shocks are not present, and approximately unity when they are). We utilize the Helmholtz equation of state (EOS; Timmes & Swesty 2000) to properly represent arbitrarily degenerate and relativistic gases. Since GASOLINE tracks the particle internal energy, while Helmholtz uses temperature as an input, a Newton-Raphson inverter is included in the EOS to determine the latter from the former. To keep the energy-temperature relation positive-definite for the inverter, we enable Coulomb corrections even when the total entropy becomes negative. SPH noise occasionally brings highly degenerate particles to below the Fermi energy. Under these conditions we set the pressure to the Fermi pressure, but let the energy freely evolve (see Sec. 2.2.1).

Like in our previous work, we ignore outer hydrogen and helium layers, composition gradients, and any nuclear reactions, in order to focus on the merger hydrodynamics. Previous work that did include nuclear reactions (Lorén-Aguilar et al. 2009; Dan et al. 2012), and in one case an outer helium layer (Raskin et al. 2012), have shown that they play a negligible role in the hydrodynamics of a $0.625 - 0.65 M_{\odot}$ CO WD merger. More massive binaries, as well as less massive ones involving a CO-He hybrid WD, may experience He or CO detonations during the merger (Pakmor et al. 2010; Raskin et al. 2012; Dan et al. 2012; Pakmor et al. 2013).

We use the same version of GASOLINE as in Ch. 2, which does not include the improvements recently introduced in GASOLINE2 (Keller et al. 2015; Tamburello et al. 2015) and CHANGA/GASOLINE (Governato et al. 2015). These include a turbulent diffusion scheme to facilitate fluid mixing (Shen et al. 2010b) and the use of the $(P_i + P_j)/(\rho_i \rho_j)$ density-averaged pressure term in the SPH force expression (Keller et al. 2014) to properly treat contact discontinuities. We also do not consider more advanced prescriptions for viscosity, such as Godunov-SPH (eg. Cha & Wood 2016), as these are generally not implemented in SPH codes. We again stress that the purpose of this work is to compare the traditional SPH formulation, used in almost all merger simulations to date, to AREPO, and we leave comparisons with improved and modified SPH schemes to future work.

3.2.3 AREPO Moving Mesh Code

We now introduce AREPO’s moving-mesh magnetohydrodynamics scheme, summarizing Springel (2010a), Pakmor et al. (2011a) and Pakmor & Springel (2013). AREPO discretizes a fluid using a mesh (i.e. a grid), much like static Eulerian codes. To overcome the traditional Eulerian code shortcomings of not being Galilean invariant, having large advection errors and having difficulty adjusting spatial resolution for complex flows, AREPO moves the mesh to follow local fluid motion. Fluxes between mesh cells are calculated in the frame of the (moving) cell walls that divide them – this preferred frame choice, in addition to the moving mesh, give the scheme a Lagrangian nature and automatic spatial refinement similar to SPH. Allowing a structured grid to move with the fluid can lead to severe mesh deformation that prevent its further evolution. AREPO circumvents this by utilizing an unstructured mesh defined by Voronoi tessellation (see Springel 2010a, Sec. 2) of a set of “mesh-generating points”, each of which corresponds to a single mesh cell. The mesh-generating points are given the velocities of the fluid they represent, and the tessellation is redone at each timestep. The result is a moving mesh that, due to the mathematical properties of Voronoi tessellation, does not suffer from mesh-tangling effects. To keep the Voronoi mesh regular (improving computational efficiency), mesh-generating point

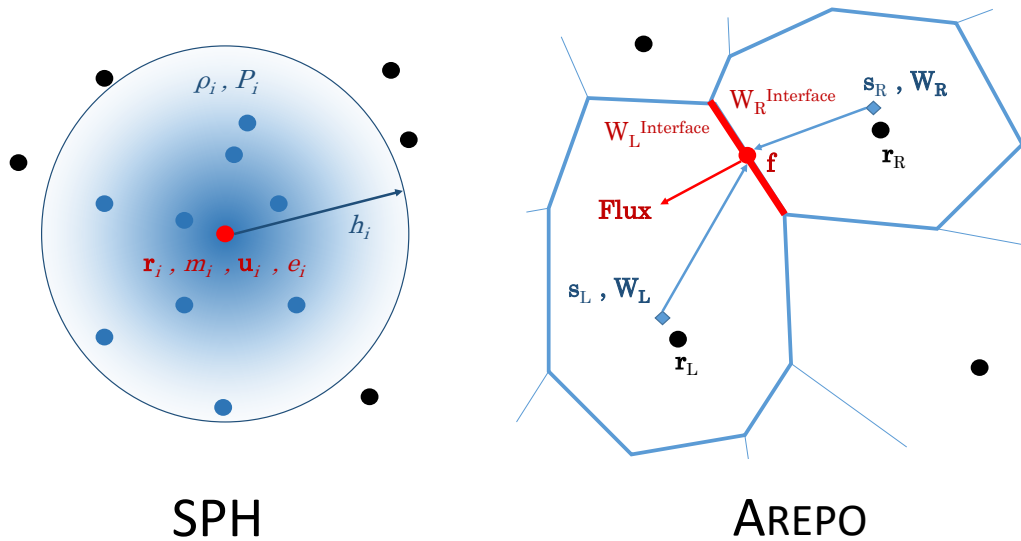


Figure 3.1: Schematics for the SPH and AREPO hydrodynamic schemes. In SPH (left), the fluid is discretized into particles, each of which possesses a position \mathbf{r}_i , mass m_i , velocity \mathbf{u}_i and specific internal energy e_i . The density ρ_i of a given particle (red point) is determined by kernel sampling its neighbors (blue) within a smoothing length h_i (Eqn. 3.8); pressure P_i is then obtained using the density and internal energy. The particle is evolved by kernel sampling nearby pressures and densities, and applying the SPH equations of motion (Eqns. 3.11 and 3.12). In AREPO (right), the fluid is discretized using an unstructured mesh defined by Voronoi tessellation. Each Voronoi cell possesses a mesh-generating point \mathbf{r}_i and a set of conserved quantities equivalent to “primitive variables” $\mathbf{W}_i = (\rho_i, \mathbf{u}_i, P_i, \mathbf{B}_i)$, i.e. the values of density, velocity, pressure and magnetic field amplitude at the cell’s center of mass \mathbf{s}_i . Note that $\mathbf{r}_i \neq \mathbf{s}_i$, but their separation is typically a few percent of the cell’s radius, and has been exaggerated above. Fluxes between two cells L and R are calculated by propagating their primitive variables $\mathbf{W}_{L,R}$ to the centroid of their interface \mathbf{f} to obtain $\mathbf{W}_{L,R}^{\text{interface}}$ (Eqn. 3.19, or Eqn. 3.23 following Pakmor et al. 2016), and then solving the Riemann problem (in the frame of the interface). The mesh is evolved by moving the mesh generating points \mathbf{r}_i at roughly the fluid velocity \mathbf{u}_i , calculating fluxes between all cells, and then updating each cell’s conserved quantities. While evolving an SPH particle requires the use of dozens of its neighbors for kernel averaging, evolving an AREPO cell only requires those neighbors directly adjacent to it.

velocities are slightly altered from their pure Lagrangian values, and additional velocity adjustments can be made to keep cells near a constant mass or volume. This representation of the fluid also couples more naturally to N -body based gravity solvers (see [Springel 2010a](#), Sec. 3), with AREPO using a nearly identical TreePM solver as the SPH code GADGET2 ([Springel 2005](#)).

On the Voronoi mesh, AREPO tracks the finite volume integral of \mathbf{U} (Eqn. 3.3) for each cell, i.e.

$$\mathbf{Q}_i = \int_{V_i} \mathbf{U} dV = \begin{pmatrix} m_i \\ \mathbf{p}_i \\ E_i \\ \mathbf{B}_i V_i \end{pmatrix}, \quad (3.16)$$

where m_i is the cell mass, \mathbf{p}_i its momentum, E_i its total energy and $\mathbf{B}_i V_i$ the magnetic field multiplied by the cell volume. The time-evolution for cell i from timestep n to $n+1$ is then given by

$$\mathbf{Q}_i^{n+1} = \mathbf{Q}_i^n - \Delta t \sum_j A_{ij} \hat{\mathbf{F}}_{ij}^{n+1/2} \quad (3.17)$$

where Δt is the timestep, j stands for all cells that border cell i , A_{ij} is the oriented area of the face dividing cells i and j and $\hat{\mathbf{F}}_{ij}$ is the estimated flux between them (positive flux means escaping from i). In practice fluxes are more easily calculated using primitive variables

$$\mathbf{W}_i = \begin{pmatrix} \rho_i \\ \mathbf{u}_i \\ P_i \\ \mathbf{B}_i \end{pmatrix} \quad (3.18)$$

(i.e. \mathbf{Q}_i/V_i) and then converted back to \mathbf{Q} . As noted earlier, fluxes are calculated in the frame of face A_{ij} to maintain Galilean invariance, so \mathbf{W} on either side of the face – which we term the “left” and “right” cells – are boosted by A_{ij} ’s velocity before being used. The geometry of this setup can be seen in the right panel of Fig. 3.1. In AREPO’s original formulation ([Springel 2010a](#)), the values of $\mathbf{W}^{\text{interface}}$ on the left and right sides of A_{ij} ’s centroid are determined from their respective cell’s \mathbf{W} using the MUSCL-Hancock (eg. [Van Leer 2006](#); MUSCL stands for “Monotonic Upstream-Centered Scheme for Conservation Laws”) approach of a piecewise linear spatial reconstruction and a first-order time-extrapolation by half a timestep:

$$\mathbf{W}_{\text{L,R}}^{\text{interface}} = \mathbf{W}_{\text{L,R}} + \frac{\partial \mathbf{W}}{\partial \mathbf{r}} \Big|_{\text{L,R}} (\mathbf{f} - \mathbf{s}_{\text{L,R}}) + \frac{\partial \mathbf{W}}{\partial \mathbf{t}} \Big|_{\text{L,R}} \frac{\Delta t}{2}, \quad (3.19)$$

where \mathbf{f} is the position of A_{ij} ’s centroid, and \mathbf{s} each cell’s center of mass. We note that the cell center of mass is not identical to the cell’s mesh generating point position \mathbf{r} (Fig. 3.1), but is generally a few percent the radius of the cell. The spatial gradient is estimated by taking advantage of the Green-Gauss theorem. Given some scalar field ϕ , its gradient is given by

$$\langle \nabla \phi \rangle_i = -\frac{1}{V_i} \sum_j \phi(\mathbf{f}_{ij}) \mathbf{A}_{ij}. \quad (3.20)$$

$\phi(\mathbf{f}_{ij})$ is ϕ at A_{ij} ’s centroid, and can be estimated by appealing to the geometric properties of Voronoi cells (see [Springel \(2010a\)](#), Sec 3.1). The temporal gradient is determined by relating it to the spatial

gradient using the Euler equations. Finally, the flux is resolved from $\mathbf{W}_{\text{L},\text{R}}^{\text{interface}}$ with a Riemann solver (in all our simulations, the Harten-Lax-van Leer – Discontinuities, or HLLD, solver; Miyoshi & Kusano 2005). Eqns. 3.19 and 3.20 were replaced in Pakmor et al. (2016) order to resolve AREPO’s angular momentum conservation issue (Sec. 3.3), but the overall flux calculation procedure remains the same as above.

The self-gravity term \mathbf{G} from Eqn. 3.2 can easily be added to the flux calculation, since, when using \mathbf{W} , gravity only changes the momentum. This change, and the corresponding one for kinetic energy, can then be appended to \mathbf{Q} (Springel 2010a, Sec. 5.2).

For the simulations in this chapter, we set $\mathbf{B} = 0$, reducing AREPO to a purely hydrodynamic simulation (Ch. 4 considers the magnetohydrodynamic case). We use the same Helmholtz EOS in AREPO that we installed into GASOLINE and also ignore composition gradients and any nuclear reactions. To assure a reasonably constant mass and volume resolutions, we use an explicit refinement scheme (Vogelsberger et al. 2012) that adds or subtracts mesh-generating points to the grid.

3.2.4 Initial Conditions and Completion Time

Our chosen WD masses are typical of the narrowly peaked empirical mass distribution of field CO WDs (Tremblay & Bergeron 2009; Kleinman et al. 2013). As in Ch. 2, we generated WDs by rescaling a sphere of particles to the proper enclosed mass-radius relation determined from 1D hydrostatic integration. We used a 50% C, 50% O composition by mass uniform throughout the star, and assumed a uniform temperature of 5×10^6 K. The stars were placed into GASOLINE for approximately 11 dynamical times (33.3 s for the $0.625 M_{\odot}$ WD and 31.3 s for the $0.65 M_{\odot}$ WD). Thermal energy and particle velocity were damped to $\sim 5 \times 10^6$ K and 0 cm s^{-1} during the first dynamical time, and left free during the remaining 10. 64 neighbors, rather than 100, were used during relaxation to minimize the number of particle pairs generated. These pairs (ex. Dehnen & Aly 2012, Springel 2010b) do not change global properties of the relaxed WDs, but do effectively reduce spatial resolution and having too many of them make transferring SPH initial conditions into AREPO problematic. Following relaxation, the density profile of both stars were consistent with the hydrostatic equilibrium solution, with the numerical central densities deviating from the 1D integrated ones by less than 1%. Since all particles have identical mass, the tenuous outer layers of the WDs are difficult to capture in GASOLINE; consequently the radii of the relaxed stars, as defined by the outermost particle, were $\sim 5\%$ smaller than the integrated ones. Even after energy damping, particle noise prevents the central temperature of the relaxed stars from reaching below $\sim 1 \times 10^7$ K, so all particle temperatures were artificially reset to $\sim 5 \times 10^6$ K.

We then placed the relaxed stars in a circular, unsynchronized binary, with initial separation $a_0 = 2.2 \times 10^9$ cm chosen (using the approximation of Eggleton 1983) so that the $0.625 M_{\odot}$ donor will just overflow its Roche lobe.² The corresponding orbital period is 49.5 s. These initial conditions do not account for the tidal bulges of the stars, and so are not fully equilibrated (eg. Dan et al. 2011). While this makes our initial conditions less realistic, it should suffice for our purpose of discovering any code dependence on merger evolution.

We generate initial conditions in AREPO by converting the SPH particles of the GASOLINE initial conditions into mesh-generating points, while retaining their conserved quantities (mass, momentum

²The 1D integrated radius was used to calculate a_0 , rather than the smaller relaxed SPH radius. This accounts for the small differences in initial conditions between this work and the equivalent simulation in Ch. 2.

and energy). These initial conditions are not guaranteed to be regular, but AREPO regularizes the mesh over just a few timesteps by nudging each cell’s mesh-generating points to their cell’s center of mass.

Our SPH particles all have the same mass of 2×10^{27} g (1.3×10^6 particles represent the system), comparable to the highest resolutions used in other recent work (Pakmor et al. 2012b; Raskin et al. 2014). We likewise use AREPO’s refinement scheme to keep cell masses within a factor of 2 of this value, and to keep adjacent cell volumes to within a relative factor of 10. AREPO’s grid refinement scheme naturally increases the resolution of our simulations over time, though, and so all resolutions stated in this work are for the start of the simulation. We additionally initialize a background grid of 10^{-5} g cm $^{-3}$ cells in AREPO to fill the vacuum surrounding the WDs – this adds only $\sim 0.005 M_{\odot}$ of material to the simulation. At identical mass resolution, the spatial resolution in GASOLINE is about a factor of 2 – 3 lower than that in AREPO due to GASOLINE’s use of more neighboring particles to obtain smoothed quantities. The two codes differ greatly regardless of resolution, however, and we believe equivalent mass resolution to be the most appropriate comparison (see Vogelsberger et al. Sec. 2.3 for complications in achieving equivalent accuracy in SPH and grid codes). In Sec. 3.5.1 we check if our results are resolution-dependent.

We run both simulations to 1000 s, substantially beyond the time when the WDs merge (at ~ 200 s). At this point, the GASOLINE simulation has reached a quasi-hydrostatic equilibrium. As we shall see in Sec. 3.4, the AREPO simulation continues its hydrodynamic evolution long after this time.

3.3 Improving Angular Momentum Conservation in Arepo

Before we describe our results, we summarize the discovery and resolution of a critical angular momentum conservation issue in AREPO.

The first simulation we performed in AREPO showed dramatic differences from our GASOLINE ones. Following the final phase of the merger, when the two WDs coalesce into one, the AREPO merger remnant featured a dense, crescent-shaped region formed from accretor material that retained its pre-merger temperature of $\lesssim 10^7$ K, while the GASOLINE remnant was relatively hot throughout its interior, with an average temperature of $\sim 2 \times 10^8$ K. Most prominently, the GASOLINE one became axisymmetric within several hundred seconds after the merger, while the AREPO remnant maintained the integrity of its non-axisymmetric crescent while launching one, and then multiple trailing spiral waves into the surrounding medium.

In the top panel of Fig. 3.2, we show the evolution of the total z-axis angular momentum $L_{z,\text{tot}}$ (top cluster of lines) for low-resolution (1×10^{28} g particles or cells) and standard-resolution (2×10^{27} g) GASOLINE and AREPO simulations. We also show the angular momentum within a cylinder oriented along the rotational axis with radius $\omega = 10^9$ cm, $L_{z,\omega < 9}$, which represents the angular momentum within the dense core of the merger remnant. Coalescence occurs at somewhat different times in the two codes (partly due to slight inconsistencies in their initial conditions that have subsequently been eliminated), so each simulation’s curve is shifted by $t_{\max(L_z)}$, the time at which $L_{z,\omega < 9}$ achieves its maximum value (a rough proxy for the end of coalescence). We see that, over ~ 1000 s, the AREPO remnant’s angular momentum drops by a factor of ~ 20 at both resolutions, behavior that is not reproduced by either GASOLINE run. The spiral waves generated in AREPO are a mechanism for transporting angular momentum (eg. Balbus 2003) and were initially presumed to be the cause of this remnant spin-down. Global angular momentum in AREPO, however, is not conserved: the

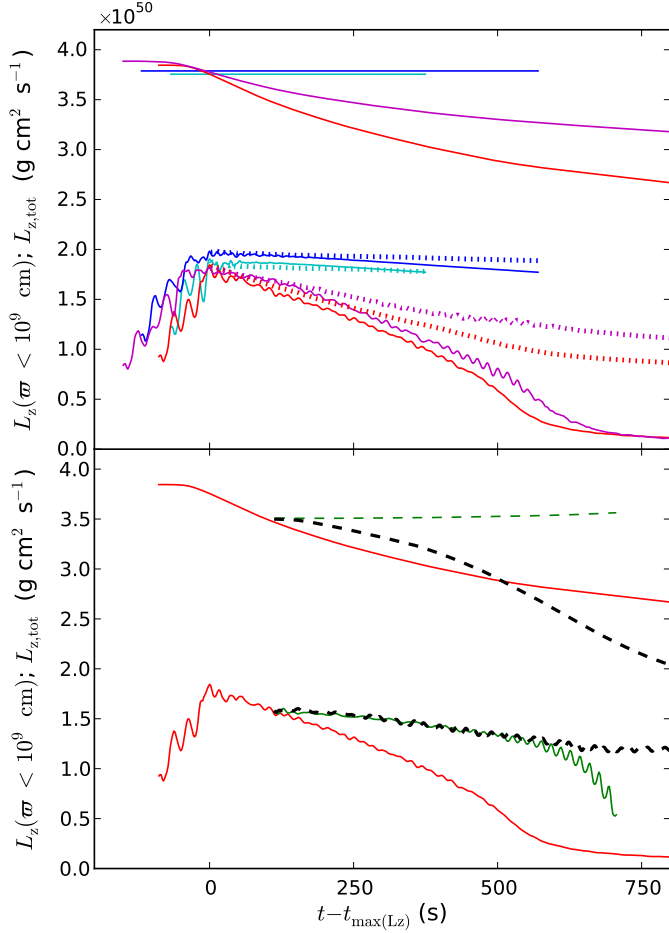


Figure 3.2: Evolution of total z -axis angular momentum $L_{z,\text{tot}}$ (top cluster of lines in each panel) and that within a cylinder of radius $\omega = 10^9 \text{ cm}$, $L_{z,\omega < 10^9}$ (bottom cluster), for various simulations in 2013-2014, before AREPO was updated to better conserve angular momentum. All curves are shifted in time by $t_{\max(L_z)}$, the time in each simulation at which $L_{z,\omega < 10^9}$ achieved its maximum value, to synchronize the start of post-merger evolution. In the top panel, red and magenta lines represent the low and standard-resolution AREPO simulations, respectively, while the cyan and blue ones represent low and standard-resolution GASOLINE ones, respectively. Dotted lines represent angular momentum balance $L_{\text{bal}}(\omega < 10^9 \text{ cm})$, which should be flat in the absence of spurious angular momentum losses. (Slightly different initial amounts of total angular momentum between AREPO and GASOLINE runs are due to inconsistencies in their initial conditions that have subsequently been eliminated.) In the bottom panel, the red line is again the low-resolution AREPO simulation, while the green line is an AREPO low-resolution run where the mesh is held static after $t = 200 \text{ s}$. The dashed black line is a FLASH simulation that uses the AREPO low-resolution run at $t = 200 \text{ s}$ for initial conditions; its loss of total angular momentum is due to having outflow boundaries.

low-resolution run loses a *third* of its angular momentum over ~ 1000 s, and the standard-resolution one about a fifth. SPH formally conserves angular momentum, and we find the $L_{z,\text{tot}}$ for GASOLINE varies in time by $\lesssim 5 \times 10^{-5}$ from its mean values at either resolution.

A moving mesh that refines in regions of high density may not properly resolve the disk of the merger remnant (which is at low-density but carries much of the remnant’s angular momentum). To better pinpoint where the angular momentum was being spuriously lost, we computed (similar to Ji et al. 2013, their Sec. 2.2.4) the theoretically expected change in L_z . For a cylinder V oriented along the rotational axis, this is given (via the Euler equations) by

$$\frac{\partial L_z}{\partial t} = - \oint_V \rho \omega v_\phi v_\omega dS + \int_V \omega \times \nabla \Phi dV \quad (3.21)$$

where the first term encapsulates advection out of the volume (including the Reynolds stress associated with wave motion; Balbus 2003; Kratter & Lodato 2016) and the second term external torque – in our case gravitational.³ Subtracting the time-integral of Eqn. 3.21 (i.e. the cumulative angular momentum change ΔL_z) from the volume’s angular momentum gives us the “balance”

$$L_{\text{bal}}(t) = L_z(t) - \Delta L_z = L_z(t) - \int_{t_0}^t \frac{\partial L_z}{\partial t'} dt'. \quad (3.22)$$

In a system with perfect angular momentum conservation, ΔL_z would account for all changes in $L_z(t)$ and $L_{\text{bal}}(t) = L_{\text{bal}}(t_0)$ would be a constant.

In Fig. 3.2, we show using dashed lines the balance for the cylinder of $\omega = 10^9$ cm, $L_{\text{bal}}(\omega < 10^9$ cm), for each of the four simulations, to check for spurious changes to the angular momentum of the merger remnant cores. While $L_{\text{bal}}(\omega < 10^9$ cm) decreases by $\sim 5\%$ in the GASOLINE simulations (likely due to artificial viscosity, not included in Eqn. 3.21), the change in L_{bal} accounts for approximately *all* of the total spurious losses in AREPO at high resolution (compare the $L_{z,\text{tot}}$ and L_{bal} lines), invalidating the hypothesis that it is the outer regions of the simulation spuriously losing angular momentum.

We then hypothesized that low-density regions near $\omega = 10^9$ cm that interact with the remnant core were underresolved. To rectify this, we performed a run which, after coalescence, included a volume refinement scheme for cells within $\omega = 10^9$ cm. This led to a dramatic increase in resolution over time, with the simulation eventually exceeding 2×10^7 cells. This run loses $\sim 5\%$ of $L_{z,\text{tot}}$ in ~ 500 s, but $\sim 30\%$ of the change in $L_{z,\omega < 9}$ over the same timespan is still spurious, meaning losses would only be rendered negligible at impractically high resolutions.

We finally turned to simulating post-merger evolution in other codes. In the bottom panel of Fig. 3.2, we show our simulation in the Eulerian code FLASH (Fryxell et al. 2000; Dubey et al. 2009) that uses the low-resolution AREPO run at $t = 200$ s for initial conditions. In FLASH, we used a 3D Cartesian grid 1.6×10^{10} cm to a side, with multiple levels of fixed-mesh refinement centered on the merger remnant so that its core is resolved with cells 7.8×10^6 cm to a side (comparable to the low-resolution AREPO run). Gravity was solved using a multipole solver with $l_{\text{max}} = 50$, and fluxes propagated with the HLLC (Harten-Lax-van Leer – Contact) Riemann solver. We also show a low-resolution AREPO run where, at $t = 200$ s, the mesh’s velocities were forced to zero, transforming AREPO into a static grid code operating on an unstructured mesh. Considering the sheer number of differences between the two simulations, they agree remarkably on the rate of change of $L_{z,\omega < 9}$ until very late times (when

³A third, pressure torque term also arises in general, but for a cylinder oriented along the axis of rotation it is analytically zero (and numerically negligible as well).

mesh drift issues corrupt the AREPO simulation). $L_{z,\text{tot}}$ for the AREPO-static run also changes by only $\sim 1\%$ over ~ 500 s. These simulations suggested AREPO’s moving mesh scheme cause spurious angular momentum loss.

Eventually, [Pakmor et al. \(2016\)](#) found two aspects of AREPO’s original hydrodynamic scheme (Sec. 3.2.3) were responsible for making the code only *first-order* convergent for non-trivial moving meshes. First, while Eqn. 3.19 provides second-order convergence on static meshes of arbitrary geometry, it only uses the initial state of the mesh itself, and so reduces to first-order on moving meshes. Second, AREPO’s estimate for $\phi(\mathbf{f}_{ij})$ in Eqn. 3.20 assumes that the cell centers of mass \mathbf{s}_i – where the value of \mathbf{W}_i is defined – and mesh-generating points \mathbf{r}_i align, which is not true for elongated cells. This first-order convergence does not inevitably cause major errors – the galaxy formation study of [Marinacci et al. \(2014\)](#) is not affected, for example – but for a rotation-dominated system being simulated over many tens of dynamical times, such as the accretion disk in [Pakmor et al. \(2016\)](#), systematic deviations in angular momentum conservation become large.

The solution is correspondingly two-fold: first, replace Eqns. 3.17 and 3.19 by a hybrid of the MUSCL and 2nd order Runge-Kutta methods:

$$\begin{aligned}\mathbf{W}'_i &= \mathbf{W}_i^n + \Delta t \frac{\partial \mathbf{W}}{\partial t} \\ \mathbf{r}'_i &= \mathbf{r}_i^n + \Delta t \mathbf{w}_i^n \\ \mathbf{Q}_i^{n+1} &= \mathbf{Q}_i^n - \frac{\Delta t}{2} \left(\sum_j A_{ij}^n \hat{\mathbf{F}}_{ij}^n(\mathbf{W}^n) + \sum_j A'_{ij} \hat{\mathbf{F}}'_{ij}(\mathbf{W}'_i) \right) \\ \mathbf{r}_i^{n+1} &= \mathbf{r}'_i,\end{aligned}\tag{3.23}$$

where \mathbf{w}_i is the velocity of the mesh-generating point (and is, as discussed above, roughly the speed of the fluid within the cell). With this method, we first make a prediction of the cell’s future primitive variables \mathbf{W}' , as well as the future Voronoi mesh. We then use both the current and predicted values to calculate an average flux (spatial extrapolation to the cell interface is implicit when calculating $\hat{\mathbf{F}}_{ij}$) and evolve the cell. The mesh velocities are assumed to be constant over Δt , so the predicted and true future mesh are identical. Second, the Green-Gauss gradient estimate is replaced with a linear least-squares one, which determines slope $\langle \nabla \phi \rangle_i$ by minimizing

$$\sum_j g_j (\phi_j - \phi_i - \langle \nabla \phi \rangle_i (\mathbf{s}_j - \mathbf{s}_i))^2,\tag{3.24}$$

where $g_j \equiv A_{ij}/|\mathbf{s}_j - \mathbf{s}_i|^2$ is a weighting function. This estimate gives the value that best reproduces the change in ϕ when traveling from cell i to any of its neighbors, and relies on cell centers of mass rather than mesh generating points. Working in concert, these Runge-Kutta and Least-Squares Fitting (RKLSF) methods make AREPO second-order convergent.

In Fig. 3.3, we show the evolution of angular momentum for AREPO-RKLSF runs (from Sec. 3.5.1) at resolutions ranging from 5×10^{28} g to 1×10^{27} g. We immediately notice that $L_{z,\omega < 9}$ no longer decreases with time, cementing the fact that the rapid spin-down seen in Fig. 3.2 was an artefact of spurious angular momentum loss. Indeed, this makes it impossible to calculate $t_{\max(L_z)}$ – we instead use “ t_c ” (discussed further in Sec. 3.4), the time when the average separation between donor and accretor material reaches a tenth of its value at the beginning of the simulation, to synchronize the start

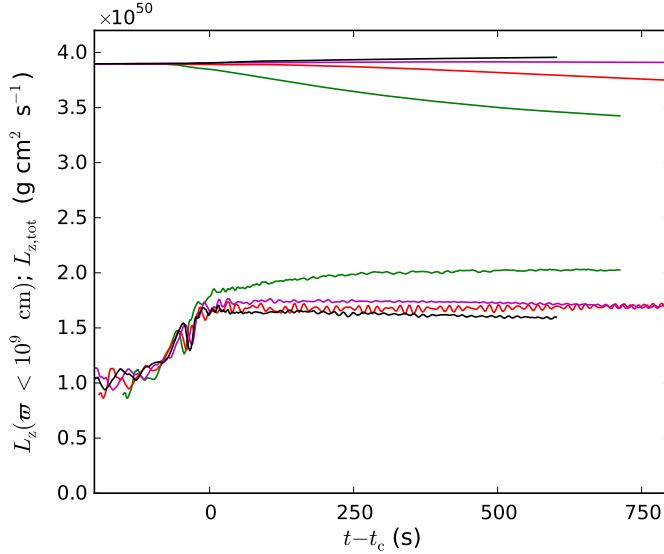


Figure 3.3: Evolution of total z -axis angular momentum $L_{z,\text{tot}}$ (top cluster of lines) and that within a cylinder of radius $\omega = 10^9 \text{ cm}$, $L_{z,\omega < 9}$ (bottom cluster) for the AREPO-RKLSF simulations. All curves are shifted in time by t_c (rather than $t_{\max(L_z)}$ like in Fig. 3.2), the time when average separation between donor and accretor material reaches a tenth of its initial value. Colors indicate initial mass resolutions of $5 \times 10^{28} \text{ g}$ (red lines), $1 \times 10^{28} \text{ g}$ (green) $2 \times 10^{27} \text{ g}$ (cyan) and $1 \times 10^{27} \text{ g}$ (blue).

of post-merger evolution. In all but the lowest-resolution run, $L_{z,\text{tot}}$ deviates by less than $\sim 4\%$ from its initial value, and at the highest resolution run of $1 \times 10^{27} \text{ g}$, or 2.5×10^6 cells, it deviates by $\sim 1.5\%$ over $\sim 840 \text{ s}$, an order of magnitude better than the 2×10^7 cell simulation without RKLSF.

The density and temperature profiles of the merger in the AREPO-RKLSF simulations also generally agree better with their GASOLINE counterparts up until the end of coalescence, but the dense crescent and spiral wave that distinguish the AREPO merger remnant remain.

3.4 Results

We now compare in detail our new AREPO simulation with a GASOLINE one. Fig. 3.4 compares snapshots of the two at various times.

The initial evolution of the two systems, shown in row 1 of Fig. 3.4, is qualitatively similar. Our initial conditions are approximate, so both stars immediately are tidally stretched by the binary potential, overshooting their Roche lobes in the process and transferring mass to each other in spurts. This eventually dies down for the $0.65 M_\odot$ accretor, and becomes steady mass transfer for the $0.625 M_\odot$ donor, just prior to it becoming fully disrupted. In reality, the donor WD should overflow first and begin a period of quasi-stable mass transfer over potentially dozens of orbits, and so our simulations, both of which experience full donor disruption in just a few orbits, overestimate the rate of early mass transfer (Dan et al. 2011).

The accretion streams in both codes are traveling at supersonic speeds ($\mathcal{M} \approx 2$) relative to the accretor when they impact, and the resulting shocks cause rapid thermalization. By the time the donor is fully disrupted a hot atmosphere has formed around the accretor, with temperatures of

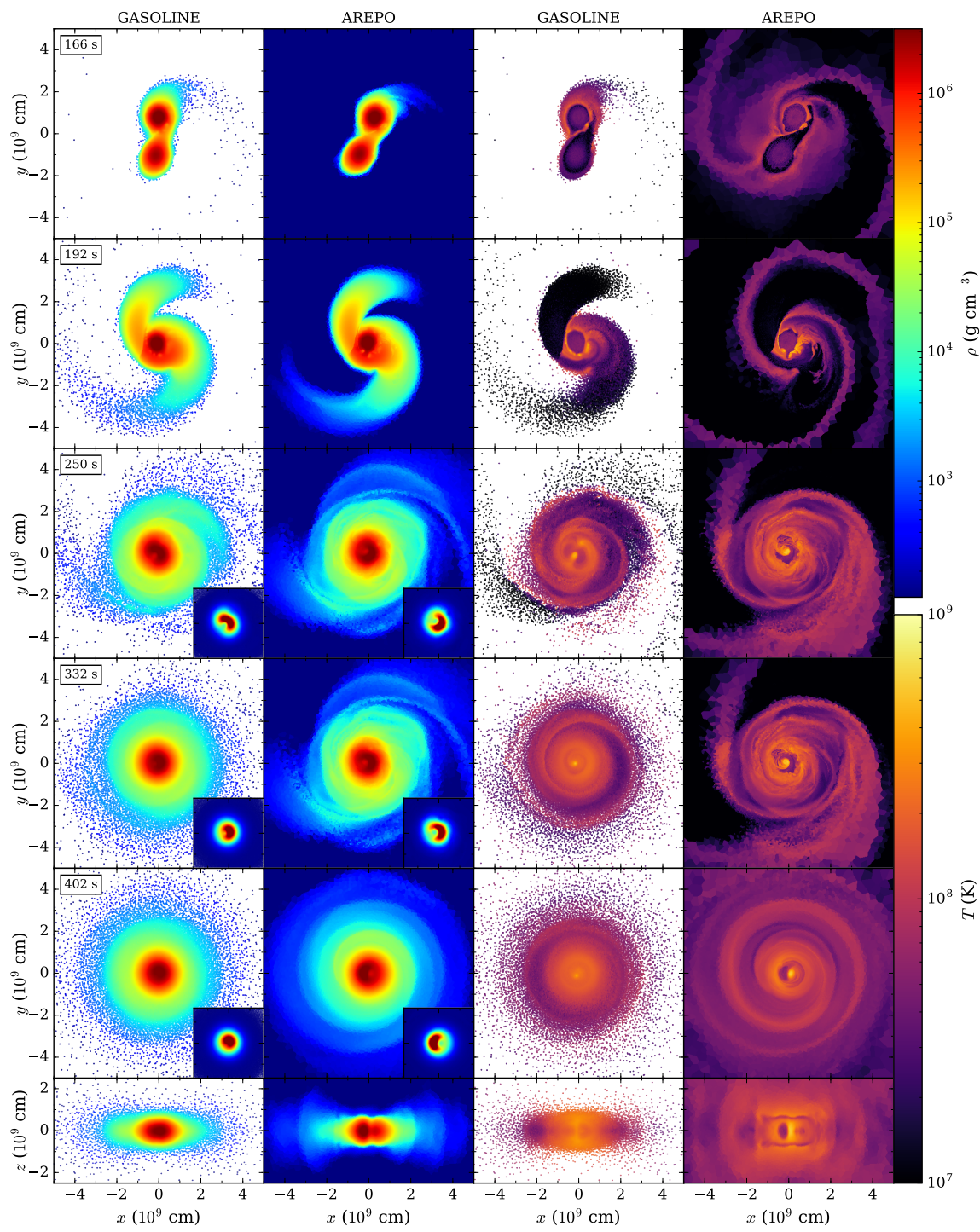


Figure 3.4: Series of equatorial (xy) plane density (left two columns) and temperature (right two columns) intensity plots for five snapshots in time (rows; the time for each snapshot is indicated at the top left of the density plots) during the GASOLINE and AREPO simulations. xz -plane plots are also included for the final snapshot.

1.6×10^8 K in AREPO and 1.9×10^8 K in GASOLINE – both about a quarter of the virial temperature, $GM_a m_P \mu / 3R_a k_B \approx 7 \times 10^8$ K – and densities of 1.8×10^5 g cm $^{-3}$ and 2.3×10^5 g cm $^{-3}$, respectively. As can be seen in Fig. 3.4 row 1, AREPO’s hot atmosphere is somewhat less extended and has more localized hotspots in temperature compared to the extended and uniform one in GASOLINE. This may be due to a combination of AREPO not oversmoothing the gradients within the atmosphere, and having superior spatial resolution for the same mass resolution.

As mass transfer continues to expand the donor and draw it closer to the accretor, eventually tidal forces between the two are strong enough to fully disrupt the donor, stretching it out into a thick stream of material that wraps around the accretor (see Fig. 3.4, row 1). In both simulations, this occurs after ~ 3.6 orbital periods of the initial binary, or ~ 180 s, by which time the donor has transferred $\sim 0.05 M_\odot$ to the accretor. During coalescence, both the density and temperature profiles appear very similar between the codes, and the destruction of the donor takes place over the same amount of time – about one orbital period (49.5 s).

Once the donor is fully disrupted, and coalescence begins, a portion of it forms an accretion stream that slides across the accretor at supersonic speeds, creating a string of Kelvin-Helmholtz vortices. In AREPO these vortices are markedly more pronounced, being both larger by $\sim 30\%$ in radius, and having a slightly higher temperature of $\sim 5 \times 10^8$ K compared to GASOLINE’s $\sim 4 \times 10^8$ K. The stream continues to inspiral toward the center of the accretor, severely deforming the accretor while carrying the string of Kelvin-Helmholtz vortices toward the center of the system. The two WDs have nearly equal masses, so material near the surface of the accretor is dredged up and mixes with the stream, and the shape of the accretor changes from a sphere into a crescent. Meanwhile, the remainder of the donor material forms a thick sub-Keplerian disk around the accretor. Coalescence is approximately complete when the average separation between material from the donor and accretor changes from its initial value of 2.2×10^9 cm to its equilibrium value of $\sim 1 \times 10^8$ cm. We thus estimate the time when coalescence is complete, t_c , by determining the time when average donor-accretor separation reaches a tenth of its initial value. We find $t_c = 228$ s for GASOLINE, and 220 s for AREPO (roughly Fig. 3.4, row 3).

In Fig. 3.5, we show profiles of density, temperature and energy for the merger remnants at 99 s (2 orbital periods) after coalescence, roughly equivalent to row 4 of Fig. 3.4. Profiles both along the orbital plane of the original binary, or “equatorial plane” (solid lines) and rotational axis (dotted) are considered, and like in Ch. 2 we map (equatorial) ϖ and (rotational) z positions to the corresponding ratio of spherical enclosed mass to total mass M/M_{tot} . The equatorial profiles are axisymmetrically averaged, while the rotational axis ones are averaged from the profiles above and below the equatorial plane. Overall, the two remnants have very similar structures: both feature a degeneracy-supported core surrounded by a rotationally supported thick disk along the equatorial plane and by a hot, thermally supported atmosphere along the axis of rotation. Following Sec. 2.3.2.3, we find the disk mass $M_{\text{disk}} = 0.24 M_\odot$ and the core-envelope mass $M_{\text{ce}} = 1.05 M_\odot$ in both simulations, though we note that the core-envelope also has substantial rotational support throughout.⁴ Both remnants’ total internal energies (1.5×10^{50} erg) are also identically divided into $\sim 30\%$ rotational, $\sim 10\%$ thermal and $\sim 60\%$ degeneracy energy. One minor difference between the two codes is the total amount of material unbound by the merger – $1.4 \times 10^{-3} M_\odot$ in GASOLINE, and $5.0 \times 10^{-4} M_\odot$ in AREPO – though this value is much smaller and harder to constrain than the bulk values above.

⁴The mass of material whose specific degeneracy energy is $> 50\%$ of their total specific energy is $\sim 0.8 M_\odot$ in both simulations, as it is in Ch. 4.

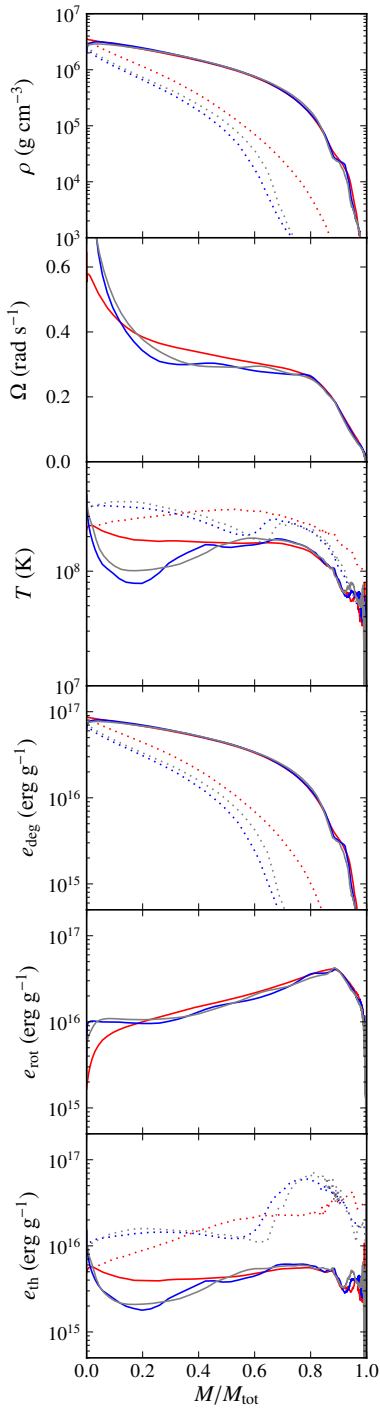


Figure 3.5: Merger remnant profiles from the GASOLINE (red), AREPO (blue) and AREPO MHD (gray; Ch. 4) simulations 99 s after coalescence (around row four of Fig. 3.4). The profiles are, from top to bottom, density ρ , angular rotation speed Ω , temperature T , specific degeneracy energy e_{deg} , specific thermal energy e_{th} , and specific rotational energy e_{rot} , all as a function of the ratio of spherical enclosed to total mass M/M_{tot} . Solid lines represent profiles on the original binary's orbital plane, while dash-dotted lines represent profiles along the rotational axis.

The simulations' profiles in Fig. 3.5 are likewise very similar in shape to one another: both, for example, have a peak density of $\sim 3 \times 10^6 \text{ g cm}^{-3}$ and a large fraction of their mass rotating nearly rigidly at $\sim 0.3 \text{ s}^{-1}$. We also show the AREPO MHD simulation from Ch. 4 in grey, and find it is similar as well, indicating that including magnetic dynamo effects lead only to minor changes in the *hydrodynamics* of the merger. The greatest discrepancy is in the temperature at small M/M_{tot} : it is a factor of ~ 2 smaller in the AREPO simulation than in the GASOLINE one.

That discrepancy, however, reflects a growing difference visible in rows 4 - 6 of Fig. 3.4. Just after coalescence, the center of the merger remnant in both simulations is clearly divided between a dense and cold crescent-shaped region, formed from the perturbed accretor WD, and a low-density void that is an order of magnitude hotter, formed by material roughly evenly mixed between donor and accretor (this void appears as a column in the xz plots of Fig. 3.4). 99 s after coalescence, the hot void has a temperature of $\sim 6 \times 10^8 \text{ K}$ in both codes, but the AREPO void is $\sim 80\%$ larger in radius and slightly less dense at $\sim 1.5 \times 10^6 \text{ g cm}^{-3}$ versus GASOLINE's $\sim 2 \times 10^6 \text{ g cm}^{-3}$. The cold crescent, meanwhile, has a density of $\sim 4 \times 10^6 \text{ g cm}^{-3}$ in both codes, but has a temperature of $\sim 2 \times 10^8 \text{ K}$ in GASOLINE versus $\sim 5 \times 10^7 \text{ K}$ in AREPO. Over the next several hundred seconds, the GASOLINE remnant's crescent becomes axisymmetric, eliminating the hot void in the process; material from the void moves off of the equatorial plane to form two $\sim 3.5 \times 10^8 \text{ K}$ hotspots along the rotational axis (row 6 of Fig. 3.4). By $t \approx 500 \text{ s}$, the GASOLINE remnant structure – an oblate spheroidal core with a roughly uniform temperature of $\sim 2 \times 10^8 \text{ K}$ (outside of the hotspots) surrounded by a stubby disk – has stopped changing on a hydrodynamic timescale (roughly equal to one binary orbital period). AREPO, on the other hand, maintains the distinction between the crescent and void, and consequently remains non-axisymmetric until the end of the simulation at 1000 s. The system's center of rotation and mass are at the midpoint along the boundary between the crescent and void, and the dense crescent revolves around this point (rather than spinning about it). This generates a lopsided gravitational potential that perturbs the surrounding disk, launching an $m = 1$ one-armed spiral wave into the surrounding medium. The pattern speed is $\Omega_p \approx 0.4 \text{ s}^{-1}$ (as is the angular speed of the crescent), and the base of the spiral wave is at $\omega \approx 1.5 \times 10^9 \text{ cm}$, where $\Omega \approx 0.2 \text{ s}^{-1}$ – in 2:1 resonance with the crescent.

Since spiral waves can transport angular momentum, we show in Fig. 3.6 the evolution of z -axis angular momentum L_z within concentric cylinders centered on the rotational axis for the two simulations. We see that all cylinders slowly lose angular momentum after coalescence in the GASOLINE simulation, consistent with the effect of artificial viscosity. In AREPO, $L_z(\omega < 3 \times 10^9 \text{ cm})$ decreases at a rate of $dL_z/dt = 1.2 \times 10^{47} \text{ g cm}^2 \text{ s}^{-2}$ (compared to $3.3 \times 10^{46} \text{ g cm}^2 \text{ s}^{-2}$ in GASOLINE), reflecting the wave's angular momentum transport. Applying Eqn. 3.21 to the cylinder, we estimate around $\sim 85\%$ of this decrease can be accounted for by advection, suggesting the spiral wave transports angular momentum through Reynolds stresses (rather than gravitational torque; Kratter & Lodato 2016). The angular momentum within $\omega = 10^9 \text{ cm}$ decreases by $\sim 5\%$ by the end of the simulation at $t = 1000 \text{ s}$, but the loss of angular momentum in the disk also results in the enclosed mass within $\omega = 10^9 \text{ cm}$ increasing by $0.02 M_\odot$ over the same timeframe. In fact, the remnant disk has transported about half of its angular momentum to much larger distances by this time; the corresponding timescale is roughly equal to that for an α -viscosity disk with $\alpha \sim 10^{-1}$. For comparison, Ji et al. (2013) simulate the magnetically-mediated viscous evolution of a $0.6 - 0.6 M_\odot$ merger remnant, and find angular momentum transport at a rate equivalent to an $\alpha = 10^{-2}$ disk, an order of magnitude smaller. At $t = 1000 \text{ s}$, AREPO's void has shrunk by about a quarter of its initial radius, but the remnant core

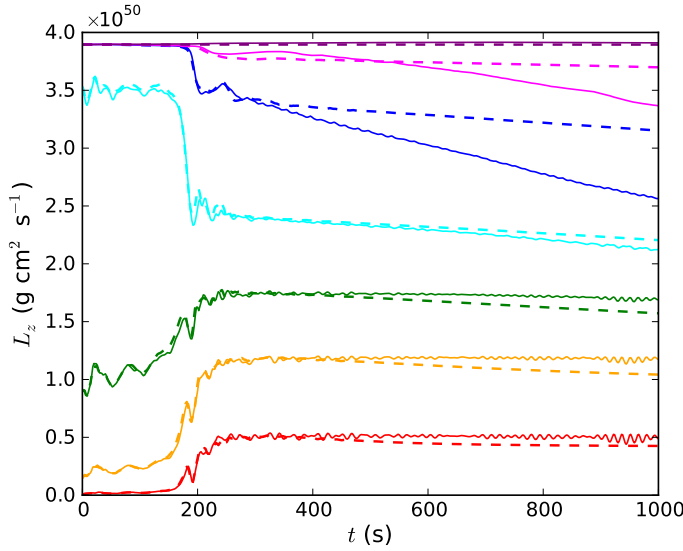


Figure 3.6: Time evolution of z -axis angular momentum L_z for AREPO (solid lines) and GASOLINE (dashed) simulations. The purple line represents total L_z , while the others represent angular momentum within concentric cylinders aligned along the rotation axis and with radii $\omega = 5 \times 10^8$ (red), 7.5×10^8 (yellow), 1×10^9 (green), 1.5×10^9 (cyan), 3×10^9 (blue) and 6×10^9 cm (magenta).

remains non-axisymmetric and the spiral wave persists, and so angular momentum transport should continue on a hydrodynamic timescale beyond the end of the simulation.

Preliminary attempts to carry the simulation even further in time in AREPO, however, have been stymied by the spurious formation of a $< 10^7$ K ring of material at the interface between donor and accretor at ~ 1000 s. The appearance of this numerical artefact, which appears at an earlier time at the lower-resolution simulations in Sec. 3.5.1, is troubling, and suggests that AREPO must be further refined before the full hydrodynamic spin-down of the remnant can be simulated. We therefore caution that the values stated above may not be accurate, particularly close to the end of the simulation, though (since our highest resolution run in Sec. 3.5.1 does not develop this issue) our qualitative results are more robust.

3.5 Discussion

To determine the robustness of our results, and provide clues to the sources of the differences between AREPO and GASOLINE simulations, we ran a number of tests varying code parameters.

3.5.1 Resolution Test

As noted in Sec. 3.2.4, an AREPO simulation with identical mass resolution to a GASOLINE one will have a factor of 2 – 3 higher spatial resolution. It is possible that the differences we observe between our simulations are not due to fundamental differences between the codes, but because our GASOLINE simulation insufficiently resolves the merger. To address this, we perform a series of GASOLINE and AREPO simulations with a mass resolutions of 5×10^{28} g (equivalent to 5.1×10^4 particles or cells

and comparable to resolutions used in parameter-space sweeps by Dan et al. 2012; 2014), 1×10^{28} g (2.6×10^5) and 1×10^{27} g (2.6×10^6). This factor of 50 range in mass resolution (~ 4 in spatial resolution) allows us to both determine the degree to which mergers in each code change with resolution, and to compare AREPO runs to GASOLINE ones at finer mass resolution.

At all four resolutions, the GASOLINE simulations exhibit very similar behavior prior to coalescence. The donor fully disrupts in at ~ 3.6 orbits of the initial binary for the two higher resolution runs, while the two lower-resolution ones disrupt slightly earlier at ~ 3.2 orbits ($\sim 155 - 165$ s). Coalescence for the highest resolution run occurs at $t_c = 230$ s, within 2 seconds of the standard resolution one, while it occurs $20 - 35$ seconds earlier for the two lower resolution runs (we note the way we determine coalescence is somewhat sensitive to changes in the detailed configuration of the remnant). Just after coalescence, all reproduce the crescent-and-void configuration, with the void being least prominent in the lowest-resolution run.

AREPO also reproduces the same qualitative evolution up to coalescence at all resolutions, but donor disruption occurs within only ~ 1.9 orbits at its lowest resolution, and in ~ 2.8 at its second lowest. The time of coalescence is likewise much sooner in the lowest resolution simulation, with $t_c = 150$ s. The highest resolution run, however, is very similar to the standard resolution one, with donor disruption occurring at ~ 3.7 orbits (~ 185 s) and t_c occurring at 234 s, close to the standard run's values. These differences are in part due to our initial conditions setup, where GASOLINE SPH particles are directly mapped to AREPO cells. WDs that are hydrostatic in GASOLINE are not precisely so in AREPO, particularly in the poorly resolved atmosphere, and we see the WDs spuriously expanding in the first few seconds. This effect leads to larger mass-transfer rates early in the merger, and is magnified with decreasing resolution. Just after coalescence, all AREPO runs reproduce the crescent-and-void configuration except in the lowest-resolution one.

In Fig. 3.7, we show the equatorial and rotational axis profiles of all simulations 99 s after t_c . The GASOLINE remnants (left column) are all remarkably similar to one another, with the sole exception of the temperature structure at the lowest resolution. The disk and core-envelope masses as well as the partitioning of internal energy are all within 3% of their values at the standard resolution reported in Sec. 3.4. The central densities of the remnants also deviate by $\lesssim 5\%$ from their mean value of 3.6×10^6 g cm $^{-3}$. The AREPO remnants (right column) are less uniform: masses and energies vary by $\sim 5 - 10\%$ from those in Sec. 3.4 for all except the lowest resolution run, which has $\sim 50\%$ more total thermal energy and a $\sim 25\%$ less massive disk. The maximum density ranges from $3 - 4 \times 10^6$ g cm $^{-3}$ for all resolutions except the lowest one, where it is $\sim 2 \times 10^6$ g cm $^{-3}$. The variations between AREPO curves in Fig. 3.7 reflect variations in their crescent and void. While at the highest two resolutions the crescent is clearly colder, with a temperature of $\sim 5 \times 10^7$ K, in the second lowest resolution run its temperature is $\sim 1 \times 10^8$ K, and in the lowest resolution one the remnant core never forms a crescent at all, instead appearing as a dumbbell-shaped object that transforms into a spherically symmetric one within ~ 500 s of coalescence. During this time, global angular momentum decreases by $\sim 12\%$ (Fig. 3.3), and a $< 10^7$ K ring of material spuriously forms at the interface between donor and accretor, both indicating that this run is too poorly resolved to simulate the merger. At all other resolutions, however, the crescent and void survive until the end of the simulation at 1000 s.

The crescent-void configuration also appears, but then fades away over several hundred seconds, in all GASOLINE simulations. To check if the longevity of the configuration is resolution-dependent, we turn to a measurement of non-axisymmetry – introduced in Sec. 2.2.3 – using $|f_i|/|f_0|$, the ratio of

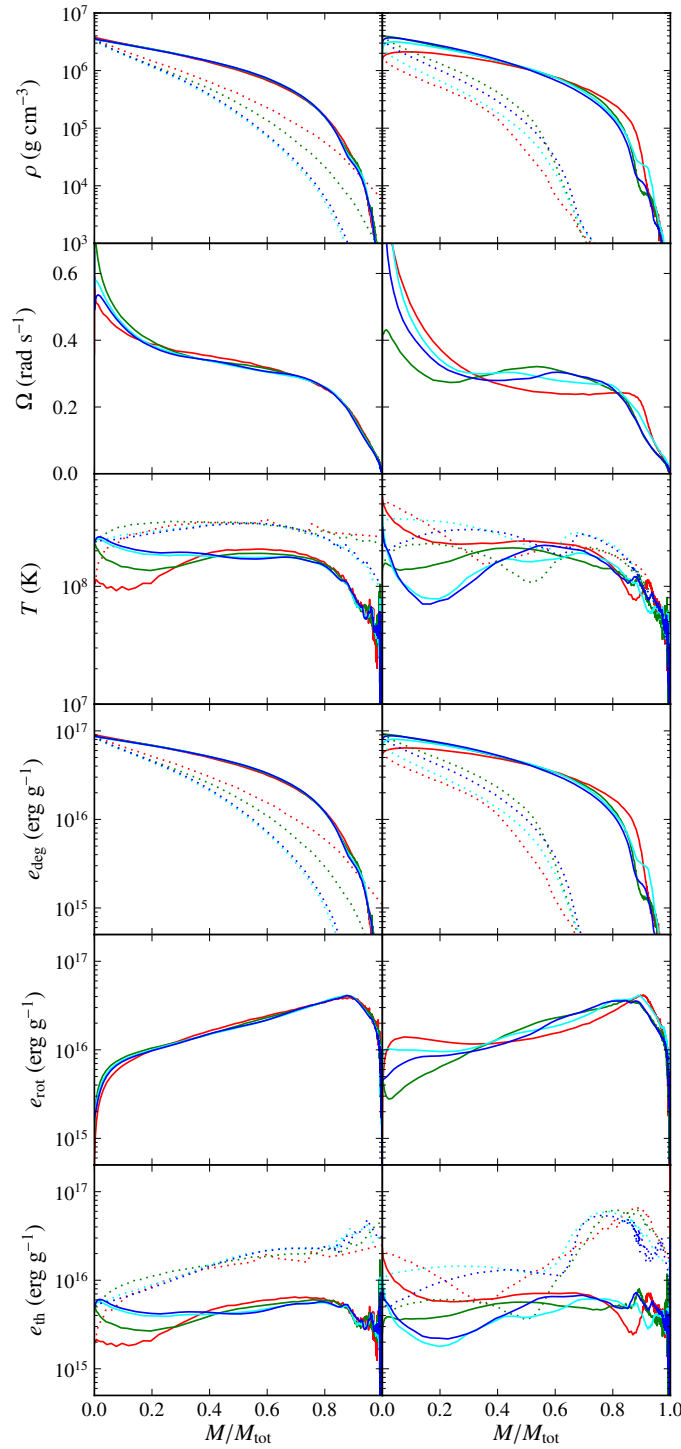


Figure 3.7: Merger remnant profiles, as in Fig. 3.5, for GASOLINE (left column) and AREPO (right) simulations of various (initial, for AREPO) mass resolutions. The resolutions are 5×10^{28} g (equivalent to 5.1×10^4 particles or cells; red lines), 1×10^{28} g (2.6×10^5 ; green), 2×10^{27} g (1.3×10^6 ; cyan), and 1×10^{27} g (2.6×10^6 ; blue).

largest non-zero to zeroth Fourier coefficient of particles or cells binned in azimuth. For all simulations, the largest non-zero Fourier coefficient is the first, and the time when the hot void disappears roughly matches the time when $|f_1|/|f_0| = 0.01$, which we call t_f . We find, from lowest to highest resolution, $t_f = 426$ s, 483 s, 515 s and 513 s, which suggests t_f is resolution dependent, but converges at $t_f \approx 500$ s. All AREPO simulations maintain $|f_1|/|f_0| \gtrsim 0.1$ for $\gtrsim 1000$ s, except for the lowest-resolution run, which drops to $|f_1|/|f_0| \approx 0.02$ by the end of the simulation.

We thus conclude that the largest difference between the GASOLINE and AREPO simulations – the survival of the crescent-void configuration long after the merger – is the case for all resolutions. The void persists for hundreds of seconds in all but the lowest-resolution AREPO simulation, while even in the highest-resolution GASOLINE one it smears away, disappearing within ~ 250 s after coalescence. This is evidence that spatial resolution alone is insufficient to explain the diverging behavior of the codes. We also find that GASOLINE’s results change little between all resolutions, while AREPO’s results only appear to agree at higher ones. This bodes well for merger parameter-space studies using low-resolution SPH simulations (eg. Ch. 2, [Dan et al. 2014](#); the latter finds similar results in their resolution study unless nuclear burning becomes important during the merger), but an equivalent study in AREPO would require a mass resolution finer than $\sim 1 \times 10^{28}$ g (and ideally closer to our standard resolution of 2×10^{27} g) to guarantee qualitative accuracy with higher-resolution runs.

3.5.2 Varying Viscosity in Gasoline

Artificial viscosity, which is essential in SPH for proper shock capture, has been a major issue for white dwarf merger simulations for decades (eg. [Guerrero et al. 2004](#); [Lorén-Aguilar et al. 2009](#)) because it spuriously shears differential rotation into rigid rotation, dumping excess energy into heat. This viscosity cannot simply be mitigated by resolution, and we cannot run our mergers with zero artificial viscosity without neglecting shock heating and introducing unphysical particle behavior (Sec. 3.2.1). We can, however, increase and reduce its strength to see what effect it has on our simulation results, as in Sec. 2.4.5.

We ran GASOLINE simulations of our merger with a mass resolution of 1×10^{28} g and artificial viscosity with fixed coefficients of either $\alpha = 0.05$, $\beta = 0.1$, or $\alpha = 1$, $\beta = 2$ (the Balsara switch is still active), comparing them to the variable-viscosity run at the same resolution in Sec. 3.5.1. The low-viscosity simulation experiences donor disruption at ~ 3.1 binary orbits, and coalescence at $t_c = 206$ s, while the high-viscosity one experiences disruption at ~ 3.4 orbits and coalescence at 220 s, values that are quite similar to those of the variable-viscosity run. This similarity is to be expected, since mass transfer and donor disruption are governed by tidal forces, which are unchanged between the simulations. During coalescence, the evolution of the variable and high-viscosity runs is similar. In the low-viscosity run, however, the donor’s accretion stream produces a contiguous hot ring around the accretor during coalescence, rather than the string of vortices seen in row 2 of Fig. 3.4, and perturbs the accretor far less. As a result, no distinct void ever forms, though the remnant core is distorted into a bean shape. Within ~ 25 s of coalescence, the void in the high-viscosity simulation is already fast-disappearing, having a radius less than half that of the variable-viscosity run. $t_f = 358$ s and 487 s for the high and low-viscosity runs, respectively, compared to 483 s for the variable one. The similarity of the latter two values is likely because the variable-viscosity run tends toward the same α and β values as the low-viscosity one in the absence of shocks (though it may also partly be coincidence, since the low-viscosity remnant does not have a hot void to begin with). At ~ 500 s, the remnant has become

axisymmetric in all three codes, but in the high-viscosity run the interior $\sim 0.8 M_{\odot}$ of the remnant is also rigidly rotating with $\Omega = 0.33 \text{ s}^{-1}$.

As expected, then, the high-viscosity simulation rapidly spins down to axisymmetry while eliminating differential rotation, showing that excess artificial viscosity contributes to the disappearance of the crescent-void configuration. The low-viscosity simulation, on the other hand, primarily shows the importance of increasing α and β during coalescence in order to properly capture shocks and shearing interactions between donor and accretor.

3.5.3 Sources of Differences Between Simulations

What explains the differences between simulations in GASOLINE and AREPO, and, critically, which is more physically accurate? This question boils down to whether or not the crescent-and-void configuration should be long-lived, as seen in AREPO, or should disappear over several hundred seconds as the remnant becomes axisymmetric, as seen in GASOLINE.

Instabilities generating persistent $m = 1$ spiral waves that carry away angular momentum are common features of astrophysical disks, and have been studied, for example, in the contexts of star formation (Adams et al. 1989; Shu et al. 1990; Lin 2015; Kratter & Lodato 2016) and supermassive black hole accretion (Hopkins & Quataert 2010). They have also been seen in WD merger remnants: Kashyap et al. (2015) map the remnant immediately after coalescence from an SPH-based (highly super- M_{Ch}) $1.0 - 1.1 M_{\odot}$ CO WD merger simulation into FLASH. They find that the merger remnant core, though not crescent-shaped, drifts off of the center of rotation and drives an $m = 1$ spiral perturbation in the disk around it for ~ 100 s. They argue this is a variant of the “ARS instability” (Adams et al. 1989; Shu et al. 1990), where non-axisymmetric perturbations acting on a star surrounded by a marginally Toomre-stable ($Q \lesssim 3$ at corotation) Keplerian disk move the star off the system’s center of mass while generating a spiral wave in the disk.

Meanwhile, recent Eulerian simulations of binary neutron star mergers (Paschalidis et al. 2015; Radice et al. 2016) see the formation of a crescent-and-void configuration with corresponding $m = 1$ spiral instabilities. Paschalidis et al. (2015) attributes the formation of their spiral wave to a dynamic instability found by Centrella et al. (2001) and Saijo et al. (2003) to occur in axisymmetric equilibrium polytropes with toroidal density structures, a ratio of kinetic to potential energy $T/|W| \gtrsim 0.14$, a relatively soft $n \lesssim 2$ polytropic EOS, and high differential rotation (Saijo et al. 2003). A similar phenomenon was observed by Ott et al. (2005) in their post-bounce core-collapse supernova core of $T/|W| \approx 0.08$. Watts et al. (2005) and Muhlberger et al. (2014) suggest this “low $T/|W|$ instability” may be a corotational shear instability, related to the Papaloizou & Pringle (1984) instability for thick accretion torii.

The conditions within our remnant are somewhat different those above. Unlike the ARS setup, our inner disk is thick (scale height and disk radius are within an order of magnitude of each other) and has a Toomre parameter of $Q \approx c_s \Omega / \pi G \Sigma \gtrsim 8$ for $\omega \geq 1 \times 10^9 \text{ cm}$ (Σ is the disk surface density), somewhat too high for the ARS instability to act. While the remnant core has a $T/|W| \approx 0.11$ following coalescence and is roughly toroidal in shape, it is already heavily perturbed and the spiral mode already visible once the transient features from the merger itself dissipate, making it difficult to identify a period of growth for the instability. The behavior of our AREPO merger remnant may represent some combination of these instabilities, or possibly a novel, but related, phenomenon. Further analysis is needed, but for now the existence of other $m = 1$ instabilities that drive angular momentum transport

lends support to the physical validity of our results.

Note that in Kashyap et al. (2015), the spiral wave drives an inflow of material into the dense remnant core, heating a region of the core at $\sim 7 \times 10^6 \text{ g cm}^{-3}$ to $\gtrsim 3 \times 10^9 \text{ K}$; this region detonates 109 s into the simulation, destroying the remnant. We also observe heating at the base of the spiral wave in our sub- M_{Ch} remnant, but this region ($\rho \approx 9 \times 10^5 \text{ g cm}^{-3}$) only reaches $\sim 3 \times 10^8 \text{ K}$, well below the $\sim 6 \times 10^8 \text{ K}$ needed for carbon ignition.

At the time of this writing, we have not yet been able to conclusively pinpoint the features in GASOLINE that cause its simulations to differ from AREPO’s. Nevertheless, we discuss below a few hints that may point the way forward. It should first be said that gravitational instability in protoplanetary disks have long been successfully simulated in SPH (Rice et al. 2005; Meru & Bate 2010; Rogers & Wadsley 2012), and for the ~ 200 s that the remnant core is visibly non-axisymmetric, an $m = 1$ spiral mode is also visible. This leads us to suspect that the difference resides in how the crescent is evolved in SPH (though we leave open the possibility that the smearing out of the wavefront due to poor resolution in the disk is also a contributing factor).

The high-viscosity run in Sec. 3.5.2 suggests artificial viscosity may play a role in prematurely smearing out the crescent even when α and β are being dynamically controlled. Our MHD merger performed in AREPO (Ch. 4) is influenced by magnetic viscosity following coalescence, and also shows the crescent becoming axisymmetric within several hundred seconds. Another possible culprit is the surface tension that results from poor discontinuity treatment in traditional SPH, which Heß & Springel (2010) shows can lead to an overdense ellipse at pressure equilibrium with its underdense surroundings spuriously deforming into a sphere. While the boundary between the crescent and void is not as sharp a discontinuity, the temperature and density do change by a factor of 3 over a single smoothing length, and so may be influenced by this effect. We can test if this is the case by performing the same SPH merger using GASOLINE2, which has improved entropy mixing and pressure-averaging across discontinuities.

3.6 Conclusions and Ramifications for Mergers

We simulated the merger of a $0.625 - 0.65 M_{\odot}$ CO WD merger in the SPH code GASOLINE and moving mesh code AREPO, to determine if the outcome of these simulations depend on the code being used. We find differences between the simulations to be small for all phases of the merger up to coalescence. Immediately following coalescence, there is a greater temperature contrast between the void and dense remnant core material in AREPO than in GASOLINE, but otherwise the remnants look remarkably similar to one another. Over the next several hundred seconds, however, the GASOLINE remnant spins down to axisymmetry, and the remnant’s temperature becomes roughly uniform. The AREPO remnant, on the other hand, maintains the integrity of a dense, crescent-shaped cold core surrounded by a hot, tenuous void for at least ~ 1000 s. The core generates a lopsided gravitational potential, which launches an $m = 1$ spiral mode into the disk. This mode rapidly transports disk angular momentum at a rate equivalent to an α -viscosity disk with $\alpha = 10^{-1}$. We suggest that this non-axisymmetric perturbation may be related to the low $T/|W|$ instability seen in neutron star mergers and core-collapse supernova remnants, and possibly the ARS instability found in protoplanetary disks, and that the perturbation may not be captured as well in GASOLINE because of SPH surface tension and artificial viscosity. If so, we expect a longer-lived crescent in simulations using SPH codes updated for improved handling of

mixing and contact discontinuities, including GASOLINE2.

Our results are of greatest consequence for post-merger evolution, which until now has been believed to occur on a viscous timescale (vK10, Shen et al. 2012), and has been simulated using Eulerian codes on axisymmetric cylindrical grids (Schwab et al. 2012; Ji et al. 2013). These are, of course, unable to directly capture non-axisymmetric features of the remnant, and we therefore stress the need to extend post-merger evolution simulations to three dimensions. A simulation that extends to 10^4 s could realistically be performed on AREPO, and we are currently investigating the source of the spurious cold ring discussed at the end of Sec. 3.4 to ensure AREPO does not generate systematic errors over this timespan. Our results likely do not qualitatively change previous conclusions about the outcome of post-merger evolution from Schwab et al. (2012) and Ji et al. (2013), as hydrodynamic waves will simply hasten the general loss of remnant angular momentum and the transformation of the disk into a hot envelope. The details of evolution may differ, though, since wave transport appears most relevant for regions of the disk beyond $\omega \approx 1.5 \times 10^9$ cm, while viscosity will also affect the remnant core. Also, traveling waves do not necessarily dissipate their energy while passing through a medium, whereas viscosity locally dissipates differential rotational energy, and so the heating of the remnant during viscous evolution may also change. Lastly, since the dense crescent remains relatively cold and maintains its integrity long after coalescence, the merger remnant may not be hottest near its center once it becomes axisymmetric, despite being considered “similar-mass” from the results of Ch. 2. This has consequences for the viability of the sub- M_{Ch} merger channel, and is discussed further in Ch. 6.1.

On the other hand, we find that bulk properties of the merger remnant immediately following coalescence do not substantially differ between our GASOLINE and AREPO simulations. Many of the conclusions reached by prior SPH merger studies (eg. LIG09, Ch. 2) might therefore be robust. Definitive evidence, however, will only come by extending our work with AREPO to mergers of CO WDs with other masses. It also remains to be seen if non-axisymmetric perturbations during post-merger evolution depend on the total mass or mass ratio of the merging binary. A parameter-space study could also pinpoint the range of remnants that experience a detonation due to rapid accretion via spiral modes, as seen in Kashyap et al. (2015).

Finally, our simulation does not contain magnetic fields, which, as will be discussed in Ch. 4, are likely to be significantly amplified during the merger and early phases of post-merger evolution. This could substantially affect the remnant’s non-axisymmetric features: for differentially-rotating magnetized neutron stars that feature the low $T/|W|$ instability, Muhlberger et al. (2014) find fields had either a suppressive or an *amplifying* effect on the instability, depending on their strength. In our own magnetized merger simulations, the remnant becomes axisymmetric within ~ 500 s after coalescence, but we use the Powell scheme for divergence cleaning (Sec. 4.6) and likely resolve the remnant disk too poorly to capture the fastest growing magnetorotational instability mode. Future investigation of post-merger MHD evolution is, therefore, also warranted.

We thank Christopher Matzner, Volker Springel, Terrence Tricco, James Wadsley, Ue-Li Pen and Stephen Ro for their insight into hydrodynamics and simulations. This work was supported by the Natural Sciences and Engineering Research Council (NSERC) Vanier Canada Graduate Scholarship and Reinhardt Endowment Travel Fund. Computations were performed on the GPC supercomputer at the SciNet HPC Consortium. SciNet (Loken et al. 2010) is funded by the Canada Foundation for

Innovation under the auspices of Compute Canada, the Government of Ontario, Ontario Research Fund - Research Excellence and the University of Toronto.

Chapter 4

Magnetized Moving Mesh Merger of a Carbon-Oxygen White Dwarf Binary

Chenchong Zhu, Rüdiger Pakmor, Marten H. van Kerkwijk, Philip Chang
The Astrophysical Journal Letters, Volume 806, Issue 1 - article id. L1, 5pp.,
2015 ([Zhu et al. 2015](#))

While simulations of white dwarf mergers are numerous, to date they have not included magnetic fields, even though they are believed to play a significant role in the evolution of the merger remnant. We simulated a $0.625 - 0.65 M_{\odot}$ carbon-oxygen WD binary merger in the magnetohydrodynamic moving mesh code AREPO. Each WD was given an initial dipole field with a surface value of $\sim 10^3$ G. As in simulations of merging double neutron star binaries, we find exponential field growth within Kelvin-Helmholtz instability-generated vortices during the coalescence of the two stars. The final field has complex geometry, and a strength $> 10^{10}$ G at the center of the merger remnant. Its energy is $\sim 2 \times 10^{47}$ ergs, $\sim 0.2\%$ of the remnant's total energy. The strong field likely influences further evolution of the merger remnant by providing a mechanism for angular momentum transfer and additional heating, potentially helping to ignite carbon fusion.

4.1 Introduction

The merging process has, in the last decade, been investigated with increasingly sophisticated 3D hydrodynamic simulations (Ch. 2, Lorén-Aguilar et al. 2009; Pakmor et al. 2010; Dan et al. 2012; 2014; Raskin et al. 2012; Moll et al. 2014). However, one fundamental piece missing in WD merger studies so far is magnetic fields.

Mergers (that do not immediately explode) are expected to produce remnants that are susceptible to magnetic dynamo processes such as the magnetorotational instability (MRI; Balbus & Hawley 1991), Tayler-Spruit dynamo (e.g. Spruit 2002), and the $\alpha\omega$ dynamo (if convection occurs in the inner disk; García-Berro et al. 2012). It has therefore long been suspected that they can generate strong fields, and recent 2D simulations of MRI in the remnant (Ji et al. 2013) have indeed shown amplification of a weak seed field to $> 10^{10}$ G. Magnetic shear from these fields transports angular momentum over a timescale of $\sim 10^4 - 10^8$ s (van Kerkwijk et al. 2010; Shen et al. 2012) – far shorter than the thermal timescale of the remnant – and also (non-locally) heats the remnant. The latter, combined with loss of rotational support from angular momentum transport, could push remnant temperatures past the point of carbon ignition ($\sim 6 \times 10^8$ K for densities between $10^5 - 10^7$ g cm $^{-3}$), leading to either stable nuclear burning or a runaway. This mechanism could potentially drive nuclear runaways even in remnants with masses below the Chandrasekhar Mass M_{Ch} that have traditionally been considered stable (van Kerkwijk et al. 2010).

While field growth after the merger has been explored, field growth *during* the merger is also expected, and can have a profound impact on the post-merger magnetic evolution. Magnetohydrodynamic (MHD) double neutron star (NS) binary merger simulations (eg. Price & Rosswog 2006; Kiuchi et al. 2014; Giacomazzo et al. 2015) have found that Kelvin-Helmholtz vortices produced along the shear interface between the coalescing stars can amplify field strengths by orders of magnitude (Obergaulinger et al. 2010; Zrake & MacFadyen 2013). The same should hold true for WD mergers. Motivated by this, we present the first MHD simulation of a CO WD binary merger.

This chapter is organized as follows: in Section 4.2, we describe AREPO and our initial conditions. The results of our simulation are in Section 4.3. In Section 4.4, we test our simulation’s robustness, and finally in Section 4.5 we discuss implications for merger outcomes and possible avenues for future research.

4.2 Methods

We employ the moving-mesh code AREPO (Springel 2010a), which solves the equations of ideal MHD on a Voronoi mesh coupled with self-gravity. We operate the code in its pseudo-Lagrangian mode, so that the mesh-generating points that define the Voronoi grid move with the local velocity of the fluid. To conserve angular momentum to within $\sim 2\%$ of its initial value, we use the latest improvements to time integration and gradient estimate (Pakmor et al. 2016). AREPO’s MHD implementation is described in Pakmor et al. (2011a) and Pakmor & Springel (2013); we use the Powell et al. (1999) eight-wave scheme for divergence control. Our simulation ignores outer hydrogen and helium layers, composition gradients, and nuclear reactions (negligible for sub- M_{Ch} CO WD mergers; Lorén-Aguilar et al. 2009; Raskin et al. 2012).

We model the merger of two CO WDs with masses of 0.625 and $0.65 M_{\odot}$, respectively, in a circular,

unsynchronized binary with initial separation $a_0 = 2.20 \times 10^9$ cm (corresponding period $P_0 = 49.5$ s), chosen (using the estimate of Eggleton 1983) such that the lower-mass WD just fills its Roche lobe. We chose masses typical of the narrowly peaked empirical mass distribution of field CO WDs (Kleinman et al. 2013). Our initial conditions are very similar to those of the $0.625 - 0.65 M_\odot$ binary simulated with smoothed particle hydrodynamics (SPH) in Ch. 2. As in Ch. 2, both WDs are generated with a uniform initial temperature of 5×10^6 K (the corresponding thermal pressure is dynamically irrelevant) and a uniform composition of equal parts carbon and oxygen by mass. They are separately relaxed to hydrostatic equilibrium using the SPH code GASOLINE (Wadsley et al. 2004) and added to AREPO by converting the SPH particles to mesh-generating points while retaining their conservative quantities (mass, momentum and energy). A uniform 10^{-5} g cm $^{-3}$ background grid fills up a 10^{12} cm box centered on the binary. Each WD is given a (dynamically irrelevant) dipole seed magnetic field with an equatorial surface value of 10^3 G (and corresponding central field of $\sim 2 \times 10^7$ G). The fields are overlapped when the two stars are placed into a binary.

The mass resolution of our simulation is $m_{\text{cell}} \approx 1 \times 10^{-6} M_\odot$. We utilize explicit refinement and derefinement (Vogelsberger et al. 2012) to keep cell masses within a factor of two of $10^{-6} M_\odot$ and to ensure adjacent cells differ by less than a factor of 10 in volume.

4.3 Results

We depict the evolution of the binary in Fig. 4.1, highlighting temperature T and magnetic field strength $|B|$. Fig. 4.2 shows the growth of total magnetic energy E_B over time.

In the first stage of the merger, up to ~ 180 s, the $0.625 M_\odot$ donor WD transfers mass to the $0.65 M_\odot$ accretor for about 3.5 orbits before fully disrupting. Because our initial conditions are approximate – the WDs are not initially tidally deformed – mass transfer begins in spurts as the WDs stretch in response to the binary potential, and occurs at a rate that is artificially high (Dan et al. 2011). The early mass transfer shears the atmospheres of both WDs. As a result, E_B grows roughly linearly in the first ~ 100 s, reaching about quadruple its initial value. Since the initial mass transfer rate is artificially high, this growth is likely an overestimate, but remains negligible compared to what follows.

By ~ 120 s, mass transfer becomes steady, and a stream of material from the donor wraps around the accretor, forming a shear layer. Along it, the Kelvin-Helmholtz instability generates a string of hot vortices that exponentially amplify their entrained magnetic fields. This is illustrated in Fig. 4.1 (row 2), where the hot vortices along the donor-accretor interface correspond to regions of high field strength. At ~ 180 s, tidal forces between the two WDs become strong enough to fully disrupt the donor, which then coalesces with the accretor over ~ 50 s. During this time, infalling donor material spirals into the accretor, severely deforming the accretor while carrying the string of magnetized vortices toward the system’s center of mass (CM). Fig. 4.2 shows E_B growing exponentially by a factor of $\sim 10^7$ over ~ 100 s, with an e -folding time $\tau = 6.4$ s, comparable to the typical turnover timescale of the largest eddies $2\pi R_{\text{eddy}} / \Delta v_{\text{shear}} \sim 3$ s, where Δv_{shear} is the velocity difference across the shear layer.

By ~ 250 s many of the vortices have merged together into a hot, rapidly rotating underdense void at the CM (Fig. 4.1, row 4). Magnetic growth within the void begins to saturate as its magnetic and kinetic energy approach equipartition. The rate of field growth slows as well, with E_B growing another two orders of magnitude over ~ 150 s before plateauing at $\sim 2 \times 10^{47}$ ergs at ~ 400 s.

In Fig. 4.3 we show the density ρ , T , $|B|$ and ratio of magnetic to rotational energy density e_B/e_{rot}

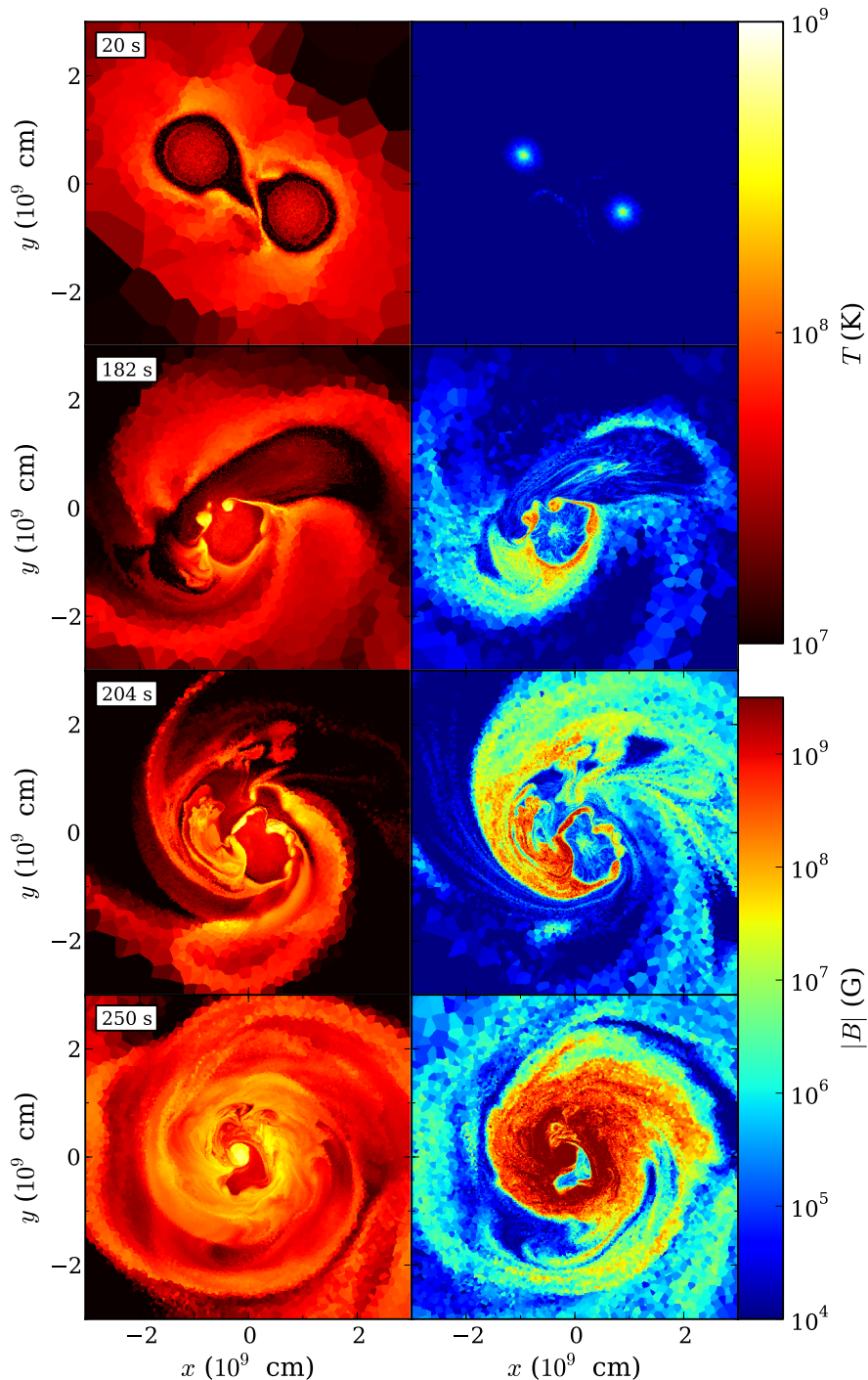


Figure 4.1: Series of temperature T (left column) and magnetic field strength $|B|$ (right) logarithmic intensity profiles in the equatorial plane of the merger for four snapshots in time (rows; time indicated at the top left of each row).

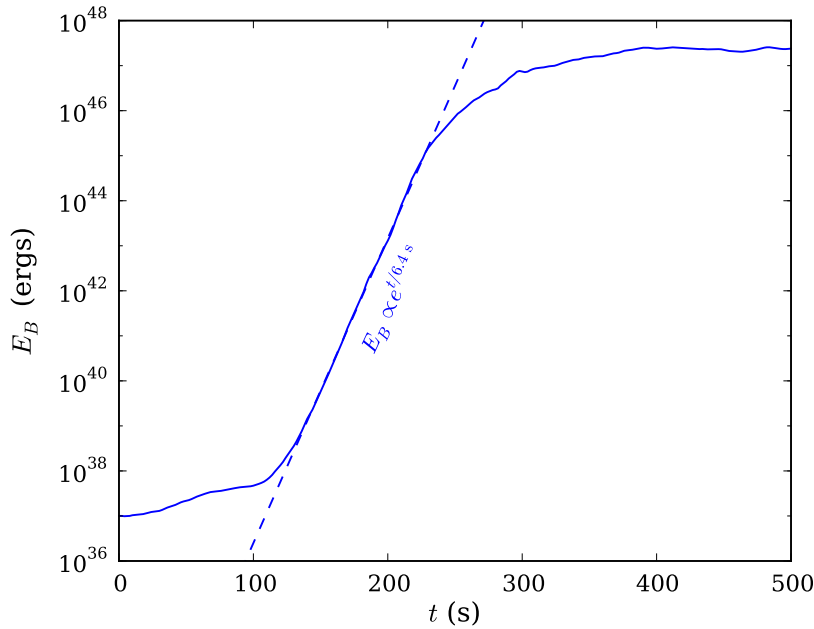


Figure 4.2: Total magnetic energy E_B over time, with a best fit to the rapid exponential growth (dashed $E_B \propto e^{t/6.4\text{s}}$ line).

of the merger remnant at 400 s. The remnant consists of a dense, degeneracy-supported core containing $\sim 60\%$ of the remnant’s mass, a partly thermally supported hot envelope that surrounds the core, and a rotationally supported disk, a configuration similar to the SPH 0.625–0.65 M_\odot remnant from Ch. 2. The AREPO remnant core, however, has distinctly non-axisymmetric density and temperature structures, unlike the SPH simulation which achieves axisymmetry ~ 170 s after coalescence (Zhu et al. 2013, online figure set Fig. 1.16). The magnetic fields are too weak during the merger to have an effect on merger dynamics, so these contrasts are due to differences in the *hydrodynamic* schemes between AREPO and SPH (Ch. 3).

The remnant magnetic field configuration is complex: while field lines are coherent along “strands” of high field strength, neighboring strands often point in opposite directions (see Fig. 4.3). In the core, the volume-averaged field strength is 4×10^{10} G, but strands of $> 10^{11}$ G field perforate the core. The field remains $> 10^9$ G near the core-disk interface at $\sim 10^9$ cm, before dropping below 10^7 G at $\gtrsim 3 \times 10^9$ cm. The total magnetic field energy is $\sim 0.2\%$ the total, $\sim 0.6\%$ the total rotational, and $\sim 6\%$ the total differential rotation energy of the remnant.¹ This energy is roughly equally partitioned into toroidal and poloidal field components, with the ratio of poloidal to total magnetic energy $E_{B\phi}/E_B = 0.62$. Studies of local field amplification within Kelvin-Helmholtz vortices predict magnetic growth saturates when the magnetic and kinetic energy densities are close to equipartition (Obergaulinger et al. 2010; Zrake & MacFadyen 2013). In our simulation, this is only the case for the strands of $> 10^{11}$ G field, where magnetic energy density is $\sim 7\%$ ($\sim 47\%$) the rotational (differential rotation) energy density (see Fig. 4.3, column 4). It is possible that because the strands are distributed throughout the core, they drive the core’s overall evolution and inhibit further magnetic amplification

¹Differential rotation energy of a cell is estimated with $E_{\text{drot}} = m_{\text{cell}}|\mathbf{v}| |\nabla \times \mathbf{v}| V_{\text{cell}}^{1/3}$.

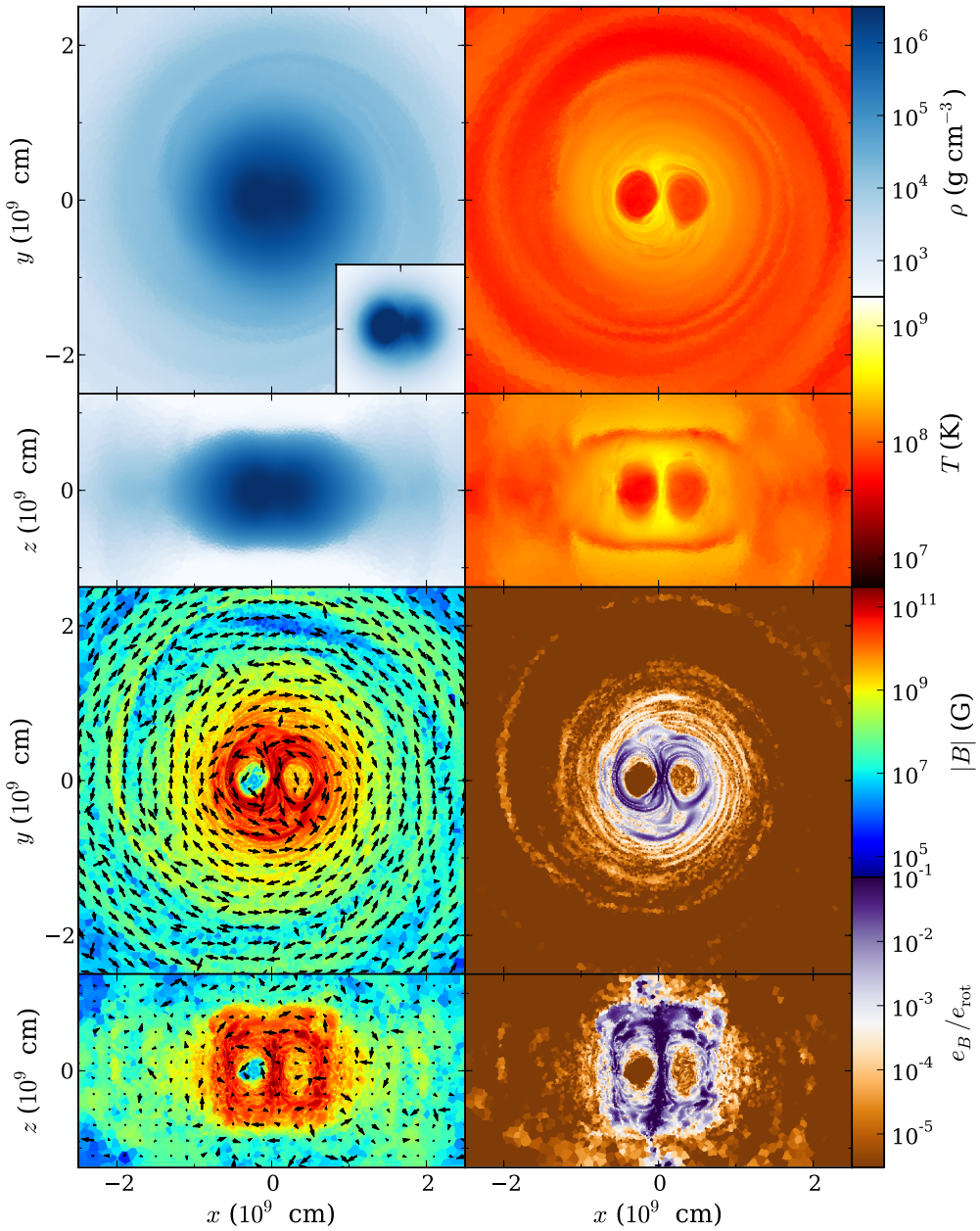


Figure 4.3: From leftmost to rightmost column, equatorial plane (top row) and polar (bottom) logarithmic intensity profiles of density ρ , temperature T , magnetic field strength $|B|$ and ratio of magnetic to rotational energy density e_B/e_{rot} for the simulation at 400 s (~ 170 s after coalescence). The equatorial plane density plot includes a linear profile of the remnant core (with the same x and y scale as the logarithmic profile) to show its shape. Arrows in the magnetic field strength plots indicate field directions, with their lengths equal to the fraction of the field that lies along the xy plane (top frame) and xz plane (bottom).

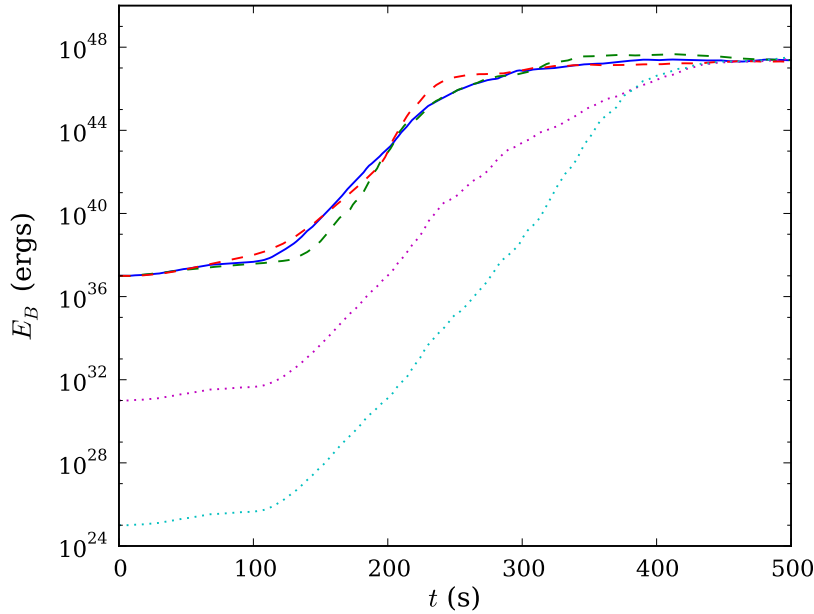


Figure 4.4: Total magnetic energy E_B over time for the fiducial (solid blue; $m_{\text{cell}} \approx 1 \times 10^{-6} M_\odot$, equatorial surface field strength 10^3 G) simulation and the robustness tests. Dashed lines represent low (green; $m_{\text{cell}} \approx 5 \times 10^{-6} M_\odot$) and high resolution (red; $m_{\text{cell}} \approx 2 \times 10^{-7} M_\odot$) simulations. Dotted lines represent 1 G (magenta) and 10^{-3} G (cyan) low initial field simulations.

in their surroundings.

Some of the magnetized accretion stream is ejected during coalescence and integrates into the inner disk ($\sim 1 - 3 \times 10^9$ cm), producing a $10^7 - 10^8$ G field by 400 s. This field has a negligible hydrodynamic effect on the disk (magnetic energy density to pressure ratio $e_B/P \approx 3 \times 10^{-5}$ at 2×10^9 cm), and, unlike the field in the core, has *not* saturated: $|B|$ continues to grow exponentially with $\tau \sim 200$ s.²

4.4 Robustness Tests

4.4.1 Resolution Test

To check that our results are not resolution-limited, we performed simulations, otherwise identical to the fiducial one in Sec. 4.3, with lower and higher mass resolutions of $m_{\text{cell}} \approx 5 \times 10^{-6} M_\odot$ and $m_{\text{cell}} \approx 2 \times 10^{-7} M_\odot$, respectively. Fig. 4.4 compares the E_B evolution between these simulations (dashed lines) and the fiducial one (solid).

The three runs are qualitatively identical. Donor disruption and the start of exponential field growth occurs ~ 0.75 orbital periods earlier at low resolution, and ~ 0.5 periods later at high, because the outer layers of the WDs are better captured and the differences in hydrostatic equilibrium between AREPO and GASOLINE are less pronounced at higher resolution. Exponential growth rates are similar between

²The remnant disk is generally poorly resolved, even at the highest resolution used in Sec. 4.4.1; this may artificially slow the disk field growth rate.

the runs - the E_B *e*-folding time is $\tau = 4.9$ s for the low resolution run, faster than $\tau = 6.4$ s for the fiducial. At high resolution, the growth curve appears to be separated into two phases, with $\tau = 7.8$ s before coalescence, and $\tau = 3.9$ s during it. The total magnetic energy at the end of exponential growth is also similar - at 400 s, E_B is $\sim 4 \times 10^{47}$ ergs in the low resolution run and $\sim 1.5 \times 10^{47}$ ergs in the high, compared to $\sim 2 \times 10^{47}$ ergs at the fiducial resolution. The fiducial and high resolution runs also qualitatively have very similar magnetic field structures by 400 s. Our fiducial resolution of $1 \times 10^{-6} M_\odot$ therefore appears sufficient for qualitatively capturing the growth and final field configuration of the merger.

In their MHD disk galaxy simulations, [Pakmor & Springel \(2013\)](#) find faster field growth and higher field strength at saturation in their lowest resolution run, which they attribute to larger divergence errors at lower resolution. We perform a similar test, and also see a trend of decreasing divergence error (and more accurate magnetic evolution) at higher resolution, though the errors of all our simulations are at least a factor of two smaller than any reported in [Pakmor & Springel \(2013\)](#). The errors are highly localized in space and trace steep magnetic gradients, suggesting they contribute only to small-scale variations in the magnetic field.

4.4.2 Changing the Seed Field Strength

To understand the dependence of our results on the initial seed field, we ran two additional simulations in which we decreased the strength of the seed field by 3 and 6 orders of magnitude leading to an initial equatorial surface field of 1 G (central field $\sim 2 \times 10^4$ G), and 10^{-3} G (~ 20 G), respectively. Fig. 4.4 shows their E_B evolution (dotted lines). We find the growth curves to be homologous between both low initial field runs and the fiducial one – differing only by the ratios of seed E_B – up to ~ 200 s, with the *e*-folding time for exponential amplification approximately 6.5 s for all three runs. By ~ 250 s, the field in the fiducial simulation begins to plateau, while amplification (of initially weaker fields) continues for several hundred more seconds in the low initial field runs. For both runs, E_B plateaus at $\sim 3 \times 10^{47}$ ergs, comparable to the fiducial $\sim 2 \times 10^{47}$ ergs. Because the fields in the low initial field runs remain dynamically irrelevant for longer, however, their structures differ from that of the fiducial run and resemble more the crescent in Fig. 4.1, row 4. The disk field does not saturate in any simulation – its strength is proportional to the strength of the seed field, and is thus much weaker in the low initial field runs. Our tests thus suggest that the exponential growth, growth timescale and plateau E_B are robust to changes in initial field strength, while the remnant field configuration is more sensitive to the choice of seed field.

4.5 Discussion

We have shown that the merger of a $0.625 - 0.65 M_\odot$ CO WD binary produces a strong, $> 10^{10}$ G magnetic field with a complex structure that winds through the remnant core and into the inner disk. Similar to previous simulations of binary NS mergers, the strong field is generated by dynamo action within Kelvin-Helmholtz vortices formed during the coalescence of the two WDs. Since these vortices are ubiquitous in WD mergers, strong magnetic fields are a likely feature of all merger remnants. The degree to which a field permeates the remnant core depends on how thoroughly the donor and accretor mix during coalescence, which itself is sensitive to initial conditions such as the degree

of synchronization between the WDs, or how accurately their tidal bulges and early mass transfer are captured (Dan et al. 2011; 2014). A parameter space study of magnetized mergers is needed to investigate the range of possible remnant field configurations.

We note that NS mergers simulated in Eulerian grid codes generally show E_B growing by only a factor of $\sim 10^2 - 10^3$ during coalescence, compared to the $\sim 10^9$ we see, despite these simulations having resolutions comparable or superior to our low resolution AREPO run. This weaker growth is also inconsistent with the amplification to local kinetic equipartition seen in small-scale simulations (Obergaulinger et al. 2010; Zrake & MacFadyen 2013), and is attributed to insufficient resolution in the NS merger simulations (Kiuchi et al. 2014; Giacomazzo et al. 2015, though see Dionysopoulou et al. 2015). Giacomazzo et al. (2015) incorporated a subgrid magnetic amplification model, calibrated using Zrake & MacFadyen (2013)'s results, into their Eulerian NS merger simulation, and found E_B amplification by a factor of $\sim 10^{10}$ over a single dynamical time.³ This suggests AREPO may be better able to resolve small-scale velocity structures than an Eulerian code at comparable resolution, or better able to couple these structures to magnetic growth. Further work is needed to understand the magnetic field growth in detail.

The density profile of the remnant remains non-axisymmetric for hundreds of seconds after coalescence. As a result, the core continues to evolve dynamically, and by 400 s has begun to launch a pair of spiral waves into the surrounding medium (see the density panel of Fig. 4.3), which transport angular momentum on a timescale rivalling that for magnetic shear. While Kashyap et al. (2015) report a similar spiral instability in their Eulerian remnant evolution simulation, SPH simulations like those of Ch. 2 rapidly achieve axisymmetry after coalescence and do not form spiral waves. As noted earlier, this difference between AREPO and SPH simulations is a product of the differences between their hydrodynamic schemes. Further study is needed to understand these differences and their consequences for remnant evolution (Ch. 3).

The post-merger evolution of the remnant has been followed to $\sim 3 \times 10^4$ s with axisymmetric cylindrical (two-dimensional) Eulerian grid simulations (Schwab et al. 2012; Ji et al. 2013). As described earlier, Ji et al. (2013)'s MHD simulation of a $0.6 - 0.6 M_\odot$ remnant shows the development of a strong magnetic field due to MRI. The subsequent heating and angular momentum transport due to the fields pushes core temperatures to ignition, supporting the possibility of a nuclear runaway within sub- M_{Ch} remnants. Their results are, however, likely sensitive both to their initial hydrodynamic conditions – which may have artificially high core temperatures – and their chosen seed magnetic field, a pure poloidal one to optimize the onset of MRI. Our much stronger poloidal-toroidal field could substantially change post-merger evolution. Moreover, the persistence of a non-axisymmetric remnant core will lead to evolution that clearly cannot be captured in a axisymmetric cylindrical grid. We therefore stress the need to perform high-resolution three-dimensional simulations of post-merger evolution to determine the final fate of the remnant.

There are a number of potentially observable consequences of the magnetic fields produced by the merger. Ji et al. (2013) note the creation of a magnetized corona and biconal jet in their simulations, which act in concert to cause an outflow of material near the remnant's poles. This outflow eventually unbinds $\sim 10^{-3} M_\odot$ of material, and Beloborodov (2014) estimates it should lead to an optical transient with a duration of ~ 1 day and peak $L \sim 10^8 L_\odot$, which should be detectable by optical surveys.

³Price & Rosswog (2006)'s SPH simulations also show strong amplification; while runs using their Euler potential MHD method suffer exaggerated field growth from improper boundary conditions, their B -based runs show similar results (Price 2012).

If a remnant later experiences a nuclear runaway and explodes as a SN Ia, its magnetic field will increase the late-time emission by trapping positrons (produced by ^{56}Co β^+ decay) that would otherwise escape the ejecta. The trapping efficiency depends on the strength and configuration of the remnant magnetic field, with a locally entangled $\sim 10^{11}$ G field – similar to our findings – well able to trap positrons past 1000 days (Ruiz-Lapuente & Spruit 1998). This is in line with observed late-time SN Ia light curves (most recently Kerzendorf et al. 2014b).

Those remnants that do not explode will retain strong fields when they reach quiescence, and populate the high-mass tail of the distribution of isolated high-field magnetic WDs (García-Berro et al. 2012; Külebi et al. 2013; Wickramasinghe et al. 2014; Briggs et al. 2015). Since these remnants will have temperatures high enough to fuse any remaining hydrogen and helium they possess, their properties might eventually be akin to the recently discovered hot DQ WDs (e.g. Dufour et al. 2013). These WDs have carbon-dominated atmospheres and $T_{\text{eff}} \approx 2 \times 10^4$ K, are often strongly magnetized (~ 1 MG) and sometimes have monoperiodic photometric variability (possibly due to rapid rotation). Their origins remain unclear (Althaus et al. 2009; Lawrie et al. 2013; Williams et al. 2013). Dunlap & Clemens (in press) recently found that, if most known hot DQs are massive ($M \gtrsim 0.95M_{\odot}$), their population’s velocity dispersion corresponds to a kinematic age much older than what would be inferred from their temperatures, suggesting that at least some hot DQs are WD-WD merger remnants. If so, their observed properties would constrain merger and remnant evolutionary models, and double-degenerate channels for SNe Ia.

We thank Christopher Thompson, Christopher Matzner, Volker Springel, Bart Dunlap, Yuri Levin, Henk Spruit, Ue-Li Pen and Stephen Ro for their insights into magnetohydrodynamics and simulations. This work utilized the SciNet HPC Consortium’s GPC supercomputer (Loken et al. 2010). C.Z. acknowledges support from the Natural Sciences and Engineering Research Council (NSERC) Vanier Canada Graduate Scholarship. R.P. acknowledges support by the European Research Council under ERC-StG grant EXAGAL-308037 and by the Klaus Tschira Foundation. P.C. is supported by the NASA ATP program through NASA grant NNX13AH43G, and NSF grant AST-1255469.

4.6 Postscript: Reconsidering Divergence Cleaning in Arepo

In Sec. 4.5 we discussed why AREPO might be capturing (at least some proxy of) rapid magnetic amplification during the merger when Eulerian simulations of NS mergers at similar resolutions do not. Since the publication of Ch. 4 as Zhu et al. (2015), it has been pointed out that the amplification could be the spurious result of AREPO’s divergence cleaning mechanism.

In most multidimensional numerical MHD schemes, the “divergence constraint” of $\nabla \cdot \mathbf{B} = 0$ is not guaranteed, and if the implicit divergence terms in Eqn. 3.1 are not considered, these schemes can in practice lead to spurious forces and magnetic instabilities (Tóth 2000; Hopkins & Raives 2016). A number of solutions exist (eg. Tóth 2000), and the most widely-used is Evans & Hawley (1988)’s constrained transport method, which staggers the different components of the magnetic field within the discretization to maintain the divergence constraint to round-off errors. This reliance on grid geometry, however, has made it challenging to implement in a moving mesh code (Mocz et al. 2014). Until the recent adoption of constrained transport in AREPO in (Mocz et al. 2016), the code instead used either the Dedner et al. (2002) or Powell et al. (1999) divergence control schemes. The former introduces an

additional conserved scalar term ψ to \mathbf{U} in Eqn. 3.2 which is coupled to $\nabla \cdot \mathbf{B}$ while simultaneously being advected and forced to exponentially decay. The latter adds a source term to the righthand side of Eqn. 3.2 that is proportional to $\nabla \cdot \mathbf{B}$, which passively advects divergence errors but does not damp them. The Dedner method is superior because it actively minimizes divergence errors rather than simply preventing their local accumulation, but its implementation in AREPO required prohibitively small timesteps and tended to become unstable in highly dynamic environments (Pakmor & Springel 2013), hence our use of the Powell scheme.

In Fig. 4.5, we show the magnetic field strength, relative divergence error and absolute relative divergence error of our fiducial merger simulation at $t = 200$ s, when the donor has just been disrupted. The (mass-weighted) average relative divergence error $\langle |\nabla \cdot \mathbf{B}|(V_{\text{cell}})^{1/3}/B \rangle = 0.18$ (where V_{cell} is the Voronoi cell volume) is typical of both this simulation and Pakmor & Springel (2013)'s galaxy disk evolution one, but much larger than typical results from Dedner cleaning-based codes (Tricco 2015; Hopkins & Raives 2016). As in Pakmor & Springel (2013), the divergence error alternates on very small scales (Fig. 4.5 middle panel), and peaks near large magnetic gradients (comparing top and bottom panels). While errors cancel over large scales (the average relative error with the sign of the divergence included is $\langle \nabla \cdot \mathbf{B}(V_{\text{cell}})^{1/3}/B \rangle = -1.4 \times 10^{-3}$), the regions of highest magnetic gradient correspond to the shear interface between donor and accretor, where we believe the field is amplified. It is therefore plausible that errors at small scales spuriously magnify the magnetic dynamo associated with the shear layer and Kelvin-Helmholtz vortices.

This hypothesis is supported by Hopkins & Raives (2016), who perform a battery of tests comparing the Dedner and Powell mechanisms for their mesh-free finite-volume code GIZMO, and show divergence errors in Powell-based simulations of advection and hydromagnetic instability lead to spurious and unstable field growth. Moreover, comparisons between Powell and constrained transport-based AREPO using simulations of MHD turbulence and disk galaxy evolution show that the Powell scheme leads to greater magnetic field amplification by up to an order of magnitude, as well as a qualitatively different field topology (Mocz et al. 2016).

Caution is therefore in order when using this chapter's results, at least until they have been compared with simulations using AREPO's new constrained transport scheme. Given that the results will likely be different, it may also be useful to conduct a simpler test case of field evolution within a single Kelvin-Helmholtz vortex at various resolutions and compare the results with those of Obergaulinger et al. (2010) and Zrake & MacFadyen (2013). Nevertheless, as discussed in Sec. 4.3, the remnant magnetic field's bulk properties following coalescence are physically plausible, and are likely to be more robust than the detailed field configuration. We use these bulk properties (alongside Ji et al. (2013)'s work) when considering magnetic simmering WDs the next chapter.

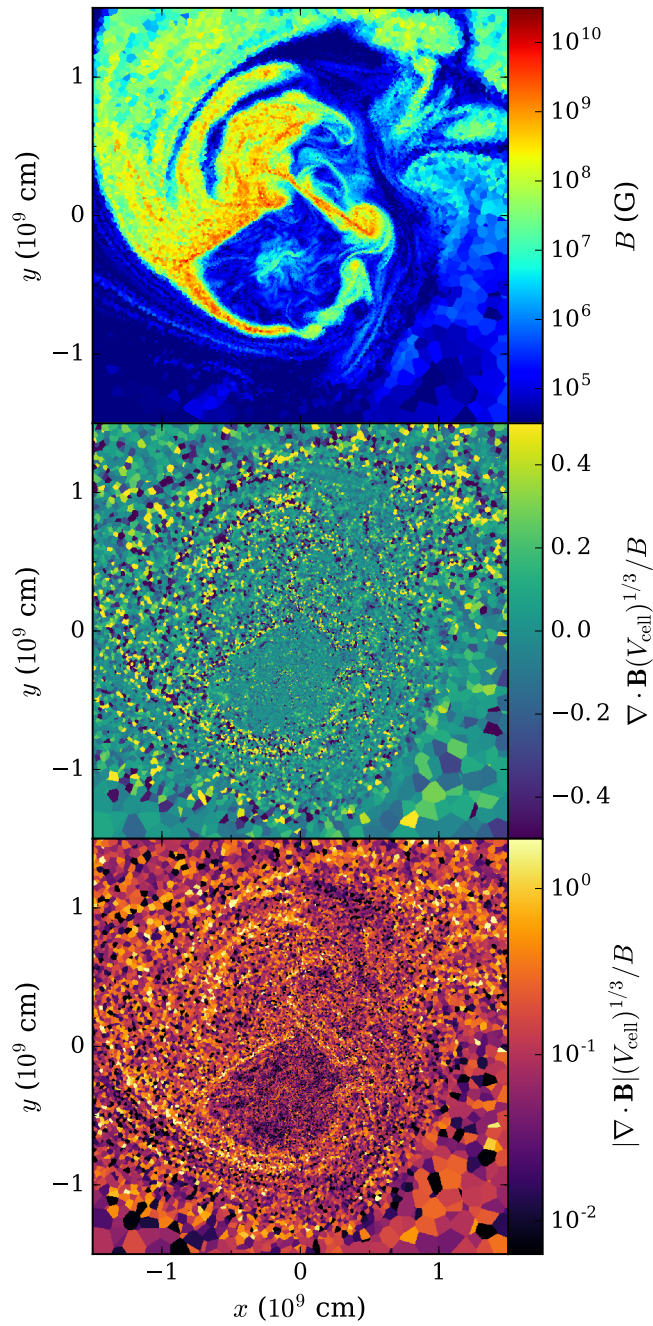


Figure 4.5: From top to bottom, equatorial plane intensity profiles for the magnetic field strength, relative divergence error (linear scale) and absolute relative divergence error (logarithmic) for the simulation at 200 s.

Chapter 5

The Evolution of Simmering Sub-Chandrasekhar Mass WDs

Chenchong Zhu, Philip Chang and Marten H. van Kerkwijk
(Zhu et al. in preparation)

When fusion is lit in the degenerate interior of a carbon-oxygen white dwarf, the resulting nuclear runaway starts with a “simmering phase”, in which convection transports energy out of the burning region. While simmering inevitably leads to some form of explosion for white dwarfs near the Chandrasekhar mass, in ones with lower mass it may instead lead to the lifting of degeneracy and expansion into a carbon-burning star. Using analytical arguments and simple models, we determine that the critical mass for explosions to be possible is $M_{\text{crit}} = 1.135 M_{\odot}$. In principle, effects from rotation and magnetic fields might lead to a change in the critical mass. For the rotation rates found in merger remnant simulations, the effect is almost certainly minimal, $\lesssim 0.01 M_{\odot}$. For magnetic fields the case is less clear, since interaction with convection is poorly understood, but simple order-of-magnitude arguments again suggests only a small effect.

5.1 Introduction

Type Ia supernovae (SNe Ia) are generally thought to be the thermonuclear explosions of carbon-oxygen white dwarfs (CO WDs). While the current body of observational evidence has greatly strengthened this hypothesis, the mechanism(s) by which a WD is agitated into exploding remains mysterious (see Howell 2011; Hillebrandt et al. 2013; Maoz et al. 2014 for recent reviews).

The traditional scenario involves slow accretion of material onto the CO WD from either a non-degenerate companion or another WD. As the CO WD approaches the Chandrasekhar mass M_{Ch} , its central density becomes sufficiently high that the rate of heating from pycnonuclear carbon fusion exceeds that of neutrino cooling. The resulting increase in central entropy establishes a convection zone that transports the heat of the nuclear burning region to the rest of the WD interior. The WD is highly degenerate, however, and does not expand in response to the heating. Instead, a nuclear runaway ensues over the next thousand years as the WD grows ever hotter, a period of evolution referred to as the simmering phase. Near- M_{Ch} WDs eventually become hot enough that the timescale for nuclear burning becomes shorter than the dynamical time – we call this “dynamical burning” – at which point an explosion becomes inevitable.

This scenario is beset by two major issues: an apparent paucity of accreting or merging CO WDs that can achieve M_{Ch} , and the difficulty for the thermonuclear explosion of a M_{Ch} WD to reproduce the properties and population-level trends of observed SN Ia (van Kerkwijk et al. 2010, henceforth vK10, and references therein). These, in turn, have spurred research into alternative formation channels where CO WDs with masses significantly *below* M_{Ch} also explode. Including them would bolster substantially the number of progenitors (eg. Badenes & Maoz 2012), and their explosions could closely resemble ordinary SNe Ia (Shigeyama et al. 1992; Sim et al. 2010).

Since hydrostatic sub- M_{Ch} WDs do not possess central densities high enough for pycnonuclear fusion, burning must be prompted either by a shockwave (that immediately triggers dynamical burning), or by heating material to $T \approx 6 \times 10^8$ K to induce fusion through high temperatures, rather than high densities. The former is presumed in eg. the double-detonation (eg. Fink et al. 2007; Woosley & Kasen 2011), violent merger (eg. Pakmor et al. 2010) and collision (eg. Lorén-Aguilar et al. 2010) scenarios. The latter is presumed in the sub- M_{Ch} CO WD merger scenario of vK10, in which two CO WDs of mass $\sim 0.65 M_{\odot}$ merge, forming a merger remnant that is differentially rotating throughout its structure, and so is susceptible to magnetohydrodynamic instabilities (Shen et al. 2012; Ji et al. 2013). It subsequently becomes strongly magnetized, leading to outward transport of angular momentum over a viscous timescale of $\sim 10^4 - 10^8$ s that robs the remnant of its rotational support (vK10, Shen et al. 2012; though see Ch. 3, Kashyap et al. 2015 for evidence of transport through spiral hydrodynamic waves). This viscous evolution compresses and adiabatically heats the remnant’s interior, which the simulation of Ji et al. (2013) suggests leads to central carbon ignition.

In the vK10 scenario, and, indeed, any situation where non-dynamical nuclear burning ignites under degenerate conditions in a sub- M_{Ch} WD, a simmering phase ensues just like in the near- M_{Ch} case. Sub- M_{Ch} WDs, however, are less dense, and their degeneracy is at least partially lifted before they reach temperatures where burning becomes dynamical, which depends only weakly on density. There is, in fact, a critical mass M_{crit} below which the simmering WD never reaches dynamical burning before becoming non-degenerate enough to expand and cool off. Even those WDs that do achieve dynamical burning may substantially expand beforehand. Since the fraction of material fused to

peak-iron products in an SN Ia depends on its progenitor's density profile, a pre-expanded WD will produce reduced, or even negligible, amounts of ^{56}Ni . Thus a nuclear runaway at the center of a sub- M_{Ch} remnant neither inevitably leads to an explosion, nor is any explosion guaranteed to resemble an SN Ia.

In this chapter, we investigate the simmering phase of sub- M_{Ch} WDs undergoing a center-lit thermonuclear runaway. In Section 5.2 we detail our semi-analytical model and its assumptions. While our motivation is to better understand the evolution of merger remnants, we keep these assumptions simple, and we stress that our models do *not* necessarily account for any specific prior evolution. We present our results in Section 5.3, determining both the value of M_{crit} and estimating the mass of radioactive ^{56}Ni produced if a detonation were to follow immediately. Simmering WDs that formed in mergers are expected to be rotating and magnetized (eg. Ch. 4, Wickramasinghe et al. 2014), and we also try to ascertain how M_{crit} and M_{Ni} change in their presence using simple prescriptions for rotational and magnetic convective suppression. Lastly, in Section 5.4, we discuss how our results apply to the vK10 scenario as well as implications for SN Ia progenitor studies in general.

5.2 Modeling Sub- M_{Ch} WD Simmering

Simmering in near- M_{Ch} WDs has been extensively studied with 1D semi-analytical calculations by eg. Woosley et al. (2004; hereafter WWK04), Lesaffre et al. (2006); Piro (2008), and Piro & Chang; (2008; hereafter PC08). We adapt the analytical machinery of WWK04 and PC08 to sub- M_{Ch} WDs. In Sec. 5.2.1 we show that the simmering phase can be approximated well by a sequence of hydrostatic WD models, and in Sec. 5.2.2 we detail our model implementation.

5.2.1 Analytical Description

For a center-lit nuclear runaway, carbon ignition is achieved when material near the center of the WD is heated past $\sim 6 \times 10^8 \text{ K}$ and the heating timescale due to carbon fusion (at $\rho \sim 10^8 \text{ g cm}^{-3}$),

$$\tau_{\text{CC}} \equiv \frac{c_p T}{\varepsilon_{\text{CC}}} \sim 10^2 \text{ yr}, \quad (5.1)$$

becomes smaller than the cooling timescale from neutrino losses $\tau_\nu \equiv c_p T / \varepsilon_\nu$.¹ ε_{CC} is the specific energy generation rate for carbon burning, ε_ν the specific energy loss rate due to neutrino creation, and c_p the specific heat at constant pressure. The energy deposited from nuclear burning steepens the temperature gradient until convection is triggered.

We will need the timescale for convective energy transport, τ_{conv} , which requires the convective luminosity L_{conv} . In steady state convection, this is equal to the nuclear luminosity, i.e.

$$L_{\text{conv}} = L_{\text{CC}} = \int_0^{R_{\text{WD}}} 4\pi r^2 \rho \varepsilon_{\text{CC}}(\rho, T) dr. \quad (5.2)$$

In a simmering WD part of L_{CC} is diverted into heating the WD, and to perform work expanding it once degeneracy begins to be lifted, reducing the convective luminosity in the upper convection zone (PC08). For simplicity, and because we mainly consider convective velocities near the center of the WD, we do not consider this effect in our models.

¹The conduction timescale, $\tau_{\text{cond}} \sim 10^6 \text{ yr}$, is far longer than either.

Near the center, and closer to the end of simmering, $\rho_7 = (\rho/10^7 \text{ g cm}^{-3}) = 3$ and $T_9 = (T/10^9 \text{ K}) = 1.2$, and the specific energy generation rate

$$\varepsilon_{\text{CC}} \approx 1.3 \times 10^{15} (\rho_7/3)^{1.3} (T_9/1.2)^{23.6} \text{ erg g}^{-1} \text{ s}^{-1} \quad (5.3)$$

is a steep function of temperature (Eqn. 5.3 was numerically derived using the `rates` module from the stellar evolution code MESA (Paxton et al. 2011)). Thus, the vast majority of the nuclear luminosity is generated within a “nuclear burning region” deep within the star. Like WWK04, we estimate the burning region’s luminosity through the use of a polytropic equation of state and an adiabatic temperature profile – i.e. $P/P_c = (\rho/\rho_c)^{\gamma_1}$, $T/T_c = (\rho/\rho_c)^{\gamma_3-1}$. At $\rho_7 = 3$ and $T_9 = 1.2$, the Helmholtz equation of state (EOS; Timmes & Swesty 2000) gives $\gamma_1 = 1.41$, and $\gamma_3 = 1.43$. We use the standard polytropic rescaling of density and radius (eg. Kippenhahn et al. 2012):

$$\begin{aligned} \theta &\equiv (\rho/\rho_c)^{\gamma_1-1}, \\ \xi &\equiv \alpha r, \end{aligned} \quad (5.4)$$

where

$$\alpha \equiv \sqrt{\frac{\gamma_1 - 1}{\gamma_1} \frac{4\pi G \rho_c^2}{P_c}}, \quad (5.5)$$

to obtain $\rho \varepsilon_{\text{CC}}(\rho, T) = \rho_c \varepsilon_{\text{CC},c} \theta^{b-1}$, where $b = (\gamma_1 - 1)^{-1}(25.3\gamma_3 - 22.9) + 1$ and $\varepsilon_{\text{CC},c} = \varepsilon_{\text{CC}}(\rho_c, T_c)$. Eqn. 5.2 then reduces to

$$L_{\text{conv}} \approx 4\pi \rho_c \varepsilon_{\text{CC},c} \frac{1}{\alpha^3} \int_0^{\xi_1} \xi^2 \theta^{b-1} d\xi. \quad (5.6)$$

Close to the WD’s center,

$$\theta \approx 1 - \frac{1}{6}\xi^2 \quad (5.7)$$

to third order, which implies the integrand of Eqn. 5.6 has a maximum at $\xi_1 = \sqrt{6/b}$. Integrating numerically,

$$\begin{aligned} L_{\text{conv}} &\approx 0.20 \frac{\rho_c \varepsilon_{\text{CC},c}}{\alpha^3} \\ &= 2.2 \times 10^{46} (\rho_7/3)^{1.3} (T_9/1.2)^{23.8} \text{ erg s}^{-1} \end{aligned} \quad (5.8)$$

For the scaling relation above, and for Eqn. 5.14 below, we use the Helmholtz EOS to numerically expand $\alpha \approx 7.0(\rho_7/3)^{0.33}(T_9/1.2)^{-0.08} \text{ cm}^{-1}$.

The convective velocity v_{conv} transporting luminosity L_{conv} can be calculated with standard mixing length theory (MLT; eg. Kippenhahn et al. 2012 Ch. 7):

$$\begin{aligned} F_{\text{conv}} &= \frac{L_{\text{conv}}}{4\pi r^2} = \frac{\rho c_P T}{g \delta l_m} v_{\text{conv}}^3 \\ v_{\text{conv}} &= \left(\frac{\delta g l_m}{c_P T} \frac{L_{\text{conv}}}{4\pi r^2 \rho} \right)^{1/3}. \end{aligned} \quad (5.9)$$

where g is the magnitude of the gravitational acceleration, $\delta = -d \ln \rho / d \ln T$ the logarithmic coefficient of thermal expansion and l_m the mixing length, which in this work we shall take to be the pressure scale height

$$H_P \equiv -\frac{P}{dP/dr}. \quad (5.10)$$

A coefficient of order a few generally included in Eqn. 5.9 has been set to unity to be consistent with PC08. Combining Eqns. 5.8 and Eqn. 5.9, we estimate the convective velocity at $r = H_P/2$:

$$\begin{aligned} v_{\text{conv}} &\approx \left(\frac{e^{\gamma_3/2\gamma_1}}{\pi} \frac{\delta g}{c_P T_c} \frac{L_{\text{conv}}}{H_P \rho_c} \right)^{1/3} \\ &\approx 0.47 \left(\frac{\delta g}{\alpha^3 H_P} \frac{\varepsilon_{CC,c}}{c_P T_c} \right)^{1/3}. \end{aligned} \quad (5.11)$$

Here, we used the fact that $H_P/2$ is the approximate length over which pressure decreases by a factor of $e^{1/2}$; correspondingly (from the adiabatic temperature gradient), $\rho \approx \rho_c \exp(-1/2\gamma_1)$ and $T \approx T_c \exp(-(\gamma_3 - 1)/2\gamma_1)$. In the same vein, we relate α to H_P using Eqns. 5.4 and 5.7:²

$$\begin{aligned} \frac{P}{P_c} &= e^{-1} = \theta^{\gamma_1/(\gamma_1-1)} \approx \left(1 - \frac{1}{6} \xi_{H_P}^2 \right)^{\gamma_1/(\gamma_1-1)} \\ \xi_{H_P} &= \alpha H_P \approx \left(6 - 6e^{-(\gamma_1-1)/\gamma_1} \right)^{1/2} = 1.2 \end{aligned} \quad (5.12)$$

We also approximate gravitational acceleration $g = Gm/r^2$ (m is the enclosed mass) at $r = H_P/2$ by noting that

$$\begin{aligned} m(H_P/2) &= \int_0^{H_P/2} 4\pi r^2 \rho dr \approx 4\pi \frac{\rho_c}{\alpha^3} \int_0^{0.6} \xi^2 \theta^{1/(\gamma_1-1)} d\xi \\ &= 0.20 \frac{4\pi \rho_c}{3\alpha^3} \end{aligned} \quad (5.13)$$

calculated using the same procedure to estimate L_{conv} . Combining Eqns. 5.12 with 5.13,

$$\begin{aligned} v_{\text{conv}} &\approx \frac{0.57}{\alpha} \left(\delta G \rho_c \frac{\varepsilon_{CC,c}}{c_P T_c} \right)^{1/3} \\ &\approx 1.4 \times 10^7 (\rho_7/3)^{0.34} (T_9/1.2)^{7.86} \text{ cm s}^{-1}, \end{aligned} \quad (5.14)$$

²The next higher term in the expansion for θ is $(n/120)\xi^4$, where n is the polytropic index. Hence, for $n \approx 3$ and $\xi_{H_P} \approx 1.2$, the approximation for θ is good to $\sim 20\%$.

where we use the Helmholtz EOS again to expand $c_P \approx 4.9 \times 10^7 (\rho_7/3)^{-0.32} (T_9/1.2)^{0.84}$ erg K⁻¹ and $\delta = 1.2 \times 10^{-1} (\rho_7/3)^{-0.64} (T_9/1.2)^{1.58}$.

Finally, we use Eqn. 5.14 to estimate the convective timescale

$$\tau_{\text{conv}} \sim \frac{H_P}{v_{\text{conv}}} \approx \frac{2.2}{\delta^{1/3}} \left(\frac{1}{G\rho_c} \right)^{1/3} \left(\frac{c_P T_c}{\epsilon_{\text{CC},c}} \right)^{1/3} \quad (5.15)$$

We use Eqn. 5.1 to rewrite $c_P T_c / \epsilon_{\text{CC},c}$ as the (central) nuclear heating timescale, and we define the dynamical time as

$$\tau_{\text{dyn}} \equiv \frac{1}{(G\rho_c)^{-1/2}}. \quad (5.16)$$

Taking $\delta^{1/3} \approx 0.49$, Eqn. 5.15 then becomes³

$$\tau_{\text{conv}} \approx 4.4 \tau_{\text{dyn}}^{2/3} \tau_{\text{CC}}^{1/3}. \quad (5.17)$$

Therefore, during the simmering phase, convection transports energy away on a timescale much smaller than the fusion heating timescale. τ_{CC} only reaches parity with τ_{conv} when they become approximately equal to the WD's dynamical adjustment time τ_{dyn} , after which nuclear burning deposits energy faster than the WD can dynamically respond, and an explosive event becomes inevitable. Since during the simmering phase $\tau_{\text{dyn}} \ll \tau_{\text{conv}} \ll \tau_{\text{CC}}$, it can be traced using a sequence of hydrostatic models where convection is able to redistribute energy over a negligible timescale.

In reality, the end of simmering and birth of a thermonuclear “flame” occurs earlier than when $\tau_{\text{CC}} = \tau_{\text{dyn}}$. WWK04 argue it happens when an individual convective blob in the nuclear burning region heats faster from burning than it cools through adiabatic expansion, i.e. when the integral

$$\int \frac{dT}{dr} + \frac{\epsilon_{\text{CC}}}{c_P v_{\text{conv}}} dr \quad (5.18)$$

diverges. This occurs shortly after Eqn. 5.18 becomes positive, when the contribution of the (always positive) ϵ_{CC} term begins to outweigh the (always negative) dT/dr term. We thus use

$$\int_0^{R_{\text{CC}}} \frac{dT}{dr} + \frac{\epsilon_{\text{CC}}}{c_P v_{\text{conv}}} dr > 0 \quad (5.19)$$

as our criterion for the end of the simmering phase, where values in the integrand are taken from the WD's stellar profile,⁴ and R_{CC} , the outer boundary of the nuclear burning region, is estimated with the implicit equation

$$\frac{L_{\text{CC}}(R_{\text{CC}})}{L_{\text{CC}}} = \frac{\int_0^{R_{\text{CC}}} 4\pi r^2 \rho \epsilon_{\text{CC}} dr}{\int_0^{R_{\text{WD}}} 4\pi r^2 \rho \epsilon_{\text{CC}} dr} = 0.95. \quad (5.20)$$

5.2.2 Semi-Analytical Model

We generate 1D hydrostatic models by solving the stellar structure differential equations

³Retaining the density and temperature scaling of $\delta^{-1/3} \propto (\rho_7/3)^{0.21} (T_9/1.2)^{-0.52}$ in Eqn. 5.15 does not substantially alter our result, since $\tau_{\text{conv}} \propto \delta^{-1/3} (\rho_7/3)^{-0.22} (T_9/1.2)^{-7.41}$ and density changes only by a factor of a few during the runaway.

⁴Eqn. 5.9 gives $v_{\text{conv}}(r=0) = 0$, leading to a singularity in Eqn. 5.19. To avoid this, we set $v_{\text{conv}}(r=0)$ to its value at the next step in the integration, where $r \sim 10^6$ cm.

$$\frac{dP}{dm} = -\frac{Gm}{4\pi r^4} \left(+\frac{1}{6\pi} \frac{\Omega^2}{r} \right) \quad (5.21)$$

$$\frac{dr}{dm} = \frac{1}{4\pi r^2 \rho} \quad (5.22)$$

$$\frac{dT}{dm} = \begin{cases} \frac{T}{P} \nabla \frac{dP}{dm}, & \text{inside the convection zone} \\ 0, & \text{otherwise} \end{cases} \quad (5.23)$$

where $\nabla \equiv d \ln T / d \ln P$. The Helmholtz equation of state closes the system of equations. The luminosity is calculated using

$$\frac{dL}{dm} = \varepsilon_{CC} \quad (5.24)$$

with ε_{CC} values provided by MESA's rates module. To obtain a model WD, we employ a shooting method that calculates a stellar profile given ρ_c , central specific entropy s_c , and vary ρ_c until a profile is obtained where mass has a relative deviation of $\lesssim 10^{-6}$ from its desired values. For the solid-body rotating WDs considered in Sec. 5.3.3, the bracketed term in Eqn. 5.21 – a 1D approximation to rotational support valid when deviations from spherical symmetry are small – becomes non-zero, and Ω is also altered during shooting until the angular momentum relative deviation is $\lesssim 10^{-6}$.

Within the convection zone, the temperature profile is given by

$$\nabla \equiv \frac{d \ln T}{d \ln P} = \nabla_{ad} + \Delta. \quad (5.25)$$

∇_{ad} is the adiabatic (isentropic) temperature gradient and is $\approx 0.3 - 0.4$ for WDs. Δ is a deviation term (always positive in our models) that can affect the runaway: an adiabatic temperature profile leads the entire WD to heat up along with the nuclear burning region, expanding as it becomes less degenerate, while an extremely steep profile will effectively decouple the burning region from rest of the WD until an explosion occurs. In the absence of rotation and magnetic fields, $\Delta = \Delta_{conv}$, the superadiabatic gradient deviation needed to transport the convective luminosity. MLT gives Δ_{conv} as

$$\Delta_{conv} = \frac{v_{conv}^2}{g\delta} \frac{H_P}{l_m^2} = \frac{v_{conv}^2}{g\delta H_P} \quad (5.26)$$

where a coefficient has again been set to unity for consistency with PC08. We shall see in Sec. 5.3.2 that $\Delta_{conv}/\nabla_{ad} \ll 1$ – as usual in stellar interiors – except near the very end of simmering.

The scale height, as defined by Eqn. 5.10, diverges as $r \rightarrow 0$. To alleviate issues with expressions that have it in the denominator, we follow Paxton et al. (2011) in using an alternate scale height,

$$H_P = \sqrt{\frac{P}{G\rho^2}}, \quad (5.27)$$

when it is smaller than H_P from Eqn. 5.10.

We assume a uniform composition of 50% carbon, 50% oxygen by mass. For simplicity, we do not consider compositional gradients, which PC08 show generate a temperature break at the boundary of the convection zone. (For merger remnants, these have likely been erased by the merging process long before the simmering phase.) We also neglect electron capture reactions such as those of the

convective Urca process (eg. Stein & Wheeler 2006) and neutronization (Piro & Bildsten 2008), as they are negligible for all but the most massive of our stars.

Like in PC08, we assume an isothermal zone of temperature T_{iso} above the convection zone; given our assumption of uniform composition, the convection boundary location is set by where the temperature of the convection zone reaches T_{iso} . By default, we set $T_{\text{iso}} = 1 \times 10^5$ K; we discuss the effects of increasing it in Sec. 5.3.1.3.

As we showed, the evolution of a simmering WD can be represented by a sequence of hydrostatic models. The sequence can be parameterized by the WD's central specific entropy s_c , which increases as the nuclear runaway unfolds.⁵ We vary s_c between models in discrete logarithmic steps of $d \log_{10}(s_c) = 5 \times 10^{-3}$. If $\nabla = \nabla_{\text{ad}}$ is assumed, each model along the sequence can be calculated independently of others, but when using Eqns. 5.25 and 5.26, the strong dependence of v_{conv} on the convective luminosity can lead to $\Delta \sim \nabla_{\text{ad}}$ when $T_c \gtrsim 1.2 \times 10^9$ K. In extreme cases, the temperature gradient – equivalently the entropy gradient – steepens to the point where the specific entropy $s(m)$ for a mass shell m is actually lower than $s_{\text{old}}(m)$ from the previous model in the sequence. This physically corresponds to the shell cooling off, which is impossible over convective timescales. Instead, convection is simply unable to transport the convective luminosity through m , and Δ_{conv} is no longer valid.

To account for this effect, we add another condition that $s(m)$ must always be larger than or equal to $s_{\text{old}}(m)$, which modifies Eqn. 5.25 to

$$\nabla = \begin{cases} \nabla_{\text{ad}} + \Delta, & s(m) > s_{\text{old}}(m) \\ \nabla_{\text{ad}} - 4\pi r^2 \rho \frac{H_p}{c_p} \frac{ds_{\text{old}}}{dm}, & \text{otherwise,} \end{cases} \quad (5.28)$$

setting a explicit temporal order to the sequence of models. In practice, $s_{\text{old}}(m)$ is obtained by fitting a spline to the previous model's entropy profile, meaning it is possible our chosen discretization of $d \log_{10}(s_c) = 5 \times 10^{-3}$ affects model sequences that use Eqn. 5.28. We tested if this was the case by generating sequences for a $1.2 M_\odot$ WD that halved or doubled the discretization step, and found changes in ρ_c and T_c of $\lesssim 0.3\%$, orders of magnitude smaller than the changes presented in subsequent sections.

5.3 Results

We now consider the simmering of sub- M_{Ch} WDs represented by models with increasing complexity and features. We first consider in Sec. 5.3.1 models where the superadiabatic deviation Δ_{conv} is neglected, and the temperature gradient is approximated with $\nabla = \nabla_{\text{ad}}$. These reproduce all the qualitative features of the runaway, and are good approximations of more complex models. We then move on to ones that include the superadiabatic temperature deviation Δ_{conv} in Sec. 5.3.2, and ones featuring a rough estimate for including rotation or magnetic fields in Sec. 5.3.3.

⁵Central temperature T_c cannot be used this way, as it is not monotonic for lower-mass WDs that expand and cool rather than explode.

5.3.1 Adiabatic Approximation

5.3.1.1 Analysis of Adiabatic Simmering Tracks

Fig. 5.1 depicts evolutionary tracks of the central density and temperature of simmering WDs with $\nabla = \nabla_{\text{ad}}$ and masses from 1.0 to $1.35 M_{\odot}$. We refer to these as “simmering tracks”. The central specific entropy along each track increases from $\lesssim 10^6 \text{ erg K}^{-1} \text{ g}^{-1}$ to $\gtrsim 2.3 \times 10^8 \text{ erg K}^{-1} \text{ g}^{-1}$. Black circles along the tracks show when Eqn. 5.19 is first satisfied, which we refer to as the “WWK04 point”, and the black dotted “WWK04” line is a power-law fit to them. Also shown are contours of neutrino cooling and carbon fusion heating timescale (dotted blue and red lines, respectively) and contours of constant entropy (dotted green). The $\tau_{\text{CC}} = \tau_{\nu}$ ignition line denotes where the fusion heating timescale becomes equal to the neutrino cooling one, above which a nuclear runaway occurs, while the $\tau_{\text{CC}} = \tau_{\text{dyn}}$ explosion line denotes when the fusion and dynamical (Eqn. 5.16) timescales are equal, above which an explosive event occurs. The $P = 2P(T=0)$ line approximates the upper bound of the region where degeneracy pressure dominates over thermal pressure.

A WD starts simmering at the intersection of its simmering track with the $\tau_{\text{CC}} = \tau_{\nu}$ line. As nuclear burning increases the WD’s entropy, it rises up and leftward along its track, the slope of which is determined by the balance between heating due to nuclear burning and adiabatic cooling due to the WD expanding. The latter becomes more prominent as the WD becomes less degenerate, eventually balancing with the former when the WD reaches a point of maximum temperature. It then starts to cool as the simmering track turns over. The cooling and expansion will eventually lead the WD back to near the $\tau_{\text{CC}} = \tau_{\nu}$ line (though at much lower density than at the start of simmering), and a stable carbon-burning star is born. Some WDs, however, reach high enough temperatures that the WWK04 point is reached before maximum temperature is; this signals the decoupling of convective energy transport and nuclear burning, and an explosive event follows. For a $1.15 M_{\odot}$ WD, simmering lasts just $\sim 10 \text{ yr}$ from ignition to reaching the WWK04 point, compared to the $\sim 1000 \text{ yr}$ needed for a M_{Ch} WD; this is because pycnonuclear fusion begins when $\tau_{\text{CC}} \sim 10^6 \text{ yr}$, rather than $\sim 10^2 \text{ yr}$ for thermonuclear fusion.

Due to our choice of s_c range, we produce models that populate the region in Fig. 5.1 beyond the WWK04 line, where our models’ assumption of instantaneous convective energy transport breaks down. While these sections of the tracks cannot be reached during simmering, we still show them in Fig. 5.1 as dot-dashed lines to indicate the tracks’ overall shape.

The simmering tracks roughly form a homology parameterized by a track’s highest temperature and a density-axis stretch factor. Tracks for more massive stars reach higher temperatures and are more horizontally stretched – the latter is due to entropy being a steeper function of density than degeneracy when $\rho \gtrsim 10^8 \text{ g cm}^{-3}$ and $T \lesssim 10^8 \text{ K}$. The $\tau_{\text{CC}} = \tau_{\nu}$ and WWK04 lines, though, reach lower temperatures at higher densities. As a result, a $1.0 M_{\odot}$ WD is already significantly less degenerate than a $1.35 M_{\odot}$ one at the start of simmering. By the point where the $1.0 M_{\odot}$ WD reaches its maximum temperature of $9.5 \times 10^8 \text{ K}$ (well short of the WWK04 line), it has expanded considerably, its central density dropping to $\rho_c = 5.6 \times 10^6 \text{ g cm}^{-3}$, a quarter of its value at the onset of simmering. It subsequently continues to expand while cooling. A $1.35 M_{\odot}$ WD, on the other hand, expands much less drastically – its central density has decreased by 35% by its WWK04 point at $\rho_c = 7.6 \times 10^8 \text{ g cm}^{-3}$, $T_c = 9.2 \times 10^8 \text{ K}$. This central temperature is comparable to the $T_c = 7.8 \times 10^8 \text{ K}$ found for a M_{Ch} WD by WWK04, and the convective velocity we find at the top of the nuclear burning region, $v_{\text{conv}}(R_{\text{CC}}) = 8 \times 10^6 \text{ cm s}^{-1}$

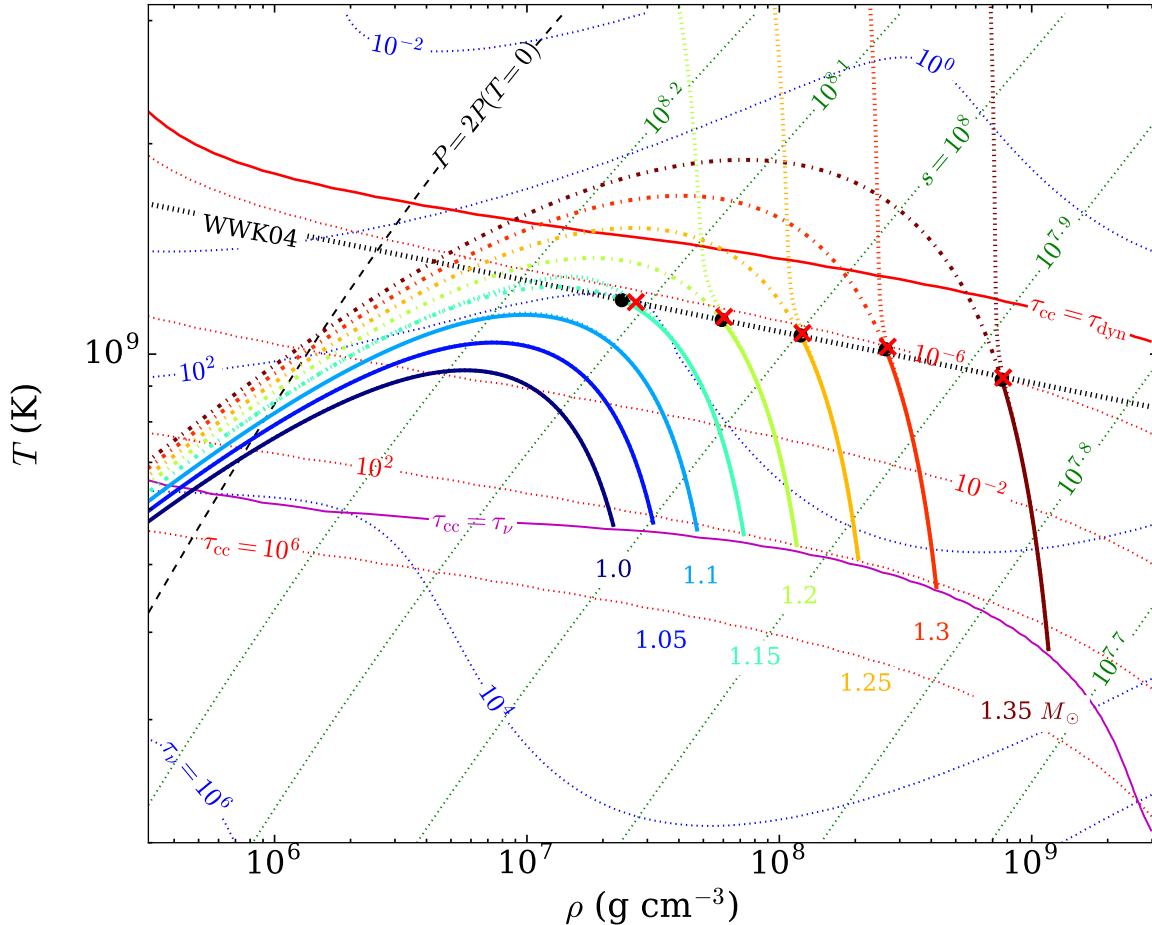


Figure 5.1: Evolution of the central temperature and density – “simmering tracks” – of simmering CO WDs with masses from $1.0 - 1.35 M_{\odot}$ (labeled in-line). Solid lines represent tracks of WDs with adiabatic temperature gradients, with dash-dotted track segments indicating regions that cannot be reached during simmering. Dotted lines represent tracks that include the superadiabatic deviation Δ_{conv} (Eqn. 5.26) required to transport the convective luminosity. Black circles along adiabatic simmering tracks indicate “WWK04 points” where Eqn. 5.19 is first satisfied signaling the end of simmering, and the black dotted WWK04 line represents a power-law fit to them. Red Xs are WWK04 points for Δ_{conv} -inclusive tracks. Also plotted are contours of constant neutrino cooling timescale τ_{ν} and carbon fusion heating timescale τ_{CC} , both in years, as well as specific entropy s in $\text{erg K}^{-1} \text{g}^{-1}$. The $\tau_{\text{CC}} = \tau_{\nu}$ and $\tau_{\text{CC}} = \tau_{\text{dyn}}$ lines denote where the fusion heating timescale becomes equal to the neutrino cooling timescale and dynamical timescale (Eqn. 5.16), respectively. Finally, the $P = 2P(T=0)$ approximates the upper bound of the region where degeneracy pressure dominates. Timescale contours were calculated using MESA (Paxton et al. 2011).

($\sim 1\%$ of the sound speed c_s) is the same value as estimated in [WWK04](#) for their M_{Ch} WD. This value tends to be higher for lower-mass WDs: $v_{\text{conv}}(R_{\text{CC}}) = 1.4 \times 10^7 \text{ cm s}^{-1}$ ($\sim 3\%$ of c_s) for a $1.15 M_{\odot}$ WD, in agreement with our estimate of Eqn. [5.14](#).

The well-ordered nature of the simmering tracks extends to the [WWK04](#) points, which is why they are well-represented by the [WWK04](#) line. The line falls just short of the $\tau_{\text{CC}} = \tau_{\text{dyn}}$ one, lying just underneath the $\tau_{\text{CC}} = 10^{-6} \text{ yr}$ contour. Unlike the other contours in Fig. [5.1](#), this line cannot be calculated independently of the assumptions of the runaway, though we find it is a good approximation for all of our models except for some in Sec. [5.3.3](#).

5.3.1.2 Estimate of M_{crit} and Minimum M_{Ni}

We turn to the central task of this paper: estimating the minimum mass M_{crit} required to reach the [WWK04](#) point, and the corresponding mass of radioactive nickel M_{Ni} produced if an explosion occurs shortly thereafter. To find M_{crit} , we generated models spaced apart by $0.005 M_{\odot}$, and find $M_{\text{crit}} = 1.145 M_{\odot}$ (black simmering track in Fig. [5.1](#)), which ends its simmering with $\rho_c = 2.0 \times 10^7 \text{ g cm}^{-3}$, $T_c = 1.2 \times 10^9 \text{ K}$.

While an explosive event becomes inevitable once the simmering phase ends, its nature – be it a deflagration, detonation, or some other phenomenon – has yet to be constrained and is beyond the scope of this work. We are, however, motivated by the resemblance of pure detonations of sub- M_{Ch} WDs to SNe Ia to make a rough estimate of the mass of ^{56}Ni , M_{Ni} , produced if the M_{crit} WD detonated immediately after simmering ends (i.e. without any further changes to its density structure). Since a detonation is supersonic, and the input energy for nuclear burning is provided by the shock itself (eg. [Seitenzahl et al. 2009](#)), nucleosynthesis in a pure detonation is, to first order, determined by the density profile of the progenitor before the explosion. Indeed, from the results of [Sim et al. \(2010\)](#), we find that M_{Ni} can be estimated to within a few percent by the mass of progenitor material with density $\rho > 10^7 \text{ g cm}^{-3}$, $M(\rho > 10^7)$ (see Fig. [5.2](#)). We can use this simple relationship to estimate that for $M_{\text{crit}} = 1.145 M_{\odot}$, $M_{\text{Ni}} = 0.30 M_{\odot}$.

Since M_{crit} is the minimum mass that can reach the [WWK04](#) point, $0.30 M_{\odot}$ is the minimum amount of ^{56}Ni produced by any adiabatically simmering WDs (in the absence of post-simmering expansion, or the triggering of a deflagration rather than a detonation). M_{Ni} , however, rises quite steeply for WDs with $M > M_{\text{crit}}$: $M(\rho > 10^7) = 0.39 M_{\odot}$ for a $1.15 M_{\odot}$ WD, and $0.78 M_{\odot}$ for a $1.2 M_{\odot}$ one. This is because the density of most material in a WD is within an order of magnitude of ρ_c , and ρ_c at the end of simmering is a steep function of mass for tracks of $M \approx M_{\text{crit}}$, since at that point they run nearly parallel to the [WWK04](#) line. Therefore, changing M_{crit} by a small value, or altering the end of simmering criterion, can substantially change the minimum M_{Ni} .

5.3.1.3 Hot Envelopes

Fig. [2.4](#) suggests mergers of WDs with similar mass lead to remnants that are heated throughout, with temperatures between $\sim 1 - 3 \times 10^8 \text{ K}$. To roughly gauge what effect this pre-runaway heating might have, we generate models identical to the ones above, but set $T_{\text{iso}} = 2 \times 10^8 \text{ K}$. We find the simmering tracks of these “hot-envelope” WDs deviate most widely from their cold counterparts at the start of simmering, where their central densities are lower by $\sim 3 - 7\%$; these differences reduce to $\sim 1 - 5\%$ at the end of simmering. By then, almost the entire interior structure of an adiabatic WD, with $T_c \gtrsim 10^9 \text{ K}$,

has $T > 2 \times 10^8$ K, making its central properties insensitive to an increase in T_{iso} . Raising T_{iso} even further may affect simmering track values more substantially, but hydrostatic solutions of WDs with $T_{\text{iso}} \gtrsim 5 \times 10^8$ K tend to have low-density atmospheres that extend to arbitrary radii, producing objects of infinite mass. Any WDs that were heated to such high temperatures by prior evolution, such as the remnant of Ji et al. (2013) post-viscous evolution, have more complicated temperature structures that, for simplicity, will not be considered in this work. Instead, they are explored in a companion paper (Heringer et al. in preparation).

5.3.2 Superadiabatic Deviation Δ_{conv}

To more accurately calculate simmering tracks, we must include the superadiabatic temperature deviation Δ_{conv} (Eqn. 5.26) needed to carry the convective luminosity. These Δ_{conv} -inclusive tracks are plotted in Fig. 5.1 as dotted lines (without indicating track segments unreachable during simmering). They are, regardless of mass, nearly identical to their adiabatic counterparts during simmering: their ρ_c and T_c at the start of simmering match to within floating point precision, and, for WDs of $M > 1.2 M_\odot$, they also differ by less than 2% at the end. While the Δ_{conv} tracks do steepen and arc away from their adiabatic counterparts, this occurs only above their WWK04 points, which are represented by red Xs in Fig. 5.1 and are well-approximated by the *adiabatic* WWK04 line. Close to M_{crit} , where the simmering tracks run nearly parallel to the WWK04 line, Δ_{conv} is more influential: the density of the $1.15 M_\odot$ WD Δ_{conv} track at its WWK04 point is $\sim 15\%$ higher than the adiabatic value. A mass parameter space search finds $M_{\text{crit}} = 1.135 M_\odot$, which ends its simmering phase with $\rho_c = 1.7 \times 10^7 \text{ g cm}^{-3}$, $T_c = 1.2 \times 10^9 \text{ K}$. While these values are very close to the ones obtained in Sec. 5.3.1.2, $M_{\text{Ni}} = M(\rho > 10^7) = 0.20 M_\odot$, which is substantially lower, reflecting its sensitivity to the end of simmering criterion.

The overall tiny effect of Δ_{conv} is due to Eqn. 5.26's dependence on the square of the ratio of convective velocity to sound speed, $v_{\text{conv}}^2 / (g H_P) \approx v_{\text{conv}}^2 / c_s^2$. Like in the adiabatic case, near the end of simmering $(v_{\text{conv}}(R_{\text{CC}})/c_s(R_{\text{CC}}))^2 \approx 1 \times 10^{-3}$ ($v_{\text{conv}}(R_{\text{CC}}) = 1.3 \times 10^7 \text{ cm s}^{-1}$) for a $1.15 M_\odot$ star, and 1×10^{-4} for a $1.35 M_\odot$ one. This small number is partly offset by the $1/\delta = -d \ln T / d \ln \rho$ term, which approaches infinity for zero-temperature degenerate material. Near the $\tau_{\text{CC}} = \tau_v$ line, however, the entropy is already sufficiently high that $1/\delta \sim 30$ for a $1.15 M_\odot$ WD, and ~ 300 for a $1.35 M_\odot$ one; these values fall to ~ 10 and ~ 100 , respectively, near the WWK04 line. Consequently, $\Delta_{\text{conv}} \sim 10^{-2}$, an order of magnitude smaller than $\nabla_{\text{ad}} \approx 0.3 - 0.4$. Once the WWK04 point is reached, the influence of Δ_{conv} grows to beyond unity at only slightly higher s_c due to the steep dependence of v_{conv}^2 on temperature, resulting in the sharp upward turn in all simmering tracks beyond that of $1.2 M_\odot$ mentioned previously.

5.3.3 Rotation and Magnetic Fields

We now turn to the inclusion of rotation and magnetic fields, which are expected features of merger remnants. These, in general, introduce complex multi-dimensional and non-local effects that are challenging to model. To obtain rough estimates, we consider only uniform rotation or magnetic fields that vary slowly over a convective scale height, ignoring their coupling with each other and with convection, and focus on how either affect M_{crit} . We first obtain a sense of this effect by estimating the superadiabatic temperature deviation Δ through energy balance arguments.

In the rotating case, the superadiabatic deviation Δ_{rot} can be estimated by equating the buoyancy and Coriolis forces:

$$2\rho\Omega v_{\text{conv}} = -g \left(\frac{d(\Delta\rho)}{dr} \right) \Delta r = g H_P \rho \left(\frac{\delta}{H_P} \Delta_{\text{rot}} \right) \quad (5.29)$$

where $\Delta\rho$ is the density difference between a convective blob and its surroundings and we set the characteristic length of convection Δr to H_P . This gives

$$\Delta_{\text{rot}} = \frac{1}{\delta} \frac{2\Omega H_P}{c_s} \frac{v_{\text{conv}}}{c_s}, \quad (5.30)$$

where we again use $g H_P \approx c_s^2$. Eqn. 5.30 resembles Eqn. 5.26, with one power of v_{conv}/c_s swapped for $2\Omega H_P/c_s \approx (\Omega^2 H_P/g)^{1/2}$, which is at most ~ 1 for rotation at break-up. Calculations of remnant viscous evolution (Shen et al. 2012; Schwab et al. 2012; Ji et al. 2013) suggest the remnant spins down to well below critical rotation, however, and so $(\Omega^2 H_P/g)^{1/2}$ is more realistically $\lesssim 10^{-1}$. Then, for a $1.15 M_\odot$ WD near the end of simmering, $\Delta_{\text{rot}} \lesssim (10^{-1}/\delta)(v_{\text{conv}}/c_s) \sim 10^{-1.5}$, an order of magnitude smaller than ∇_{ad} ; thus rotational convective suppression is a minor effect.

In the (non-rotating) magnetized case, we can make a similar estimate by equating the buoyancy and Lorentz forces:

$$\frac{B^2}{4\pi H_P} = -g \left(\frac{d(\Delta\rho)}{dr} \right) \Delta r = \rho g \delta \Delta_{\text{mag}}, \quad (5.31)$$

where we use the assumption that the magnetic field varies slowly over H_P . This gives

$$\Delta_{\text{mag}} = \frac{1}{\delta} \frac{B^2}{4\pi P}, \quad (5.32)$$

where $\rho g = P/H_P$ (Eqns. 5.10 and 5.21). Calculations of magnetic field amplification in mergers (Ch. 4) or during viscous evolution (Ji et al. 2013) suggest a saturation field strength of $\sim 10^{11}$ G at the center of the remnant. Given that $P \gtrsim 10^{24}$ dyn cm $^{-2}$ at the centers of $\gtrsim 1.1 M_\odot$ WDs, this gives $B^2/4\pi P \lesssim 10^{-3}$, and $\Delta_{\text{mag}} \lesssim 10^{-3}/\delta$. Near the $\tau_{\text{CC}} = \tau_v$ line, this value can be quite large, but near the end of simmering it becomes minor (eg. $\sim 10^{-2}$ for a $1.15 M_\odot$ WD).

The above suggest that for reasonable rotation rates and magnetic field strengths, their effects on the simmering phase should be small. To confirm this, we implemented the formulation of Stevenson (1979; hereafter S79). S79 incorporates rotation and externally imposed magnetic fields (both assumed, as above, to be slowly varying over H_P) into Rayleigh-Bénard convection. It predicts the convective steady state – in particular both Δ and the modified convective velocity – by finding the growth rates of convective modes using linear stability analysis (S79 Sec. 2), and then equating them to their non-linear cascade rates, picking the mode with the greatest heat flux to represent the motion as a whole. While this is *ad hoc*, in the rotation-dominated and unmagnetized limit S79’s theory reproduces well the convection simulations of Barker et al. (2014) over a wide range of rotation rates. We summarize our results below; further detail can be found in Sec. 5.6.

For WDs with sub-critical uniform rotation, we confirm that the effect of rotation on simmering is small. During simmering, v_{conv} increases by orders of magnitude, while Ω decreases by half an order of magnitude as the WD expands (to conserve angular momentum). This leads $2\Omega H_P/v_{\text{conv}}$ to approach unity, and Δ_{rot} to approach Δ_{conv} , near the end of simmering for WDs with initial angular speed Ω_i at about a quarter of break up speed Ω_{crit} . We also find that $v_{\text{conv}} \propto (\Delta_{\text{rot}}/\Delta_{\text{conv}})^{-1/4}$ changes very little, justifying our use of its non-rotating value in the approximation above. For moderate values of Ω ,

then, simmering tracks shift by only a few percent in density and temperature from their non-rotating versions in Sec. 5.3.2. For simmering when $\Omega_i \rightarrow \Omega_{\text{crit}}$, Eqn. 5.30 suggests Δ_{rot} becomes comparable to ∇_{ad} , but our models show that this is overshadowed by the centrifugal pressure support term in Eqn. 5.21, and the net effect is a slight reduction of ρ_c and T_c for a model with a given s_c . This effect increases M_{crit} to $1.14 M_\odot$ for WDs with $\Omega/\Omega_{\text{crit}} = 0.5$, though we caution that deviations from spherical symmetry not included in our model become significant near critical rotation.

Likewise, we find that simmering tracks for non-rotating WDs with $M \approx M_{\text{crit}}$ shift by only a few percent when including magnetic fields as high as 10^{12} G, consistent with Eqn. 5.32. When performing a parameter-space search for M_{crit} , we alter field strength with mass by keeping the ratio $E_B/|E_{\text{tot}}|$ fixed. For $E_B/|E_{\text{tot}}| = 2.9 \times 10^{-5}$, which corresponds to $B(r=0) = 1 \times 10^{11}$ G in a $1.15 M_\odot$ WD at the start of simmering, $M_{\text{crit}} = 1.13 M_\odot$. If we consider field strengths much larger than what is expected for merger remnants, however, we find that, while the simmering track still changes negligibly, the convective velocity v_{conv} becomes proportional to $1/B$ and is dramatically reduced, affecting when Eqn. 5.19 is first satisfied. A $1.15 M_\odot$ WD threaded by a 10^{12} G field sees its convective velocity reduced by a factor $\sim 10 - 100$, and reaches the WWK04 point at $T = 8 \times 10^8$ K, far lower than the (adiabatic) WWK04 line in Fig. 5.1. We determine M_{crit} for WDs with $E_B/|E_{\text{tot}}| = 2.8 \times 10^{-3}$, which corresponds to $B(r=0) = 1 \times 10^{12}$ G in a $1.15 M_\odot$ WD at the start of simmering, to be $1.02 M_\odot$, a reduction of more than $0.1 M_\odot$ from the non-magnetized value.

At this strong-field limit, however, the WWK04 point is also well-short of the $\tau_{\text{CC}} = \tau_{\text{dyn}}$ line, meaning that a WD that reaches the point must continue to heat up before it can explode. This heating may eventually lead to an extremely steep temperature gradient that allows for rapid convective energy transport before dynamical burning is reached, but this is beyond the ability for our model to follow. Moreover, we strongly caution that S79’s magnetic formulation may not accurately reflect non-linear magnetoconvection, except perhaps in the case of weak fields, and does not include magnetic dynamo processes, which are likely to be efficient in simmering WDs. We discuss these further in Sec. 5.4.3.

5.4 Discussion

5.4.1 Comparison to Observed $M_{\text{tot}}\text{-}M_{\text{Ni}}$ Relations

We have estimated the range of masses of centrally-simmering sub- M_{Ch} WDs that explode, as well as their corresponding M_{Ni} yields assuming a pure detonation immediately after simmering. Putting aside the possibility that extremely strong magnetic fields could affect v_{conv} , we have also determined that this range does not significantly change when including Δ_{conv} , rotation or magnetic fields. It is then interesting to consider in the abstract whether these could reproduce a substantial portion of the SN Ia parameter space, and, to that end, we compare our results to estimates of ejected mass and ^{56}Ni yields for observed SNe Ia. In Fig. 5.2, we plot the $M_{\text{Ni}} - M_{\text{tot}}$ relationship for adiabatic and Δ_{conv} -inclusive WDs, as well as the relationship (also derived using $M(\rho > 10^7)$) from the pure detonation of uniform 10^5 K cold WD for comparison. Additionally, results from the pure detonation simulations of Sim et al. (2010) are plotted to show the accuracy of the $M(\rho > 10^7)$ estimate. Alongside these, we plot the best-fit relationship to the ejected and synthesized ^{56}Ni masses of 337 observed “normal” (Branch et al. 2006) SNe Ia from Scalzo et al. (2014b), and the estimated M_{tot} and M_{Ni} of 31 normal SNe Ia from Childress et al. (2015). Scalzo et al. (2014b) derives their $M_{\text{Ni}} - M_{\text{tot}}$ relationship from the observed

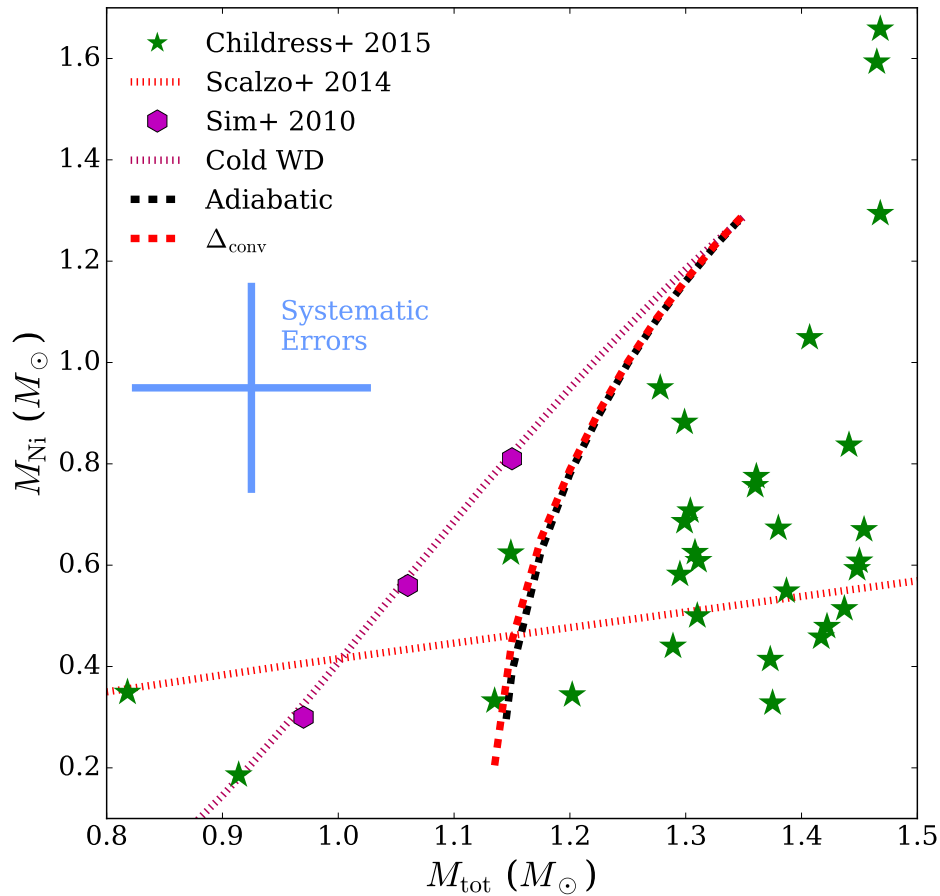


Figure 5.2: Relationships between total ejected mass M_{tot} and synthesized ^{56}Ni mass M_{Ni} for adiabatic and Δ_{conv} -inclusive WDs that experience a pure detonation immediately after the end of simmering, estimated using Sim et al. (2010). Also plotted are the M_{tot} and M_{Ni} yields of 31 observed SNe Ia from Childress et al. (2015), and the relationship derived by Scalzo et al. (2014b) from 337 observed SNe Ia. Childress et al. (2015)'s systematic error bars, indicating how much their values can be shifted in unison, are also included. The dashed magenta line is the relationship for the pure detonation of cold (uniform 10^5 K) WDs, with the simulation results of Sim et al. (2010) overdrawn.

bolometric light curve (using a range of simulated explosion models as priors; Scalzo et al. 2014a), and Childress et al. (2015) use Scalzo et al. (2014b)’s method of estimating M_{tot} while obtaining M_{Ni} from the evolution of the [Co III] $\lambda 5893$ emission complex during the SN Ia nebular phase.

As expected from previous analysis, the $M_{\text{Ni}} - M_{\text{tot}}$ relationship changes little between the adiabatic and Δ_{conv} -inclusive WDs, being separated by a $M_{\text{tot}} \lesssim 0.01 M_{\odot}$ for any given M_{Ni} . While not plotted, we also found that this is true for WDs rotating at 50% of critical, and those with $\sim 10^{11}$ G magnetic fields. The previously-noted steep dependence of M_{Ni} on M_{tot} near M_{crit} is clear as well: a linear fit around $M_{\text{tot}} = 1.15 M_{\odot}$ gives $dM_{\text{Ni}}/dM_{\text{tot}} \approx 10$ (for both curves), making it difficult to accurately estimate a minimum M_{Ni} . This also leads to a fine-tuning problem: to produce M_{Ni} between $\sim 0.3 - 0.6 M_{\odot}$ – typical M_{Ni} yields in Scalzo et al. (2014b) and Childress et al. (2015) – requires M_{tot} to lie in a narrow range between $\sim 1.13 - 1.17 M_{\odot}$. It is not obvious why a progenitor channel would favor this mass range, though we note the distribution of field CO WD masses is very narrowly peaked (at $0.65 M_{\odot}$; eg. Tremblay & Bergeron 2009; Kleinman et al. 2013), possibly indicating that merging CO WD binaries masses fall within a narrow range.

Nevertheless, the $M_{\text{Ni}} - M_{\text{tot}}$ relationship from pure detonations of centrally simmering CO WDs does not resemble the observed ones. Childress et al. (2015)’s values could be systematically offset by $\sim 0.1 M_{\odot}$ in M_{tot} and $\sim 0.2 M_{\odot}$ in M_{Ni} , but these apply to the points as a whole, and we also do not reproduce the shape of Childress et al. (2015)’s distribution. This issue is not unique to our work - Scalzo et al. (2014b) and Childress et al. (2015) plot theoretical $M_{\text{Ni}} - M_{\text{tot}}$ curves for a wide range of proposed SN Ia progenitor classes, ranging from sub- M_{Ch} WDs undergoing a double-detonation (equivalent to the Cold WD line in Fig. 5.2) to M_{Ch} pure deflagrations, and find no individual class able to reproduce the entire observed $M_{\text{Ni}} - M_{\text{tot}}$ parameter space. If their results indeed reflect the true $M_{\text{tot}} - {}^{56}\text{Ni}$ relationship of SNe Ia, either multiple progenitor channels are necessary, or a novel understanding of progenitors must arise.

5.4.2 Implications for Mergers as SN Ia Progenitors

Regardless of whether simmering sub- M_{Ch} WDs can reproduce observations, what implications do our results have on double-degenerate CO WD mergers as SN Ia progenitors, in particular the channel of vK10 involving sub- M_{Ch} merger remnants that ignite central nuclear fusion following their viscous evolution? A direct mapping of post-viscous remnants onto our hydrostatic simmering WDs is not possible since their structures are quite complex, and in general their temperature profiles are substantially shallower than the convective ones used in our models. Moreover, much of their mass exists as a hot, tenuous envelope that surrounds and exerts little pressure support on their dense, degeneracy-supported “cores”. As a rough estimate, we can consider the evolution of these cores as separate from their envelopes (the transition region between the two might resemble the hot atmospheres in Sec. 5.3.1.3, and thus not affect the core’s evolution).

Regardless of their initial conditions, the simmering tracks of a remnant core cannot simultaneously increase in temperature and density, since this would require part of their structure to cool (Sec. 5.2.2). They also cannot exist, for longer than a few convective timescales, to the right of the rising portion of the simmering track of the same mass in Fig. 5.1, i.e. the portion of the track between the start of simmering and either the WWK04 point or the point of maximum temperature. Doing so would mean its temperature gradient has become steeper than the convective one, and convective energy transport will rapidly lower the gradient back to the convective one (like for stars to the right of the Hayashi

track). As a consequence of these two restrictions, M_{crit} will increase for those WDs with shallow temperature profiles. With this in mind, meaningful conclusions can be made by examining the central densities and core masses M_{core} of post-viscous remnants.

To our knowledge, the sole published viscous evolution simulation of a sub- M_{Ch} double CO WD merger remnant is that of [Ji et al. \(2013\)](#). They find, by the end of their simulation, the central density and temperature of their $0.6 - 0.6 M_{\odot}$ remnant are $\sim 5 \times 10^6 \text{ g cm}^{-3}$ and $\sim 9 \times 10^8 \text{ K}$, respectively, well above the $\tau_{\text{CC}} = \tau_{\nu}$ line. Indeed, its $\tau_{\text{CC}} \sim 1 \text{ yr}$, much smaller than the $\gtrsim 10^4 \text{ yr}$ thermal contraction timescale ([Shen et al. 2012](#)), so the remnant will begin to simmer. The mass of the remnant that is within $r = 1.5 \times 10^9 \text{ cm}$ (the approximate outer boundary of the dense core in [Ji et al. 2013](#) Fig. 1) is $\sim 1.07 M_{\odot}$ (Suoqing Ji and Robert Fisher private communication, 2016), $\sim 0.06 M_{\odot}$ lower than M_{crit} . The remnant's central density is a factor of ~ 4 lower than that for the $\sim 1.05 M_{\odot}$ simmering track at the same temperature and a factor of ~ 6 lower than that for the M_{crit} simmering track.⁶ The most likely fate of this system is therefore expansion and possibly stable nuclear burning. The relatively small difference between M_{core} and M_{crit} suggests a merger remnant $\sim 0.1 M_{\odot}$ more massive might possess a core mass in excess of M_{crit} . That core's central density, though, may still be too low for simmering to end in an explosion.

For a broader parameter space of post-viscous remnants, we turn to the simple estimate of viscous evolution outcomes made in Sec. 2.6. While it tends to overestimate compression, particularly for remnants from similar-mass mergers, when compared to [Schwab et al.](#) (and follow-up work in [Raskin et al. 2014](#)) and [Ji et al. \(2013\)](#), it nevertheless gives a rough estimate of the post-viscous remnant parameter space. Taking our estimate at face value, we find that only those remnants from mergers with primary WD masses above $\sim 0.8 M_{\odot}$ have $\rho_c \gtrsim 3 \times 10^7 \text{ g cm}^{-3}$, which also suggests that only remnants with total masses above M_{Ch} are likely to achieve dynamical burning following viscous spin-down. Note that the most massive of these may have instead already exploded from extreme temperatures during their mergers (for primary WD masses $\gtrsim 0.9 M_{\odot}$; [Pakmor et al. 2010; 2011b](#)), or due to hydrodynamic instabilities immediately afterward (for primaries $\gtrsim 1 M_{\odot}$; [Kashyap et al. 2015](#)).

If explosion is in fact not possible following viscous evolution, then sub- M_{Ch} remnants that ignite carbon fusion will experience expansion instead, and eventually possible stable nuclear burning as a carbon star. Given their properties, they are candidate progenitors for isolated high-field magnetic WDs (eg. [García-Berro et al. 2012](#)), in particular hot DQ WDs ([Dunlap & Clemens 2015; Dunlap 2015](#) and references therein), which have hot, carbon-dominated atmospheres and appear to be massive, rapidly rotating and strongly magnetized.

5.4.3 Accuracy of Magnetized Simmering Models

We found in Sec. 5.3.3 that $\lesssim 10^{11} \text{ G}$ magnetic fields negligibly affect simmering, while $\gtrsim 10^{12} \text{ G}$ ones could dramatically affect v_{conv} , but there are reasons to be cautious about these results, particularly in the strong field limit.

First, S79 does not include convective dynamo processes that amplify the magnetic field. The vigorous convection zone found toward the end of simmering is an ideal environment for such processes – analogous to the highly magnetized central convection zones of A and B main sequence

⁶The remnant in ([Ji et al. 2013](#)) has not lost all of its rotational support by the end of their simulation, so its central density will continue to increase early in its simmering phase. As less than a third of its initial angular momentum remains, however, it is unlikely to increase by a factor of ~ 4 .

stars (eg. [Brun et al. 2005](#); [Featherstone et al. 2009](#); [Augustson et al. 2016](#)). Amplification saturates when $e_B/e_{\text{conv}} \sim 1$, i.e. when,

$$B_{\text{eq}} \sim v_{\text{conv}} \sqrt{8\pi\rho}. \quad (5.33)$$

For WDs at the end of simmering, $B_{\text{eq}} \sim 3 \times 10^{11} - 1 \times 10^{12}$ G. These values match or exceed any magnetic fields generated by the merger or viscous evolution (though having fields in place at the start of simmering may increase the saturation field strength by up to another order of magnitude; [Featherstone et al. 2009](#)), rendering even the low-field calculations uncertain. Additionally, the turbulent nature of the dynamo will generate a highly tangled magnetic field that varies significantly over short length scales, unlike the large-scale fields assumed in this work; Eqn. 5.31 would then suggest a much larger Δ_{mag} ([Chabrier et al. 2007](#)).

Second, studies of nonlinear magnetoconvection (eg. [Proctor & Weiss 1982](#)) indicate that in steady state, magnetic fields are concentrated into high-flux bundles where the convective flow is truncated, surrounded by regions where convection continues uninhibited. The amount of convective suppression depends on the volume fraction the bundles occupy. When the ratio e_B/e_{conv} between magnetic and convective kinetic energy densities becomes higher than unity, the bundles merge and convection is effectively suppressed. This physical picture (which is fundamentally multi-dimensional) shares little resemblance with S79 (Henk Spruit private communication, 2016), and no magnetic equivalent of [Barker et al. \(2014\)](#)'s examination of rotating convection has been conducted to see if S79 at least phenomenologically captures it.

Our model's inability to accurately follow magnetoconvection and include dynamo processes therefore constitutes the greatest uncertainty of this work. While we have estimated that including rotation without magnetic fields is important only because it modifies the hydrostatic balance of the WD, rotation coupled with both convection and magnetic fields may additionally lead to unexpected emergent behavior. The multidimensional nature of magnetoconvection may also alter the end of simmering criterion – for example, if burning material is trapped within a flux bundle, it may locally run away and lead to dynamical burning even if convection is unhindered elsewhere in the WD. We thus stress the need for more detailed investigation into WD magnetoconvection, potentially utilizing MHD convective simulations, in the future.

5.5 Conclusions

We investigated using simple estimates the outcome of simmering for sub- M_{Ch} WDs, and find that the minimum mass M_{crit} that achieves dynamical burning and explodes, rather than expanding and cooling, is $1.135 M_{\odot}$. We also estimate that including rotation or $\lesssim 10^{11}$ G magnetic fields alters this value by less than $\sim 0.01 M_{\odot}$ and $\sim 0.02 M_{\odot}$, respectively. Stronger, $\sim 10^{12}$ G fields, which may be generated through convective dynamo processes, could affect simmering much more substantially, but are beyond the scope of our models. Examining merger remnants in Ch. 2, and the simulation of [Ji et al. \(2013\)](#), we estimate that the majority of sub- M_{Ch} post-viscous remnants are too underdense to remain degenerate until dynamical burning if simmering were to set in. Even if they could explode, they would still produce very little ^{56}Ni . This presents an issue for the viability of the [vK10](#) channel, as it suggests most sub- M_{Ch} remnants do not explode as SNe Ia.

Ours is a first-order estimate of the simmering process. Aside from the clear need for more advanced prescriptions of magnetoconvection, future models would also benefit from including eg. modifications to the convective velocity structure resulting from heating or work to expand the WD as it becomes non-degenerate (PC08, though their effects will primarily be felt far from center of the WD). A more accurate analysis of the simmering of post-viscous merger remnants could be made by directly using their simulated density, temperature and rotation profiles as initial conditions. We also use the analytic 1D criterion of WWK04 to determine the end of simmering, and better estimates can be made by taking into account the range of temperatures and velocities of individual convective flows. This has already been done for M_{Ch} WDs using 3D hydrodynamic simulations (Kuhlen et al. 2006; Zingale et al. 2009; 2011; Nonaka et al. 2012), which could be extended to lower-mass WDs.

We have also estimated the $M_{\text{tot}}-M_{\text{Ni}}$ relationship of simmering sub- M_{Ch} WDs that reach explosion and find that they, like many other models, do not correspond to the observed SN Ia $M_{\text{tot}}-M_{\text{Ni}}$ relationships of Scalzo et al. (2014b) and Childress et al. (2015). In particular, our most massive WDs produce too much ^{56}Ni to reproduce the bottom right of Fig. 5.2, which would not be the case if the temperature structure at the end of simmering were substantially shallower than in our models. Such a structure could potentially be produced if the burning were not center-lit, but occurred in an off-center shell that remained degenerate throughout the runaway, and we explore this possibility in the companion paper to this work (Heringer et al. in preparation).

We are very grateful to Ken Shen, whose discussion with MHvK on the existence and value of M_{crit} years ago served as the original inspiration for this paper, and to Henk Spruit for his insights into magnetoconvection and its implementation in our models. We also thank Chris Matzner, Yuri Levin and Chris Thompson for helpful comments, and Suoqing Ji and Robert Fisher for both valuable feedback and for sharing the end-state of their viscous evolution simulation. Our calculations made extensive use of Frank Timmes' Helmholtz EOS and sections of MESA by Bill Paxton and the MESA consortium, and we thank them for making these codes publicly available.

5.6 Appendix: Convective Suppression due to Rotation and Magnetic Fields

In this appendix, we detail our calculations of rotating and magnetized simmering WDs. In general, their inclusion greatly complicates the treatment of convection inside a star by introducing non-spherically symmetric alterations to the convective structure, non-ideal magnetohydrodynamic (MHD) effects, and coupling, generally non-local, between the magnetic field, rotation profile and convective structure. Because the purpose of this work is to provide only rough estimates for the effects of rotation and magnetic fields, a full treatment of these is well beyond its scope. We instead implement the simple modifications to Δ and v_{conv} derived by S79.

S79 linearizes the Boussinesq MHD equations. By assuming the convection is Rayleigh-Bénard (planar geometry, with uniform vertical gravitational field and background temperature gradient) and that all perturbations to fluid variables can be written as sums of modes $\propto \exp(\mathbf{k} \cdot \mathbf{x} + \sigma t)$, he obtains the dispersion relation

$$\begin{aligned} \sigma^4 + \sigma^2 & \left(2 \frac{(\mathbf{k} \cdot \mathbf{B})^2}{4\pi\rho} + \frac{(2\Omega \cdot \mathbf{k})^2}{k^2} + N_*^2 \frac{k_\perp^2}{k^2} \right) + \\ & \left(\frac{(\mathbf{k} \cdot \mathbf{B})^2}{4\pi\rho} \right)^2 + \left(\frac{(\mathbf{k} \cdot \mathbf{B})^2}{4\pi\rho} \right) N_*^2 \frac{k_\perp^2}{k^2} = 0 \end{aligned} \quad (5.34)$$

in the limit of zero magnetic dissipation; σ is the temporal growth rate of a given mode and $N_*^2 = -g\delta\Delta/H_P$ is the Brunt-Väisälä (buoyancy) frequency. S79 then assumes that, for modes with $\sigma > 0$, the non-linear terms in the Boussinesq equations eventually limit their growth, leading to σ equaling the nonlinear cascade rate $\sim kv$ at the convective steady state (Barker et al. 2014). He also assumes convection at steady state is dominated by the mode that transports the greatest heat flux. The former assumption leads to a relationship between σ , the mode velocity v (equivalent to v_{conv}) and wavevector \mathbf{k} :

$$\sigma = v/k. \quad (5.35)$$

Eqns. 5.34 and 5.35 can then be combined with the mode heat flux

$$F = \frac{\rho c_P T}{g\delta} \frac{\sigma^2}{k^2} \left(\sigma + \frac{1}{\sigma} \frac{(\mathbf{k} \cdot \mathbf{B})^2}{4\pi\rho} \right) \quad (5.36)$$

to determine the one that dominates thermal transport.

For non-rotating, unmagnetized WDs, this formulation reproduces Eqns. 5.9 and 5.26 from MLT, except with prefactor coefficients:

$$F_{\text{conv}} = \frac{4\pi}{25} \left(\frac{5}{2} \right)^{5/2} \frac{\rho c_P T}{g\delta l_m} v_{\text{conv}}^3, \quad (5.37)$$

$$\Delta_{\text{conv}} = \frac{25\pi^2}{6} \frac{v_{\text{conv}}^2}{g\delta} \frac{H_P}{l_m^2}. \quad (5.38)$$

S79 point out that, for his formulation to reproduce the current age, luminosity and effective temperature of the Sun within a 1D stellar evolution model, it must be calibrated by using $l_m \approx 3H_P$. In order to be consistent with our non-rotating and unmagnetized results from before, we shall continue to use Eqns. 5.9 and 5.26 rather than Eqns. 5.37 and 5.38 when considering rotation and magnetic fields below. We consider the result of using these modified coefficients in Sec. 5.6.3.

For WDs that are rotating or magnetized, S79 finds that his Δ and v_{conv} can be written as multiplicative factors of the Δ_{conv} and v_{conv} of Eqns. 5.37 and 5.38 (using the same F_{conv}). As such, we define $v_{\text{conv},0}$ and Δ_0 as the convective velocity and temperature gradient calculated assuming *no* rotation or magnetic field.

To further simplify our estimates, we shall assume that the rotation is solid-body and magnetic fields vary slowly over a scale height, and we will consider rotation separately from magnetic fields. The former is enforced by our use of S79's model, since its Rayleigh-Bénard setup assumes Ω and \mathbf{B} are constant over its vertical lengthscale (H_P). At least for rotation, it is also a plausible representation of merger remnant cores, which tend to eliminate differential rotation during post-merger viscous evolution. Considering rotation and magnetic fields separately allows us to independently gauge

the relative importance of each to the runaway. S79's theory also does not include coupling between rotation, convection and magnetic fields. This neglects, in particular, magnetic field amplification by convective dynamos, which is discussed further in Sec. 5.4.3.

5.6.1 Simmering of Rotating White Dwarfs

The exact solution in the rotating case is given by S79:

$$\begin{aligned}\frac{\Delta_{\text{rot}}}{\Delta_0} + \frac{6}{25\pi^2} R_o^2 &= \left(\frac{\Delta_{\text{rot}}}{\Delta_0}\right)^{5/2} \\ \frac{v_{\text{conv}}}{v_{\text{conv},0}} &= \left(\frac{\Delta_{\text{rot}}}{\Delta_0}\right)^{-1/4}\end{aligned}\quad (5.39)$$

where Rossby number

$$R_o = \frac{v_{\text{conv},0}}{2\Omega l_m} = \frac{v_{\text{conv},0}}{2\Omega H_P} \quad (5.40)$$

is a proxy for the ratio between convective and rotational velocities in the convection zone.⁷ S79 (their Eqn. 43) provide approximations to Eqn. 5.39 in the limits of very large and very small R_o (their Eqns. 42 - 43), and in lieu of solving for $\Delta_{\text{rot}}/\Delta_0$ during integration, we use the approximation

$$\frac{\Delta_{\text{rot}}}{\Delta_0} \approx \left(1 + \left(0.23R_o^{-4/5}\right)^2\right)^{1/2}, \quad (5.41)$$

where $0.23R_o^{-4/5}$ is the S79 approximation for $\Delta_{\text{rot}}/\Delta_0$ for $R_o \ll 1$:⁸

$$\frac{\Delta_{\text{rot}}}{\Delta_0} \approx 0.23R_o^{-4/5}. \quad (5.42)$$

Eqn. 5.41 is accurate to within 3% of the exact $\Delta_{\text{rot}}/\Delta_0$ for all R_o , and $v_{\text{conv}}/v_{\text{conv},0} = (\Delta_{\text{rot}}/\Delta_0)^{-1/4}$ to within 1%. Eqn. 5.42 can be approximated by $\Delta_{\text{rot}} \sim \delta^{-1}(H_P\Omega/c_s)(v_{\text{conv}}/c_s)$, which can be compared to a naïve implementation of the (1D analog of the) Solberg-Høiland stability criterion, $\Delta_{\text{Solberg}} \sim \delta^{-1}(H_P\Omega/c_s)^2$ (eg. Tassoul 2000 Sec. 3.4.2). The replacement of one $H_P\Omega/c_s$ term with v_{conv}/c_s accounts for the lack of suppression along the axis of rotation, and the turbulent cascade of polar convection into modes orthogonal to the rotation axis in the nonlinear regime (Barker et al. 2014).

Notably, this formulation has been tested in the $R_o \ll 1$ limit by Barker et al. (2014), who show through simulations of rotating Rayleigh-Bénard convection that $\Delta_{\text{rot}} \propto \Omega^{4/5}$ and $v_{\text{conv}} \propto \Omega^{-1/5}$ over $10^{-4} \lesssim R_o \lesssim 10^{-1}$, consistent with S79. While not a simulation of a convecting star, this lends credence to S79's assumptions for convective transport and nonlinear mode saturation.

Conservation of angular momentum and solid-body rotation are both assumed for the entirety of the runaway, constraining Ω such that it only needs to be specified for one model along the simmering track; naturally, we choose the one at the start of simmering. This is done by specifying the model's s_c to be that for the start of simmering in the (non-rotating) adiabatic track of the same mass WD. Since we

⁷Like Barker et al. (2014), we assume $\mathbf{g} \parallel \boldsymbol{\Omega}$ for our calculations; in the case where the two are misaligned, the convective suppression is reduced by a factor $\mathbf{g} \cdot \boldsymbol{\Omega}/g\Omega$.

⁸Using a quadrature averaging of the S79 $R_o \ll 1$ and $R_o \gg 1$ expressions is impossible because they do not cross each other.

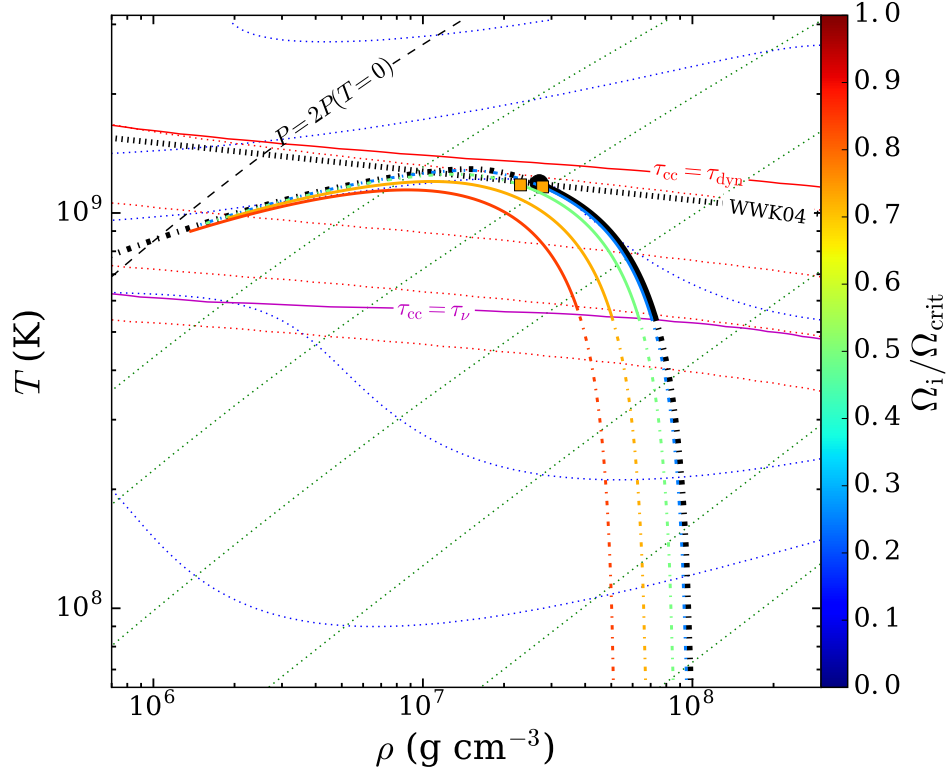


Figure 5.3: Simmering tracks for (unmagnetized) solid-body rotating $1.15 M_{\odot}$ WDs. Track color represents $\Omega_i/\Omega_{\text{crit}}$, the ratio of the WD's angular speed at the start of simmering to its numerically determined break-up value, and the thicker black track is the non-rotating Δ_{conv} -inclusive $1.15 M_{\odot}$ one from Fig. 5.1. WWK04 points are a black circle for the non-rotating track and orange squares for the rotating ones; the curves with $\Omega_i/\Omega_{\text{crit}} > 0.75$ never satisfy Eqn. 5.19. Dash-dotted track segments indicate solutions that cannot be reached during simmering. All other lines and symbols are as in Fig. 5.1.

show below that rotation does not substantially affect the runaway, this is a reasonable approximation for the start of simmering s_c in the rotating case. We then set the WD angular speed at this point, Ω_i , to some fraction of its critical value Ω_{crit} . To determine Ω_{crit} , profiles are generated with increasing angular speed until a pressure inversion ($dP/dm > 0$) is detected during integration. By Eqn. 5.21, this means that the layer dm is spinning at near-Keplerian speeds; the corresponding angular speed Ω_{crit} is then analogous to the solid-body break-up angular speed (though not equal to it, since Eqn. 5.21 assumes spherical symmetry). Note that this procedure is only done to set Ω to a reasonable fraction of the break-up angular speed near the start of simmering, and does not otherwise affect our runaway calculations.

In Fig. 5.3, we plot the simmering tracks of $1.15 M_{\odot}$ WDs with $\Omega_i/\Omega_{\text{crit}}$ varying from 25% - 85% of $\Omega_{\text{crit}} = 0.61 \text{ s}^{-1}$ ($1.15 M_{\odot}$ is chosen for its proximity to the adiabatic M_{crit} value). Below 10^8 K , the rotating WD tracks shift leftward (in density) from the non-rotating one (thick black line) – from a factor of 0.03 for $\Omega_i/\Omega_{\text{crit}} = 0.25$ to a factor of 1.9 for $\Omega_i/\Omega_{\text{crit}} = 0.85$ – due to centrifugal support supplementing degeneracy pressure. This partial lifting of degeneracy competes with the convective suppression effects of rotation. S79 notes the suppressive effect can be estimated by combining Eqns. 5.26 and 5.42:

$$\Delta_{\text{rot}} \approx 0.23 R_o^{-4/5} \Delta_0 \sim \left(\frac{\Omega H_P}{v_{\text{conv},0}} \right)^{4/5} \frac{v_{\text{conv},0}^2}{g H_P} = \Delta_0^{3/5} \left(\frac{\Omega^2 H_P}{g} \right)^{2/5}. \quad (5.43)$$

All stars have $\Omega^2 H_P \lesssim g$, and so at best $\Delta_{\text{rot}} \sim \Delta_0^{3/5}$. For a $1.15 M_\odot$ WD rotating at less than a third of the critical rate, $\Delta_0 \sim 10^{-2}$ near the end of simmering (Sec. 5.3.2) and $\Delta_{\text{rot}} \lesssim 10^{-1.5}$, a $\lesssim 10\%$ deviation to ∇_{ad} . Our calculations give even more modest values: $\Delta_{\text{rot}}/\nabla_{\text{ad}} \sim 0.03$ ($\Delta_{\text{rot}}/\Delta_0 \sim 1$) near the WWK04 point of both the $\Omega_i/\Omega_{\text{crit}} = 0.25$ and $\Omega_i/\Omega_{\text{crit}} = 0.50$ tracks. These are lower than what Eqn. 5.43 predicts because for small values of Ω_i , $R_o \sim 1$ near the end of simmering and Eqn. 5.41 approaches its non-rotating counterpart. At the start of simmering, $R_o \ll 1$ and $\Delta_{\text{rot}}/\Delta_0 \sim 200$ for the $\Omega_i/\Omega_{\text{crit}} = 0.50$ track, but $\Delta_0 \sim 10^{-7}$ at this point, and so it makes little difference to the overall runaway. Near critical rotation, Eqn. 5.43 predicts $\Delta_{\text{rot}} \sim 10^{-1}$ which is more comparable to ∇_{ad} , but our calculations show centrifugal support has a much larger effect on the runaway by lowering both ρ_c and T_c of a model with a given s_c . This, in fact, reduces the effect of convective suppression by lowering v_{conv} . Thus, rotation primarily serves to lift degeneracy and prevent a WD from reaching its WWK04 point. At a modest $\Omega_i/\Omega_{\text{crit}} = 0.25$, the WD reaches its WWK04 point with $\rho_c = 2.8 \times 10^7 \text{ g cm}^{-3}$, only $\sim 3\%$ higher than its non-rotating counterpart. As rotation increases, ρ_c at the WWK04 point decreases: it is 15% lower for the $\Omega_i/\Omega_{\text{crit}} = 0.50$ track, and tracks with higher rotation rates fail to reach the WWK04 point entirely.

The convective velocity, meanwhile, has a very shallow dependency on $\Delta_{\text{rot}}/\Delta_0$. At the end of simmering, $v_{\text{conv}}(R_{\text{CC}}) = 1.1 \times 10^7 \text{ cm s}^{-1}$ for both the $\Omega_i/\Omega_{\text{crit}} = 0.25$ and $\Omega_i/\Omega_{\text{crit}} = 0.50$ tracks, comparable to the non-rotating value of $v_{\text{conv}}(R_{\text{CC}}) = 1.3 \times 10^7 \text{ cm s}^{-1}$ (Sec. 5.3.2). The $\sim 20\%$ difference in $v_{\text{conv}}(R_{\text{CC}})$ is due to the sensitivity of ϵ_{CC} and the WWK04 criterion to changes in temperature.

From the above analysis, it is unsurprising that a mass parameter space sweep for simmering WDs with $\Omega_i/\Omega_{\text{crit}} = 0.50$ yields $M_{\text{crit}} = 1.14 M_\odot$.

Our results near critical rotation should be taken with a grain of salt, since deviations from spherical symmetry not reproducible by our model become significant. However, a merger remnant is unlikely to be critically rotating at the start of simmering. As mentioned previously, studies of post-merger viscous evolution all find the remnant core spins down to well below critical rotation (Shen et al. 2012; Schwab et al. 2012; Ji et al. 2013). While these works do not constrain the amount of vestigial rotation, we have shown above that modest rotation rates in general do little to influence the runaway.

5.6.2 Simmering of Magnetized White Dwarfs

Like in the rotating case, the exact solution for the (dissipationless) magnetic case has no simple analytical form. S79 finds in the limit of large Alfvén ratio

$$A = \frac{v_A^2}{v_{\text{conv},0}^2} = \frac{B^2}{4\pi\rho v_{\text{conv},0}^2} \quad (5.44)$$

that Δ_{mag} and v_{conv} can be approximated as⁹

⁹We assume the magnetic field is aligned with the gravitational vector, and hence $\cos^2 \phi = 1$ in Sec. 4 of S79. We have also corrected a coefficient error in S79's $v_{\text{conv}}/v_{\text{conv},0}$ expression.

$$\begin{aligned}\frac{\Delta_{\text{mag}}}{\Delta_0} &= 0.24A \\ \frac{v_{\text{conv}}}{v_{\text{conv},0}} &= 1.21A^{-1/2}\end{aligned}\quad (5.45)$$

Again, in lieu of solving for $\Delta_{\text{mag}}/\Delta_0$ exactly during integration, we use the approximations

$$\begin{aligned}\frac{\Delta_{\text{mag}}}{\Delta_0} &\approx \left(1 + (0.24A)^{6/5}\right)^{5/6}, \\ \frac{v_{\text{conv}}}{v_{\text{conv},0}} &\approx \left(1 + \left(1.21A^{-1/2}\right)^{-13/4}\right)^{-4/13}.\end{aligned}\quad (5.46)$$

Exponents $6/5$ and $-13/4$ were obtained by empirically minimizing these functional forms to the numerically calculated exact solutions over a range $10^{-4} < A < 10^4$. $\Delta_{\text{mag}}/\Delta_0$ in Eqn. 5.46 is accurate to within 2% of its exact solution, and $v_{\text{conv}}/v_{\text{conv},0}$ to within 3%. We assume the magnetic field is frozen to its corresponding mass shell m throughout the runaway, changing in strength to satisfy conservation of flux $d\Phi \propto Br^2$ (i.e. $B(m) \propto 1/r(m)^2$), meaning that, analogous to the rotation case above, the magnetic field only needs to be specified for one model in the runaway. We again take the s_c of this model to be that for the start of simmering in the equivalent adiabatic simmering track. We set the initial field profile $B_0(m)$ to be one where

$$d_{\text{mag}} = \frac{B_0^2}{8\pi P} \quad (5.47)$$

is held constant, suggested by [MacDonald & Mullan \(2009\)](#), who use it to study magnetic convective suppression in brown dwarfs, as a reasonable profile for a star whose density does not vary wildly over most of its interior. The spherically averaged magnetic field profile of the merger remnant in Ch. 4 also resembles Eqn. 5.47 near the center of its core, though caution must be used comparing a recently formed merger remnant with a hydrostatic simmering WD. The central initial field strength $B_{c,i}$ is restricted to below 10^{12} G to keep $d_{\text{mag}} \ll 1$ ($d_{\text{mag}} = 0.01$ when $B_{c,i} = 2.0 \times 10^{12}$ G for a $1.15 M_\odot$ WD at the ignition line). This allows us to leave out magnetic terms in Eqn. 5.21.

Fig. 5.4 depicts simmering tracks for a $1.15 M_\odot$ with $B_{c,i} = 1 \times 10^{10} - 1 \times 10^{12}$ G. Across the entire range of field strengths, the shift in the simmering track shape due to Δ_{mag} is small. The ρ_c values of the magnetized tracks deviate by $\lesssim 5\%$ from the non-magnetized one, even for the strongest field strengths being considered. This is because, for $A \gg 1$, Eqn. 5.45 can be rewritten as

$$\Delta_{\text{mag}} \approx \frac{1}{\delta} \frac{B^2}{16\pi\rho g H_P} = \frac{1}{\delta} \frac{B^2}{16\pi P'} \quad (5.48)$$

or $d_{\text{mag}}/2\delta$. Note that Eqn. 5.48 is identical to Eqn. 5.32, obtained by balancing the buoyancy and Lorentz forces, and a similar expression is derived in [MacDonald & Mullan \(2009\)](#) based on one from [Gough & Tayler \(1966\)](#). Since we consider fields with $d_{\text{mag}} < 3 \times 10^{-3}$, Δ_{mag} is large only when $1/\delta$ is. This is the case close to the $\tau_{\text{CC}} = \tau_v$ line, leading to $\Delta_{\text{mag}}/\nabla_{\text{ad}} \sim 0.2$ for the $B_{c,i} = 10^{12}$ G track, but for colder and highly degenerate WDs their temperature profile has little influence on their density profile. When $T \gtrsim 10^9$ K, $1/\delta$ is much smaller and Δ_{mag} approaches Δ_{conv} in value.

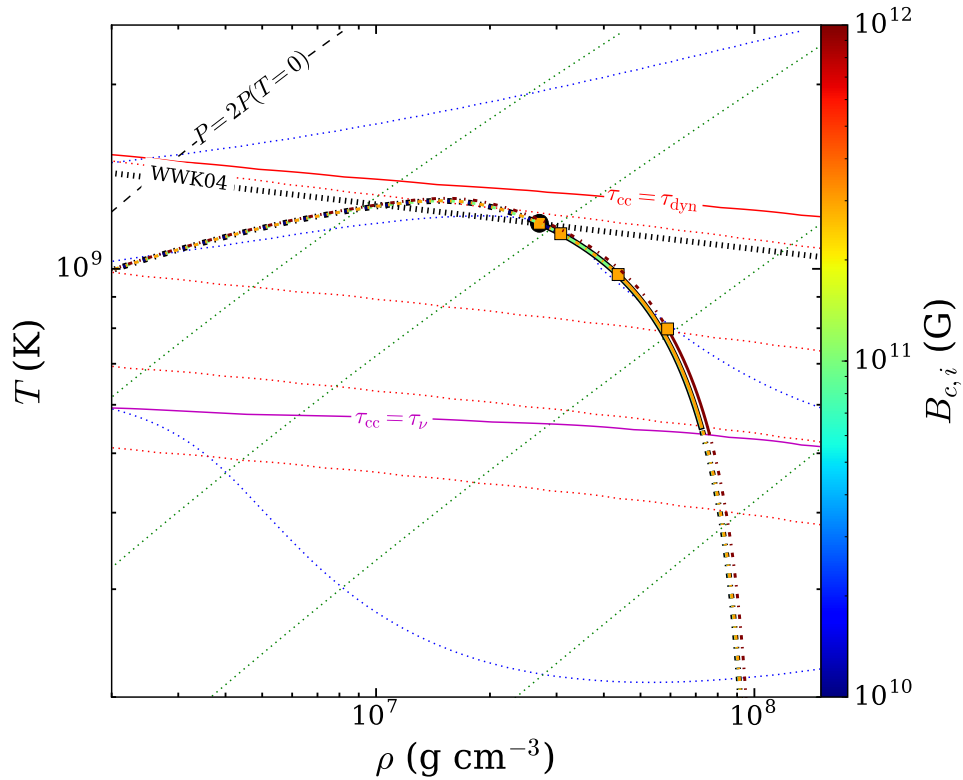


Figure 5.4: Simmering tracks for (non-rotating) magnetized $1.15 M_\odot$ WDs. Track color represents the central magnetic field strength at the start of simmering, $B_{c,i}$, and the thicker black dotted track is the non-magnetized Δ_{conv} -inclusive $1.15 M_\odot$ one from Fig. 5.1. All other lines and symbols are as in Fig. 5.3, except that the orange circles represent WWK04 points for the magnetized (rather than rotating) tracks.

v_{conv} , however, is proportional to $A^{-1/2}$ when $A \gg 1$, and can be many orders of magnitude smaller than $v_{\text{conv},0}$ during the earlier phases of simmering. For the $B_{c,i} = 1 \times 10^{12}$ G track, v_{conv} is reduced so much that Eqn. 5.19 is satisfied at $\rho_c = 5.9 \times 10^7$ g cm $^{-3}$, $T_c = 8.0 \times 10^8$ K, well-below the adiabatic WWK04 line. At the WWK04 point for the $B_{c,i} = 1 \times 10^{12}$ G run, $A \sim 3 \times 10^3$, and hence $v_{\text{conv}}(R_{\text{CC}}) = 1.3 \times 10^4$ cm s $^{-1}$, a factor of ~ 30 smaller than $v_{\text{conv},0}$ and $\sim 10^3$ smaller than $v_{\text{conv}}(R_{\text{CC}})$ at the end of simmering for the unmagnetized track. This reduction appears only for $B_{c,i} \gtrsim 3 \times 10^{11}$ G; for the $B_{c,i} = 1 \times 10^{11}$ G one, simmering ends when $A \sim 10^{-1}$, and ρ_c and T_c deviate from their non-rotating values by 14% and 4%, respectively.

We perform a parameter space search of WDs with either low or high-strength magnetic fields. Strength is defined as the magnetic to total energy ratio $E_B/|E_{\text{tot}}|$; “low” means $E_B/|E_{\text{tot}}| = 2.9 \times 10^{-5}$ and “high” means $E_B/|E_{\text{tot}}| = 2.8 \times 10^{-3}$, equivalent to $B_{c,i} = 1 \times 10^{11}$ G and $B_{c,i} = 1 \times 10^{12}$ G, respectively, for a $1.15 M_{\odot}$ WD at the start of simmering. Similar to the non-rotating case, the low field search yields $M_{\text{crit}} = 1.13 M_{\odot}$. The high field search yields $M_{\text{crit}} = 1.02 M_{\odot}$, a reduction of more than $0.1 M_{\odot}$ from the non-magnetized case. The latter estimates are the most uncertain out of all those in this work, which is discussed at length in the main paper.

However, we have already mentioned in Sec. 5.4.3 that these results, particularly those at the high-field limit, must be treated with caution. S79’s magnetic formulation has not yet been numerically tested and may not accurately reflect non-linear magnetoconvection, except perhaps in the case of weak fields. Moreover, dynamo processes are likely to be efficient in simmering WDs and will likely lead to $\sim 10^{12}$ G fields near the end of simmering, dominating over any fossil fields from prior evolution.

5.6.3 Sensitivity to Mixing Length Theory Coefficients

We noted above that that S79’s formulation reproduced the equations of MLT in the non-rotating, unmagnetized limit, except for differing prefactor coefficients, and that to reproduce the properties of the Sun it had to further be calibrated by setting $l_m \sim 3$. Both l_m and the coefficients vary among different formulations of convection. To get a sense of the robustness of our estimate for M_{crit} and M_{Ni} to these variations, we generate a simmering track for a $1.15 M_{\odot}$ WD where we replace the “default” Eqns. 5.9 and 5.26 with Eqns. 5.37 and 5.38, respectively, and set $l_m = 3$. This is practically equivalent to rescaling v_{conv} by a factor of 0.85, and Δ_{conv} by a factor of 3.26.

In Fig. 5.5, we compare the S79 coefficient (SC; solid red line) track with the one using default coefficients (solid black). There is little difference between the two lines until close to the end of simmering, where increased superadiabaticity leads to a steepening of the SC track; it ends simmering with 20% higher ρ_c . Adding 50% critical rotation or a 10^{11} G magnetic field yields additional deviations of $\sim 10\%$ in ρ_c near the end of simmering. A mass parameter-space search of M_{crit} for the SC tracks yields $M_{\text{crit}} = 1.12 M_{\odot}$, a deviation on par with those seen in previous sections.

The S79 coefficients only modify v_{conv} by 15%, so the deviations above are due to the change in Δ . Since Eqn. 5.26 also depends on v_{conv} , modifying it can result in comparable changes. In Fig. 5.5 we show tracks calculated using Eqn. 5.26 as is, but multiplying a factor of 2 (“2v”; blue dashed) or 1/2 (“v/2”; cyan dashed) to Eqn. 5.9. The larger Δ in the 2v track leads it to steepen near the end of simmering like the SC one, while the v/2 track more resembles the adiabatic one in Fig. 5.1. Altering v_{conv} also changes where Eqn. 5.19 is satisfied. The v/2 track reaches its WWK04 point when $v_{\text{conv}}(R_{\text{CC}}) = 4.4 \times 10^6$ cm s $^{-1}$ and with 18% higher ρ_c (6% lower T_c), than the default track; the 2v track ends simmering when $v_{\text{conv}}(R_{\text{CC}}) = 4.3 \times 10^7$ cm s $^{-1}$, but also with 16% higher ρ_c (7% higher T_c)

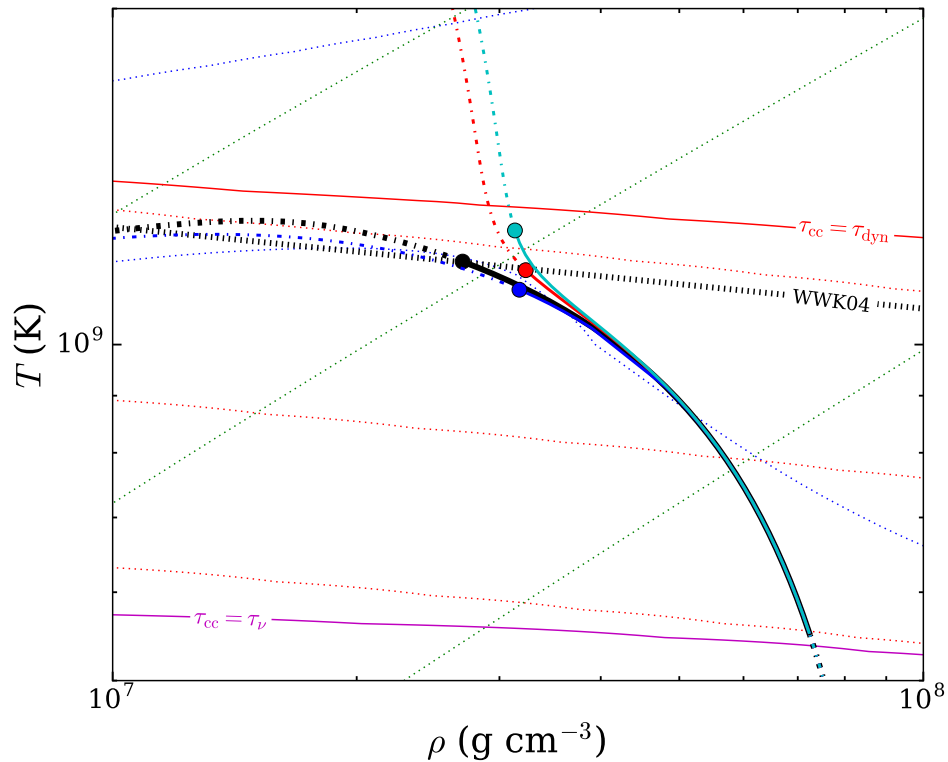


Figure 5.5: Comparison of a simmering track for a non-rotating, unmagnetized $1.15 M_{\odot}$ WDs calculated using Eqns. 5.37 and 5.38 (red line) with the “default” $1.15 M_{\odot}$ one that uses Eqns. 5.9 and 5.26 from Fig. 5.1 (black). Also plotted are tracks which use Eqn. 5.26 but multiply a prefactor of 2 (blue) or $1/2$ (cyan) to Eqn. 5.9. Circles along each track indicate their respective WWK04 points. All other lines and symbols are as in Fig. 5.3.

due to it being steeper. A search of M_{crit} for $v/2$ and $2v$ tracks both give $M_{\text{crit}} = 1.12 M_{\odot}$.

We thus find that changing MLT coefficients leads to changes in the simmering tracks and to M_{crit} on par with including the convective superadiabaticity Δ_{conv} in Sec. 5.3.2. Likewise, these deviations are also ultimately too small to significantly change our results.

Chapter 6

Conclusion

What, then, has our body of work, as well as the numerous other recent investigations into mergers and post-merger evolution, taught us about the fate of sub- M_{Ch} CO WD mergers? Are there systems that compress and heat enough during post-merger evolution to ignite degenerate carbon burning near their centers, which then leads to an explosion? Below, I summarize our current understanding of these systems and the sub- M_{Ch} merger channel scenario proposed by [vK10](#), and suggest avenues for future exploration.

6.1 Mergers and Early Post-Merger Evolution

In Ch. 2, we used SPH simulations of double CO WD mergers to explore the range of possible merger remnants and determine which among them are candidates for ignition under highly degenerate conditions during post-merger evolution. The properties most important for this are the temperature and degree of rotational support of the dense remnant core, as both determine the temperature and density the center of the core will reach during post-merger evolution. We find that dissimilar-mass mergers result in cold and slowly-rotating cores that are unlikely to subsequently ignite, while similar-mass ones have cores that are heated and partly rotationally supported throughout. The (rough) dividing line between the two classes is a density ratio between donor and accretor WD of $q_{\rho} \simeq 0.6$, equivalently a difference between their masses of $\Delta M \simeq 0.1 M_{\odot}$.

Since the publication of Ch. 2, [Dan et al. \(2014\)](#) published their study of remnants from synchronized WD mergers with exact initial conditions. They find that for all of their merger remnants – even ones we deem similar-mass – the mass enclosed within the radius of maximum temperature $M_{\text{enc}}(T_{\text{max}})$ is approximately the mass of the accreting WD, and the temperature at the remnant’s center is a factor of at least a few lower. Their similar-mass mergers also do not substantially mix, as ours do. [Dan et al. \(2014\)](#) link these differences to their use of synchronized and exact initial conditions, consistent with our findings in Sec. 2.4 that synchronization and longer periods of mass-transfer prior to coalescence make merger remnants resemble dissimilar-mass ones.

In Ch. 3 we compared a similar-mass $0.625 - 0.65 M_{\odot}$ merger simulated using SPH with one using the moving mesh code AREPO. The two simulations produce very similar results, including for the degree of mixing between the two WDs, up to coalescence. Following coalescence, however, the AREPO remnant retains a dense core that is a factor of ~ 2 colder than its surroundings until the end of the

simulation.

Taken together, these results raise the question of whether any merger remnants can have substantially heated cores, or if our results from Ch. 2 are contingent upon the hydrodynamic scheme being used, the accuracy of the simulation’s initial conditions and the synchronization of the WDs. Resolving this issue will require further simulations. The influence of the hydrodynamic scheme will be more definitively understood once we determine if spurious SPH surface tension and artificial viscosity are the root causes of the differences between GASOLINE and AREPO simulations. The influence of accurate initial conditions can best be determined by implementing the non-rotating close binary equilibrium solution (Uryū & Eriguchi 1998) into a merger simulation. We have made preliminary attempts to implement such a solution into GASOLINE, with promising results. Resolution of the synchronization debate will come with a better understanding of the influence of tides in close WD binaries, perhaps through observational determination if they are synchronized (eg. through measuring the rotational velocities of eclipsing binary WDs through rotational broadening of hydrogen lines or the Rossiter-McLaughlin effect; Piro 2011).

Further complicating matters is the dramatic amplification of an initially insignificant magnetic field during the merger, as presented in Ch. 4. The powerful, $> 10^{10}$ G equilibrium field could serve as an alternate source of heat for the remnant core by dissipating (potentially non-local) differential rotation. We observe some of this core heating in our simulation following coalescence. We have already noted, however, that the configuration of our equilibrium field is suspect due to our use of the Powell divergence-cleaning scheme (Sec. 4.6). Following coalescence, we also notice that our equilibrium field diffuses into adjacent regions of low field. Hopkins & Raives (2016) shows that the Powell scheme does not properly advect an equilibrated magnetic field loop, instead generating spurious field growth and diffusion at the interface between the loop and its surroundings. This suggests the diffusion we see is also spurious, and it prevents us from accurately capturing magnetically mediated viscous evolution and heating.

Uncertainty regarding the hydrodynamics of the merger, discussed above, may also affect the magnetic field evolution. The remnant field configuration will depend on the properties of the shear layer that develops between the two WDs just prior to their coalescence. Ch. 2 and Dan et al. (2014) show that in synchronized mergers contact between the WDs is less violent and leads to a less severe shear layer. Moreover, during the merger the field is advected into the system’s center of mass, which causes the remnant core to be highly magnetized. This might not happen in the merger of a synchronized system, where the accretor is not disrupted as severely.

Ch. 3 also showed the appearance of an $m = 1$ spiral mode in the remnant disk due to its gravitational perturbation by the non-axisymmetric remnant core. This spiral mode hydrodynamically transports the angular momentum on a timescale an order of magnitude faster than estimates of the magnetically-mediated viscous evolution. Unlike viscosity, traveling waves do not necessarily dissipate differential rotation energy locally, and so the heating of the remnant disk due to wave transport may look quite different from that due to viscosity. The MHD simulation of Ch. 4, however, shows the remnant core becoming axisymmetric ~ 500 s after coalescence, likely as a result of magnetic stresses acting on its differential rotation. Therefore, the lifetime of this wave transport will also depend on magnetic field growth during the merger, and possibly the magnetorotational instability (likely not properly captured in our AREPO simulation) acting on remnant disk.

These questions regarding magnetic field growth, the field configuration of the remnant, and its

effect on the $m = 1$ spiral mode could be resolved with future merger simulations in AREPO using its new constrained transport scheme for both synchronized and non-synchronized WD binaries. It will also be interesting to see if accurate initial conditions in either case lead to the formation of a less severe non-axisymmetry during coalescence, which would weaken the remnant’s spiral mode and reduce the rate at which it transports angular momentum.

We note that the uncertainties discussed above all make it less likely for the remnant core to be heated, spun-up or highly magnetized. Thus, the temperature and angular velocity within the cores of similar-mass remnants in Ch. 2 are likely to be upper limits.

6.2 Viscous Evolution and Ignition

Once the merger remnant becomes axisymmetric, it will continue to transport angular momentum on a viscous timescale. This leads to compressional heating of the remnant core, which simulations (Schwab et al. 2012; Ji et al. 2013; Raskin et al. 2014) have shown generally lead to a factor of ~ 2 increase in density and temperature (rather than the order of magnitude increase in both estimated in vK10). In their simulation of the viscous evolution of a $0.6 - 0.6 M_{\odot}$ merger remnant, Ji et al. (2013) find this increase leads to carbon ignition at the center of the remnant, but the remnant they use for initial conditions is at a higher density, and substantially higher temperature, than the corresponding remnant in our parameter space (Fig. 2.16). In Sec. 2.6.1, we used a simplified prescription of post-merger compressional heating to predict central ignition for remnants whose accretor mass is $\gtrsim 0.8 M_{\odot}$, and ignition in off-center hourglass-shaped hotspots for similar-mass remnants whose accretor mass is $\gtrsim 0.5 M_{\odot}$, but this simple prescription tends to overestimate the amount of compression similar-mass merger remnants experience, and cannot properly evolve off-center hotspots.

Other than Ji et al. (2013), there is a lack of sub- M_{Ch} viscous evolution simulations available in the literature. A parameter space study of post-merger evolution using the techniques of Schwab et al. (2012) or Ji et al. (2013) is needed to determine which systems in the sub- M_{Ch} merger parameter space evolve to either center or off-center ignition. These will, of course, be most useful if performed after the uncertainties in Sec. 6.1 are better understood, and revised merger simulations – that follow the evolution of the remnant until it becomes axisymmetric and any spiral modes have dissipated – are available for use as initial conditions.

The evolution of the off-center hotspots in similar-mass remnants is particularly intriguing, since these hotspots extend into highly degenerate material. The hot void in the $0.625 - 0.65 M_{\odot}$ AREPO merger remnant is a factor of ~ 3 lower than the peak density within the dense crescent, but remains partly degenerate as well, and may deform into a hot ring once the AREPO remnant becomes axisymmetric. Simulations of these remnants will be able to determine if the ignition of these hotspots can be done under degenerate conditions, as well as, in general, how off center ignition must be in order to initialize stable shell burning rather than a nuclear runaway.

6.3 Ignition, Simmering and Explosions

In Ch. 5 we investigated the simmering phase of idealized sub- M_{Ch} WDs with central nuclear fusion to determine which among them achieve dynamical burning and some form of explosion, rather than lift their degeneracy, expand and cool. We find the minimum mass M_{crit} of a CO WD that achieves

dynamical burning to be $1.135 M_{\odot}$, and that M_{crit} changes by less than $\sim 0.01 M_{\odot}$ if the WD possesses sub-critical solid-body rotation, and by less than $\sim 0.02 M_{\odot}$ if it possesses $\lesssim 10^{11} \text{ G}$ magnetic fields. The idealized WDs we use do not represent realistic merger remnants following their viscous evolution, which may ignite simmering off-center, and generally have more complex density and temperature profiles. We argue in Sec. 5.4.2 that conclusions can nevertheless be drawn by comparing M_{crit} and the typical densities of simmering WDs that reach dynamical burning to the masses and central densities of the dense cores of post-viscous merger remnants. The results of Ji et al. (2013) suggest that similar-mass merger remnants with $M_{\text{tot}} \gtrsim 1.3 M_{\odot}$ might have dense cores with masses $\gtrsim M_{\text{crit}}$, but all sub- M_{Ch} remnants from both simulations and our simple estimates from Sec. 2.6.1 appear to be too underdense to achieve dynamical burning.

While these results are suggestive, they are not definitive. If a merger remnant ignites fusion off-center, the simmering phase will occur in a shell, which may be geometrically different than simmering due to center-lit fusion (in the same way that shell burning differs from core burning in post-main sequence stars). It would therefore be useful to characterize how M_{crit} shifts with the location of nuclear fusion with the same methods we used in Ch. 5 for center-lit simmering.

We have also estimated the $M_{\text{tot}}-M_{\text{Ni}}$ relationship for those WDs that reach dynamical burning if they were to experience a detonation at the end of their simmering phase, and find that only a narrow range of M_{tot} is able to produce M_{Ni} yields typical of SNe Ia, which is in contrast to the observed $M_{\text{tot}}-M_{\text{Ni}}$ relationship (Scalzo et al. 2014b; Childress et al. 2015). This range could be widened if burning were moved to a shell, as an overall shallower temperature profile can allow for an object of a given mass to have a lower central density, reducing its ^{56}Ni yield in a detonation. In a companion work to Ch. 5 (Heringer et al., in preparation), we find that this is indeed the case, and the range of systems can better reproduce the spread of observed points from Childress et al. (2015). The off-center hotspots in merger remnants, mentioned above, could eventually lead to shell burning in some remnants, but this must be confirmed through viscous evolution simulations.

Lastly, our models' implementation of magnetic fields is rudimentary (Sec. 5.4.3), and may not reflect more detailed and multidimensional studies of magnetoconvection. This might not matter for WDs with a $\lesssim 10^{11} \text{ G}$ field, since by the end of simmering the kinetic energy density dominates over the magnetic one within their convection zones and magnetic effects will be negligible. However, stronger, $\sim 10^{12} \text{ G}$ fields could be generated during simmering through convective dynamo processes, which our implementation also does not include. These fields might lead to a substantial reduction in the convective velocity, or trap burning material within non-convection flux bundles. Further studies, ideally guided by simulations of magnetoconvection inside highly degenerate material, are needed.

If powerful magnetic fields can indeed completely suppress convection, this will, at best, prevent any changes in the temperature and density structure of the WD once nuclear burning is lit. If we assume this is the case, we can estimate the nucleosynthetic yields of our sub- M_{Ch} merger remnants. In Fig. 6.1, we show the total ejected mass M_{tot} and synthesized ^{56}Ni mass M_{Ni} of all the post-viscous remnants generated by the simple post-merger viscous evolution estimate in Sec. 2.6.1 – regardless of whether or not they are predicted to ignite nuclear burning – if they were to detonate with no change to their structure. M_{Ni} is estimated by the mass of remnant material with density $\rho > 10^7 \text{ g cm}^{-3}$. It is not obvious how much of the tenuous post-viscous envelope should be included when estimating M_{tot} , since some of it might have been ejected out to large distances. We assume M_{tot} is the total mass of the merger remnant for the points in Fig. 6.1, but extend lines leftward from the points by the masses of

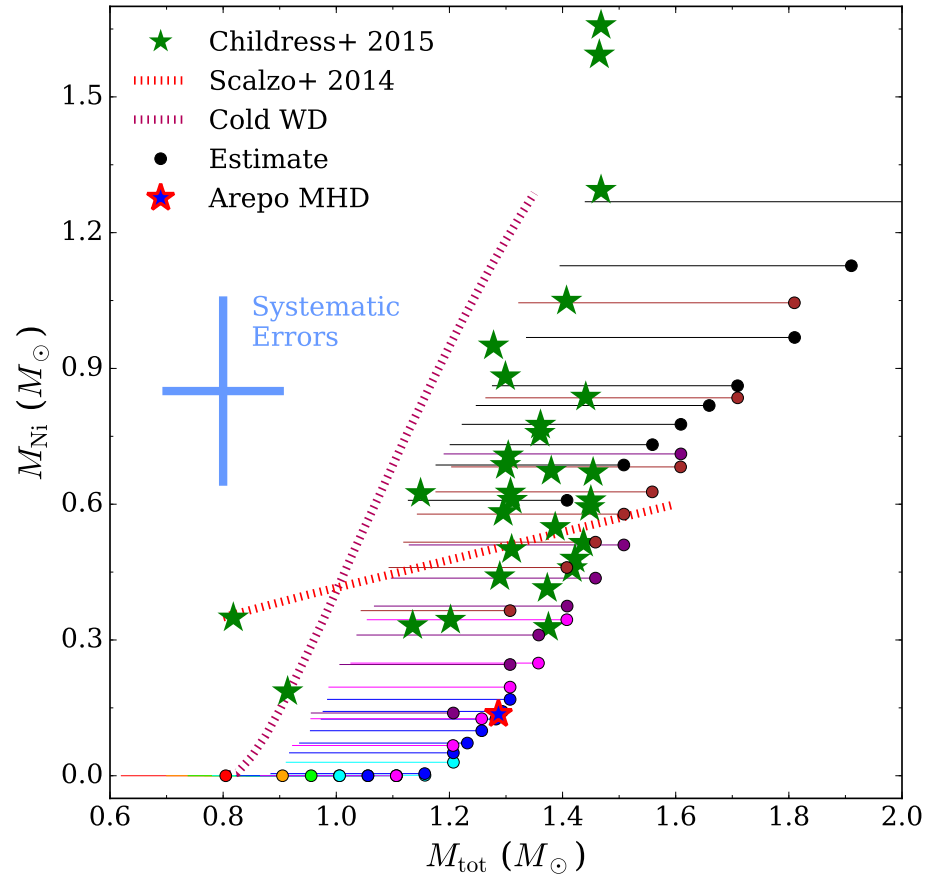


Figure 6.1: Relationships between total ejected mass M_{tot} and synthesized ^{56}Ni mass M_{Ni} for the merger remnants of Sec. 2.6.1 if they were to (artificially) experience a pure detonation immediately after their estimated viscous spin-down. M_{Ni} is estimated by the mass of all remnant material with density $\rho > 10^7 \text{ g cm}^{-3}$, $M(\rho > 10^7)$. For the points, M_{tot} is estimated as the total mass of the remnant, but we also extend lines leftward from each point to indicate how much of M_{tot} is in the tenuous envelope. Colors indicate accretor mass, as in Fig. 2.3. Also plotted is the estimate for the AREPO MHD $0.625 - 0.65 M_{\odot}$ remnant (Ch. 4; red-blue star). All other features are as in Fig. 5.2.

the envelopes to bracket their inclusion.

Keeping in mind that our simple estimate tends to overestimate the amount of compression during viscous evolution, particularly for similar-mass mergers (Sec. 2.8), we see that only mergers with $M_{\text{tot}} \gtrsim M_{\text{Ch}}$ produce more than $\sim 0.2 M_{\odot}$ of ^{56}Ni . Since more realistic simulations of viscous evolution predict less core compression, and not all remnants will ignite fusion, Fig. 6.1 estimates the upper limit of ^{56}Ni produced by the sub- M_{Ch} merger channel, and poses a challenge to its viability for producing normal SNe Ia.

6.4 What are the Outcomes of CO WD Mergers?

Considering the number of hurdles above, it appears that mergers of two CO WDs whose total mass is substantially below M_{Ch} , including our fiducial $0.625 - 0.65 M_{\odot}$ merger, are unlikely to produce normal SNe Ia. The more massive among them may ignite carbon burning, but these will probably become partly non-degenerate and expand before they achieve dynamical burning, eventually transforming their composition to O and Ne before cooling to become massive, highly-magnetized WDs. Similar-mass *super- M_{Ch}* WDs, on the other hand, may follow vK10’s evolutionary channel to ignite highly degenerate nuclear burning and eventually explode: mergers with accretors of $\gtrsim 0.8 M_{\odot}$ create remnants that easily ignite nuclear burning during post-merger evolution and satisfy both the mass and central density constraints suggested by our simmering study. Moreover, our rough estimate in Fig. 6.1 shows they would produce ^{56}Ni masses consistent with normal SNe Ia. This scenario for producing SNe Ia from super- M_{Ch} mergers is qualitatively different from the traditional one of slow accretion in eg. Yoon et al. (2007), though limiting explosion candidates to super- M_{Ch} systems still leads to the same issue of rates affecting all other scenarios that require extremely massive WDs (Sec. 1.3.1).

These super- M_{Ch} binary systems, however, may have already exploded in a violent merger (Sec. 1.3.2), or shortly after coalescence due to accretion-heating from an $m = 1$ spiral mode (Kashyap et al. 2015). The minimum masses required for either are not well-known (see Dan et al. 2012; Sato et al. 2016 for recent estimates for violent mergers), so it remains a task for future parameter-space merger studies to constrain them.

6.5 Observational Avenues of Exploration

Finally, we stress the potential of observational work in shedding light on this subject. Recently revealed properties of the hot DQ WD population tantalizingly suggest they represent double CO WD merger remnants that did not explode (Sec. 1.5). Many of their fundamental properties, such as their masses and space density, remain poorly understood, but the Gaia mission will provide a much more complete sample of WDs and their parallaxes to help constrain these values (Dunlap 2015). Future observations will allow us to judge more confidently whether hot DQs are merger remnants. If they are, the population’s properties will serve as an observational check for the theoretical evolutionary scenarios in this work.

It may also be possible to spot merger remnants during their thermal evolution phase described in Sec. 2.8. Schwab et al. (2016) consider the observable properties of their $1.5 M_{\odot}$ merger remnant, and calculate that it radiates on the order the Eddington luminosity for a $1.5 M_{\odot}$ star ($\sim 10^5 L_{\odot}$), and may also generate clouds of dust in its outermost layers, which will be launched as an optically thick

wind. This drives the remnant's photosphere out to $\sim 10^{15}$ cm, with a corresponding photospheric temperature of ~ 500 K, as well as possibly R CrB-like variability of the remnant's luminosity. Schwab et al. (2016) note these features are similar to those of extreme AGB stars (eg. Blum et al. 2006), and perhaps can be discovered using the same observational techniques. Since sub- M_{Ch} remnants have the same order of magnitude total energy as M_{Ch} ones, their observed properties will be similar.

We have not yet modeled any explosions that might arise from our merger remnants, or their photometric and spectroscopic appearance, but other groups have done so for systems at various stages of the merger and post-merger evolution. For example, Raskin et al. (2014) and van Rossum et al. (2015) simulate the pure detonation of super- M_{Ch} merger remnants just after coalescence, and show that the resulting light curves and spectra are strongly dependent on viewing angle due to interactions between the ejecta and remnant disk producing an hourglass-shaped explosion. The light curves of these "tamped explosions" also tend to evolve more slowly (their decline from peak light take a factor of ~ 1.5 times longer) than typical SNe Ia, due to their lower ^{56}Ni production compared to hydrostatic WDs of the same mass. For remnants that have undergone viscous evolution before exploding, Raskin et al. (2014) find up to a factor of ~ 2 increase in ^{56}Ni production compared to the tamped explosions due to the compression of the remnant core. Post-viscous remnants will also have a tenuous envelope of several $0.1 M_{\odot}$, and Piro & Morozova (2015)'s simulations of explosions within such envelopes find a early peak at ~ 1 day in their light curves, from the shock-cooling of the envelope, that is up to a few percent the peak brightness of the explosion. Examining the existence and frequency of such features in observed SNe Ia – for example, by using spectropolarimetry (eg. Bulla et al. 2015) to quantify asymmetry in explosions or by searching for excess early-time light (eg. Marion et al. 2016) to detect explosion-envelope interaction – is another means of observationally assessing our theoretical scenarios.

These new observational studies, alongside the theoretical and numerical ones discussed earlier, may clarify many of the outstanding questions posed throughout this thesis. With luck, they will also lead to a clearer understanding of the fates of CO WD merger products and the origins of SNe Ia.

Bibliography

- Abbott, B. P., Abbott, R., Abbott, T. D., et al. 2016, Physical Review Letters, 116, 131102
- Adams, F. C., Ruden, S. P., & Shu, F. H. 1989, ApJ, 347, 959
- Agertz, O., Moore, B., Stadel, J., et al. 2007, MNRAS, 380, 963
- Althaus, L. G., García-Berro, E., Cársico, A. H., Miller Bertolami, M. M., & Romero, A. D. 2009, ApJ, 693, L23
- Amaro-Seoane, P., Aoudia, S., Babak, S., et al. 2013, GW Notes, Vol. 6, p. 4-110, 6, 4
- Arnett, D. 1996, Supernovae and Nucleosynthesis
- Aspden, A. J., Bell, J. B., Dong, S., & Woosley, S. E. 2011, ApJ, 738, 94
- Augustson, K. C., Brun, A. S., & Toomre, J. 2016, ArXiv e-prints, arXiv:1603.03659
- Badenes, C., & Maoz, D. 2012, ApJ, 749, L11
- Balbus, S. A. 2003, ARA&A, 41, 555
- Balbus, S. A., & Hawley, J. F. 1991, ApJ, 376, 214
- Barker, A. J., Dempsey, A. M., & Lithwick, Y. 2014, ApJ, 791, 13
- Barstow, M. A., Jordan, S., O'Donoghue, D., et al. 1995, MNRAS, 277, 971
- Beloborodov, A. M. 2014, MNRAS, 438, 169
- Benz, W., Cameron, A. G. W., Press, W. H., & Bowers, R. L. 1990, ApJ, 348, 647
- Benz, W., Thielemann, F.-K., & Hills, J. G. 1989, ApJ, 342, 986
- Bildsten, L., Shen, K. J., Weinberg, N. N., & Nelemans, G. 2007, ApJ, 662, L95
- Bloom, J. S., Kasen, D., Shen, K. J., et al. 2012, ApJ, 744, L17
- Blum, R. D., Mould, J. R., Olsen, K. A., et al. 2006, AJ, 132, 2034
- Branch, D. 1998, ARA&A, 36, 17
- Branch, D., Dang, L. C., Hall, N., et al. 2006, PASP, 118, 560
- Briggs, G. P., Ferrario, L., Tout, C. A., Wickramasinghe, D. T., & Hurley, J. R. 2015, MNRAS, 447, 1713

- Brown, W. R., Kilic, M., Allende Prieto, C., & Kenyon, S. J. 2010, *ApJ*, 723, 1072
- Brown, W. R., Kilic, M., Hermes, J. J., et al. 2011, *ApJ*, 737, L23
- Brown, W. R., Kilic, M., Kenyon, S. J., & Gianninas, A. 2016, *ApJ*, 824, 46
- Brun, A. S., Browning, M. K., & Toomre, J. 2005, *ApJ*, 629, 461
- Bulla, M., Sim, S. A., & Kromer, M. 2015, *MNRAS*, 450, 967
- Burkart, J., Quataert, E., Arras, P., & Weinberg, N. N. 2013, *MNRAS*, 433, 332
- Carrasco, J. M., Catalán, S., Jordi, C., et al. 2014, *A&A*, 565, A11
- Centrella, J. M., New, K. C. B., Lowe, L. L., & Brown, J. D. 2001, *ApJ*, 550, L193
- Cha, S.-H., & Wood, M. A. 2016, *MNRAS*, 458, 480
- Chabrier, G., Gallardo, J., & Baraffe, I. 2007, *A&A*, 472, L17
- Chandrasekhar, S. 1931, *ApJ*, 74, 81
- Childress, M. J., Hillier, D. J., Seitzenzahl, I., et al. 2015, *MNRAS*, 454, 3816
- Chiosi, E., Chiosi, C., Trevisan, P., Piovan, L., & Orio, M. 2015, *MNRAS*, 448, 2100
- Churazov, E., Sunyaev, R., Isern, J., et al. 2014, *Nature*, 512, 406
- Claeys, J. S. W., Pols, O. R., Izzard, R. G., Vink, J., & Verbunt, F. W. M. 2014, *A&A*, 563, A83
- Clark, D. H., & Stephenson, F. R. 1977, *The historical supernovae*
- Clayton, G. C. 2012, *Journal of the American Association of Variable Star Observers (JAAVSO)*, 40, 539
- Cullen, L., & Dehnen, W. 2010, *MNRAS*, 408, 669
- Dan, M., Guillochon, J., Brüggen, M., Ramirez-Ruiz, E., & Rosswog, S. 2015, *MNRAS*, 454, 4411
- Dan, M., Rosswog, S., Brüggen, M., & Podsiadlowski, P. 2014, *MNRAS*, 438, 14
- Dan, M., Rosswog, S., Guillochon, J., & Ramirez-Ruiz, E. 2011, *ApJ*, 737, 89
- . 2012, *MNRAS*, 422, 2417
- de Val-Borro, M., Edgar, R. G., Artymowicz, P., et al. 2006, *MNRAS*, 370, 529
- Dedner, A., Kemm, F., Kröner, D., et al. 2002, *Journal of Computational Physics*, 175, 645
- Dehnen, W., & Aly, H. 2012, *MNRAS*, 425, 1068
- Dessart, L., Burrows, A., Livne, E., & Ott, C. D. 2007, *ApJ*, 669, 585
- Dessart, L., Burrows, A., Ott, C. D., et al. 2006, *ApJ*, 644, 1063
- Di Stefano, R. 2010, *ApJ*, 719, 474
- Di Stefano, R., Fisher, R., Guillochon, J., & Steiner, J. F. 2015, ArXiv e-prints, arXiv:1501.07837

- Dilday, B., Howell, D. A., Cenko, S. B., et al. 2012, *Science*, 337, 942
- Dionysopoulou, K., Alic, D., & Rezzolla, L. 2015, *Phys. Rev. D*, 92, 084064
- Dolag, K., Vazza, F., Brunetti, G., & Tormen, G. 2005, *MNRAS*, 364, 753
- D'Souza, M. C. R., Motl, P. M., Tohline, J. E., & Frank, J. 2006, *ApJ*, 643, 381
- Dubey, A., Reid, L. B., Weide, K., et al. 2009, ArXiv e-prints, arXiv:0903.4875
- Duffell, P. C., & MacFadyen, A. I. 2011, *ApJS*, 197, 15
- Dufour, P., Ben Nessib, N., Sahal-Bréchot, S., & Dimitrijević, M. S. 2011, *Baltic Astronomy*, 20, 511
- Dufour, P., Fontaine, G., Liebert, J., Schmidt, G. D., & Behara, N. 2008, *ApJ*, 683, 978
- Dufour, P., Liebert, J., Fontaine, G., & Behara, N. 2007, *Nature*, 450, 522
- Dufour, P., Vornanen, T., Bergeron, P., & Fontaine, A., B. 2013, in *Astronomical Society of the Pacific Conference Series*, Vol. 469, 18th European White Dwarf Workshop., 167
- Dunlap, B. H. 2015, PhD thesis, University of North Carolina at Chapel Hill
- Dunlap, B. H., & Clemens, J. C. 2015, in *Astronomical Society of the Pacific Conference Series*, Vol. 493, 19th European Workshop on White Dwarfs, ed. P. Dufour, P. Bergeron, & G. Fontaine, 547
- Eggleton, P. P. 1983, *ApJ*, 268, 368
- Evans, C. R., & Hawley, J. F. 1988, *ApJ*, 332, 659
- Featherstone, N. A., Browning, M. K., Brun, A. S., & Toomre, J. 2009, *ApJ*, 705, 1000
- Feiden, G. A., & Chaboyer, B. 2012, *ApJ*, 761, 30
- Ferrario, L., de Martino, D., & Gänsicke, B. T. 2015, *Space Sci. Rev.*, 191, 111
- Filippenko, A. V. 1997, *ARA&A*, 35, 309
- Fink, M., Hillebrandt, W., & Röpke, F. K. 2007, *A&A*, 476, 1133
- Fink, M., Röpke, F. K., Hillebrandt, W., et al. 2010, *A&A*, 514, A53
- Fink, M., Kromer, M., Seitenzahl, I. R., et al. 2014, *MNRAS*, 438, 1762
- Fisher, R., & Jumper, K. 2015, *ApJ*, 805, 150
- Foley, R. J., Challis, P. J., Chornock, R., et al. 2013, *ApJ*, 767, 57
- Fryer, C. L., Brown, P. J., Bufano, F., et al. 2009, *ApJ*, 707, 193
- Fryxell, B., Olson, K., Ricker, P., et al. 2000, *ApJS*, 131, 273
- Fuller, J., & Lai, D. 2012, *MNRAS*, 421, 426
- . 2014, *MNRAS*, 444, 3488

- Gaburov, E., Johansen, A., & Levin, Y. 2012, *ApJ*, 758, 103
- Gaensicke, B., Tremblay, P.-E., Barstow, M., et al. 2015, ArXiv e-prints, arXiv:1506.02653
- García-Berro, E. 2013, in IAU Symposium, Vol. 281, Binary Paths to Type Ia Supernovae Explosions, ed. R. Di Stefano, M. Orio, & M. Moe, 52–59
- García-Berro, E., Kilic, M., & Kepler, S. O. 2016, International Journal of Modern Physics D, 25, 1630005
- García-Berro, E., Lorén-Aguilar, P., Aznar-Siguán, G., et al. 2012, *ApJ*, 749, 25
- García-Senz, D., Cabezón, R. M., Arcones, A., Relaño, A., & Thielemann, F. K. 2013, *MNRAS*, 436, 3413
- Giacomazzo, B., Zrake, J., Duffell, P. C., MacFadyen, A. I., & Perna, R. 2015, *ApJ*, 809, 39
- Giammichele, N., Bergeron, P., & Dufour, P. 2012, *ApJS*, 199, 29
- Gianninas, A., Kilic, M., Brown, W. R., Canton, P., & Kenyon, S. J. 2015, *ApJ*, 812, 167
- Gilfanov, M., & Bogdán, Á. 2010, *Nature*, 463, 924
- Gingold, R. A., & Monaghan, J. J. 1977, *MNRAS*, 181, 375
- Goedbloed, J. P. H., & Poedts, S. 2004, Principles of Magnetohydrodynamics
- Gokhale, V., Peng, X. M., & Frank, J. 2007, *ApJ*, 655, 1010
- Gough, D. O., & Tayler, R. J. 1966, *MNRAS*, 133, 85
- Governato, F., Weisz, D., Pontzen, A., et al. 2015, *MNRAS*, 448, 792
- Guerrero, J., García-Berro, E., & Isern, J. 2004, *A&A*, 413, 257
- Guillochon, J., Dan, M., Ramirez-Ruiz, E., & Rosswog, S. 2010, *ApJ*, 709, L64
- Hachisu, I., Kato, M., & Nomoto, K. 2010, *ApJ*, 724, L212
- Hamann, W.-R. 1997, in IAU Symposium, Vol. 180, Planetary Nebulae, ed. H. J. Habing & H. J. G. L. M. Lamers, 91
- Hamuy, M., Trager, S. C., Pinto, P. A., et al. 2000, *AJ*, 120, 1479
- Han, Z., Podsiadlowski, P., Maxted, P. F. L., Marsh, T. R., & Ivanova, N. 2002, *MNRAS*, 336, 449
- Hayes, J. C., Norman, M. L., Fiedler, R. A., et al. 2006, *ApJS*, 165, 188
- Hayward, C. C., Torrey, P., Springel, V., Hernquist, L., & Vogelsberger, M. 2014, *MNRAS*, 442, 1992
- Heber, U. 2016, ArXiv e-prints, arXiv:1604.07749
- Hernquist, L., & Katz, N. 1989, *ApJS*, 70, 419
- Herwig, F. 2005, *ARA&A*, 43, 435
- Heß, S., & Springel, V. 2010, *MNRAS*, 406, 2289

- Hillebrandt, W., Kromer, M., Röpke, F. K., & Ruiter, A. J. 2013, *Frontiers of Physics*, 8, 116
- Hillebrandt, W., & Niemeyer, J. C. 2000, *ARA&A*, 38, 191
- Hillman, Y., Prialnik, D., Kovetz, A., & Shara, M. M. 2016, *ApJ*, 819, 168
- Holcomb, C., Guillochon, J., De Colle, F., & Ramirez-Ruiz, E. 2013, *ApJ*, 771, 14
- Hopkins, P. F. 2013, *MNRAS*, 428, 2840
- . 2015, *MNRAS*, 450, 53
- Hopkins, P. F., & Quataert, E. 2010, *MNRAS*, 407, 1529
- Hopkins, P. F., & Raives, M. J. 2016, *MNRAS*, 455, 51
- Howell, D. A. 2011, *Nature Communications*, 2, 350
- Hoyle, F., & Fowler, W. A. 1960, *ApJ*, 132, 565
- Hu, C.-Y., Naab, T., Walch, S., Moster, B. P., & Oser, L. 2014, *MNRAS*, 443, 1173
- Hurley, J. R., Pols, O. R., & Tout, C. A. 2000, *MNRAS*, 315, 543
- Iben, Jr., I., & Tutukov, A. V. 1984, *ApJS*, 54, 335
- . 1985, *ApJS*, 58, 661
- Idan, I., Shaviv, N. J., & Shaviv, G. 2013, *MNRAS*, 433, 2884
- Ilkov, M., & Soker, N. 2012, *MNRAS*, 419, 1695
- Jeffery, C. S. 2014, in *IAU Symposium*, Vol. 301, Precision Asteroseismology, ed. J. A. Guzik, W. J. Chaplin, G. Handler, & A. Pigulski, 297–304
- Ji, S., Fisher, R. T., García-Berro, E., et al. 2013, *ApJ*, 773, 136
- Johansson, J., Woods, T. E., Gilfanov, M., et al. 2014, *MNRAS*, 442, 1079
- Justham, S., Podsiadlowski, P., & Han, Z. 2011, *MNRAS*, 410, 984
- Kaiser, N., Burgett, W., Chambers, K., et al. 2010, in *Proc. SPIE*, Vol. 7733, Ground-based and Airborne Telescopes III, 77330E
- Kashi, A., & Soker, N. 2011, *MNRAS*, 417, 1466
- Kashyap, R., Fisher, R., García-Berro, E., et al. 2015, *ApJ*, 800, L7
- Katz, B., & Dong, S. 2012, ArXiv e-prints, arXiv:1211.4584
- Katz, M. P., Zingale, M., Calder, A. C., et al. 2016, *ApJ*, 819, 94
- Keller, B. W., Wadsley, J., Benincasa, S. M., & Couchman, H. M. P. 2014, *MNRAS*, 442, 3013
- Keller, B. W., Wadsley, J., & Couchman, H. M. P. 2015, *MNRAS*, 453, 3499

- Kepler, S. O., Pelisoli, I., Jordan, S., et al. 2013, MNRAS, 429, 2934
- Kerzendorf, W. E., Childress, M., Scharwächter, J., Do, T., & Schmidt, B. P. 2014a, ApJ, 782, 27
- Kerzendorf, W. E., Taubenberger, S., Seitenzahl, I. R., & Ruiter, A. J. 2014b, ApJ, 796, L26
- Khokhlov, A. M. 1991, A&A, 245, 114
- Kippenhahn, R., Weigert, A., & Weiss, A. 2012, Stellar Structure and Evolution, doi:10.1007/978-3-642-30304-3
- Kissin, Y., & Thompson, C. 2015, ApJ, 809, 108
- Kiuchi, K., Kyutoku, K., Sekiguchi, Y., Shibata, M., & Wada, T. 2014, Phys. Rev. D, 90, 041502
- Kleinman, S. J., Kepler, S. O., Koester, D., et al. 2013, ApJS, 204, 5
- Kozai, Y. 1962, AJ, 67, 591
- Kratter, K. M., & Lodato, G. 2016, ArXiv e-prints, arXiv:1603.01280
- Kremer, K., Sepinsky, J., & Kalogera, V. 2015, ApJ, 806, 76
- Kromer, M., Sim, S. A., Fink, M., et al. 2010, ApJ, 719, 1067
- Kromer, M., Fink, M., Stanishev, V., et al. 2013, MNRAS, 429, 2287
- Kuhlen, M., Woosley, S. E., & Glatzmaier, G. A. 2006, ApJ, 640, 407
- Külebi, B., Ekşi, K. Y., Lorén-Aguilar, P., Isern, J., & García-Berro, E. 2013, MNRAS, 431, 2778
- Külebi, B., Jordan, S., Nelan, E., Bastian, U., & Altmann, M. 2010, A&A, 524, A36
- Kushnir, D., Katz, B., Dong, S., Livne, E., & Fernández, R. 2013, ApJ, 778, L37
- Lai, D., Rasio, F. A., & Shapiro, S. L. 1994, ApJ, 437, 742
- Lawrie, K. A., Burleigh, M. R., Dufour, P., & Hodgkin, S. T. 2013, MNRAS, 433, 1599
- Leibundgut, B., Kirshner, R. P., Phillips, M. M., et al. 1993, AJ, 105, 301
- Lepo, K., & van Kerkwijk, M. 2013, ApJ, 771, 13
- Lesaffre, P., Han, Z., Tout, C. A., Podsiadlowski, P., & Martin, R. G. 2006, MNRAS, 368, 187
- Lewis, B. T., Bate, M. R., & Tricco, T. S. 2016, ArXiv e-prints, arXiv:1606.06972
- Li, W., Filippenko, A. V., Chornock, R., et al. 2003, PASP, 115, 453
- Li, W., Bloom, J. S., Podsiadlowski, P., et al. 2011a, Nature, 480, 348
- Li, W., Leaman, J., Chornock, R., et al. 2011b, MNRAS, 412, 1441
- Lidov, M. L. 1962, Planet. Space Sci., 9, 719
- Liebert, J., Bergeron, P., & Holberg, J. B. 2005, ApJS, 156, 47

- Liebert, J., Ferrario, L., Wickramasinghe, D. T., & Smith, P. S. 2015, *ApJ*, 804, 93
- LIGO Scientific Collaboration, Aasi, J., Abbott, B. P., et al. 2015, *Classical and Quantum Gravity*, 32, 074001
- Lin, M.-K. 2015, *MNRAS*, 448, 3806
- Livio, M., & Riess, A. G. 2003, *ApJ*, 594, L93
- Livne, E. 1990, *ApJ*, 354, L53
- Loken, C., Gruner, D., Groer, L., et al. 2010, *Journal of Physics Conference Series*, 256, 012026
- Lorén-Aguilar, P., Isern, J., & García-Berro, E. 2009, *A&A*, 500, 1193
- . 2010, *MNRAS*, 406, 2749
- LSST Science Collaboration, Abell, P. A., Allison, J., et al. 2009, ArXiv e-prints, arXiv:0912.0201
- Lubow, S. H., & Shu, F. H. 1975, *ApJ*, 198, 383
- Lucy, L. B. 1977, *AJ*, 82, 1013
- MacDonald, J., & Mullan, D. J. 2009, *ApJ*, 700, 387
- Maeda, K., Taubenberger, S., Sollerman, J., et al. 2010a, *ApJ*, 708, 1703
- Maeda, K., Benetti, S., Stritzinger, M., et al. 2010b, *Nature*, 466, 82
- Maguire, K., Taubenberger, S., Sullivan, M., & Mazzali, P. A. 2016, *MNRAS*, 457, 3254
- Maoz, D., Badenes, C., & Bickerton, S. J. 2012, *ApJ*, 751, 143
- Maoz, D., Mannucci, F., Li, W., et al. 2011, *MNRAS*, 412, 1508
- Maoz, D., Mannucci, F., & Nelemans, G. 2014, *ARA&A*, 52, 107
- Maoz, D., Sharon, K., & Gal-Yam, A. 2010, *ApJ*, 722, 1879
- Marinacci, F., Pakmor, R., & Springel, V. 2014, *MNRAS*, 437, 1750
- Marion, G. H., Brown, P. J., Vinkó, J., et al. 2016, *ApJ*, 820, 92
- Marquardt, K. S., Sim, S. A., Ruiter, A. J., et al. 2015, *A&A*, 580, A118
- Marsh, T. R. 2011, *Classical and Quantum Gravity*, 28, 094019
- Marsh, T. R., Dhillon, V. S., & Duck, S. R. 1995, *MNRAS*, 275, 828
- Marsh, T. R., Nelemans, G., & Steeghs, D. 2004, *MNRAS*, 350, 113
- Mazurek, T. J., Meier, D. L., & Wheeler, J. C. 1977, *ApJ*, 213, 518
- Mazzali, P. A., Chugai, N., Turatto, M., et al. 1997, *MNRAS*, 284, 151

- Mennekens, N., Vanbeveren, D., de Greve, J., & de Donder, E. 2010, in Astronomical Society of the Pacific Conference Series, Vol. 435, Binaries - Key to Comprehension of the Universe, ed. A. Prša & M. Zejda, 33
- Meru, F., & Bate, M. R. 2010, MNRAS, 406, 2279
- Mitchell, N. L., McCarthy, I. G., Bower, R. G., Theuns, T., & Crain, R. A. 2009, MNRAS, 395, 180
- Miyaji, S., Nomoto, K., Yokoi, K., & Sugimoto, D. 1980, PASJ, 32, 303
- Miyoshi, T., & Kusano, K. 2005, Journal of Computational Physics, 208, 315
- Mochkovitch, R., & Livio, M. 1989, A&A, 209, 111
- Mocz, P., Pakmor, R., Springel, V., et al. 2016, ArXiv e-prints, arXiv:1606.02310
- Mocz, P., Vogelsberger, M., & Hernquist, L. 2014, MNRAS, 442, 43
- Moll, R., Raskin, C., Kasen, D., & Woosley, S. E. 2014, ApJ, 785, 105
- Moll, R., & Woosley, S. E. 2013, ApJ, 774, 137
- Monaghan, J. J. 2005, Reports on Progress in Physics, 68, 1703
- Morris, J. P., & Monaghan, J. J. 1997, Journal of Computational Physics, 136, 41
- Muhlberger, C. D., Nouri, F. H., Duez, M. D., et al. 2014, Phys. Rev. D, 90, 104014
- Nandez, J. L. A., Ivanova, N., & Lombardi, Jr., J. C. 2014, ApJ, 786, 39
- Napiwotzki, R., Karl, C. A., Nelemans, G., et al. 2007, in Astronomical Society of the Pacific Conference Series, Vol. 372, 15th European Workshop on White Dwarfs, ed. R. Napiwotzki & M. R. Burleigh, 387
- Nelemans, G. 2010, Ap&SS, 329, 25
- Nelemans, G., Portegies Zwart, S. F., Verbunt, F., & Yungelson, L. R. 2001a, A&A, 368, 939
- Nelemans, G., Yungelson, L. R., & Portegies Zwart, S. F. 2001b, A&A, 375, 890
- Nelemans, G., Yungelson, L. R., Portegies Zwart, S. F., & Verbunt, F. 2001c, A&A, 365, 491
- Nielsen, M. T. B., Gilfanov, M., Bogdán, Á., Woods, T. E., & Nelemans, G. 2014, MNRAS, 442, 3400
- Nielsen, M. T. B., Voss, R., & Nelemans, G. 2013, MNRAS, 435, 187
- Nomoto, K., & Iben, Jr., I. 1985, ApJ, 297, 531
- Nonaka, A., Aspden, A. J., Zingale, M., et al. 2012, ApJ, 745, 73
- Nugent, P. E., Sullivan, M., Cenko, S. B., et al. 2011, Nature, 480, 344
- Obergaulinger, M., Aloy, M. A., & Müller, E. 2010, A&A, 515, A30
- Ohlmann, S. T., Röpke, F. K., Pakmor, R., & Springel, V. 2016, ApJ, 816, L9
- Olling, R. P., Mushotzky, R., Shaya, E. J., et al. 2015, Nature, 521, 332

- Ott, C. D., Ou, S., Tohline, J. E., & Burrows, A. 2005, *ApJ*, 625, L119
- Paczyński, B. 1971, *ARA&A*, 9, 183
- Pakmor, R., Bauer, A., & Springel, V. 2011a, *MNRAS*, 418, 1392
- Pakmor, R., Edelmann, P., Röpke, F. K., & Hillebrandt, W. 2012a, *MNRAS*, 424, 2222
- Pakmor, R., Hachinger, S., Röpke, F. K., & Hillebrandt, W. 2011b, *A&A*, 528, A117
- Pakmor, R., Kromer, M., Röpke, F. K., et al. 2010, *Nature*, 463, 61
- Pakmor, R., Kromer, M., Taubenberger, S., et al. 2012b, *ApJ*, 747, L10
- Pakmor, R., Kromer, M., Taubenberger, S., & Springel, V. 2013, *ApJ*, 770, L8
- Pakmor, R., & Springel, V. 2013, *MNRAS*, 432, 176
- Pakmor, R., Springel, V., Bauer, A., et al. 2016, *MNRAS*, 455, 1134
- Papaloizou, J. C. B., & Pringle, J. E. 1984, *MNRAS*, 208, 721
- Paschalidis, V., East, W. E., Pretorius, F., & Shapiro, S. L. 2015, *Phys. Rev. D*, 92, 121502
- Paxton, B., Bildsten, L., Dotter, A., et al. 2011, *ApJS*, 192, 3
- Paxton, B., Cantiello, M., Arras, P., et al. 2013, *ApJS*, 208, 4
- Paxton, B., Marchant, P., Schwab, J., et al. 2015, *ApJS*, 220, 15
- Perets, H. B., Gal-Yam, A., Mazzali, P. A., et al. 2010, *Nature*, 465, 322
- Perlmutter, S., Aldering, G., Goldhaber, G., et al. 1999, *ApJ*, 517, 565
- Peters, P. C., & Mathews, J. 1963, *Physical Review*, 131, 435
- Phillips, M. M. 1993, *ApJ*, 413, L105
- Phillips, M. M., Li, W., Frieman, J. A., et al. 2007, *PASP*, 119, 360
- Piersanti, L., Tornambé, A., & Yungelson, L. R. 2014, *MNRAS*, 445, 3239
- Piro, A. L. 2008, *ApJ*, 679, 616
- . 2011, *ApJ*, 740, L53
- Piro, A. L., & Bildsten, L. 2008, *ApJ*, 673, 1009
- Piro, A. L., & Chang, P. 2008, *ApJ*, 678, 1158
- Piro, A. L., & Morozova, V. S. 2015, ArXiv e-prints, arXiv:1512.03442
- Piro, A. L., Thompson, T. A., & Kochanek, C. S. 2014, *MNRAS*, 438, 3456
- Powell, K. G., Roe, P. L., Linde, T. J., Gombosi, T. I., & De Zeeuw, D. L. 1999, *Journal of Computational Physics*, 154, 284

- Prada Moroni, P. G., & Straniero, O. 2009, A&A, 507, 1575
- Price, D. J. 2008, Journal of Computational Physics, 227, 10040
- . 2012, Journal of Computational Physics, 231, 759
- Price, D. J., & Rosswog, S. 2006, Science, 312, 719
- Pritchett, C. J., Howell, D. A., & Sullivan, M. 2008, ApJ, 683, L25
- Proctor, M. R. E., & Weiss, N. O. 1982, Reports on Progress in Physics, 45, 1317
- Radice, D., Bernuzzi, S., & Ott, C. D. 2016, ArXiv e-prints, arXiv:1603.05726
- Raskin, C., Kasen, D., Moll, R., Schwab, J., & Woosley, S. 2014, ApJ, 788, 75
- Raskin, C., Scannapieco, E., Fryer, C., Rockefeller, G., & Timmes, F. X. 2012, ApJ, 746, 62
- Raskin, C., Scannapieco, E., Rockefeller, G., et al. 2010, ApJ, 724, 111
- Rau, A., Kulkarni, S. R., Law, N. M., et al. 2009, PASP, 121, 1334
- Read, J. I., Hayfield, T., & Agertz, O. 2010, MNRAS, 405, 1513
- Rebassa-Mansergas, A., Rybicka, M., Liu, X.-W., Han, Z., & García-Berro, E. 2015a, MNRAS, 452, 1637
- Rebassa-Mansergas, A., Liu, X.-W., Cojocaru, R., et al. 2015b, MNRAS, 450, 743
- Rice, W. K. M., Lodato, G., & Armitage, P. J. 2005, MNRAS, 364, L56
- Riess, A. G., Press, W. H., & Kirshner, R. P. 1996, ApJ, 473, 88
- Riess, A. G., Filippenko, A. V., Challis, P., et al. 1998, AJ, 116, 1009
- Rogers, P. D., & Wadsley, J. 2012, MNRAS, 423, 1896
- Rosswog, S. 2009, New A Rev., 53, 78
- . 2015, International Journal of Modern Physics D, 24, 1530012
- Ruiter, A. J., Belczynski, K., & Fryer, C. 2009, ApJ, 699, 2026
- Ruiter, A. J., Belczynski, K., Sim, S. A., et al. 2011, MNRAS, 417, 408
- Ruiter, A. J., Belczynski, K., Sim, S. A., Seitenzahl, I. R., & Kwiatkowski, D. 2014, MNRAS, 440, L101
- Ruiter, A. J., Sim, S. A., Pakmor, R., et al. 2013, MNRAS, 429, 1425
- Ruiz-Lapuente, P., & Spruit, H. C. 1998, ApJ, 500, 360
- Saijo, M., Baumgarthe, T. W., & Shapiro, S. L. 2003, ApJ, 595, 352
- Saio, H., & Jeffery, C. S. 2000, MNRAS, 313, 671
- . 2002, MNRAS, 333, 121
- Saio, H., & Nomoto, K. 1985, A&A, 150, L21

- . 1998, *ApJ*, 500, 388
- Sato, Y., Nakasato, N., Tanikawa, A., et al. 2016, *ApJ*, 821, 67
- Scalzo, R., Aldering, G., Antilogus, P., et al. 2014a, *MNRAS*, 440, 1498
- Scalzo, R. A., Ruiter, A. J., & Sim, S. A. 2014b, *MNRAS*, 445, 2535
- Schwab, J., Quataert, E., & Bildsten, L. 2015, *MNRAS*, 453, 1910
- Schwab, J., Quataert, E., & Kasen, D. 2016, ArXiv e-prints, arXiv:1606.02300
- Schwab, J., Shen, K. J., Quataert, E., Dan, M., & Rosswog, S. 2012, *MNRAS*, 427, 190
- Segretain, L., Chabrier, G., & Mochkovitch, R. 1997, *ApJ*, 481, 355
- Seitenzahl, I. R., Ciaraldi-Schoolmann, F., & Röpke, F. K. 2011, *MNRAS*, 414, 2709
- Seitenzahl, I. R., Meakin, C. A., Townsley, D. M., Lamb, D. Q., & Truran, J. W. 2009, *ApJ*, 696, 515
- Seitenzahl, I. R., Kromer, M., Ohlmann, S. T., et al. 2016, ArXiv e-prints, arXiv:1606.00089
- Shakura, N. I., & Sunyaev, R. A. 1973, *A&A*, 24, 337
- Shen, K. J. 2015, *ApJ*, 805, L6
- Shen, K. J., & Bildsten, L. 2014, *ApJ*, 785, 61
- Shen, K. J., Bildsten, L., Kasen, D., & Quataert, E. 2012, *ApJ*, 748, 35
- Shen, K. J., Kasen, D., Weinberg, N. N., Bildsten, L., & Scannapieco, E. 2010a, *ApJ*, 715, 767
- Shen, K. J., & Moore, K. 2014, *ApJ*, 797, 46
- Shen, S., Wadsley, J., & Stinson, G. 2010b, *MNRAS*, 407, 1581
- Shigeyama, T., Nomoto, K., Yamaoka, H., & Thielemann, F.-K. 1992, *ApJ*, 386, L13
- Shu, F. H., Tremaine, S., Adams, F. C., & Ruden, S. P. 1990, *ApJ*, 358, 495
- Sim, S. A., Röpke, F. K., Hillebrandt, W., et al. 2010, *ApJ*, 714, L52
- Soker, N. 1998, *AJ*, 116, 1308
- Soker, N., Kashi, A., García-Berro, E., Torres, S., & Camacho, J. 2013, *MNRAS*, 431, 1541
- Springel, V. 2005, *MNRAS*, 364, 1105
- . 2010a, *MNRAS*, 401, 791
- . 2010b, *ARA&A*, 48, 391
- Spruit, H. C. 2002, *A&A*, 381, 923
- . 2013, ArXiv e-prints, arXiv:1301.5572
- Stein, J., & Wheeler, J. C. 2006, *ApJ*, 643, 1190

- Stevenson, D. J. 1979, *Geophysical and Astrophysical Fluid Dynamics*, 12, 139
- Stritzinger, M., Leibundgut, B., Walch, S., & Contardo, G. 2006, *A&A*, 450, 241
- Sullivan, M., Conley, A., Howell, D. A., et al. 2010, *MNRAS*, 406, 782
- Tamburello, V., Mayer, L., Shen, S., & Wadsley, J. 2015, *MNRAS*, 453, 2490
- Tassoul, J.-L. 2000, *Stellar Rotation*
- Taubenberger, S., Benetti, S., Childress, M., et al. 2011, *MNRAS*, 412, 2735
- Timmes, F. X., & Swesty, F. D. 2000, *ApJS*, 126, 501
- Toonen, S., Claeys, J. S. W., Mennekens, N., & Ruiter, A. J. 2014, *A&A*, 562, A14
- Toonen, S., Nelemans, G., & Portegies Zwart, S. 2012, *A&A*, 546, A70
- Tóth, G. 2000, *Journal of Computational Physics*, 161, 605
- Townsley, D. M., & Bildsten, L. 2004, *ApJ*, 600, 390
- Trac, H., Sills, A., & Pen, U.-L. 2007, *MNRAS*, 377, 997
- Tremblay, P.-E., & Bergeron, P. 2009, *ApJ*, 696, 1755
- Tremblay, P.-E., Cummings, J., Kalirai, J. S., et al. 2016, ArXiv e-prints, arXiv:1606.05292
- Tricco, T. 2015, in American Astronomical Society Meeting Abstracts, Vol. 225, American Astronomical Society Meeting Abstracts, 211.06
- Tsebrenko, D., & Soker, N. 2015, *MNRAS*, 447, 2568
- Tylenda, R., Hajduk, M., Kamiński, T., et al. 2011, *A&A*, 528, A114
- Uryū, K., & Eriguchi, Y. 1998, *ApJS*, 118, 563
- van Kerkwijk, M. H. 2013, *Philosophical Transactions of the Royal Society of London Series A*, 371, 20120236
- van Kerkwijk, M. H., Chang, P., & Justham, S. 2010, *ApJ*, 722, L157
- Van Leer, B. 2006, *Communications in Computational Physics*, 1, 138
- van Rossum, D. R., Kashyap, R., Fisher, R., et al. 2015, ArXiv e-prints, arXiv:1510.04286
- Vandenbroucke, B., & De Rijcke, S. 2016, *Astronomy and Computing*, 16, 109
- Verbunt, F., & Rappaport, S. 1988, *ApJ*, 332, 193
- Vogelsberger, M., Sijacki, D., Kereš, D., Springel, V., & Hernquist, L. 2012, *MNRAS*, 425, 3024
- Wadsley, J. W., Stadel, J., & Quinn, T. 2004, *New A*, 9, 137
- Waldman, R., Sauer, D., Livne, E., et al. 2011, *ApJ*, 738, 21

- Watts, A. L., Andersson, N., & Jones, D. I. 2005, *ApJ*, 618, L37
- Webbink, R. F. 1984, *ApJ*, 277, 355
- Wegg, C., & Phinney, E. S. 2012, *MNRAS*, 426, 427
- Whelan, J., & Iben, Jr., I. 1973, *ApJ*, 186, 1007
- Wickramasinghe, D. T., & Ferrario, L. 2005, *MNRAS*, 356, 1576
- Wickramasinghe, D. T., Tout, C. A., & Ferrario, L. 2014, *MNRAS*, 437, 675
- Williams, K. A., Montgomery, M. H., Winget, D. E., Falcon, R. E., & Bierwagen, M. 2016, *ApJ*, 817, 27
- Williams, K. A., Winget, D. E., Montgomery, M. H., et al. 2013, *ApJ*, 769, 123
- Woosley, S. E., & Kasen, D. 2011, *ApJ*, 734, 38
- Woosley, S. E., Kerstein, A. R., & Aspden, A. J. 2011, *ApJ*, 734, 37
- Woosley, S. E., Kerstein, A. R., Sankaran, V., Aspden, A. J., & Röpke, F. K. 2009, *ApJ*, 704, 255
- Woosley, S. E., & Weaver, T. A. 1994, *ApJ*, 423, 371
- Woosley, S. E., Wunsch, S., & Kuhlen, M. 2004, *ApJ*, 607, 921
- Yamanaka, M., Kawabata, K. S., Kinugasa, K., et al. 2009, *ApJ*, 707, L118
- Yoon, S.-C., Podsiadlowski, P., & Rosswog, S. 2007, *MNRAS*, 380, 933
- York, D. G., Adelman, J., Anderson, Jr., J. E., et al. 2000, *AJ*, 120, 1579
- Zhang, X., & Jeffery, C. S. 2012a, *MNRAS*, 426, L81
- . 2012b, *MNRAS*, 419, 452
- Zhang, X., Jeffery, C. S., Chen, X., & Han, Z. 2014, *MNRAS*, 445, 660
- Zhu, C., Chang, P., van Kerkwijk, M. H., & Wadsley, J. 2013, *ApJ*, 767, 164
- Zhu, C., Pakmor, R., van Kerkwijk, M. H., & Chang, P. 2015, *ApJ*, 806, L1
- Zingale, M., Almgren, A. S., Bell, J. B., Nonaka, A., & Woosley, S. E. 2009, *ApJ*, 704, 196
- Zingale, M., Nonaka, A., Almgren, A. S., et al. 2011, *ApJ*, 740, 8
- Zorotovic, M., Schreiber, M. R., & Gänsicke, B. T. 2011, *A&A*, 536, A42
- Zrake, J., & MacFadyen, A. I. 2013, *ApJ*, 769, L29